

12-2016

Design, Fabrication and Measurement of a Plasmonic Enhanced Terahertz Photoconductive Antenna

Nathan Matthias Burford
University of Arkansas, Fayetteville

Follow this and additional works at: <https://scholarworks.uark.edu/etd>



Part of the [Electromagnetics and Photonics Commons](#), and the [Electronic Devices and Semiconductor Manufacturing Commons](#)

Citation

Burford, N. M. (2016). Design, Fabrication and Measurement of a Plasmonic Enhanced Terahertz Photoconductive Antenna. *Graduate Theses and Dissertations* Retrieved from <https://scholarworks.uark.edu/etd/1841>

This Dissertation is brought to you for free and open access by ScholarWorks@UARK. It has been accepted for inclusion in Graduate Theses and Dissertations by an authorized administrator of ScholarWorks@UARK. For more information, please contact uarepos@uark.edu.

Design, Fabrication and Measurement of a Plasmonic Enhanced Terahertz Photoconductive Antenna

A dissertation submitted in partial fulfillment
of the requirements for the degree of
Doctor of Philosophy in Microelectronics-Photonics

by

Nathan M. Burford
Southeast Missouri State University
Bachelor of Science in Physics, Engineering Physics, 2011
University of Arkansas
Master of Science in Microelectronics-Photonics, 2013

December 2016
University of Arkansas

This dissertation is approved for recommendation to the Graduate Council.

Dr. Magda El-Shenawee
Dissertation Director

Dr. Shui-Qing Yu
Committee Member

Dr. Morgan Ware
Committee Member

Dr. Joseph Herzog
Committee Member

Dr. Rick Wise
Ex-Officio Member

The following signatories attest that all software used in this dissertation was legally licensed for use by Nathan M. Burford for research purposes and publication.

Mr. Nathan M. Burford, Student

Dr. Magda El-Shenawee, Dissertation Director

This dissertation was submitted to <http://www.turnitin.com> for plagiarism review by the TurnItIn company's software. The signatories have examined the report on this dissertation that was returned by TurnItIn and attest that, in their opinion, the items highlighted by the software are incidental to common usage and are not plagiarized material.

Dr. Rick Wise, Program Director

Dr. Magda El-Shenawee, Dissertation Director

Abstract

Generation of broadband terahertz (THz) pulses from ultrafast photoconductive antennas (PCAs) is an attractive method for THz spectroscopy and imaging. This provides a wide frequency bandwidth (0.1-4 THz) as well as the straightforward recovery of both the magnitude and phase of the transmitted and/or reflected signals. The achieved output THz power is low, approximately a few microwatts. This is due to the poor conversion of the femtosecond laser used as the optical pump to useable current inside the antenna semiconducting material. The majority of THz power comes from the photocarriers generated within ~ 100 nm distance from the antenna electrodes. However, the optical beam covers larger spot size, therefore much of the absorbed optical photons do not contribute to the THz power.

The goal of this work is to advance the design, fabrication, and measurement of THz-PCAs to generate significantly improved output power. This work proposed a plasmonic enhanced thin-film photoconductive antenna to enhance optical carrier generation in the PCA. The electromagnetic wave equations were solved in order to compute the enhanced plasmonic field in the semiconductor. The Poisson's and the drift-diffusion equations were solved in order to compute the carrier dynamics inside of the semiconductor. A parametric optimization was implemented in order to design the plasmonic nanodisks and the thickness of the ultrathin photoconductive layer. These solutions and optimizations were achieved using the commercial package COMSOL[®] Multiphysics model. The PCAs' fabrication was accomplished using the electron beam lithography for patterning the plasmonic nanostructures, the molecular beam epitaxy for the sample growth, the lapping/selective etching for the epitaxial liftoff, and standard microfabrication practices for patterning the antenna and device packaging. The PCA was characterized utilizing a tunable pulsed laser system with a 100 fs pulse width for the optical

excitation and a Gentec-EO pyroelectric power detector for measurement of the output THz power. Also, the spectral characterization of the PCA was conducted, in collaboration with Teraview LTD in their site at UK, using a THz time-domain spectroscopy experimental set-up. The results demonstrate the enhancement in the output THz power of the plasmonic thin-film PCAs in comparison with conventional THz-PCAs.

Acknowledgements

The work in this dissertation was supported in part by the National Science Foundation under grants numbers 1548550 and 1006927, MRI numbers 1228958 and 0722625 and cyber infrastructure award number EP-0918970. Any opinions, findings, and conclusions or recommendations expressed in this material are those of the author and do not necessarily reflect the views of the National Science Foundation. This work was also supported through the University of Arkansas Engineering Research and Innovation Seed Funding Program and the University of Arkansas Doctoral Academy Fellowship.

I would like to express sincere appreciation to my advising professor, Dr. Magda El-Shenawee. Working for you these five and a half years has been a great honor. Experiencing first-hand the time and effort you put into the development of your students has been an incredibly humbling experience. I'm certain that my future will be forever changed (for the better) through having the privilege of working for you.

A special thanks to Ken Vickers. If it were not for your dedication to outreach and growth of the MicroEP program, I would have never ended up at the University of Arkansas. Needless to say, my life would look quite different. Thank you to Dr. Rick Wise, Renee Hearon, and the MicroEP community for all of their support throughout the years. Thank you also to the faculty and staff of the Electrical Engineering Department; Dr. Juan Balda for always having TA positions available, Connie Howard and Sharon Brasko for taking care of funding, purchasing and travel, and Daniel Klein for ensuring that the computers and network were always running efficiently. Achieving a Ph.D. would not be possible without such a hard working support system.

The ambitious goals of this research were only made possible through the help of several individuals. Thank you to Dr. Vasyl Kunets for the growth of the LT-GaAs sample used in this work, Andrian Kuchuk for training and technical support of the Institute for Nanoscience and Engineering's microfabrication facilities, Dr. Joseph Herzog and Stephen Bauman for their assistance with electron beam lithography, and Dr. Shui-Qing Yu for providing experimental space and equipment. Thank you also to Mike Evans of Teraview LTD. I feel that I've gained more knowledge of the experimental considerations of terahertz devices in my five days spent at Teraview than I could have gained through another three years of Ph.D. work. The help from all of these individuals was greatly appreciated.

Thank you to my amazing fiancé, Grace. Dating someone through two years of Ph.D. work and experiencing an engagement as they are finishing their dissertation cannot be easy, but you have never wavered in your support. Thank you also to my siblings, Janessa and Matthew, for their inspiration over the years.

Above all, thank you to my parents, Lenny and Jane Burford. I am blessed beyond understanding to have been born to such supportive parents. Thank you for being there and having confidence in me every step of the way.

Table of Contents

Chapter 1. Introduction	1
1.1. Introduction to THz Photoconductive Antennas.....	1
1.1.1. Applications of THz Imaging and Spectroscopy	3
1.1.2. Theory of Terahertz Photoconductive Antennas (PCAs)	4
1.2. Photoconductive Material Development.....	9
1.2.1. Challenges	9
1.2.2. Gallium Arsenide (GaAs)	10
1.2.3. InGaAs (InGaAs)	15
1.2.4. Indium Gallium Arsenide/Indium Aluminum Arsenide (InGa(Al)As) Heterostructures	16
1.2.5. Other Group III-V Materials.....	19
1.2.6. Summary and Outlook	20
1.3. Large Area Emitters	20
1.3.1. Challenges.....	20
1.3.2. Large Aperture Dipoles.....	21
1.3.3. Interdigitated Electrodes	22
1.3.4. Dipole Arrays.....	26
1.3.5. Summary and Outlook	27
1.4. Plasmonic Nanostructures.....	28
1.4.1. Challenges.....	28
1.4.2. Early Examples of Unbiased Nanostructured THz Emitters	29
1.4.3. Gap-Located Nanostructures	32
1.4.4. Nanostructured Electrodes	35
1.4.5. Summary and Outlook	39

1.5. Broadband Performance.....	39
1.5.1. Challenges.....	39
1.5.2. Broadband Dipole Antenna.....	40
1.5.3. Ultrabroadband Emission and Detection	42
1.5.4. Summary and Outlook	44
1.6. Concluding Remarks.....	44
Chapter 2. Plasmonic Thin-Film Terahertz Emitter Design and Computational Modeling	45
2.1. Conceptual Plasmonic Thin-Film Terahertz Emitter Design.....	45
2.2. Approximations for Reducing the Computational Domain	48
2.3. Finite Element Method Modeling using COMSOL [®] Multiphysics.....	49
2.4. Optical Response	50
2.5. Electrical Response	54
2.6. Approximations of the Mathematical Formulation.....	56
2.7. Model Validation	57
2.8. Proposed THz PCA Electrode Configurations	62
2.9. Numerical Convergence.....	66
2.10. Optimization of Nanodisk Array Geometry	67
2.11. Optical Field Comparison of THz PCA Electrode Configurations	74
2.12. Comparison of Optically Induced Photocurrent in the THz PCA Configurations	76
2.13. Discussion of the Carrier Screening Effect.....	81
2.14. Terahertz Emission from the Calculated Optically Induced Photocurrent	82
Chapter 3. Fabrication Process of the Plasmonic Thin-Film THz Emitter	86
3.1. Overview of the Fabrication Process	86
3.2. First-Round of Plasmonic Thin-Film THz Emitter Fabrication	90
3.2.1. MBE Wafer Growth.....	90

3.2.2. Photolithography Patterning of the Antenna Electrodes.....	90
3.2.3. Wafer Mounting and Substrate Removal.....	96
3.2.4. Electron Beam Lithography.....	103
3.2.5. Device Packaging.....	111
3.3. Failure Analysis of First-Round Prototype Devices.....	114
3.3.1. I-V Characteristics.....	115
3.3.2. THz Transmission Characterization of Substrate and Adhesive Materials.....	117
3.3.3. Modeling of THz Transmission Through PCA Substrate.....	121
3.4. Second-Round of Plasmonic Thin-Film THz Emitter Fabrication.....	131
3.4.1. MBE Wafer Growth.....	131
3.4.2. Photolithography Patterning of the Antenna Electrodes.....	134
3.4.3. Wafer Mounting and Substrate Removal.....	139
3.4.4. Device Packaging.....	140
Chapter 4. Experimental Characterization of the Fabricated Devices.....	143
4.1. Pyroelectric Detection of Relative Emitted THz Power.....	143
4.2. Methods for Analyzing the THz Spectral Characteristics.....	148
4.3. Spectral Characterization in a THz Time-Domain Spectroscopy System.....	152
Chapter 5. Summary and Conclusions.....	171
Appendix A: Description of Research for Popular Publication.....	191
Appendix B: Executive Summary of Newly Created Intellectual Property.....	194
Appendix C: Potential Patent and Commercialization Aspects of listed Intellectual Property Items.....	195
C.1 Patentability of Intellectual Property (Could Each Item Be Patented).....	195
C.2 Commercialization Prospects (Should Each Item Be Patented).....	195
C.3 Possible Prior Disclosure of IP.....	196
Appendix D: Broader Impact of Research.....	197

D.1 Applicability of Research Methods to Other Problems	197
D.2 Impacts of Research Results on U.S. and Global Society	197
D.3 Impact of Research Results on the Environment	198
Appendix E: Microsoft Project for Ph.D. MicroEP Degree Plan	199
Appendix F: Identification of All Software Used in Research and Dissertation Generation.....	201
Appendix G: All Publications Published, Submitted and Planned	202
Appendix H: Copyright Permissions	204

List of Figures

Figure 1.1.1: The electromagnetic spectrum.....	1
Figure 1.1.2: Output power versus frequency for various THz source technologies [2].....	2
Figure 1.1.2.1: Illustrative example of pulsed THz generation in a PCA. (top) Femtosecond optical pulse propagates into the photoconductor, generates a transient photocurrent which drives the antenna and is reemitted as a broadband THz pulse. (bottom) Time profile of the carrier generation (red trace) and photocurrent in the antenna gap for photoconductive material with (gray trace) short carrier lifetime and (blue trace) long carrier lifetime.	5
Figure 1.1.2.2: Schematic diagram of the typical configuration of electro-optic sampling of THz pulses in a time-domain spectroscopy system.	7
Figure 1.2.2.1: (Left) TEM photograph of annealed LT-GaAs layer and (right) sheet conductance and cluster diameter as functions of annealing temperature. Reproduced from [53] with permission from the Electronics and Telecommunications Research Institute.	13
Figure 1.2.4.1: (a) Embedded photoconductor; (b) electron trapping; (c) multilayer structure. Reprinted from [107] with permission from OSA Publishing.....	18
Figure 1.3.3.1: (a) Micrograph of terahertz array antenna device. (b) Cross-sectional view of terahertz antenna array. Reprinted from [123], with permission of AIP Publishing.	23
Figure 1.4.2.1: (a) Schematic diagrams of the nanostructured Au/Cu ₂ O Schotky junction THz emitter. The pump laser pulses are incident on the sample, generating THz pulses. A nanograting is fabricated at the interface to facilitate the excitation of surface plasmons. (b, c) False color SEM image of the grating after the deposition of Au and Cu ₂ O, respectively. Reprinted with permission from [149]. Copyright 2016 American Chemical Society.	31
Figure 1.4.3.1: (a) SEM image of the 20 μm dipole on SI-GaAs substrate. (b) The active area of the hexagonal plasmonic array. (c) The active area of the strip plasmonic array. The diagram shows apex angle θ , gap size d and periodicity p . Reprinted from [153] with permission from OSA Publishing.	34
Figure 1.4.4.1: Optical microscope image of H-dipole structure and SEM of the fabricated nano-electrodes. Reprinted with permission from [160] under the Creative Commons Attribution 4.0 International License.	35
Figure 1.4.4.2: THz emission from the large-aperture PCAs: (a) Time-domain curves. (b) FFT spectra. Reprinted with permission from [160] under the Creative Commons Attribution 4.0 International License.....	38

Figure 1.5.3.1: (a) The temporal THz wave form and, (b) its corresponding Fourier transform amplitude spectrum (upper trace, solid line), together with spectrum measured in the presence of PTFE sample (lower trace, dotted line). Reprinted from [175], with permission of AIP Publishing.	43
Figure 2.1.1: Illustration of the proposed plasmonic thin-film THz-PCA design, 3D isometric view of the THz-PCA mounted on a Si THz lens (not to scale).	46
Figure 2.1.2: x-y plane top view of the device, antenna electrode locations outlined by the dashed black lines. Computational domain is indicated by the dot-dashed outline (not to scale).	47
Figure 2.1.3: x-z plane cross section view, nanodisk array located on top of the 120 nm thick LT-GaAs photoconductive layer, THz-PCA anode and cathode located on the bottom of the LT-GaAs. Device is mounted with adhesive to the Si lens for mechanical support as well as coupling of the THz radiation out of the device. Computational domain is indicated by the dot-dashed outline (not to scale).	48
Figure 2.7.1: Comparison of the calculated photocurrent at the center of the gap. Solid trace represents the results found using this model, X marks are points traced from Figure 8 in Moreno et al. [46].	59
Figure 2.7.2: Optical power density at the center of the gap vs. depth inside the LT-GaAs. Dashed line represents the Beer-Lambert approximation utilized in [46], solid line represents this work, the full-wave solution of Maxwell's equation.	60
Figure 2.7.3: Comparison of the calculated photocurrent enhancement to experimentally values reported by Berry et al. [71]. Solid line with circle marks represent calculated results using this model, X marks represent the reference results calculated from the inset data of Figure 3b in the work of Berry et al. [71].	62
Figure 2.8.1: Anode current versus time for a conventional style THz-PCA under 100 fs pulsed optical excitation. Carrier lifetime varied from 0.48 ps (solid line) to 48 ps (dashed line).	63
Figure 2.8.2: Illustrations of the various THz-PCA electrode designs considered in this work. (a) bottom-located-thin-film, (b) plasmonic bottom-located-thin-film, (c) plasmonic nanograting [71] top-located electrodes, and (d) conventional top-located electrodes.	64
Figure 2.9.1: Anode photocurrent vs. time for the P-BLTF as a function of total number of mesh cells utilized in the FEM solution.	66
Figure 2.9.2: Anode current pulse FWHM (left) and peak (right) for the P-BLTF design as a function of total number of mesh elements.	67
Figure 2.10.1: Cross section illustration of the computational domain utilized in the nanodisk array optimization.	68

Figure 2.10.2: Average electric field in the LT-GaAs layer without nanodisks as a function of thickness T	69
Figure 2.10.3: 2D plots of the average electric field inside the LT-GaAs layer as a function of incident wavelength and (top) radius R , (middle) edge-to-edge spacing d , and (bottom) height h of the gold nanodisks.	70
Figure 2.10.4: Average peak electric field in the LT-GaAs layer as a function of nanodisk height for constant $R = 100$ nm and $d = 320$ nm.	71
Figure 2.10.5: Average peak electric field in the LT-GaAs layer as a function of incident wavelength and nanodisk height for constant $R = 100$ nm and $d = 320$ nm.	72
Figure 2.10.6: (a) Average electric field absorbed in the LT-GaAs layer under 1 V/m optical excitation as a function of excitation wavelength and (b) optical power reflectance spectrum. Dashed and solid lines represent the BLTF and P-BLTF designs, respectively. .	73
Figure 2.11.1: Electric field distribution at partial 2D cross sections of the computational domain for the conventional (a), nanograting (b), P-BLTF (c) and BLTF (d) designs. Cross sections centered at the focus of the optical excitation.	75
Figure 2.12.1: Anode photocurrent response versus time for each of the four THz-PCA electrode designs.	76
Figure 2.12.2: Peak anode photocurrent of each of the four electrode designs as a function of carrier recombination time $\tau_{n,p}$	79
Figure 2.12.3: FWHM of each of the four electrode designs as a function of carrier recombination time $\tau_{n,p}$	80
Figure 2.14.1: Illustration of the computational domain representation of the THz PCA. (a) y-z plane, (b) x-z plane, (c) isometric view, (d) full x-y plane, and (e) expanded x-y plane view of the dipole antenna.	84
Figure 2.14.2: Time step convergence of the emitted THz electric field and comparison between COMSOL [®] Multiphysics and ANSYS [®] HFSS.	85
Figure 3.1.1 Illustrative overview of the plasmonic thin-film THz emitter fabrication. (a) MBE wafer growth, (b) antenna electrodes patterning, (c) flip-mounting to Si carrier, (d) substrate removal, and (e) electron beam lithography patterning of metal nanodisk array.	87
Figure 3.1.2: Summary of process steps required for each of the three THz PCA designs.	89
Figure 3.2.2.1: Layouts of the microstrip, dipole, and bowtie (white color represents metal).	91
Figure 3.2.2.2: Pattern layout of the first round photomask.	92

Figure 3.2.2.3: Illustrated overview of the first round photolithography process.	93
Figure 3.2.2.4: Microscope images of the developed photoresist on LT-GaAs for varying exposure time. Image is taken over the bias pad of the antenna pattern.	94
Figure 3.2.2.5: Microscope image of bowtie antenna pattern after metallization and liftoff. Zoomed images shows sonication induced damage to the microstrip line.	95
Figure 3.2.3.1: Illustrate of flip-mounting of the sample to the Si carrier substrate.	96
Figure 3.2.3.2: Illustration of the Logitech PM5 Lapping and Polishing System.	97
Figure 3.2.3.3: MBE GaAs wafer sample flip mounted onto an Si carrier wafer just as the $\text{Al}_{0.85}\text{Ga}_{0.15}\text{As}$ layer is starting to be exposed (left) and just after the $\text{Al}_{0.85}\text{Ga}_{0.15}\text{As}$ is fully exposed (right).	99
Figure 3.2.3.4: Illustration of a non-level mounted GaAs sample and the non-uniform lapping and etching it causes.	100
Figure 3.2.3.5: Photograph of a non-level mounted MBE GaAs sample on glass during the substrate removal etching process.	101
Figure 3.2.3.6: Microscope image of a BLTF THz PCA fabricated using the first round fabrication methods.	102
Figure 3.2.4.1: Measured nanodisk spacing S_{actual} for an array with input nanodisk spacing of 520 nm (top vertical axis) and absolute error (bottom vertical axis) as a function magnification scale (horizontal axis).	104
Figure 3.2.4.2: Difference in d_{actual} and d_{input} for d_{input} varying from 100 to 200 nm as a function of ED.	105
Figure 3.2.4.3: SEM images of Ti/Au nanodisk arrays fabricated on GaAs using EBL. $d_{\text{input}} = 150$ nm and (a) ED = 600 $\mu\text{C}/\text{cm}^2$, (b) ED = 300 $\mu\text{C}/\text{cm}^2$, and (b) ED = 200 $\mu\text{C}/\text{cm}^2$	106
Figure 3.2.4.4: Illustration of the method used for aligning the THz-PCA pattern with the EBL system.	108
Figure 3.2.4.5: Microscope and SEM image of P-BLTF anode after nanodisk array fabrication.	110
Figure 3.2.5.1: PCB and switching box for device packaging and testing.	111
Figure 3.2.5.2: Cross section illustration of the device mounted to the PCB.	112
Figure 3.3.1.1: Hypothesized gap resistance contributions in the P-BLTF device.	115
Figure 3.3.1.2: Average I-V characteristics of the first round fabricated devices.	116

Figure 3.3.2.1: Photograph of the Teraview TPS Spectra 300 system utilized to characterized the THz properties of the antenna materials.	118
Figure 3.3.2.2: Photograph of the JB Weld and SU-8 2000.5 sample preparation for THz spectroscopic characterization.	119
Figure 3.3.2.3: Real and imaginary refractive index values calculated from THz TDS transmission measurements of the various substrate materials.....	120
Figure 3.3.3.1: Geometry of the multi-layer transmission analysis of the THz PCA structure using the simple model.	121
Figure 3.3.3.2: Convergence of Equation (3.3.3.1) to Equation (3.3.3.2) as d_1 is decreased.	124
Figure 3.3.3.3: Effect of changing the PCA substrate material with no adhesive layer present.	125
Figure 3.3.3.4: THz transmission through various substrate materials with addition of 1, 5, 10 and 50 μm thick JB Weld Epoxy adhesive layers.....	126
Figure 3.3.3.5: THz transmission through various substrate materials with addition of 1, 5, 10 and 50 μm thick SU-8 2000.5 adhesive layers.	127
Figure 3.3.3.6: Fourier transform of the electric field transmitted into the Si lens layer calculated using COMSOL [®] for the various substrate materials without adhesive layers.	129
Figure 3.3.3.7: Fourier transform of the electric field transmitted into the Si lens layer calculated using COMSOL [®] for the various substrate materials, with and without 5 (dashed) and 50 (solid) μm JB Weld (blue) and SU-8 (red) adhesive layers.	130
Figure 3.4.1.1: Comparison of the second round MBE wafer structure with the original first round structure.	132
Figure 3.4.1.2: 4 μm gap resistance as a function of 10 min duration anneal temperature.	134
Figure 3.4.2.1: Photomask of the second generation fabrication process. (a) full photomask, (b) single device, and (c) dipole antenna structure.	135
Figure 3.4.2.2: Second round photolithography process implementing the image reversal process to generate negative photoresist sidewalls.	137
Figure 3.4.3.1: Photograph of the bonding of THz antennas on MBE GaAs sample to the HRFZ Si substrates prior to GaAs substrate removal.	139
Figure 3.4.4.1: Illustration of the photolithography pattern utilized to extend the antenna electrodes onto the Si surface of the sample.	141

Figure 3.4.4.2: Image of the final device mounted to the leadless chip carrier and zoomed image of the device surface. Antenna electrodes under the LT-GaAs layer are not visible due to limitations of the microscope used to acquire this image.	142
Figure 4.1.1: Illustration (top) and photograph (bottom) of the experimental setup for pyroelectric detection of the average output THz power of the devices.	144
Figure 4.1.2: Illustration of the method utilized for visualizing the focused optical excitation beam location on the THz PCA surface.	146
Figure 4.1.3: Output THz power versus optical pump power for devices C6 (red), T6 (green) and P6 (blue).	147
Figure 4.1.4: Optical to THz conversion efficiency versus optical pump power devices C6 (red), T6 (green) and P6 (blue).	148
Figure 4.2.1: Measured time-dependent electric field waveform of a THz pulse emitted from device C2 (left) and frequency spectrum acquired from the Fourier transform (right).	149
Figure 4.2.2: Frequency spectrum of the measured time-dependent electric field waveform of a THz pulse emitted from device C2 with (red solid) and without (dashed black) water absorption lines present in the trace.	150
Figure 4.2.3: Illustration of the method for utilizing a 2 mm aperture to prevent non-dipole THz emission from reaching the receiver.	151
Figure 4.3.1: Time-domain measurements of the emitted THz pulses from devices C2 (red), T2 (green) and P2 (blue) under 5 mW optical excitation and 50 V bias voltage.	153
Figure 4.3.2: Fourier transform spectra of the time-domain measurements of the emitted THz pulses from devices C2 (red), T2 (green) and P2 (blue) under 5 mW optical excitation and 50 V bias voltage.	154
Figure 4.3.3: Time-domain measurements (left) and Fourier transform spectra (right) of the emitted THz pulses from device C2 as a function of optical pump power.	155
Figure 4.3.4: Time-domain measurements (left) and Fourier transform spectra (right) of the emitted THz pulses from device T2 as a function of optical pump power.	156
Figure 4.3.5: Time-domain measurements (left) and Fourier transform spectra (right) of the emitted THz pulses from device P2 as a function of optical pump power.	157
Figure 4.3.6: Peak-to-peak THz field extrapolated from time-domain measurements as a function of optical pump power for devices C2 (red), T2 (green) and P2 (blue).	158
Figure 4.3.7: THz TSP extrapolated from frequency-domain spectrum as a function of optical pump power for devices C2 (red), T2 (green) and P2 (blue).	159

Figure 4.3.8: Fourier transform spectra of the time-domain measurements of devices C2 (blue and red) and reference (black and gray) both with (blue and gray) and without (red and black) 2 mm aperture.	160
Figure 4.3.9: Fourier transform spectra of the time-domain measurements of devices T2 (blue and red) and reference (black and gray) both with (blue and gray) and without (red and black) 2 mm aperture.	161
Figure 4.3.10: Fourier transform spectra of the time-domain measurements of devices P2 (blue and red) and reference (black and gray) both with (blue and gray) and without (red and black) 2 mm aperture.	162
Figure 4.3.11: Time-domain measurements of the emitted THz pulses from devices Reference (black), C2 (solid red) and C4 (dashed red).....	163
Figure 4.3.12: Time-domain measurements of the emitted THz pulses from devices Reference (black), T1 (solid green), T2 (large dash green), T4 (medium dash green) and T5 (small dash green).....	164
Figure 4.3.13: Time-domain measurements of the emitted THz pulses from devices Reference (black), P1 (solid blue), P2 (large dash blue) and P3 (medium dash blue).	165
Figure 4.3.14: Fourier transform spectra of the time-domain measurements of the emitted THz pulses from devices Reference (black), C2 (solid red), C4 (dashed red), T1 (solid green), T2 (large dash green), T4 (medium dash green), T5 (small dash green), P1 (solid blue), P2 (large dash blue) and P3 (small dash blue). All measurements taken at 50 V bias voltage and 10 mW optical pump power.....	167
Figure 4.3.15: Total output THz power for all devices.....	168
Figure 4.3.16: Output THz power versus bias voltage for devices C2 (solid red), C4 (dashed red), T2 (solid green), T4 (dashed green), P2 (solid blue) and P3 (dashed blue)..	169

List of Tables

Table 1.2.6.1: Summary of photoconductive material development for THz PCAs.....	20
Table 1.3.5.1: Summary of large area emitter THz PCAs	27
Table 1.4.5.1: Summary of plasmonic nanostructure enhanced THz PCAs.....	39
Table 1.5.4.1: Summary of broadband performance of THz PCAs.....	44
Table 2.4.1: Defining parameters with typical values for femtosecond laser excitation of THz PCAs	51
Table 2.5.1: Electrical Properties and Constants of Equations 2.5.1-2.5.4.....	55
Table 2.7.1: Optical Properties and Constants of Equations (2.4.7)-(2.5.4) for Validation Study with Moreno et al. [46].	58
Table 2.7.2: Optical Properties and Constants of Equations 2.4.7-2.5.4 for Validation Study with Berry et al. [71].	61
Table 2.8.1: Optical Properties and Constants of Equations 2.4.7-2.5.4 for Comparison Study of the BLTF, P-BLFT, Nanograting and Conventional PCA Designs.	65
Table 2.13.1: Summary of the Expected Carrier Screening Effect.....	82
Table 3.2.4.1: Measured S_{actual} and d_{actual} as a function of S_{input} and d_{input} . Optimum parameters are highlighted in bold.....	107
Table 3.2.5.1: Dark and light photocurrent measurements of the first round devices under a DC 10 V bias.....	114
Table 3.4.2.1: Optimization results of the second round photolithography process.....	138

Chapter 1. Introduction

1.1. Introduction to THz Photoconductive Antennas

Terahertz (THz) is the name given to the region of the electromagnetic spectrum lying between the microwave band (<100 GHz) and the far infrared band (>10 THz) [1]. This region is often referred to as “the last frontier” for electromagnetic waves, since historically there has been comparatively little work to observe the science and develop the applications of THz waves. The reason for this is simple; efficient generation and detection of THz is an exceedingly non-trivial problem. As shown in Figure 1.1.1, THz lies in the transitional region of the electromagnetic spectrum, between the classically described electronics region (radio, microwaves and millimeter waves) and the photonic region (infrared, visible, UV and x-ray) where the quantum nature of light becomes dominant.

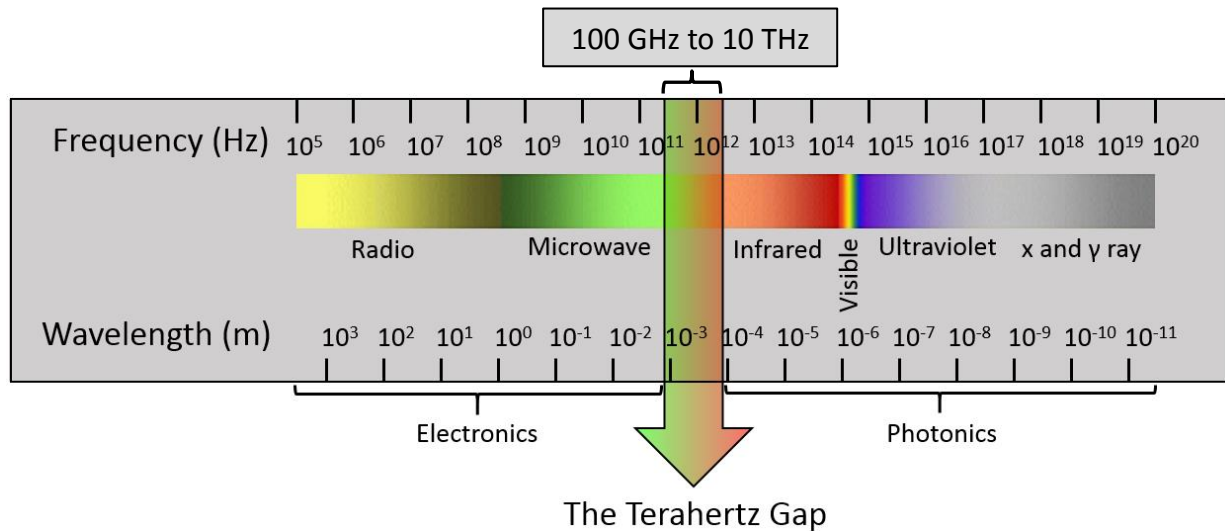


Figure 1.1.1: The electromagnetic spectrum.

Approaching the THz regime from either of these regions comes with unique challenges, as illustrated in Figure 1.1.2. Here, the output power as a function of frequency is plotted for

various THz source technologies [2]. Increasing the operating frequency of microwave devices is limited by the carrier mobility of the oscillating semiconductor [3]. On the other hand, reducing the energy of emitted photons generated by electron transitions in a semiconductor is inhibited by the fact that the energy of THz photons is less than the thermal energy at room temperature [4]. Other methods have been utilized which combine aspects of both photonics and electronics [5], [6], though these come with their own list of challenges.

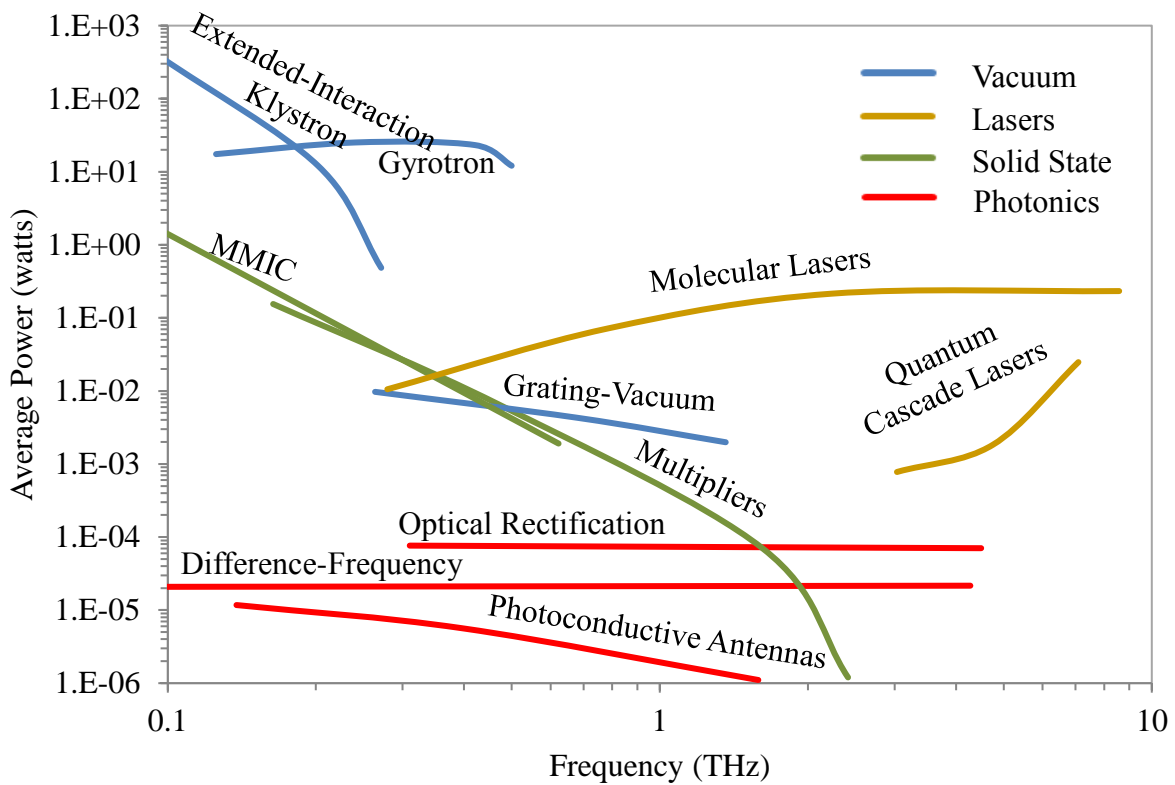


Figure 1.1.2: Output power versus frequency for various THz source technologies [2].

However, the challenges facing the various methods of THz generation and detection have not stopped the development of this technology. This dissertation is organized as follows. In this chapter, a brief overview of the applications of THz imaging and spectroscopy technology will be given, along with the working mechanisms of THz photoconductive antennas (PCAs).

Following this will be an in-depth review of the current literature focused mostly on the various key aspects of THz photoconductive antenna (PCA) technology, while selected other technologies such as photomixers, unbiased surface emission, and optical rectification will be discussed briefly. In Chapter 2, the proposed plasmonic thin-film THz PCA device will be presented, including a conceptual overview of the device working mechanisms. The theory and validation of a computational model developed using COMSOL[®] Multiphysics will be discussed, along with numerical comparison of the proposed plasmonic thin-film device with other proposed devices from the literature. Chapter 3 will present details of the plasmonic thin-film THz PCA fabrication process. That chapter will be divided into fabrication process for the first round of devices, failure mode analysis of the first round devices, and modified fabrication process for the second round of devices. The experimental results will be summarized in Chapter 4, including THz power measurements and spectral characterization of three variations of the device design. Chapter 5 will summarize and conclude the work, as well as discuss avenues for future research in this area.

1.1.1. Applications of THz Imaging and Spectroscopy

Although THz technology is not nearly as mature as the technology of other regions of the electromagnetic spectrum, many practical applications have been proposed and are currently under development. One of the earliest commercial applications of THz imaging and spectroscopy is nondestructive screening of pharmaceuticals. Changes in solid state crystal form [6] and spectral fingerprinting of chemical compounds have been demonstrated [7], [8]. Spectral fingerprinting has been proposed for security applications as well, since the nondestructive nature of THz waves could allow penetration into materials to detect hidden narcotics and explosives [9]–[11]. Many works have studied the potential use of THz imaging and time-

domain reflectometry as a quality control tool in electronics fabrication and packaging [12]–[20]. Biomedical imaging using THz radiation has been proposed and studied for the purpose of cancer imaging [21]–[27] and burn wound assessment [28]–[30]. Several in-depth reviews are available for the wide range of applications of THz imaging and spectroscopy technology [9], [10], [23], [31]–[37].

1.1.2. Theory of Terahertz Photoconductive Antennas (PCAs)

Emission and detection of pulsed broadband THz radiation from optically pumped PCAs were first accomplished in the late 1980's by the research groups of THz pioneers David Auston [38]–[41] and Daniel Grischkowsky [1], [42], [43]. The concept of generation of pulsed THz radiation from a PCA is illustrated in Figure 1.1.2.1(a). Here, an example of a femtosecond optical pulse with a pulse duration of less than 1 ps is incident on a PCA. The PCA consists of a DC biased metal dipole antenna patterned on a photoconductive substrate. The optical pulse is incident on the antenna gap, propagates into the photoconductor, and begins to generate photocarriers inside the photoconductor as it is absorbed. The generated photocarriers are accelerated in the DC bias field, producing a transient photocurrent which drives the dipole antenna and ultimately re-emits as a THz frequency pulse [38]–[41], [44], [45]. The transient response of the PCA is illustrated in Figure 1.1.2.1(b-e). As the optical pulse is absorbed in the photoconductor, carriers are generated at a rate proportional to optical pulse (red trace). The photocarriers respond by accelerating along the DC bias field, thus generating a transient photocurrent with a rise time approximately proportional to the incident optical pulse rise time (gray trace). After the photocurrent peaks, as shown in Figure 1.1.2.1(d), the decay time is then

dictated by the electrical properties of the photoconductor, rather than the temporal profile of the optical pulse [44].

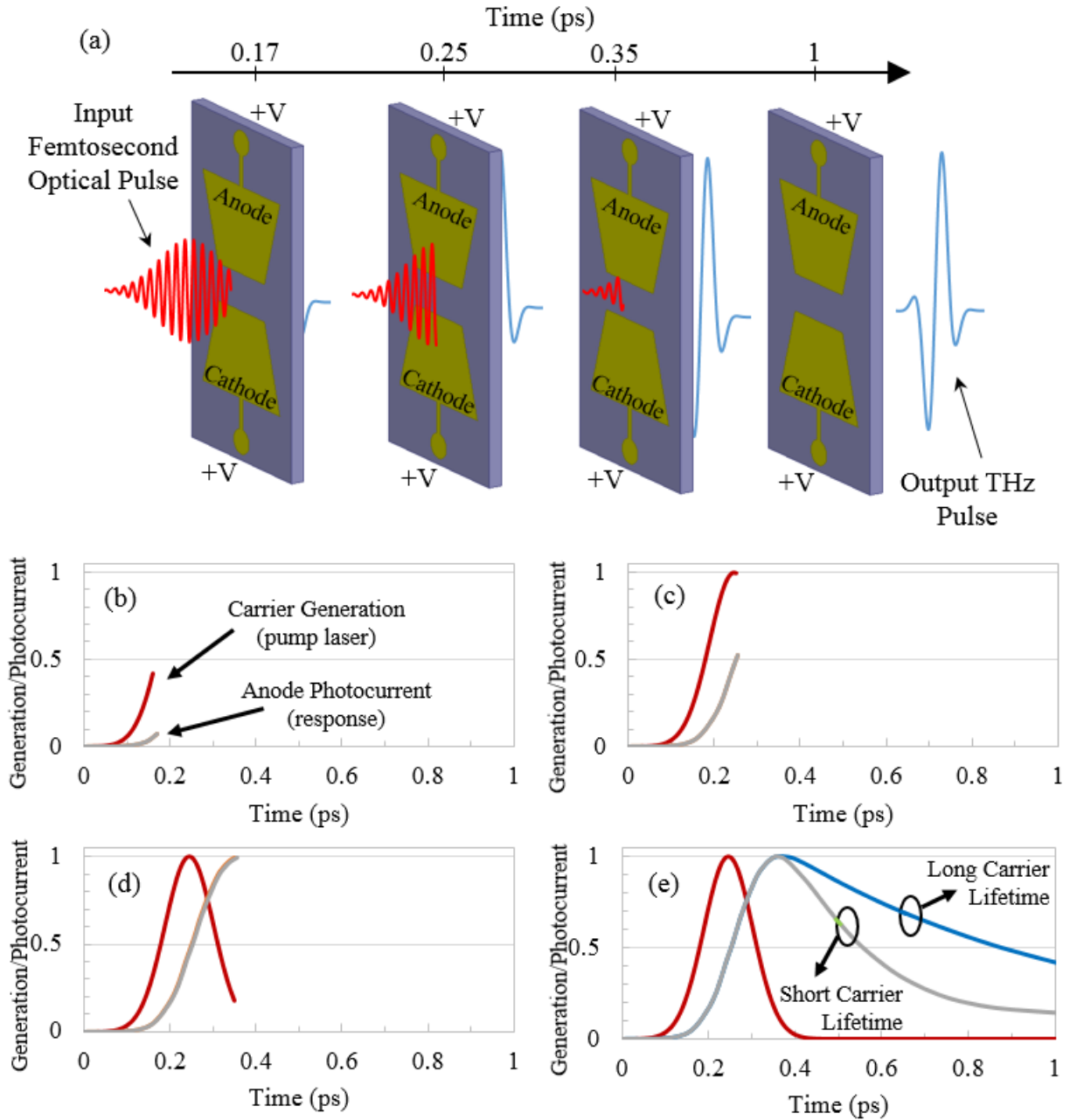


Figure 1.1.2.1: Illustrative example of pulsed THz generation in a PCA. (top) Femtosecond optical pulse propagates into the photoconductor, generates a transient photocurrent which drives the antenna and is reemitted as a broadband THz pulse. (bottom) Time profile of the carrier generation (red trace) and photocurrent in the antenna gap for photoconductive material with (gray trace) short carrier lifetime and (blue trace) long carrier lifetime.

As shown in Figure 1.1.2.1(e), if the photoconductor has a short carrier lifetime (gray trace) the photocarriers generated by the optical pulse will begin to recombine immediately after the optical pulse is fully absorbed [44]–[46]. In contrast, if the photoconductor has a long carrier lifetime (blue trace) the generated photocarriers will continue to contribute to the photocurrent after the optical pulse is fully absorbed. This has the effect of broadening the photocurrent pulse, which would in turn broaden the output pulse and reduce the overall THz frequency bandwidth. To prevent this, photoconductors with sub-picosecond carrier lifetime are often utilized, with low temperature grown gallium arsenide (LT-GaAs) being the most common [47]–[60].

Detection of the emitted THz pulses is often accomplished either through the use of calibrated THz power detectors such as bolometers [31], [51], [61]–[64] and pyroelectric detectors [10], [65]–[69], or more completely by electro-optic sampling of the THz pulse in a time-domain spectroscopy (TDS) configuration [8], [39], [40], [44], [67], [70]. The later method allows extraction of the temporal profile of the THz field. The schematic of a THz time-domain system is shown in Figure 1.1.2.2. THz is generated through the previously described conversion of a femtosecond optical pulse to broadband THz pulse at the emitter [38]–[41], [44], [45]. The emitter is biased with a DC voltage and often the time-averaged photocurrent will be measured as well. In general, the power of the emitted THz pulse is proportional to the measured photocurrent across the dipole antenna [44], [46], [71], [72].

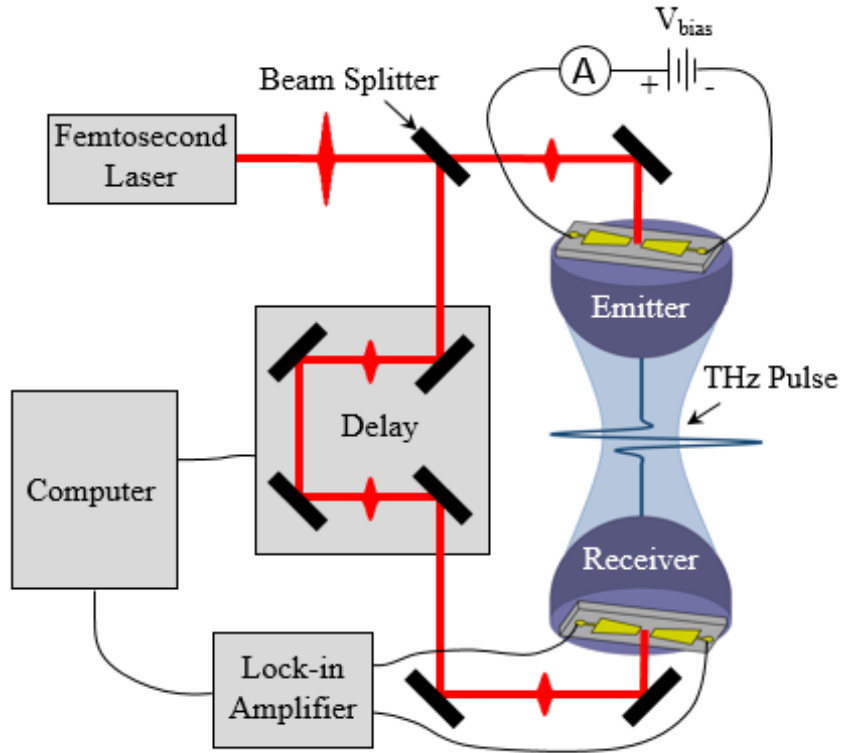


Figure 1.1.2.2: Schematic diagram of the typical configuration of electro-optic sampling of THz pulses in a time-domain spectroscopy system.

In order to measure the emitted THz pulse, another PCA is utilized as the receiver. Unlike the emitter, the receiver PCA does not have an external DC bias. Instead, the emitted THz beam is focused on the dipole antenna such that the beam polarization is aligned across the antenna gap [1], [44], [73]. As the THz pulse propagates into the antenna, it induces a transient bias voltage across the gap. To measure this transient voltage, a portion of the femtosecond optical pulse is split from the source beam, propagated through an adjustable optical delay line and focused in the gap of the receiver PCA. This provides a narrow impulse of photocarriers at a time which can be controlled by the optical delay line. When the photocarrier impulse and THz field induced transient voltage overlap in time, a measurable photocurrent proportional to the instantaneous antenna voltage will be induced across the antenna. By sweeping the optical delay line, the

photocurrent impulse signal is convoluted with the THz field induced transient voltage signal. Collecting and correlating both the optical delay position and induced photocurrent data allows the temporal profile of the THz pulse to be measured. The coherent nature of this detection method provides a high signal-to-noise ratio, since it greatly reduces the effects of blackbody radiation and other sources of THz radiation on the receiver [73].

Although the exact nature of THz generation in PCAs is not universally agreed upon, currently there are three main modalities in which THz generation in a PCA can be explained; the transient acceleration of carriers in the bulk semiconductor [52], [62], [72], [74], the instantaneous drop in dipole gap resistivity after optical pulse absorption [46], [75], and direct collection of photocarriers by the antenna electrodes [67], [71], [76], [77]. When a femtosecond optical pulse is incident in the gap of a THz PCA, electron-hole pairs are generated everywhere in the gap, proportional to the local intensity of the incident optical pulse [44], [46], [72]. The photocarriers are accelerated along the DC bias field and recombined a short distance later. This induces time-varying surface currents on the device structure, which in turn produces a propagating THz pulse, E_{THz} , described by [72],

$$E_{\text{THz}}(\mathbf{r}, t) = -\frac{1}{4\pi\epsilon_0 c^2} \frac{\partial}{\partial t} \int \frac{J_s\left(\mathbf{r}', t - \frac{|\mathbf{r} - \mathbf{r}'|}{c}\right)}{|\mathbf{r} - \mathbf{r}'|} ds'. \quad (\text{Equation 1.1.2.1})$$

Here, J_s is the spatially and temporally dependent surface current on the emitter surface, \mathbf{r} is the spatial vector of the location of the THz field, \mathbf{r}' is spatial vector of the location of the surface current which is integrated across the emitter surface ds' , c is the speed of light in vacuum and ϵ_0 is the permittivity of free space. From Equation 1.1.2.1 it can be seen that the radiated THz field will be dependent on the net surface currents in a PCA emitter. By

considering the various sources of surface currents it is possible to describe the different mechanisms of THz emission [44], [46], [72].

The first cause of THz generation arises directly from the generation and acceleration of charge in the photoconductor, known as the current surge model [68]. Electron-hole pairs generated in the gap will be separated, accelerate along the bias electric field, and be recombined a short time later [52], [68], [74], [78]. For the second cause of THz generation, consider the state of the PCA device prior to optical excitation. Due to the parallel-line nature of the device, there is a capacitive energy stored across the gap in the form of positive and negative charge accumulation at the anode and cathode, respectively [75]. The magnitude of this charge is dependent on the device geometry, bias voltage, and gap resistivity [75], [79]. The gap resistivity, which also determines the bias electric field distribution in the photoconductor, is dependent on the carrier concentration inside the photoconductor. Exciting the gap with an optical pulse causes sharp rise in the carrier concentration and, consequently, a drop in resistivity. This causes a THz frequency oscillation in the antenna metallization as the bias field responds [44], [72], [75]. The third cause of THz generation comes from optical injection of current directly into the antenna electrodes [72], [75], [80]. Any photocarriers generated in sufficient proximity to the antenna electrodes will be collected by the antenna before they recombine. This acts as a driving current that, provided the induced current pulse is sufficiently short, also induces THz oscillations in the antenna [72], [75], [80].

1.2. Photoconductive Material Development

1.2.1. Challenges

Since the first demonstrations of early photoconductive switches, the main factor enabling their effective performance has been the selection of specific photoconductive materials with

necessary electro-optic characteristics [39], [47], [48], [81]. The common perception is that for a PCA emitter or detector to have broadband performance, the photoconductive material must have a sub-picosecond carrier lifetime. However, this is only one of several factors which must be balanced in order to optimize the PCA performance. In addition to a low carrier lifetime, maintenance of relatively high carrier mobility, appropriate bandgap, high breakdown voltage, suppression of zero bias photocurrent, and maximizing the material dark resistivity all play a role in a complex relationship which influences a PCA's output power, maximum optical pump power and bias voltage, bandwidth, and signal-to-noise ratio (SNR) [53], [75], [82]–[84].

Thus far, the most studied and promising materials for THz PCAs have included bulk gallium arsenide (GaAs) [47]–[60], bulk indium gallium arsenide (InGaAs) [64], [85]–[92], alternating nano-scale multi-layers of InGaAs and indium aluminum arsenide (InAlAs) [93]–[100], and select other group III-VI semiconductors [82], [101]–[104]. The following sections will individually address each material system, reviewing key works and summarizing their unique contributions and applications to the development of THz PCA technology.

1.2.2. Gallium Arsenide (GaAs)

Although the earliest demonstrations of PCA technology utilized argon ion (Ar^{3+}) irradiated crystalline silicon epitaxially grown on sapphire (SOS) [39], [81], GaAs has long been the preferred material for PCAs. GaAs has a room temperature bandgap of 1.424 eV (871 nm) [105], making it compatible with the titanium-doped sapphire (Ti^{3+} :sapphire) femtosecond-pulsed laser sources commonly used to excite PCAs. GaAs is normally utilized in one of three forms; semi-insulating GaAs (SI-GaAs), low-temperature grown GaAs (LT-GaAs), and ion-implanted GaAs, such as nitrogen (GaAs:N^{3-}).

Early works by Warren et al. [47], Gupta et al. [48] and Harmon et al. [49] studied the effects of GaAs growth temperature on the carrier lifetime and THz PCA performance. Warren et al. utilized LT-GaAs (250 °C growth temperature), SI-GaAs, and SOS based PCAs in a THz TDS setup to compare effectiveness of each as both transmitters and receivers [47]. Under 70 fs optical pulse excitation, identical performance was found in the SI-GaAs and LT-GaAs samples acting as emitters, with both the LT-GaAs and SOS acting as receivers. This indicated similar quality in the crystal structure of the GaAs samples. Comparing the configuration using GaAs samples as both emitter and receiver with the configuration using only SOS samples demonstrated 5 times higher peak in the detected THz signal and a 0.71 ps pulse width [47]. Gupta et al. compared PCA performance in a TDS configuration using LT-GaAs and chromium-doped GaAs (GaAs:Cr³⁺) [48]. For the LT-GaAs samples, the LT-GaAs was grown by molecular beam epitaxy (MBE) at temperatures between 200-250 °C. GaAs growth in this temperature range leads to two benefits; high level of crystallinity, which in turn leads to higher carrier mobility, and excess As³⁺ within the crystal structure manifesting as point defects. These point defects act as recombination centers, drastically reducing the carrier lifetime. Gupta et al. showed that LT-GaAs samples grown at 190 °C and 200 °C yielded a carrier lifetime below 400 fs. By comparison, the GaAs:Cr³⁺ samples grown at temperatures above 250 °C yielded carrier lifetimes greater than 50 ps.[48] The work of Harmon et al. further explained the nature of growth temperature and post growth annealing on GaAs carrier lifetime [49]. Here, GaAs thin-films were epitaxially grown on top of a sacrificial lift-off layer to allow removal and differential transmission measurements to be performed. Differential transmission measurements allowed the carrier lifetime to be derived. By combining this with transmission electron microscope (TEM)

imaging, it was found that the carrier lifetime is directly related to the spacing of the excess As³⁺ clusters [48].

Tani et al. studied LT-GaAs growth temperature and anneal time effects [50] along with their performance characteristics when implemented in THz PCA emitters [51]. LT-GaAs grown at 250 °C and annealed post-growth at 600 °C for five min was found to yield a 0.3 ps carrier lifetime [50]. PCA dipoles with different electrode shapes were fabricated and compared with SI-GaAs with a ~100 ps carrier lifetime [51]. As with the results of Gupta et. al. [48], the emitted pulse shapes of both emitters was comparable, with the amplitude of the SI-GaAs based emitter being over 5 times higher than the LT-GaAs emitter [51]. However, this was observed at relatively low optical pump power (15 mW) and low DC bias (30 V). Analysis of the dark I-V and output THz power vs. input optical power characteristics showed the LT-GaAs based emitters to have higher saturation thresholds as compared to the SI-GaAs. At biases above 5 V, the LT-GaAs emitter showed a linear I-V relationship for bias fields as high as 200 kV/cm, with a drastically higher dark resistance compared to the SI-GaAs emitter. Higher dark resistance indicated a higher breakdown voltage, and was demonstrated by showing breakdown in a 5 μm gap dipole at biases of 160 V for the LT-GaAs, as compared to 50-70 V for the SI-GaAs [51]. Similar work by Stone et al. compared SI and LT-GaAs PCAs with various large electrode dipole geometries [52]. Triangular, circular, and square dipoles were characterized using a Golay cell detector to measure their power emission spectrum, with the frequency domain peak frequency location and FWHM bandwidth being the comparing factors [52]. In all geometries, the LT-GaAs based emitters had higher peak frequency and higher bandwidth, with the largest bandwidth of 0.9 THz being observed in the LT-GaAs based circular dipole [52]. Additionally, it was observed that for conditions yielding similar output THz power, the LT-GaAs based emitters

produced lower photocurrent than their SI-GaAs based counterparts [52]. With lower photocurrent, thermal effects arising from high optical pump power and bias voltages were reduced [52]. Later work by Moon et al. demonstrated that post-growth annealing of LT-GaAs allowed the sheet resistance and carrier lifetime to be manipulated [53]. Annealing causes the excess As^{3+} precipitates to form clusters within the crystal structure, the size and spacing of which are controlled by growth temperature and post-growth anneal temperature. Removing the As^{3+} precipitates from their uniform distribution as antisites in the crystal structure had the positive effect of increasing the material resistance, as well as the negative effect of increasing the carrier lifetime [53]. TEM imaging of the post-growth annealed LT-GaAs as well as the relationship between sheet conductance and cluster diameter with anneal temperature are shown in Figure 1.2.2.1 (Figure 2(a) and Figure 3(a) in [53]). It was shown that for a given growth temperature, the post-grown anneal temperature can be tuned to yield an optimum THz emission performance. It was found that in the range of 500 °C to 620 °C, the maximum peak-to-peak THz pulse intensity was observed for post-growth anneal temperatures between 540 °C and 580 °C, for growth temperatures of 200 °C and 230 °C [53].

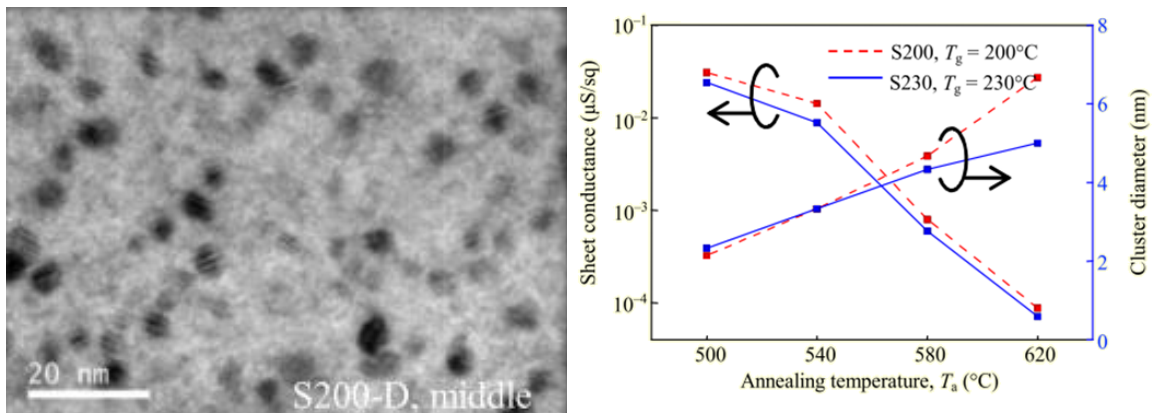


Figure 1.2.2.1: (Left) TEM photograph of annealed LT-GaAs layer and (right) sheet conductance and cluster diameter as functions of annealing temperature. Reproduced from [53] with permission from the Electronics and Telecommunications Research Institute.

In addition to low-temperature growth, several groups have investigated the use of ion-implanted GaAs for THz [54]–[60]. Liu et al. characterized the effect of As^{3+} ion implantation of SI-GaAs acting as both PCA emitters [54] and receivers [55]. Similar to low-temperature growth of GaAs, ion implantation of As^{3+} in SI-GaAs introduces excess As^{3+} impurities within the crystal structure. However, GaAs: As^{3+} was claimed to have a benefit of improved controllability of the excess As^{3+} concentration and uniformity as compared to LT-GaAs. Although performance of the two materials is comparable at low bias voltage, the GaAs: As^{3+} PCA exhibited a higher bias voltage breakdown threshold above 60 kV/cm as well as a higher optical pump saturation point [54]. The broadband THz performance of GaAs: As^{3+} was characterized as a detector in a TDS configuration, where a 15 fs optical pump was used to excite a ZnTe crystal emitter and generate broadband (47 THz) pulses, as well as gate the GaAs based detectors [55]. Comparing GaAs: As^{3+} , SI-GaAs, and LT-GaAs it was found that SNR and bandwidth was greatest for the LT-GaAs detector (>40 THz bandwidth) due to the comparably short carrier lifetime, while the GaAs: As^{3+} and SI-GaAs had lower bandwidths of 32 and 24 THz, respectively [55]. The noise was attributed to thermal noise in the photoconductor, arising from residual photocurrents. Therefore, Liu et al. proposed that the noise in the GaAs: As^{3+} emitter could be reduced by increasing the ion-implantation depth, as this would effectively increase the effective carrier mobility while retaining a short carrier lifetime [55].

Salem et al. compared THz PCAs based on arsenic [56], [57], hydrogen (GaAs: H^+) [56], [58], oxygen (GaAs: O^{2-}) [56], [57], and nitrogen (GaAs: N^{3-}) [56] ion implantation. Lowest THz pulse intensity was observed in the GaAs: N^{3-} PCA, while the GaAs: H^+ , GaAs: As^{3+} and GaAs: O^{2-} all demonstrated comparable output THz intensities when operated in the saturation regime of the optical pump power (90 mW) [56]. Use of GaAs: H^+ as both the emitter and receiver was

demonstrated in a TDS configuration to provide a SNR nearing 10^4 from 0.1 to 1 THz [58]. Although the work by Salem et al. [56] indicated poor relative performance in GaAs:N³⁻, this material was shown by Winnerl et al. [59] to have 40 times better SNR than SI-GaAs based detectors, and nearly the same SNR of LT-GaAs. Additionally, GaAs:N³⁻ PCAs operating in a photomixing configuration have been shown to have a higher, bias independent cutoff frequency as compared to LT-GaAs, which exhibited decreasing cutoff frequency with increasing bias voltage [60].

1.2.3. InGaAs (InGaAs)

In more recent years, the group III-VI ternary compound indium gallium arsenide (In_xGa_{1-x}As) has been investigated as a potential candidate for THz PCA photoconductive material [64], [85]–[92]. The benefit of this material is its potential to achieve 0.8 eV room temperature bandgaps, which allows for 1.55 μm optical excitation. This is an advantage when considering practical implementation of THz PCA based systems as 1.55 μm wavelength pulsed laser systems can be fully fiber based without consideration of dispersion effects. Although generation and detection of THz pulses in LT-GaAs PCAs has been demonstrated using 1.55 μm optical pulses [106], significant reduction in performance has been observed as compared to 800 nm excitation. This is mainly due to the lower absorption efficiency of LT-GaAs at 1.55 μm, since absorption at this sub-bandgap wavelength requires interband transitions in order to excite carriers to the conduction band [106]. Therefore, materials with bandgaps at or below 0.8 eV have been sought out for use with 1.55 μm fiber laser systems.

As previously discussed, short carrier lifetime photoconductors are needed in order to have the sub-picosecond response necessary for THz generation and detection. For InGaAs, iron

doping (InGaAs:Fe²⁺) has been shown to provide the effective recombination sites needed for a sup-picosecond carrier lifetime [64], [85], [86], [90]. Suzuki and Tonouchi demonstrated reduction of the emitted THz pulse from 0.68 to 0.57 ps in InGaAs PCA emitters due to Fe²⁺ implantation under identical operating conditions [85]. Additionally, InGaAs:Fe²⁺ demonstrated higher optical pump saturation power as well as higher breakdown voltage, indicating further improvement in performance at higher operating conditions [85]. Utilized as a detector, annealing at 580 °C was shown to improve the detection SNR from 50 to 133 [86]. Metalorganic chemical vapor deposition (MOCVD) grown InGaAs:Fe²⁺ was investigated across 830 nm to 1.55 μm optical excitation as an emitter by Wood et al. [64], and later as a detector by Hatem et al. [90] As emitters, the highest THz power of 9 μW was observed around 1.2 μm excitation wavelength [64]. As detectors, peak SNR of 125 was observed at 5 mW optical excitation with bandwidth limited by the excitation pulse width [90]. MBE grown nanoparticle embedded InGaAs was studied by Salas et al. [91] and Murakumo et al. [92] InGaAs based nanocomposites containing rare-earth arsenide nanospheres were proposed as a possible material for THz PCAs [91]. Of the four materials studied, LaAs had over an order of magnitude higher dark resistivity and three times lower mobility as compared to erbium arsenide (ErAs), lutetium arsenide (LuAs) and gadolinium arsenide (GdAs) under similar growth conditions [91]. Use of InAs:Er³⁺ quantum dot embedded InGaAs has been shown to provide higher optical saturation intensity, an attractive property for high power THz emitters [92].

1.2.4. Indium Gallium Arsenide/Indium Aluminum Arsenide (InGa(Al)As) Heterostructures

InGa(Al)As multi-quantum wells (MQWs) and superlattices have been proposed as potential materials for THz PCAs [93]–[100]. Similar to bulk InGaAs, InGa(Al)As can achieve strong

optical absorption under 1.55 μm wavelength excitation, due to its tunable bandwidth. However, unlike bulk InGaAs, the highly tunable electro-optic properties of InGa(As)As have been proposed as an avenue to achieve equivalent (or better) THz PCA performance at 1.55 μm that LT-GaAs achieves at 800 nm [107]. Although earlier works proposed InGa(Al)As based materials for THz PCAs [93], [108], the first InGa(Al)As based THz PCA operating at 1.5 μm was demonstrated in 2008 by Sartorius et al. [107]. Alternating layers of 12 nm InGaAs:Be²⁺ and 8 nm InAlAs were grown on InP wafers to form the PCA substrate. An illustration of this configuration, showing the separate embedded photoconductor, electron trapping layer and combined multilayer structure is shown in Figure 1.2.4.1 (Figure 4 in [107]). The InGaAs:Be²⁺ acted as the photoconducting region and was grown using standard low temperature methods for bulk InGaAs, however, incorporation of Be²⁺ during growth allowed the material dark resistivity to be increased by balancing against the As³⁺ antisites [107]. To further increase the net dark resistivity and decrease carrier lifetime, the InAlAs layers were included. This material had a higher dark resistivity than the InGaAs:Be²⁺ and acted as a deep level trapping site for electrons [107]. Conventional THz PCA electrodes were fabricated on these materials to form both emitters and detectors, which were then incorporated into an all fiber THz TDS experimental setup. Sub-1 ps THz pulses with bandwidth extending above 2 THz were reported along with a SNR of nearly three orders of magnitude [107].

Other works have elaborated on this concept to further study this material's potential for all fiber THz TDS systems [94]–[100]. Roehle et al. utilized InGa(Al)As multilayers and employed a mesa-etching process to effectively increase the generated photocurrent while decreasing dark current [95]. This led to a 27.5x increase in detected THz amplitude as compared to a non-mesa PCA [95]. Other demonstrations of InGa(Al)As multilayer based THz PCAs have attempted to

further optimize growth conditions, which are critical for maximum THz performance [96], [98]–[100]. Using a mesa style emitter with 2 nm indium aluminum arsenide (InAlAs) barriers, 400°C InGaAs growth temperature with no doping, high THz output powers of 64 μW were achieved at 32 mW optical excitation [100]. Additionally, erbium arsenide (ErAs) quantum dot incorporation into the InAlAs trapping layers has been studied and shown to provide up to 1 V/cm amplitude THz pulses at 100 mW excitation wavelength [97]. Most recent work by Dietz et al. has shown optimal growth conditions for 1060 nm excitation [109] along with a further study of optimized Be^{2+} doping for 1.55 μm excitation detectors [110]. Over 6 THz detection bandwidth and 90 dB dynamic range was reported for detectors fabricated on InGa(Al)As multilayers with Be^{2+} doping concentrations of $4 \times 10^{18} \text{ cm}^{-3}$ [110].

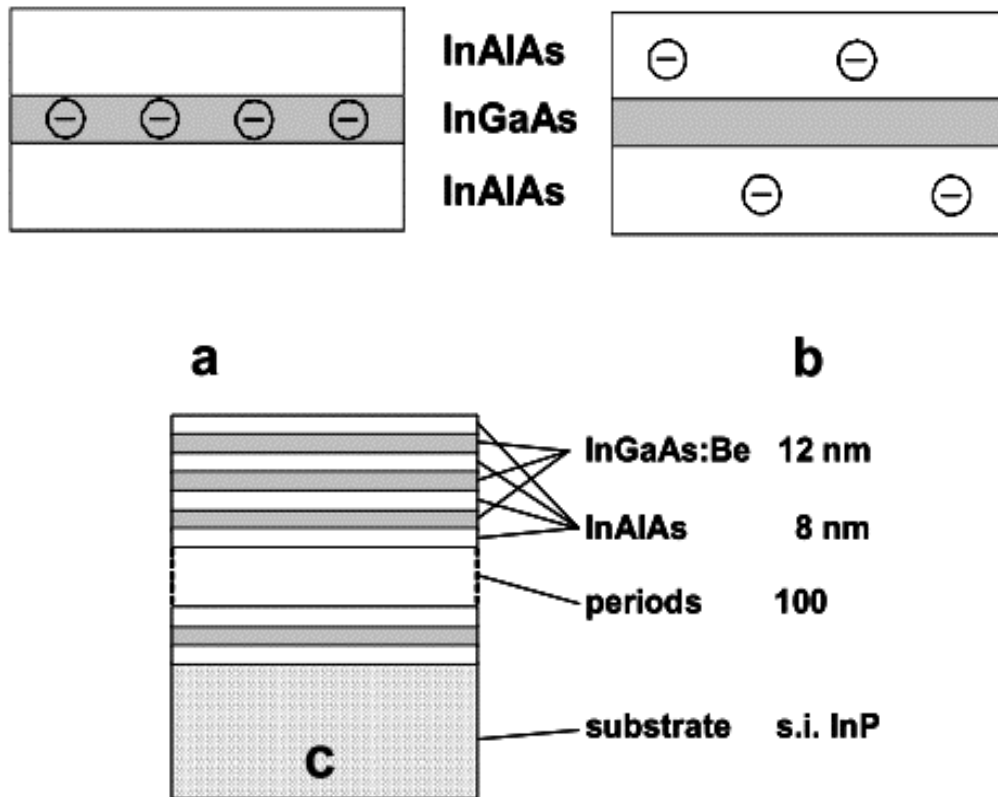


Figure 1.2.4.1: (a) Embedded photoconductor; (b) electron trapping; (c) multilayer structure. Reprinted from [107] with permission from OSA Publishing.

1.2.5. Other Group III-V Materials

Although GaAs and InGa(Al)As are the most widely studied material systems for THz PCA development, several other group III-V materials have been investigated as well [61], [101]–[104], [111], [112]. THz emission in antimony (Sb) based materials such as InSb [101], GaAsSb [102], GaSb [111] and GaInSb [112] has been studied by several groups, although only the work of Sigmund et al. fabricated and characterized THz PCAs on the material [102]. 1 THz bandwidths were observed in a THz TDS system utilizing GaAsSb material in the PCA emitter and detector, although more studies of the growth conditions were needed to fully evaluate the potential of this material for THz PCAs [102]. GaBiAs was grown at two different temperatures and used for THz PCA fabrication by Bertulis et al. [103] Four times higher THz field amplitudes were observed in a 330 °C grown sample as compared to a 280 °C growth [103]. GaAs embedded superlattices of rare-earth arsenides of ErAs and LuAs were used in CW photomixing in plasmonic PCAs [61]. In all cases, the rare-earth arsenide based photomixers outperformed LT-GaAs photomixers at operation frequencies below 1 THz, though output power was higher in LT-GaAs for higher frequencies [61]. Collier et al. fabricated THz PCAs on InP to study the effects of surface roughening on the THz emission [104]. Although surface roughening showed no effect on the amplitude and bandwidth of THz emission, around one order of magnitude suppression of the photocurrent was observed [104]. This indicated that such emitters could have higher operation thresholds as compared to non-textured materials, allowing for enhanced THz performance [104].

1.2.6. Summary and Outlook

The advantages, disadvantages, and key performance milestones for each of the material systems discussed are summarized in Table 1.2.6.1. Although LT-GaAs remains the standard for THz PCAs, the potential for all fiber based TDS systems remains an attractive motivator for investigating and developing other photoconductive materials systems. Remaining challenges for lower bandgap THz PCA materials include reaching comparable (or better) carrier lifetime, mobility, breakdown threshold, quantum efficiency, and reproducibility to that of standard LT-GaAs devices.

Table 1.2.6.1: Summary of photoconductive material development for THz PCAs.

	Advantages	Disadvantages	Key Reported Performance Milestones
GaAs	Most efficient material for 800 nm excitation Well understood growth and optimization	Poor absorption at 1.55 μm	10^4 SNR [58] 60 kV/cm Breakdown Threshold [54]
InGaAs	1.55 μm excitation	Decreased gap dark resistivity	4 μW Output THz Power [64] 125 SNR [90]
InGa(Al)As Heterostructures	1.55 μm excitation comparable dark resistivity to LT-GaAs	Complex material growth	10^3 SNR [107] 6 THz Bandwidth [110] 1 V/cm THz Amplitude [97]
Other Group III-V	Potential 1.55 μm excitation	New materials with limited understanding	1 THz Bandwidth, 10^2 SNR (GaAsSb) [102]

1.3. Large Area Emitters

1.3.1. Challenges

One of the major limiting factors of THz PCA technology is saturation at high optical pump powers [51], [72], [78], [113], [114]. Under no optical illumination, the photoconductor has a fixed carrier concentration N_D or N_A , where N_D is the donor carrier concentration and N_A is the acceptor carrier concentration [105]. Illuminating the photoconductor induces an optical carrier concentration, N_{opt} , which induces an increase in the total carrier concentration of $N_{\text{tot}} = N_{D,A} +$

N_{opt} . Changes in the material carrier concentration translates to a proportional change in electronic properties, namely the imaginary part of the permittivity. For optical pump powers where $N_{\text{opt}} \geq N_{\text{D,A}}$ the imaginary part of the permittivity will begin to increase, causing nonlinear increase in the surface reflectivity of the air-photoconductor interface [114]. Therefore, during operation of high optical pump power beyond the $N_{\text{opt}} = N_{\text{D,A}}$ region the output THz power will experience a nonlinear increase, eventually reaching a saturation point where increase optical pump power produces little to no increase in output THz power [114]. This effect is exaggerated as the optical pump is focused to a smaller spot size [78], [113].

1.3.2. Large Aperture Dipoles

Overcoming the saturation limits of PCAs has been demonstrated through the implementation of large device apertures. This was first observed in the early 1990s by the research efforts of THz pioneer David Auston [74], [78], [113], [115], [116]. These PCAs consisted of parallel microstrip line dipole antennas with gaps ranging from 130 μm to 4 mm. Various materials, including SOS [74], [78], [115], InP [74], [78], [113], and GaAs [74], [78], [113], [116] have been considered for use in these devices. Although initial work utilized large aperture PCAs to demonstrate THz beam steering [74], [115], it was noted that these devices have the added benefit of improved power scaling due to reduction of the saturation effect [113], [115]. Extensive theoretical and experimental work was later performed to fully understand the saturation characteristics [78]. The emitted THz pulses were measured in a TDS configuration to obtain the relationship between emitted pulse amplitude and incident optical fluence. InP and GaAs based emitters were found to have similar THz amplitudes, around twice that of SOS

emitters. In all cases, the large aperture emitters were shown to generate emitted THz pulses with peak amplitude electric field values within 90% of the DC bias field value [78].

Later works have further studied the properties of large aperture THz PCAs [52], [62], [72]. Benicewicz, Roberts and Taylor fabricated 500 μm gap microstrip dipoles on InP:Fe²⁺ and SI-GaAs and studied their saturation properties in a THz TDS experimental configuration [72]. A comparison of the radiated electric field for devices fabricated along different crystallographic axes showed only slight variation. This variation was unable to be described by the theoretical model and was attributed to variation in the material properties across the wafer, not the specific crystal orientation [72]. The radiated THz power as a function of optical fluence and bias voltage was measured, with excellent agreement being observed with the proposed theoretical model [72]. Budiarto et al. studied the effects of AC biasing of a GaAs based THz PCA with 3 cm electrode gaps [62]. The emitted THz pulse intensity was measured as a function of optical fluence for two different emitter AC bias frequencies, 0.1 and 1 KHz and four different bias voltage amplitudes. In all instances, the 1 KHz bias frequency increased the intensity of the emitted THz in the saturation regime [62]. At the highest observed bias field of 6 kV/cm no saturation was observed for optical fluence up to 90 $\mu\text{J}/\text{cm}^2$ [62]. Large aperture emitters were studied as well by Stone et al., although the laser utilized in this study was not powerful enough to provide the high optical fluence necessary to observe saturation effects [52].

1.3.3. Interdigitated Electrodes

Similar to large aperture dipoles, attempts to overcome the saturation limits of conventional THz PCAs have investigated increasing the device active area by implementing interdigitated electrodes [59], [66], [75], [79], [99], [117]–[127]. This configuration consists of a single anode

and cathode, each connected to a number of open ended parallel microstrips. The anode and cathode microstrips were interwoven such that the space between two adjacent anode microstrips was occupied by a cathode microstrip, and vice versa, with a fixed gap distance between the two electrodes. An illustration and device photograph of this configuration is shown by the work of Awad et al. in Figure 1.3.3.1 (Figure 1 in [123]). By this method, active areas of a few hundred μm^2 have been produced, allowing the optical power to be spread over a larger area to reduce the saturation effect [120]. Unlike large aperture PCAs, interdigitated PCAs have the added benefit of enhancing the near anode effect [119]. By reducing the saturation effects, these electrode configurations have shown promise for providing high optical to THz conversion efficiency even at high optical pump powers.

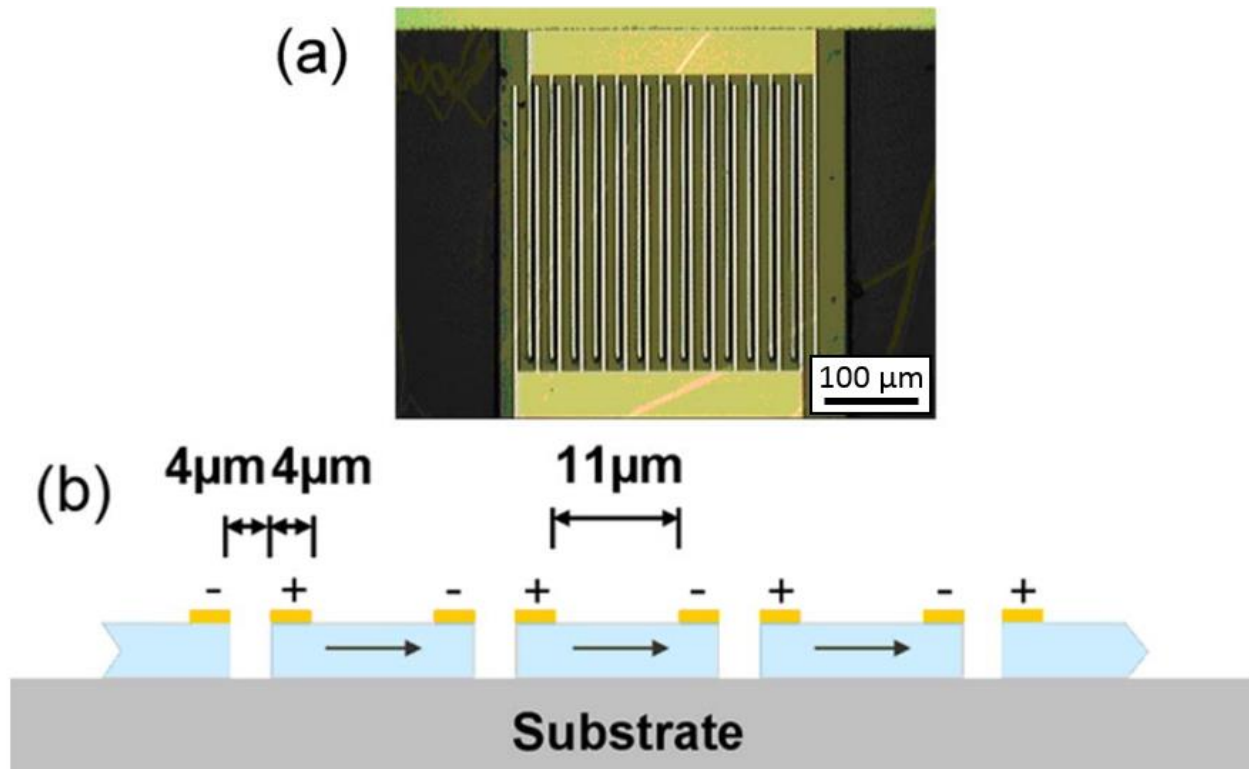


Figure 1.3.3.1: (a) Micrograph of terahertz array antenna device. (b) Cross-sectional view of terahertz antenna array. Reprinted from [123], with permission of AIP Publishing.

Interdigitated electrodes for improved performance in THz PCA photomixers were proposed by several groups in the early 1990s [117]–[119]. The first truly broadband photomixer implementing interdigitated electrodes for terahertz generation up to 3.8 THz was demonstrated in 1995 by Brown et al. [120]. Using a log spiral antenna with 1.8 μm gap interdigitated electrodes, maximum output power of 10 μW was observed at a 0.3 THz operational frequency, with measureable radiation up to 3.8 THz reported [120]. Brown later developed a model for predicting the performance of an interdigitated THz photomixer [79]. Here, it was proposed that by implementing a reflecting layer under the LT-GaAs and tuning the thickness of the LT-GaAs cavity, the absorption of the incident optical pump could be optimized. This increased the output THz power by a factor of 7, due to improved quantum efficiency of the device [79]. Later work by Gregory et al. extensively studied THz PCA photomixers with varied interdigitated electrodes [75]. Photomixers with 3, 5 and 11 finger interdigitated electrodes were fabricated and characterized under CW and pulsed operation. Spatial mapping of the emitted THz radiation as a function of location of a focused optical excitation was performed for an 11 finger device. The results here showed no enhancement of THz emission when focused at the electrode tips, as well as no near anode enhancement effects. For CW operation, the larger active region provided by a larger number of electrode fingers did not provide enhanced THz emission. At higher THz frequencies above 0.4 THz, the increased capacitance led to a high frequency roll off in the device performance. However, at sub-0.4 THz operation, larger device active area could provide advantages of more efficiency heat dissipation and reduced sensitivity to beam drift [75].

Many others have utilized interdigitated electrodes in various THz PCA designs for pulsed operation [59], [97], [99], [121], [124], [128], [129]. Dreyhaupt et al. proposed a novel modification to the interdigitated electrode design to overcome an inherent limitation of this

configuration [121]. In standard interdigitated electrodes, the bias electric field direction is rotated 180 degrees between adjacent gaps. The carriers generated accelerate in opposing directions, leading to a net destructive interference in the emitted electromagnetic field. By incorporating a shadow mask which blocks the incident optical excitation in every other gap, photogeneration only occurs in regions with the same bias field directions. This leads to a net constructive interference, providing high intensity THz pulse emission up to 85 V/cm [121]. This was expanded upon in later works, including demonstration of an interdigitated PCA for THz detection using an unfocused optical gating pulse [124], study of the dependence of generation and detection performance on GaAs carrier lifetimes [59], and emission of 2.5 V/cm THz pulses in InGaAs heterostructure emitters under 1.55 μm wavelength optical excitation [99]. All works indicate that improved performance was achieved by implementation of the interdigitated large active area [59], [97], [99], [121], [124], [128], [129].

Hattori et al. characterized a seven element array of larger area interdigitated electrode emitters [122]. This was compared to emitter arrays of non-interdigitated large area emitters comprised of parallel microstrips with 3 μm gaps. Here, it was found that the non-interdigitated array produced nearly two times greater peak THz emission, although they require 6 kV bias voltage to achieve the same gap bias field as the interdigitated emitter under 30 V bias voltage [122]. Others have implemented shadow masks for interdigitated PCAs [66], [126], [127], with reports of 20 THz ultrabroadband performance under collinear operation [127] and high pulsed operation average powers of 3.8 mW [66]. Awad et al. presented an alternative method for preventing the destructive interference occurring in non-shadowed interdigitated PCAs [123]. Here, rather than blocking the incident optical pulse, the photoconductive material in every other gap of the device was etched away. In addition to preventing destructive interference this has the

added benefit of allowing the active area of the device to be increased since the etched region gaps can be reduced while still allowing the majority of the electric field to fall in the non-etched gaps [123]. A similar device configuration was studied by Acuna et al. which demonstrated peak THz fields of 15 V/cm and 40,000 Hz^{1/2} SNR under electro-optic sampling [125].

1.3.4. Dipole Arrays

Periodic arrays of dipole electrodes have been proposed for improving various aspects of THz PCA performance [116], [130]–[133]. Early work by Froberg et al. fabricated a linear array of parallel microstrip dipole emitters on SI-GaAs [116]. Each of the 64 electrodes were individually biased, while the entire array was illuminated with a train of 200 fs optical pulses. It was shown that by controlling the bias of the individual electrodes, the direction and profile of the emitted THz pulses could be tuned [116]. Various works by Klatt et al. studied electrode arrays utilizing the photo-Dember effect for THz generation [130], [131]. The photo-Dember effect arises from the optically induced space-charge gradient in unbiased semiconductors due to the difference in electron and hole diffusion coefficients [130]. This effect was shown to be enhanced near the edge of an unbiased metal electrode [130], with photo-Dember excitation of electrode arrays showing comparable THz generation as interdigitated PCA emitters [131]. Berry, Hashemi and Jarrahi fabricated a 3x3 array of log spiral antennas with nanoscale plasmonic electrodes [132]. Using an array of optical microlenses, the incident optical pump was divided into nine separate beams and focused onto the active area of each device. The net output THz radiation was shown to reach record high average power levels of 1.9 mW at an average pump power of 320 mW [132]. Microlens arrays were also utilized by Singh and Prabhu to excite the individual active areas of an interdigitated THz PCA emitter [133]. The microlens

array was utilized to separate and focus the optical excitation such that only regions leading to constructive interference were excited, rather than utilizing a shadow mask or etching the photoconductor in these regions [133].

1.3.5. Summary and Outlook

The advantages, disadvantages, and key performance milestones for large area emitter THz PCAs are summarized in Table 1.3.5.1. These devices offer potential for drastically increasing the optical-to-THz conversion efficiency, which is necessary for high output THz power or efficient excitation of multiple devices with a single laser source. However, as device active area increases, the driving current can no longer be considered a point source, leading to potential phase interference issues not present in single dipole emitters. Additionally, most large area emitters have complex fabrication and/or packaging considerations. As solutions to these problems continue to be sought out, large area emitters will likely develop into standard THz PCA technology.

Table 1.3.5.1: Summary of large area emitter THz PCAs

	Advantages	Disadvantages	Key Reported Performance Milestones
Larger Aperture Dipoles	Reduced saturation effects	Order of magnitude higher bias voltage required	No saturation up to 90 $\mu\text{J}/\text{cm}^2$ optical fluence [62]
Interdigitated Electrodes	Reduced saturation effects	Increased fabrication complexity and unable to incorporate broadband antenna designs	15-85 V/cm THz Amplitude [121], [125]
Dipole Arrays	Reduced saturation effects	Increased optical alignment complexity	1.9 mW output THz power [132]

1.4. Plasmonic Nanostructures

1.4.1. Challenges

Several groups have studied the use of plasmonic nanostructures in both THz PCA emitters as well as receivers. Similar to large-area emitters, nanostructures attempt to more efficiently utilize the incident optical pump. As previously discussed, THz generation in conventional PCAs occurs mainly due to the photocarriers that are generated in the high bias field region (i.e. at the surface) and near the antenna anode [75], [80]. However, in conventional PCAs only a small fraction of the incident photons are absorbed near the surface, with even less being absorbed in a region near enough to the antenna anode for the generated carriers to be collected on a sub-picosecond time scale. This translates to a distance of around 100 nm or less from the antenna anode [71]. As an example, consider an 800 nm wavelength, 5 μm diameter optical beam focused in the gap of a LT-GaAs THz PCA centered over the anode edge. Anode illumination has been shown to generate the highest levels of THz power, as compared to middle of gap of cathode illumination [80]. Here, less than 2% of the total photons are incident in a lateral distance 100 nm or less from the antenna anode, and only around 13% of these are absorbed in the first 100 nm depth of the LT-GaAs. Therefore, considering only THz generation from the carriers that are collected by the anode, less than 0.3% of the incident photons are theoretically able to contribute to THz generation. The remaining photons are lost either by reflection from the anode metallization or are absorbed too far (>100 nm) from the anode to be collected before recombining [71].

Plasmonics have been proposed as a viable solution to overcome this inherent limitation in conventional THz PCA design. “Plasmonics” refers to the study of the collective electron oscillations that occur in sub-wavelength sized metallic nanostructures when excited by an

external optical wave [134]. These oscillations have been shown to enhance the optical near field by orders of magnitude, with the oscillation frequency, magnitude and spatial location of the enhancement being tunable by the size, shape and surrounding medium of the nanostructures [135]–[137]. Plasmonics have been proposed and demonstrated extensively in solar cell technology [135]–[139]. Plasmonic enhancement of THz PCAs follows a similar approach, where the nanostructures are designed to enhance the optical excitation field in regions inside the photoconductive material where the generated carriers most efficiently convert to output THz radiation.

1.4.2. Early Examples of Unbiased Nanostructured THz Emitters

The first examples of using metal nanostructures for THz generation were not PCAs. Instead, THz was generated through a process called “optical rectification” [4], [5], [140]–[142]. Similar to PCA generation, optical rectification uses sub-picosecond optical pulse to excite an unbiased semiconductor, electro-optic crystal, or metal surface. The optical field induces oscillations in the material which follow the intensity envelope of the pulse, rather than the electric field. These oscillations in the material then re-emit as a propagating THz pulse [5]. Although optical rectification using unbiased semiconductors and electro-optic crystals has existed nearly as long as PCA technology [40], the first demonstration of THz generation from a nanostructured metal surface did not take place until 2006 [143]. This early work of Welsh, Hunt and Wynne studied THz surface emission from nanostructured metal surfaces excited by 800 nm wavelength optical pulses [143]. Here, it was found that the nanostructured metal surfaces had much higher optical-to-THz conversion efficiency than flat metal surfaces. However, the peak THz field from the nanostructured metal surface was still around one order of magnitude lower than the peak field

emitted from a zinc telluride (ZnTe) electro-optic crystal. Additionally, it was found that the THz-optical power dependence did not follow a quadratic dependence expected from optical rectification alone. Instead, the power dependence followed an $x^{3.4}$ behavior, indicating other processes such as surface plasmon excitation [143]. This work was the first evidence that THz generation utilizing plasmonic nanostructures could be possible.

Several later works continued to explore THz emission from metallic nanostructured surfaces [144]–[148]. Welsh and Wynne expanded on their initial work by studying a periodic nanoscale grating structure etched into fused silica and coated in a thin metal layer. Characterization of the optical absorption spectrum showed a narrow absorption peak characteristic of plasmonic resonance. This peak could be tuned from around 670 nm to 870 nm central wavelength across a 20° to 50° incident angle range [145]. For gratings coated in a 40 nm gold (Au) layer, the maximum output THz field was around 50% lower than the field generated from a 0.5 mm thick ZnTe crystal. When coated in 45 nm of silver (Ag), however, the THz field dropped to over two orders of magnitude lower [145]. Theoretical studies by Gao et al. investigated ordered arrays of metal nanodisks, rings and pyramids on a glass surface [146]. The intensity of THz radiation emitted from these surfaces was shown to be highly dependent on the nanostructure geometry, although geometry did not alter the bandwidth of the emitted THz [146].

Extensive experimental work by Polyushkin et al. utilized nanosphere lithography techniques to fabricate triangular nanostructure arrays and study their THz emission characteristics [147]. Similar to previous works, it was found that the intensity of the output THz pulses was highly dependent on the size and shape of the nanostructures. Although the output THz intensity was around 10x lower than a standard ZnTe crystal, it was noted that certain applications could take advantage of the extremely thin (sub-micron) nature of these nanoplasmonics emitters [147].

Ramakrishnan et al. compared randomly nanostructured metal films to continuous ones, observing up to 24x enhancement of output THz intensity as compared to continuous films [148]. However, it was noted that the highest THz intensities observed were still nearly two orders of magnitude lower than conventional THz PCA emitters [148]. Further work by Ramanandan et al. demonstrated that absorption in the region near the Schottky junction of the device is critical for THz generation, more so than the total amount of light absorbed [149]. This configuration is illustrated in Figure 1.4.2.1(a) (Figure 1(a) in [149]), where the THz surface emission is enhanced by the optical interaction with the nanograting surface plasmons. SEM images of the fabricated device before and after cuprous oxide (Cu_2O) deposition are shown in Figure 1.4.2.1(b) and Figure 1.4.2.1(c) (Figure 1(b) and Figure 1(c) in [149]) [149].

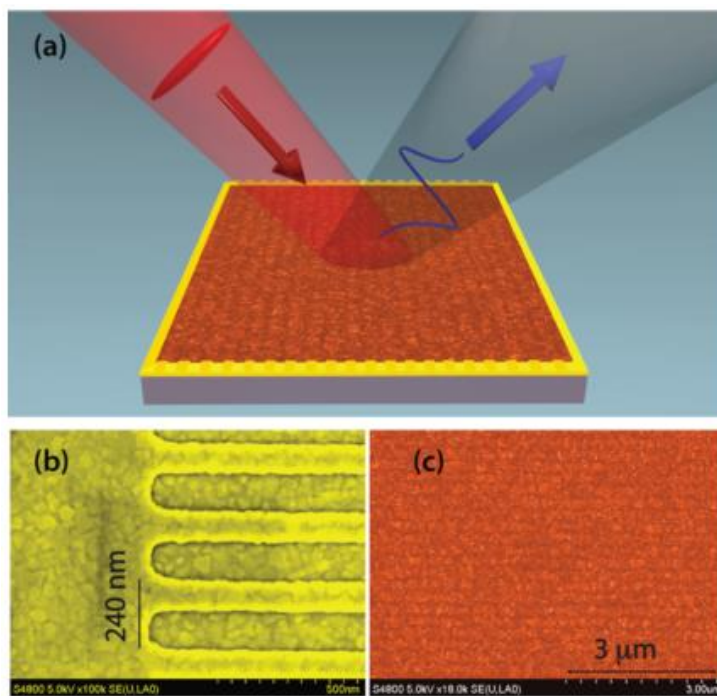


Figure 1.4.2.1: (a) Schematic diagrams of the nanostructured Au/ Cu_2O Schottky junction THz emitter. The pump laser pulses are incident on the sample, generating THz pulses. A nanograting is fabricated at the interface to facilitate the excitation of surface plasmons. (b, c) False color SEM image of the grating after the deposition of Au and Cu_2O , respectively. Reprinted with permission from [149]. Copyright 2016 American Chemical Society.

Several uniform conclusions can be drawn from the works studying THz emission from nanostructured metal surfaces. First, the generated THz oscillations are a direct result of the plasmon oscillations in the nanostructures. Second, there is a strong dependence on the intensity of the output THz on the magnitude of the nanostructure plasmon resonance. Third, the intensity of the emitted THz is generally one order of magnitude lower than that of a ZnTe crystal, though the drastically reduced thickness of the emitter could provide advantages in certain applications. Although the previously described works presented THz generation through unbiased optical-plasmon interactions alone, they were inspiration for later works combining nanoplasmonics and PCA technology for producing high power pulsed THz sources.

1.4.3. Gap-Located Nanostructures

The first demonstration of enhanced THz PCA performance through incorporation of plasmonic nanostructure arrays was given in 2011 by Park et al. [150]. Standard bowtie dipole antennas were patterned on SI-GaAs substrates, followed by electron beam lithography patterning of periodic nanostructure arrays in the dipole gap. Four different configurations were compared; two nanosquare arrays and two nanograting arrays with 75 nm and 150 nm widths. Reflectance measurements illustrated minimum reflectance in the 75 nm nanosquares at an 800 nm excitation wavelength. Comparing the nanostructured PCAs to conventional ones, it was found that the greatest improvement in output THz power was observed in the 75 nm nanograting arrays, which increased the 0.1-1.1 THz average power by a factor of 2.27 [150]. The work was continued by Park et al. [151], [152] where the electron beam lithography was replaced with an annealing process to self-assemble Ag nanoislands, and where the previously studied nanogratings [150] were further optimized to improve THz emission. The self-assembled

Ag nanoislands showed 0.1-1.1 THz average power enhancement by a factor of 2, lower than the nanograting studies [150]. Measurements of the optical spectrum extinction coefficient of the array were compared to measured output THz power of the array for varied nanograting width [152]. It was found that when the peak in the extinction coefficient centered at the 800 nm excitation wavelength the output THz power enhancement across the 0.1-1.1 THz range was maximized at 2.4x [152].

Others have incorporated gap-located nanostructures into THz PCAs in order to improve aspects of the device performance. Jooshesh et al. fabricated PCAs with ordered arrays of hexagonal and grating nanostructures in the antenna gap, as well as a reference conventional non-plasmonic dipole emitter, all on SI-GaAs [153]. SEM images of the fabricated devices are shown in Figure 1.4.3.1 (Figure 1 in [153]). Comparing the plasmonic structures to the conventional reference, it was found that the hexagonal structures had the greatest enhancement of the THz pulse peak at a factor of around 5.5 at an optical pump power of 2 mW [153]. Further work exploited an additional advantage of gap-located plasmonic nanograting structures [154]. Here, it was demonstrated that these plasmonic structures could enable efficient absorption of photons with energy significantly below the bandgap of LT-GaAs. Exciting different PCAs with 1.57 μm wavelength femtosecond pulses, it was shown that LT-GaAs based PCAs with the nanograting structures produced THz pulses with peak amplitude over 11 times greater than a conventional LT-GaAs PCA. Even more significant was that the peak THz field of the plasmonic LT-GaAs PCA was around 1.8 times greater than that of a commercially available conventional PCA based on InGaAs, which had a bandgap below the excitation wavelength [154]. This enhanced performance was attributed to the introduction of midgap states in the LT-GaAs due to the presence of the plasmonic nanostructures. These midgap states allow for two photon

absorptions in order to efficiently excite photocarriers from the valence to conduction band [154]. A unique architecture for a thin-film THz PCA detector was recently proposed by Mitrofanov et al. [155]. This device consisted of a thin 280 nm LT-GaAs layer located between an AlAs/Al_{0.2}Ga_{0.8}As distributed Bragg reflector (DBR) and a periodic array of Au plasmonic nanostructures. The nanostructures and DBR worked in unison to effectively trap the incident photons in the LT-GaAs layer, increasing the optical absorption and generated photocarriers. The detectors showed a 50% increase in detected photocurrent when the nanostructures are included. This was achieved while maintaining a high dark resistivity of the device, which is necessary to minimize detection noise [155].

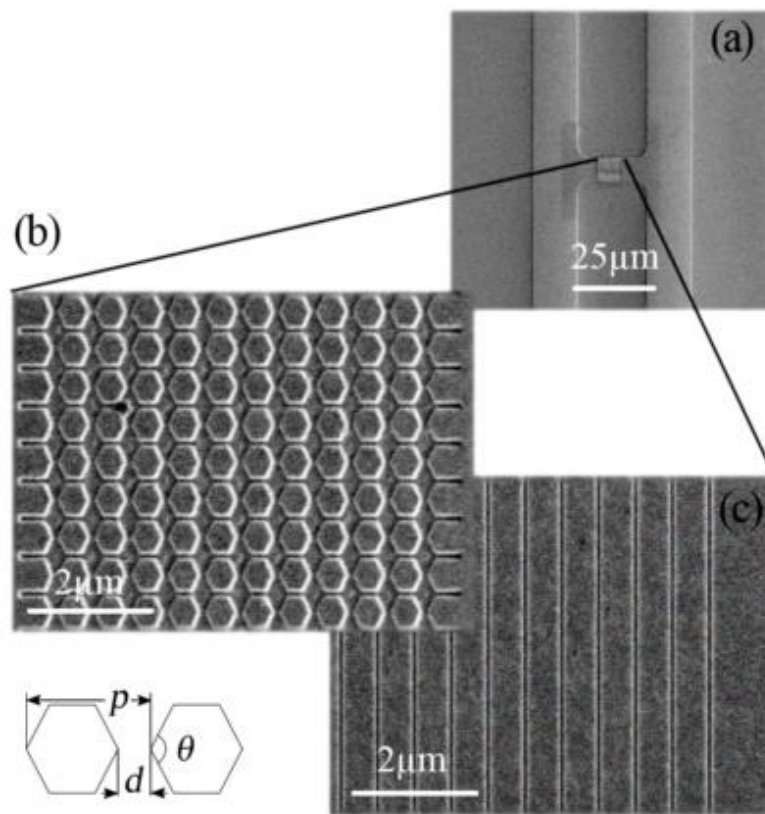


Figure 1.4.3.1: (a) SEM image of the 20 μm dipole on SI-GaAs substrate. (b) The active area of the hexagonal plasmonic array. (c) The active area of the strip plasmonic array. The diagram shows apex angle θ , gap size d and periodicity p . Reprinted from [153] with permission from OSA Publishing.

1.4.4. Nanostructured Electrodes

In addition to THz PCAs with gap-located nanostructures, several works have investigated nanostructuring of the antenna electrodes directly [61], [66], [67], [71], [132], [156]–[159]. The key distinction here is that in this configuration the nanostructured regions are electrically continuous with either the anode or cathode, rather than being electrically isolated. An example of this from the work of Moon et al. is shown in Figure 1.4.4.1 (Figure 1(a) in [160]).

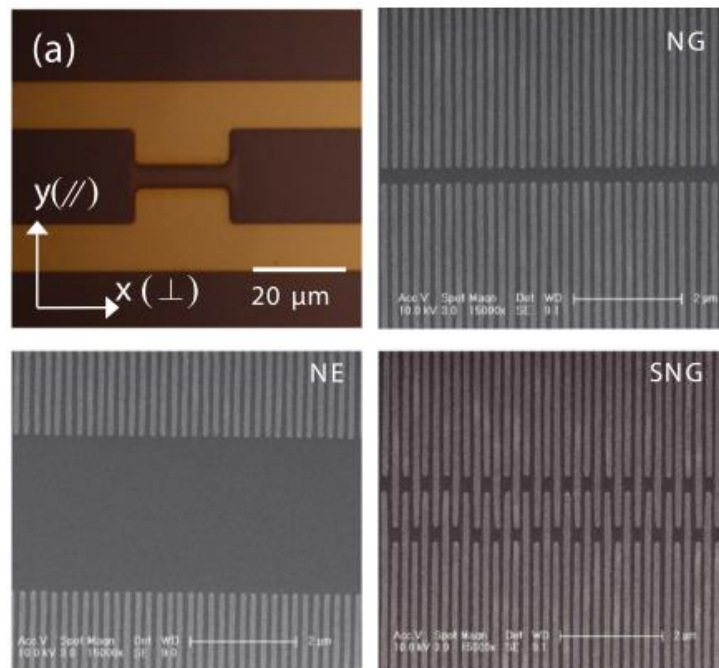


Figure 1.4.4.1: Optical microscope image of H-dipole structure and SEM of the fabricated nano-electrodes. Reprinted with permission from [160] under the Creative Commons Attribution 4.0 International License.

Here, a microscope image of a standard dipole antenna structure is shown, along with SEM images of the various nanoplasmonic grating structures fabricated as part of the dipole electrodes [160]. Most work investigating nanostructured electrodes attempt to enhance the near-anode effect, the high output THz power that is observed when the optical pump is centered over the anode. By nanostructuring the antenna electrodes, the effective area of the near-anode region can

be increased such that the full area of the incident optical pump falls on the near-anode region. Additionally, the plasmonic resonances of the nanostructures can be tuned in such a way as to concentrate the incident optical pump in the near-field region of the anode, thus increasing the optical absorption inside the photoconductor near the anode. One of the first theoretical predictions of this effect was made by Zhong et al., where a narrow cone shaped anode fully embedded in a LT-GaAs layer was studied. Finite-difference time-domain studies illustrated that plasmonic enhancement of the optical field near the anode could be as high as 164 times greater in a nanoscale cone electrode as compared to a microscale cone electrode [156].

Early fabrication and experimental demonstration of a THz PCA with nanostructured electrodes was performed in 2012 by Berry and Jarrahi [157]. Anode-ground-cathode dipole antennas were patterned on an $\text{In}_{0.53}\text{Ga}_{0.47}\text{As}$ photoconducting layer, with a 1 μm gap from the electrodes to the center ground and a 100/100 nm nanograting array incorporated into the electrodes [157]. These arrays, which were computationally studied in previous work [158], increase the optical absorption which takes place near the antenna electrodes [157]. Emitted THz pulsed from fabricated devices were shown to maintain a narrow 590 fs pulse width and generated an average output THz power up to 5 μW under 7 V bias and 85 mW optical power [157]. This concept was expanded on in several works [66], [67], [71], [132], [159]. Utilizing a 3x3 array of log-periodic dipoles with nanograting electrodes, high average output THz power of 1.9 mW was demonstrated under a 320 mW optical pump power. These antennas, fabricated on LT-GaAs, required a microlens array for individual focusing of the incident optical pump onto the active area of each device [66]. The highest observed optical-to-THz conversion efficiency was demonstrated by designing a three-dimensional array of nanostructured electrodes [67]. In this example, the nanostructured electrodes consisted of rows of nanopillars etched into a LT-

GaAs substrate with Au contact electrodes patterned on the sides and bottoms. These structures were shown to further localize the incident optical pump near the antenna anode, and demonstrated a 7.5% optical-to-THz conversion efficiency at a 60 V bias and 1.4 mW optical pump power [67]. Utilizing the plasmonic nanograting design of [71], [132], a large area emitter was fabricated and demonstrated to produce a record high 3.8 mW average THz power across the 0.1-5 THz range [66]. This design has the advantage of not requiring alignment of a microlens array as in [132] as well as requiring comparatively less complicated fabrication methods for the plasmonic electrodes as compared to [67].

Plasmonic nanostructured electrodes have been studied by several other groups as well [77], [160]–[162]. Heshmat et al. fabricated THz PCAs on LT-GaAs with interdigitated electrodes that had 100 nm anode-cathode gaps [161]. The emitted THz pulse peak-to-peak amplitude was found to be 2x greater than that of a commercially available conventional emitter. The improvement was even greater when compared to similar shaped conventional emitters fabricated on LT-GaAs and SI-GaAs, which gave 10x and 40x improvement, respectively [161]. Tanoto et al. fabricated and compared THz PCAs with tip-to-tip and interdigitated nanograting electrodes in a CW photomixing configuration [77]. A bolometer was utilized to measure the output THz intensity as a function of optical beat frequency. It was found that the tip-to-tip configuration had around two orders of magnitude increase in the THz intensity as well as increased bandwidth. Finite-difference time-domain (FDTD) simulations supported these measurements, showing that the calculated optical field enhancement matched the out THz intensity enhancement [77].

Moon et al. experimentally compared three different nanograting designs; nanograting electrodes with 3 μm and 200 nm anode-cathode gaps, and nanograting electrodes with partially

interdigitated nanogratings between the anode and cathode [160]. All devices showed increased power output at low optical excitation power as compared to a reference, nonplasmonic PCA, as shown in the time-domain waveform and fast Fourier transform (FFT) spectra in Figure 1.4.4.2 (Figure 5 in [160]).

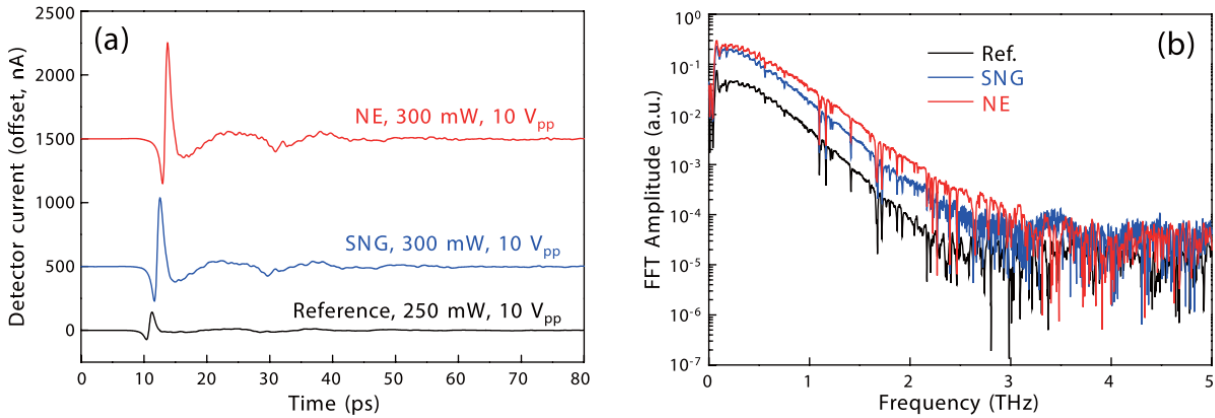


Figure 1.4.4.2: THz emission from the large-aperture PCAs: (a) Time-domain curves. (b) FFT spectra. Reprinted with permission from [160] under the Creative Commons Attribution 4.0 International License.

The enhancement was attributed to two mechanisms; plasmonic enhancement of the optical field near the electrodes and enhancement of the DC bias field near the electrodes. The dominating mechanism depended on the power of the incident optical pump, which indicated that nanogratings with the 3 μm gap was dominated by plasmonic enhancement while the partially interdigitated nanograting electrode was dominated by bias field enhancement [160]. Computational work by Burford and El-Shenawee using COMSOL[®] Multiphysics proposed a thin-film PCA emitter utilizing metal nanodisk arrays to enhance the optical absorption in the photoconductor [163]. It was shown that the combination of the plasmonic structures and thin-film photoconducting layer effectively localized the optical absorption near the antenna anode, increasing the peak induced photocurrent by nearly 3 orders of magnitude [163].

1.4.5. Summary and Outlook

The advantages, disadvantages, and key performance milestones for plasmonic nanostructure THz PCAs are summarized in Table 1.4.5.1. Similar to the large area emitters, these devices offer potential for high device quantum efficiency, with some devices combining nanostructured electrodes with large area emitter designs to yield record high output THz power of 3.8 mW from a PCA device [66]. However, due to lack of maturity in nanoscale lithography technology, fabrication of such ordered metallic nanostructures remains far more complex than standard THz PCA devices. This is exaggerated by the high sensitivity of the optical-plasmon interaction with the nanostructure geometry, which increases the need for high fabrication standards. As nanofabrication processes become increasingly standardized, incorporation of plasmonic nanostructures may also become industry standard for THz PCA technology.

Table 1.4.5.1: Summary of plasmonic nanostructure enhanced THz PCAs.

	Advantages	Disadvantages	Key Reported Performance Milestones
Gap Located Nanostructures	Increased quantum efficiency	Decreased gap dark resistivity and complex fabrication	2.1 nA peak THz current [154]
Nanostructured Electrodes	Increased quantum efficiency and no increase in gap dark resistivity	Complex fabrication	3.8 mW output THz power, 5 THz bandwidth [66]

1.5. Broadband Performance

1.5.1. Challenges

One of the attractive properties of pulsed THz emission from PCAs is the broadband nature of the emitted radiation. Typically, usable bandwidths in the range of 0.1 to 4 THz are readily achievable in LT-GaAs based PCA emitters pumped with 100 fs pulses [44]. There is significant motivation for increasing the spectral power density of higher frequency components. However,

several challenges exist in standard THz TDS configurations that limit the usable frequency bandwidth. Broadband performance requires dipole antennas with uniform radiation resistance and low reactance across the desired bandwidth [132]. For the wide bandwidths desired in THz TDS, this often leads to a tradeoff with other performance characteristics [75]. There are also inherent limitations in the available bandwidth of the optical femtosecond pulse. Although narrower pulse widths with a wider available bandwidth are available, high THz frequency losses in the PCA substrate often prevents the extension to higher frequencies using these sub-100 femtosecond excitation [70]. Propagation through the PCA substrate has a detrimental effect on the THz bandwidth, especially in GaAs. GaAs has a phonon absorption resonance centered at around 8.3 THz. The absorption loss for a THz pulse propagating through 500 μm (typical substrate thickness) of GaAs increases rapidly with frequency, falling to 50% of the original signal strength at around 3.3 THz [164]. This absorption loss is a major limiting factor in the bandwidth of the emitted THz pulses and is why utilizing below 100 fs optical pulses in these configurations does not significantly improve the bandwidth.

1.5.2. Broadband Dipole Antenna

Early THz PCAs, as well as many still in use today, utilized simple dipole antenna structures such as parallel microstrip lines [42] or face-to-face dipoles [41], [73] as the primary radiating elements. The major disadvantage of using such simple radiating elements is that they are inherently single and narrow band. Although the coherent detection nature of THz TDS systems offers high signal-to-noise [165], losses outside of the dipole's resonant frequency range can be a significant source of performance degradation [75]. Utilizing established microwave engineering

concepts, several works have aimed to implement multi and/or broadband dipole structures in order to improve the radiation efficiencies of these THz antennas [63], [67], [132], [166]–[172].

To the author's best knowledge, the first attempt to study the use of broadband antennas in THz PCAs was made in 1991 by Dykaar et al. [166]. This early work compared broadband log spiral and log periodic antenna patterns to simple face-to-face dipoles, with results indicating that the broadband antennas could yield an order of magnitude response improvement [166]. Log periodic antennas were also studied by Gitin et al. [167] and Mendis et al. [63]. In sub-0.1 THz frequencies the response was found to be highly multiband, with resonant frequencies corresponding to the various lengths of the periodic elements [167]. Brown et al. fabricated GaAs based THz PCAs with square spiral antennas and tested their polarization characteristics in a photomixing configuration [168]. This antenna was predicted to have a continuous, broadband response at lower THz frequencies (< 1 THz). However, experimental results showed narrow resonance peaks occurring across the 0.1-1 THz measurement range. These results were attributed to the discrete nature of the antenna pattern, where each turn of the square spiral acted as an individual radiating element with a single, narrow resonance [168]. The same antenna was implemented in a pulsed optical excitation scheme to study the effects of photoconductive material and substrate [169], [170].

A bullseye dipole with periodic grooves in the dipole metallization was studied by Liu, Shou, and Nahata [171]. This structure utilized THz frequency plasmon-polariton resonances along the periodic grooves to produce a narrow, two times greater resonance peak at a single frequency as compared to a simple dipole. Numerical simulations indicated that this resonance peak can be tuned by adjusting the size and period of the periodic grooves [171]. More recently, logarithmic spiral antennas were combined with nanostructured electrodes to improve the radiation

efficiency of THz PCAs [67], [132]. Numerical simulations indicated that the log spiral maintains a much more uniform radiation resistance and lower reactance than the more common bowtie dipoles, with experimental results showing around 4x higher radiated powers [132].

1.5.3. Ultrabroadband Emission and Detection

Standard configurations of THz TDS setups have a major inherent limitation of their available bandwidth. In all TDS setups, the optical pulse excitation is incident on the electrode side of the PCA, since it would be unable to penetrate the optically thick substrate material in order to excite photocarriers in the dipole gap [39], [44], [73]. The generated THz radiation is emitted in both directions, however, the majority of TDS setups only utilize the forward propagating THz radiation (i.e. the radiation which passes through the PCA substrate, propagating in the same direction as the optical pulse). The reason for this is that it reduces the experimental setup complexity, since the optical and THz beam paths do not overlap [173]. As previously mentioned, this is at the cost of loss of bandwidth due to absorption loss in the GaAs substrate.

One of the first works observing this effect was reported by Kono et al. [174]. Here, a SI InP electro-optic crystal pumped with 15 fs optical pulses was utilized as a source of broadband (>20 THz) radiation. The same 15 fs optical pump was utilized to gate a LT-GaAs PCA detector in a conventional setup where the optical pump and THz beam are incident on opposite sides of the detector. A discontinuous frequency band up to around 20 THz was observed with a strong absorption band between 7 and 9 THz due to the GaAs detector substrate absorption [174]. Later works using a similar setup implemented a collinear detection scheme, where the optical gating pump of the detector was aligned with the transmitted THz radiation and both were incident on

the antenna side of the detector [55], [70], [82], [173]. PCAs gated with 15 fs pulses were demonstrated to achieve the same bandwidth as electro-optical sampling with a ZnTe crystal [70]. Modulation of the optical delay using the shaker method was utilized to measure time-derivatives of the THz waveforms, which expanded the detectable emission from a ZnTe crystal up to 60 THz [173]. Others have demonstrated the use of these broadband detection schemes to characterize vibrational modes in various materials, including cytidine [175] and maltose [176]. A 40 fs THz pulse measured by Shen et al. is shown in Figure 1.5.3.1(a) along with the Fourier transform spectrum illustrating a bandwidth beyond 30 THz in Figure 1.5.3.1(b) (Figure 2 in [175]). Additional, spectral measurements of polytetrafluoroethylene (PTFE) are shown as the dotted trace in Figure 1.5.3.1(b). Here, PTFE vibrational modes up to 19.2 THz were observed [175]. More recent work has characterized the high power, broadband forward emission of a LT-GaAs PCA with interdigitated electrodes [127]. Here, a bandwidth of up to 20 THz was observed. Reducing the incident pulse power caused a uniform reduction of THz power across the spectrum, while increasing the pulse width reduced the high frequency components of the signal [127].

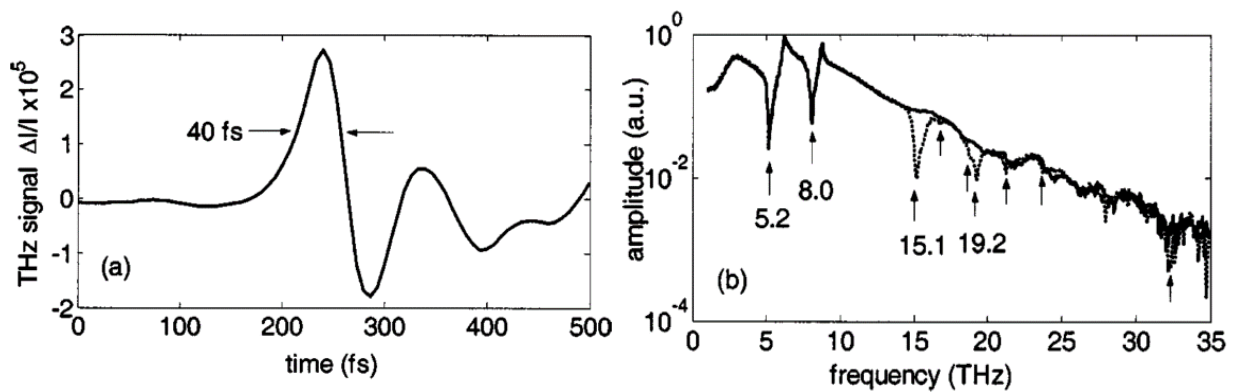


Figure 1.5.3.1: (a) The temporal THz wave form and, (b) its corresponding Fourier transform amplitude spectrum (upper trace, solid line), together with spectrum measured in the presence of PTFE sample (lower trace, dotted line). Reprinted from [175], with permission of AIP Publishing.

1.5.4. Summary and Outlook

The advantages, disadvantages, and key performance milestones for plasmonic nanostructure THz PCAs are summarized in Table 1.5.4.1. Design of broadband antennas show potential for increasing the useable THz bandwidth. However, it is clear that other factors such as varying polarization and resonant/no resonant regions across the desired operating band would likely need to be accounted for when implementing these complex antenna geometries into practical THz PCA systems. Shorter optical pulses and collection of surface emitted THz waves have demonstrated ultrabroadband pulse emission, reaching well into the far-infrared optical regime. However, since the optical beam cannot be isolated from the THz beam, safety becomes a concern for practical applications. Therefore, these configurations are currently limited to laboratory research.

Table 1.5.4.1: Summary of broadband performance of THz PCAs.

	Advantages	Disadvantages	Key Reported Performance Milestones
Broadband Dipole Antenna Design	Increased emission bandwidth	Trade-off with polarization control	4x increased total THz power comparing log spiral to bowtie [132]
Ultrabroadband Emission and Detection	Full THz band coverage	Experimental setup not practical for many applications	60 THz detection bandwidth [173]

1.6. Concluding Remarks

From this review it is apparent that there are many avenues to the ultimate goal of improving the performance of THz PCA technology. Each of these show continuing promise for further improvement of THz TDS systems. However, it is likely that the next generation of pulsed THz systems will implement several of these methods in order to achieve superior performance as compared to current standard technology.

Chapter 2. Plasmonic Thin-Film Terahertz Emitter Design and Computational Modeling

This chapter will present the geometry and concept behind the plasmonic terahertz emitter, as well as the computational modeling that was utilized to optimize and study the device.

The majority of the work presented in this chapter has been published in the Journal of the Optical Society of America B, in the article titled “Computational Modeling of Plasmonic Thin-Film Terahertz Photoconductive Antennas” [163]. This was the work of the author of this dissertation, along with the advising professor of the author. The author of this dissertation was the primary author of the publication and as such there will be notable similarities in the voice and style of the two works.

2.1. Conceptual Plasmonic Thin-Film Terahertz Emitter Design

In order to overcome low optical-to-THz conversion efficiency of conventional THz-PCAs, a new plasmonic enhanced thin-film design was proposed. Thin-film photovoltaics have been proposed and extensively demonstrated for use in solar cell technology [136], [137], [177], [178]. In such applications, high quality active and sacrificial layers a few hundred nanometers in thickness are epitaxially grown [179]. The active layers can then be “peeled” off through a process called “epitaxial lift off”, allowing a single substrate to be reused and yield multiple high quality solar cells [179]. In solar cells, however, this leads to lower device performance compared to their thick substrate based counterparts [177], [178]. Much of the incident light is reflected out or passed through the photovoltaic thin-film before being absorbed. To overcome this, the addition of plasmonic metal nanostructures on the thin-film surface has been proposed to concentrate the incident optical energy in the near-field of the nanostructures. This increases

the total photon density in the photoconductive layer, consequently improving the photocarrier generation rate [136], [137].

We propose a new plasmonic thin-film THz-PCA design which utilizes the characteristics of thin-film solar cells to offer improved optical-to-THz conversion efficiency. The device geometry is illustrated in Figure 2.1.1 - Figure 2.1.3. Figure 2.1.1 shows a 3D view of the THz-PCA chip mounted on a high resistivity Si lens. The LT-GaAs layer is rendered as semi-transparent to allow the location of the antenna anode and cathode to be easily observed, as well as to illustrate the fact that such thick layers are semi-transparent to the naked eye. The infrared optical pump is incident from the $-z$ -direction and focused over the antenna anode. Photocarriers generated in the LT-GaAs contribute to a driving current for the antenna, producing THz radiation which is coupled out of the device by the Si lens.

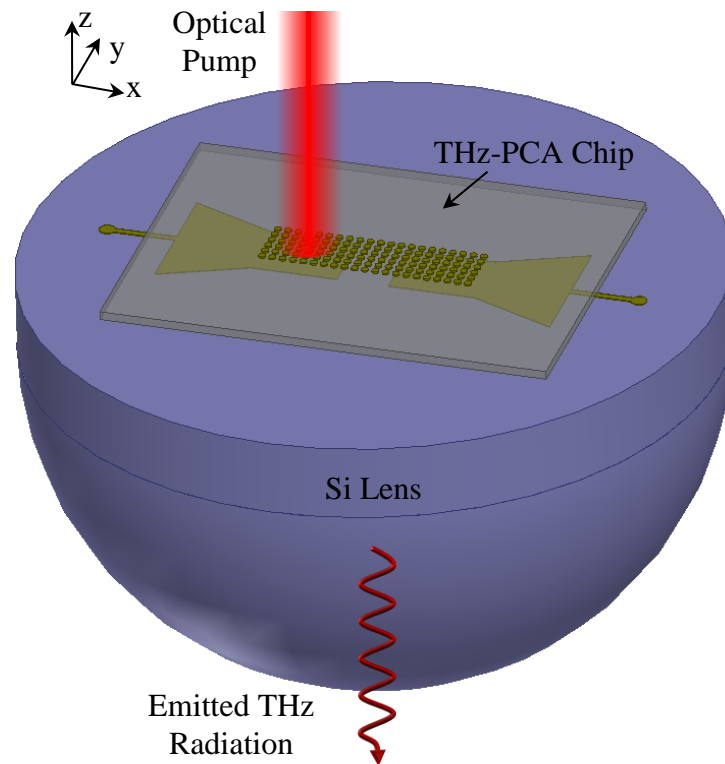


Figure 2.1.1: Illustration of the proposed plasmonic thin-film THz-PCA design, 3D isometric view of the THz-PCA mounted on a Si THz lens (not to scale).

A top view of the x-y plane is shown in Figure 2.1.2. The location of the antenna anode and cathode is illustrated by the dashed black line, as these are located under the LT-GaAs layer. A Au nanodisk array covers the top of the LT-GaAs across the relative location of the antenna anode, gap, and cathode. The nanodisk array is included over all regions to allow future investigation of plasmonic enhanced optical excitation of regions other than the anode. Additionally, fabrication of the actual device would be simplified by roughly aligning a large nanodisk array over the entire region rather than fine alignment to ensure the array is only over the anode.

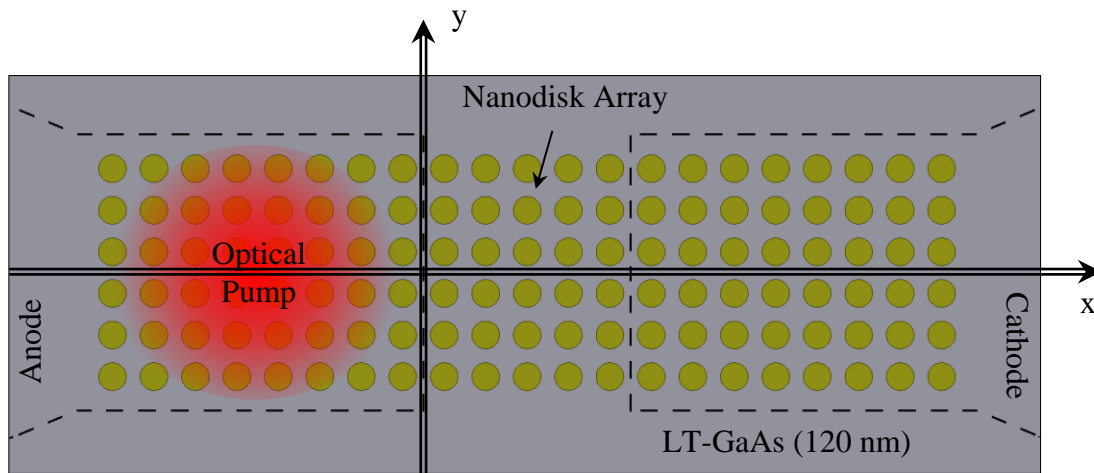


Figure 2.1.2: x-y plane top view of the device, antenna electrode locations outlined by the dashed black lines. Computational domain is indicated by the dot-dashed outline (not to scale).

Figure 2.1.3 shows a x-z cross section of the device taken at the y-coordinate corresponding to the device center. The computational domain to be considered in this work is outlined in Figure 2.1.2 and Figure 2.1.3 by the dot-dashed outline. The THz-PCA anode and cathode are located on the bottom of the LT-GaAs thin-film layer, while an array of plasmonic nanodisks is located on the top surface. In the gap separating the anode and cathode there is a dielectric adhesive layer, since during fabrication such a layer will be necessary to attach the device to the

Si lens. The incident optical pump excites plasmon resonances in the nanodisk array, leading to the enhanced optical field in the LT-GaAs layer. In addition to the plasmonic enhancement, the proposed thin-film PCA will have improved performance due to complete usage of the available optical pump area. In LT-GaAs, only the carriers generated within around 100 nm from the anode will be collected. The carriers generated further away will recombine due to the sub-picosecond carrier lifetime of the material. Therefore, in a conventional PCA where the optimal location of the optical pump is centered on the anode edge [80], the generated carriers will be much less than those generated in the proposed thin-film PCA where the optical pump is centered over the anode.

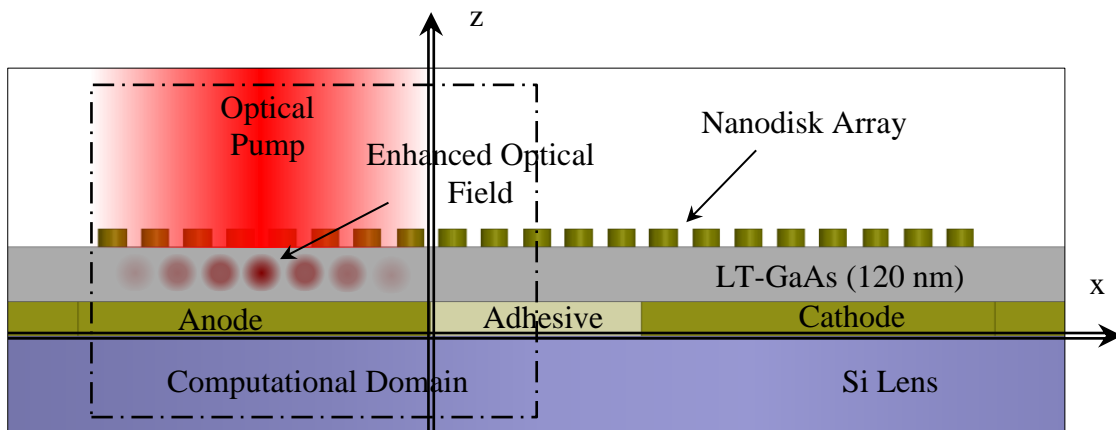


Figure 2.1.3: x-z plane cross section view, nanodisk array located on top of the 120 nm thick LT-GaAs photoconductive layer, THz-PCA anode and cathode located on the bottom of the LT-GaAs. Device is mounted with adhesive to the Si lens for mechanical support as well as coupling of the THz radiation out of the device. Computational domain is indicated by the dot-dashed outline (not to scale).

2.2. Approximations for Reducing the Computational Domain

Due to the fine meshing requirements needed to accurately solve the near field of plasmonic nanostructures [136], [137], [180], several approximations are made to reduce the computational domain as shown in Figure 2.1.2 and Figure 2.1.3.

- 1) Considering only the interaction between the optically induced photocurrent and the electrode induced DC bias in the LT-GaAs, the antenna radiating element, microstrip lines and bias pads are neglected.
- 2) Asymmetric optical excitation focused on the anode as shown in Figure 2.1.3 allows the domain to be reduced by half at the center of the gap.
- 3) Geometric periodicity allows plasmonic electrode structures with periodicity along the y-direction to be modeled while greatly reducing the computational complexity as shown in Figure 2.1.3.

These approximations allow the computational domain to be reduced to a point where nanoscale structuring of the electrodes can be modeled with sufficiently fine meshing with reasonable computational resources. To illustrate this, consider that some of the configurations to be discussed in this work require approximately 500,000 mesh elements in the photoconductor region to ensure numerical accuracy. Without implementing approximation 2) and 3), the number of mesh cells needed to produce the same level of refinement would be at least 50 times larger, on the order of 25 million mesh elements.

2.3. Finite Element Method Modeling using COMSOL[®] Multiphysics

Unless specified otherwise, the numerical modeling presented in this dissertation was performed using the commercially available Finite Element Method (FEM) solver COMSOL[®] Multiphysics. The FEM is a powerful tool for analyzing the physics complex 3D geometries that cannot be solved for analytically. In general, the FEM works by discretizing the computational

domain into individual volumetric elements, assigning solution points to each element (corners, edge centers, face centers, etc.), applying interpolation functions between solution points, and solving a set of partial differential equations at all solutions points such that continuity and boundary conditions are satisfied. The physics that can be analyzed through this method vary greatly, including propagation of mechanical stress and strain, thermal energy transfer, fluid flow and most important to this dissertation, the electromagnetic wave interaction and the transport of charges in semiconductors.

As previously discussed, the generation of THz pulses in a photoconductive antenna involves the photogeneration of electron-hole pairs inside a photoconductor using an ultrashort optical pulse, collection of the generated carriers by a DC biased metal dipole antenna, and reemission of a propagating transient THz pulse.

Computational modeling was divided into two steps: 1) the optical response found by calculation of the spatial distribution of the optical field using the frequency-domain form of the electromagnetic wave equation; and, 2) the electronic response found by solving the time-domain forms of the coupled drift-diffusion and Poisson's equations under carrier generation derived from the optical field from the first step. By implementing several approximations to decouple the optical and electrical responses, the model complexity was reduced while still accounting for the primary factors determining the induced THz photocurrent response.

2.4. Optical Response

To properly model the femtosecond laser pulse excitation in COMSOL, an expression for the spatially and temporally varying electric field excitation must be defined in terms of standard femtosecond laser defining parameters. Femtosecond lasers are most often characterized by their

average power, half power beam width (HPBW), pulse time duration, and repetition rate. These parameters, units, and range typical values are summarized in Table 2.4.1.

Table 2.4.1: Defining parameters with typical values for femtosecond laser excitation of THz PCAs

Parameter	Symbol	Units	Typical Value
Average Power	P_{ave}	mW	0.1-100
HPBW	$D_{x,y}$	μm	5+
Pulse Time Duration	D_t	fs	80-200
Repetition Rate	f_p	MHz	50-100

To begin, first consider the expression for the time-averaged laser power,

$$P_{ave} = f_p P_{max,t} \int_0^{1/f_p} \exp\left(4 \ln(0.5) \frac{(t - t_0)^2}{D_t^2}\right) dt. \quad (\text{Equation 2.4.1})$$

t_0 indicates the time location of the pulse peak, a useful parameter for modeling but with no physical significance. By making the approximation,

$$\int_0^{1/f_p} = \int_{-\infty}^{\infty},$$

Equation Equation 2.4.1 reduces to,

$$P_{ave} = f_p P_{max,t} \frac{D_t}{2} \sqrt{-\frac{\pi}{\ln(0.5)}}. \quad (\text{Equation 2.4.2})$$

The error introduced in this approximation, considering typical values for the parameters, is on the order of $1 - \text{erf}(10^5)$, which is too small to easily compute. Rewriting, the peak power in time is,

$$P_{max,t} = P_{ave} \frac{2}{f_p D_t} \sqrt{-\frac{\ln(0.5)}{\pi}}. \quad (\text{Equation 2.4.3})$$

Assuming a Gaussian distribution of power in the x and y dimensions, the power density (in space and time) can be related to the peak power by,

$$P_{\max,t} = \int_{-\infty}^{\infty} \int_{-\infty}^{\infty} S_{\max,t,x,y} \exp\left(4 \ln(0.5) \frac{(x - x_0)^2}{D_x^2}\right) \exp\left(4 \ln(0.5) \frac{(y - y_0)^2}{D_y^2}\right) dx dy$$

$$P_{\max,t} = -S_{\max,t,x,y} \frac{\pi D_x D_y}{4 \ln(0.5)}. \quad (\text{Equation 2.4.4})$$

$S_{\max,t,x,y}$ is the temporal and spatial peak in the power density, x_0 and y_0 correspond to the spatial location of the peak. $S_{\max,t,x,y}$ is related to the peak electric field by,

$$S_{\max,t,x,y} = \frac{E_{\max,t,x,y}^2}{\eta_0} \quad (\text{Equation 2.4.5}),$$

where η_0 is the electromagnetic wave impedance. For all instances in this work, the wave excitation occurs in air and wave impedance is $\eta_0 = 120\pi$ (Ω). Combining Equations 2.4.3, 2.4.4, and 2.4.5 allows for the peak electric field to be written in terms of known laser parameters,

$$E_{\max,t,x,y} = \sqrt{\frac{P_{\text{ave}} 8 \eta_0}{f_p D_x D_y D_t}} \left(-\frac{\ln(0.5)}{\pi}\right)^{3/4}. \quad (\text{Equation 2.4.6})$$

The full expression for the optical electric field excitation is,

$$\vec{E}_{\text{inc}}(x, y) = \hat{a}_e \sqrt{\frac{P_{\text{ave}} 8 \eta_0}{f_p D_x D_y D_t}} \left(-\frac{\ln(0.5)}{\pi}\right)^{3/4} \dots$$

$$\dots \exp\left(2 \ln(0.5) \frac{(x - x_0)^2}{D_x^2}\right) \exp\left(2 \ln(0.5) \frac{(y - y_0)^2}{D_y^2}\right) \quad (\text{Equation 2.4.7})$$

Here, \hat{a}_e is the electric field polarization unit vector. Considering the approximations discussed in Chapter 2.2 of this Dissertation, the Gaussian dependence in the y-direction is neglected (i.e. $y - y_0 = 0$). With an expression for the optical excitation derived, the

computational domain's optical response was determined by solving the electromagnetic wave Equation 2.4.8,

$$\nabla \times \mu_r^{-1}(\nabla \times \vec{E}) - k_0^2 \left(\epsilon_r - \frac{j\lambda\sigma}{2\pi c\epsilon_0} \right) \vec{E} = 0. \quad (\text{Equation 2.4.8})$$

Here, ϵ_r , σ and μ_r are the relative electrical permittivity, electrical conductivity, and magnetic permeability for the material, k_0 and ϵ_0 are the free space propagation constant and permittivity, λ is the wave excitation wavelength, c is the speed of light in vacuum and \vec{E} is the complex electric field vector.

Upon solving Equation 2.4.8, the optical field distribution \vec{E} was found everywhere in the computational domain. From here, the vector components of the power flux density can be calculated from Equations 2.4.9, 2.4.10, and 2.4.11, where $\hat{\eta}$ is the material dependent complex wave impedance.

$$P_{ox}(x, y, z) = \frac{1}{2\hat{\eta}} \text{Re} \left(|E_y|^2 - |E_z|^2 \right) \quad (\text{Equation 2.4.9})$$

$$P_{oy}(x, y, z) = \frac{1}{2\hat{\eta}} \text{Re}(|E_z|^2 - |E_x|^2) \quad (\text{Equation 2.4.10})$$

$$P_{oz}(x, y, z) = \frac{1}{2\hat{\eta}} \text{Re} \left(|E_x|^2 - |E_y|^2 \right) \quad (\text{Equation 2.4.11})$$

The total power flux density in units of W/m^2 is,

$$\left(P_s(x, y, z) = \left(|P_{ox}(x, y, z)|^2 + |P_{oy}(x, y, z)|^2 + |P_{oz}(x, y, z)|^2 \right)^{1/2} \right). \quad (\text{Equation 2.4.12})$$

In order to derive an expression for the carrier generation rate inside of the photoconductor, an approximation was made that each photon with energy $E_p > E_g$ (where E_g is the semiconductor bandgap energy) absorbed in the photoconductor [105] generates a single electron-hole pair. The time-dependent carrier generation rate was approximated by [105],

$$g(x, y, z, t) = (4\pi k_{PC}/hc) P_s(x, y, z) \exp\left(4 \ln(0.5) \frac{(t - t_0)^2}{D_t^2}\right), \quad (\text{Equation 2.4.13})$$

where k_{PC} is the imaginary part of the refractive index for the photoconductor, h is Planck's constant, and c is the speed of light in vacuum. Equation 2.4.13 gives both the spatial and temporal carrier generation, in units of $s^{-1}m^{-3}$ inside the photoconductive region.

The boundary conditions for the optical response are periodic on the x-z boundaries and absorbing impedance-matched boundaries are assumed on all other faces. The excitation was incident in the -z-direction, with polarization and center location varying depending on the configuration of the electrodes under consideration. The various model parameters utilized in Equations 2.4.7 – 2.4.13 vary throughout the different studies of this work. Therefore, tables will be included to summarize the values used in each case.

2.5. Electrical Response

With the optically induced carrier generation derived from the optical response analysis, the time-dependent carrier dynamics can be solved. The model utilized for this step was the standard, time-domain form of the coupled Poisson's and drift-diffusion equations (Equations 2.5.1, 2.5.2, and 2.5.3).

$$\epsilon_0 \nabla \cdot (\epsilon_r \nabla V) = q(n - p - N_D + N_A) \quad (\text{Equation 2.5.1})$$

$$\begin{aligned} \frac{\partial n}{\partial t} = & -\frac{1}{q} \nabla \cdot \left\{ -\mu_n q \nabla (V + \chi) n + \mu_n k_B T G \left(\frac{n}{N_c} \right) \nabla n \right\} \dots \\ & \dots - r(x, y, z) + g(x, y, z, t) \end{aligned} \quad (\text{Equation 2.5.2})$$

$$\begin{aligned} \frac{\partial p}{\partial t} = & \frac{1}{q} \nabla \cdot \left\{ -\mu_p q \nabla (V + \chi + E_g) p + \mu_p k_B T G \left(\frac{p}{N_v} \right) \nabla p \right\} \dots \\ & \dots - r(x, y, z) + g(x, y, z, t) \end{aligned} \quad (\text{Equation 2.5.3})$$

The unknowns in this system of equations are V , n and p , the electric potential, electron concentration and hole concentration, respectively. q is the electron charge, ϵ_0 is the permittivity of free space and k_B is the Boltzmann constant. For clarity, all other quantities are defined in Table 2.5.1, with associated nominal values used in this work to model LT-GaAs.

Table 2.5.1: Electrical Properties and Constants of Equations 2.5.1-2.5.4.

Symbol	Description	Units	Value
ϵ_r	LT-GaAs	None	13.3
N_D	Donor Doping Concentration	$1/\text{cm}^3$	$1 \cdot 10^{15}$
N_A	Acceptor Doping Concentration	$1/\text{cm}^3$	0
μ_n	Low-field Electron Mobility	$\text{m}^2/\text{V/s}$	0.8
μ_p	Low-field Hole Mobility	$\text{m}^2/\text{V/s}$	0.047
E_g	Bandgap	V	1.424
χ	Electron Affinity		4.07
T	Room Temperature	K	300
N_c	Conduction Band Density of States	$1/\text{m}^3$	$2.18 \cdot 10^{-23}$
N_v	Valence Band Density of States	$1/\text{m}^3$	$5.43 \cdot 10^{-24}$
τ_n	SRH Electron Lifetime	s	$480 \cdot 10^{-12}$
τ_p	SRH Hole Lifetime	s	$480 \cdot 10^{-12}$
γ_n	Electron Degeneracy Factor	None	2
γ_p	Hole Degeneracy Factor	None	4
C_n	Auger Electron Coefficient	cm^6/s	$7 \cdot 10^{-30}$
C_p	Auger Hole Coefficient	cm^6/s	$7 \cdot 10^{-30}$
$n_{i,\text{eff}}$	Effective Intrinsic Carrier Concentration	$1/\text{m}^3$	$1.23 \cdot 10^{-12}$

As demonstrated by Moreno et al. [181], the inclusion of field dependent carrier mobility significantly impacts the outcome of numerical modeling of THz-PCAs through the drift-diffusion equations. To account for this, the empirical Caughey-Thomas model was utilized to modify the electron and hole mobility, μ_n and μ_p , at varied electric fields [182]. Carrier recombination was described by the Schottky-Read-Hall and Auger recombination models [105].

$$r(x, y, z) = \frac{np - \gamma_n \gamma_p n_{i,\text{eff}}^2}{\tau_p (n + \gamma_n n_{i,\text{eff}}) + \tau_n (p + \gamma_p n_{i,\text{eff}})} \dots$$

$$\dots + (C_n n + C_p p)(np - \gamma_n \gamma_p n_{i,\text{eff}}^2) \quad (\text{Equation 2.5.4})$$

It is important to note that for the electrical response only the LT-GaAs layer was considered. The boundary conditions on the x-z faces are periodic, at the anode/LT-GaAs surface and gap-centered y-z face ohmic contact boundaries with fixed bias voltages $V = V_{\text{bias}}$ and $V_{\text{bias}}/2$, respectively. All other faces are electrical insulation boundaries.

2.6. Approximations of the Mathematical Formulation

It is important to consider the approximations used in this model. The optical pulse is time-dependent and non-monochromatic. As such, the variation of the wavelength dependent material properties should be considered in order to provide a complete description. However, the bandwidth of the femtosecond pulse is relatively narrow, $\Delta\lambda = 9.4$ nm for a pulse with center frequency $\lambda = 800$ nm and width of $D_t = 100$ fs. Of all the materials considered in this model, the highest variance across this bandwidth range occurs in the conductivity of Au up to 3.28%. Although the error this approximation introduces may not be significant here, it is important to note that wider bandwidth pulses will introduce increased variance in the material optical properties.

A second effect arising from the conductivity time-dependence on the optically induced carrier concentration is neglected in this model. This is the carrier screening effect, where excited carriers in the photoconductor will contribute to an increase in the effective optical conductivity [114]. The effect manifests as an increase in surface reflectivity as the pulse propagates into the photoconductor and excites additional carriers. This approximation has led the proposed model to utilize underestimated conductivity leading to overestimation of the induced photocurrent. An analysis of this effect is discussed later.

The above approximations resulted from neglecting iterations between the optical and electrical computational domains at each time step. Currently, solving the optical domain a single time requires approximately 43 min on a dual Intel six-core Xeon X5670 2.93 GHz processor system, in addition to around 1.5 hours to complete the time-stepping in the electrical domain. Inclusion of the carrier screening effect (i.e. the increase in conductivity with time) would require the optical domain to be solved at each of the 200 or more iterations of the time stepping process currently used in the model.

2.7. Model Validation

In order to demonstrate the validity of the proposed model, comparison against both computational and experimental work from the literature was performed here. For comparison of this work to other models, consider the computational work established by Moreno et al. [46], where the FDTD method and a similar set of coupled Poisson's/Drift-Diffusion equations were utilized. The method in [46] did not utilize any of the domain reduction approximations proposed here, thereby providing a more complete analysis of the electro-optical interaction in conventional THz-PCAs. Another distinct difference was that the model in [46] did not calculate the spatially dependent optical field through the solving of Maxwell's equations. Rather, Moreno et al.'s method approximates the optical field with an analytical Gaussian dependence in the lateral direction and a Beer-Lambert dependence in the depth of the photoconductor. Described in [46] was a face-to-face dipole antenna with a 5 μm gap, located on LT-GaAs. The transient photocurrent was calculated at the center of the gap (see Figure 8 in [46]). Similarly, using the proposed method here, the photocurrent at the gap center is calculated in a conventional THz-PCA geometry of same dimensions as the face-to-face dipole described in [46]. Table 2.7.1

summarizes the model parameters use in this study for Equations 2.4.7 – 2.5.4. Note that the value of $P_{ave} = 3.57$ mW is higher than that reported in [46]. This accounts for the air/LT-GaAs reflection losses in our model, which are not considered in [46]. It is important to note that the Gaussian beam formulation of this work appears different than that used in [46]. However, the Gaussian dependence in both x and t is numerically identical in both works.

Table 2.7.1: Optical Properties and Constants of Equations (2.4.7)-(2.5.4) for Validation Study with Moreno et al. [46].

Symbol	Description	Units	Value
λ	Free Space Wavelength	nm	780
P_{ave}	Average Laser Power	mW	3.57
f_p	Laser Pulse Repetition Rate	MHz	80
x_o	Pulse x-axis Center Location	μm	2.5
t_o	Pulse Center Location (time)	ps	3
D_x	Pulse HPBW (x-direction)	μm	3
D_y	Pulse HPBW (y-direction)	μm	3
D_t	Pulse FWHM (time)	fs	133
V_{bias}	DC Bias Voltage	V	30
ϵ_r	Ti [183]	None	-6.61
ϵ_r	Au [184]	None	-22.5
ϵ_r	LT-GaAs [185]	None	13.7
σ	Ti [183]	S/m	$42 \cdot 10^3$
σ	Au [184]	S/m	$2.4 \cdot 10^3$
σ	LT-GaAs [185]	S/m	$1.1 \cdot 10^3$
μ_r	Magnetic Permeability (all regions)	None	1
k_{PC}	Photoconductor Extinction Coefficient of LT-GaAs [185]	None	0.0625
\hat{a}_e	\vec{E}_{inc} Polarization Unit Vector	None	\hat{a}_x

Comparison of the results from Moreno et al. to calculations utilizing the model proposed in this work is illustrated in Figure 2.7.1. The solid line is the photocurrent calculated using the proposed model at a point located at the center of the gap and surface of the photoconductor and the X marks represent the corresponding results taken from [46]. The optical excitation is temporally centered at $t_0 = 3$ ps in both cases. Both results are normalized to the peak value of $0.02 \text{ A}/\mu\text{m}^2$ reported in [46]. The results from this work have a peak value of $0.0126 \text{ A}/\mu\text{m}^2$

occurring at 3.09 ps and a full-width at half-maximum (FWHM) of 0.42 ps. In comparison, the reference results of Moreno et al. have a peak value of $0.02 \text{ A}/\mu\text{m}^2$ occurring at 3.12 ps and a FWHM of 0.63 ps.

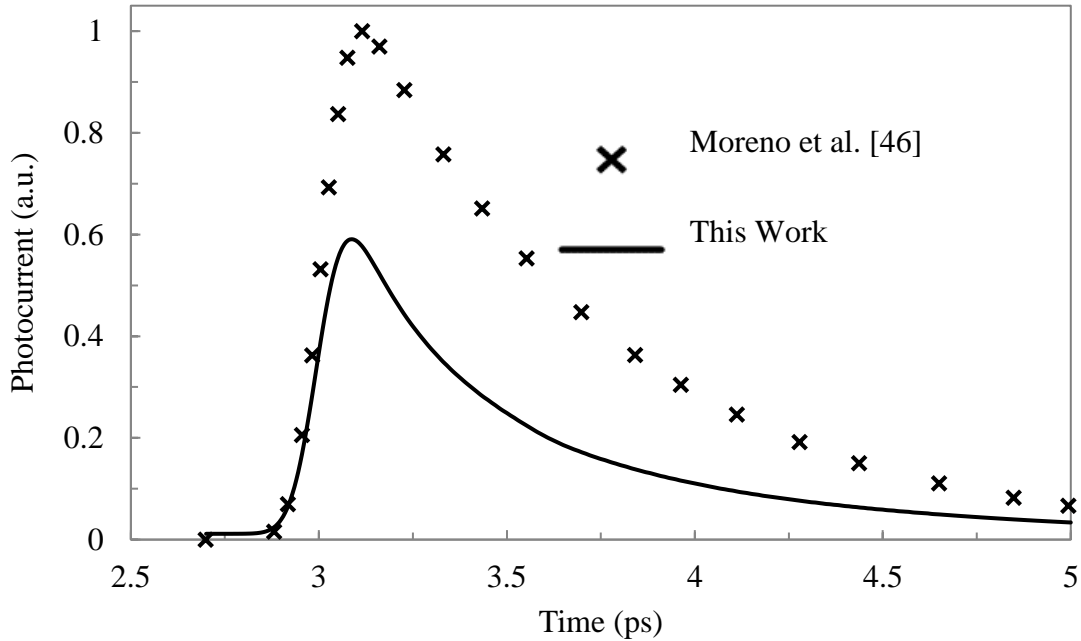


Figure 2.7.1: Comparison of the calculated photocurrent at the center of the gap. Solid trace represents the results found using this model, X marks are points traced from Figure 8 in Moreno et al. [46].

The general trend observed in both models agrees, but the peak amplitude of the current model is almost 58% of the peak in [46]. There are notable differences in the two methods. This difference is mainly due to the approximation of the wave equation solution. In this work, the wave equation is solved using the computational FEM method while in [46] the wave equation was approximated using the Beer-Lambert equation. A comparison of the power density inside the LT-GaAs at the center of the gap is shown in Figure 2.7.2, demonstrating almost a 53% difference between the two methods. The difference in the power density nearly matches the difference in the peak photocurrent in Figure 2.7.2. In addition, for the carrier mobility model, we used the Caughey-Thomas equation as function of the local electric potential [182]. The work

of Moreno et al. used the MINIMOS set of equations where the effects of lattice, impurity, and surface carrier scattering were included [186]. These differences in the carrier mobility model as well as the differences in the Beer-Lambert approximation in [46] and the full wave solution of the optical field in our model are the main contributors leading to a lower photocurrent and optical power density observed in this work as compared to [46].

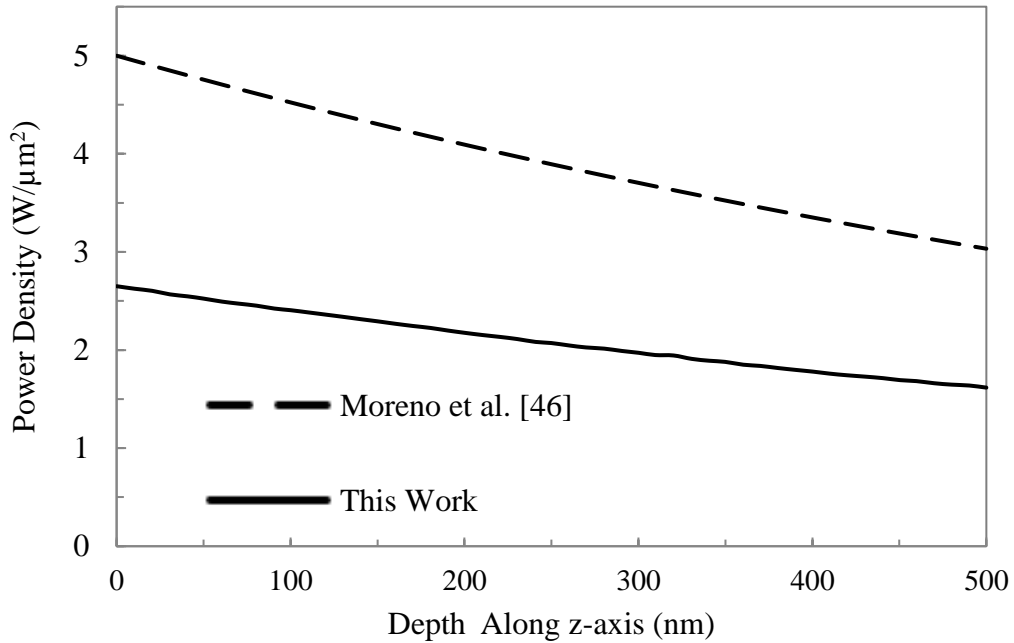


Figure 2.7.2: Optical power density at the center of the gap vs. depth inside the LT-GaAs. Dashed line represents the Beer-Lambert approximation utilized in [46], solid line represents this work, the full-wave solution of Maxwell’s equation.

Another validation is presented here with the plasmonic enhancement of photocurrent that has been experimentally observed in the work of Berry et al. [71]. The two electrode configurations are a conventional, non-plasmonic electrode and the plasmonic electrodes with a nanoscale grating geometry. The same configurations in [71] were modeled and the numerical results were compared with their experimental data. The time-averaged photocurrent collected by

the antenna was calculated for both configurations as a function of incident optical power, P_{ave} .

Table 3 summarizes the model parameters use in this study for Equations 2.4.7-2.5.4.

Table 2.7.2: Optical Properties and Constants of Equations 2.4.7-2.5.4 for Validation Study with Berry et al. [71].

Symbol	Description	Units	Value
λ	Free Space Wavelength	nm	800
P_{ave}	Average Laser Power	mW	0.5 - 25
f_p	Laser Pulse Repetition Rate	MHz	76
x_o	(conventional)	μm	0
x_o	(nanograting)	μm	-2.5
t_o	Pulse Center Location (time)	ps	0
D_x	Pulse HPBW (x-direction)	μm	5
D_y	Pulse HPBW (y-direction)	μm	5
D_t	Pulse FWHM (time)	fs	200
V_{bias}	DC Bias Voltage	V	40
ϵ_r	Ti [183]	None	-6.21
ϵ_r	Au [184]	None	-24.1
ϵ_r	LT-GaAs [185]	None	13.6
σ	Ti [183]	S/m	$42 \cdot 10^3$
σ	Au [184]	S/m	$2.5 \cdot 10^3$
σ	LT-GaAs [185]	S/m	$1.0 \cdot 10^3$
μ_r	Magnetic Permeability (all regions)	None	1
k_{PC}	Photoconductor Extinction Coefficient of LT-GaAs [185]	1/cm	0.086
\hat{a}_e	(conventional)	None	\hat{a}_x
\hat{a}_e	(nanograting)	None	\hat{a}_y

Comparison of the current model to experimentally observed reference results in [71] is illustrated in Figure 2.7.3. This shows the photocurrent enhancement, defined as the ratio of time-averaged photocurrents of the plasmonic and conventional antennas, as a function of incident optical power. The X marks represent the reference results calculated from the inset data of Figure 3b in the work of Berry et al. [71]. The open circles are the results calculated using the model here. In general, there is a good agreement in the trend and in the magnitude of the photocurrent enhancement. At $P_{ave} = 5$ mW, the difference between the reference and calculation was minimal at less than 2%. In conclusion, the current model demonstrates good agreement

with the experimental work of [71]. For optical powers greater than 5 mW, the model slightly overestimates the photocurrent enhancement. Local heating has been observed in THz-PCAs under high optical pump power, which can reduce the quantum efficiency of the device [154]. The model assumes a constant 300 K temperature and currently does not account for local heating, which could explain the difference between the current model and experimental data in [71].

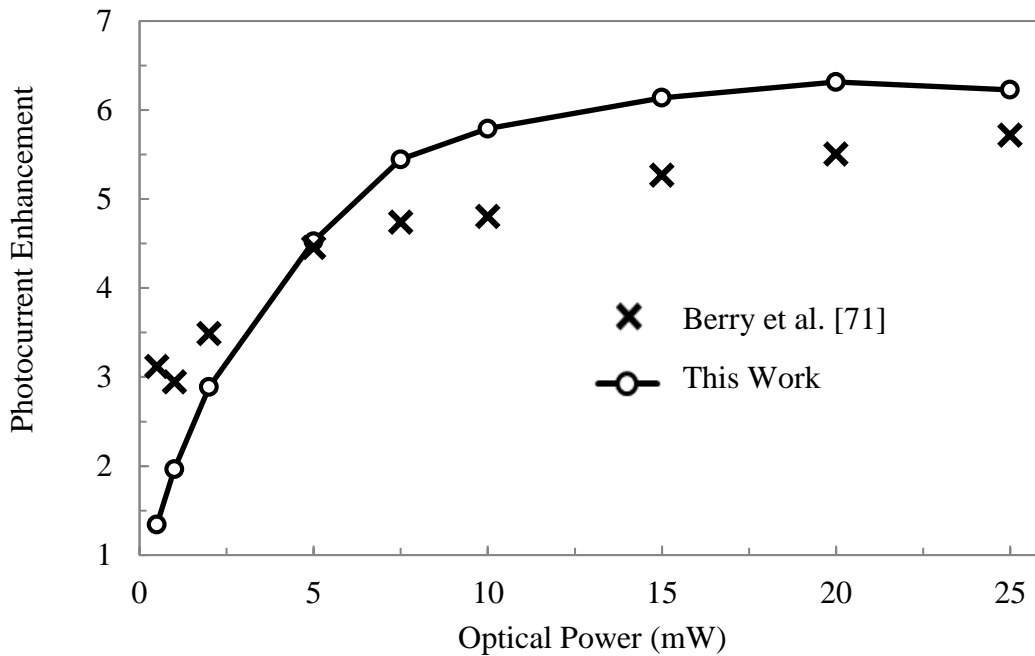


Figure 2.7.3: Comparison of the calculated photocurrent enhancement to experimentally values reported by Berry et al. [71]. Solid line with circle marks represent calculated results using this model, X marks represent the reference results calculated from the inset data of Figure 3b in the work of Berry et al. [71].

2.8. Proposed THz PCA Electrode Configurations

With the computational methodology validated against both theoretical and experimental examples from the literature, the next step is to analyze the THz-PCA electrodes with new

geometric configurations. As previously discussed, the main cause of the low optical-to-THz power conversion in PCAs comes from short (<1 ps) carrier lifetime necessary to achieve ultrafast operation. This is illustrated in Figure 2.8.1, which shows computational results of the transient electrode current in a conventional PCA with a 0.48 ps carrier lifetime (solid line) and 48 ps carrier lifetime (dashed line). Here, it is noticed that the 0.48 ps carrier lifetime allows for the transient current to more closely follow the profile of the excitation, resulting in a narrower pulse and better THz performance as compared to the 48 ps carrier lifetime case.

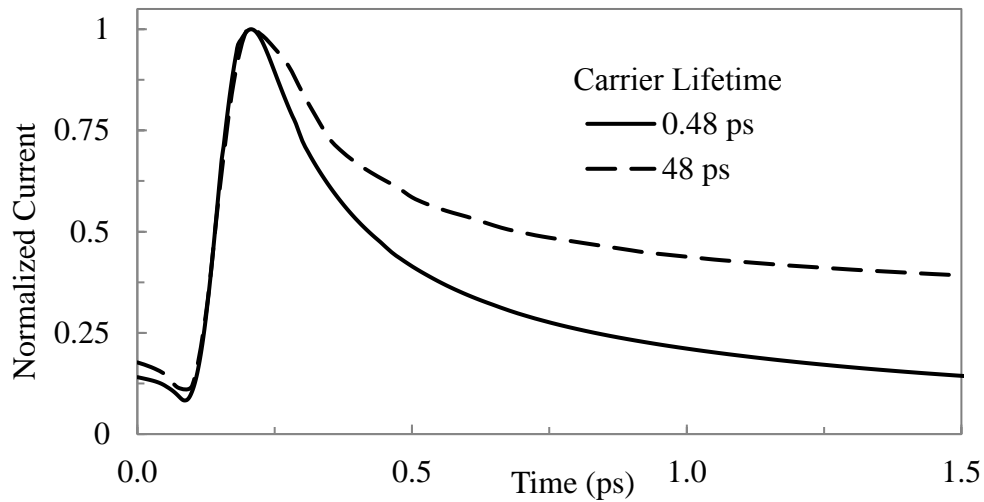


Figure 2.8.1: Anode current versus time for a conventional style THz-PCA under 100 fs pulsed optical excitation. Carrier lifetime varied from 0.48 ps (solid line) to 48 ps (dashed line).

To overcome this, we propose the new “bottom-located thin-film” (BLTF) and “plasmonic bottom-located thin-film” (P-BLTF) THz-PCA geometries, as illustrated in Figure 2.8.2(a) and Figure 2.8.2(b), respectively. In addition to these new electrode designs, top-located plasmonic nanograting electrode and conventional electrode designs are considered for comparison, shown in Figure 2.8.2(c) and Figure 2.8.2(d). The plasmonic nanograting design has been previously studied by other groups [66], [67], [71], [76], [132], [157] and for this work the geometry

proposed by Berry et al. will be utilized [71]. The THz performance can be compared between designs by considering two characteristics of the induced current pulse; the peak value of the current and the pulse FWHM. As a first approximation, higher peak current indicates higher total THz power, while a low FWHM will give a wider THz bandwidth.

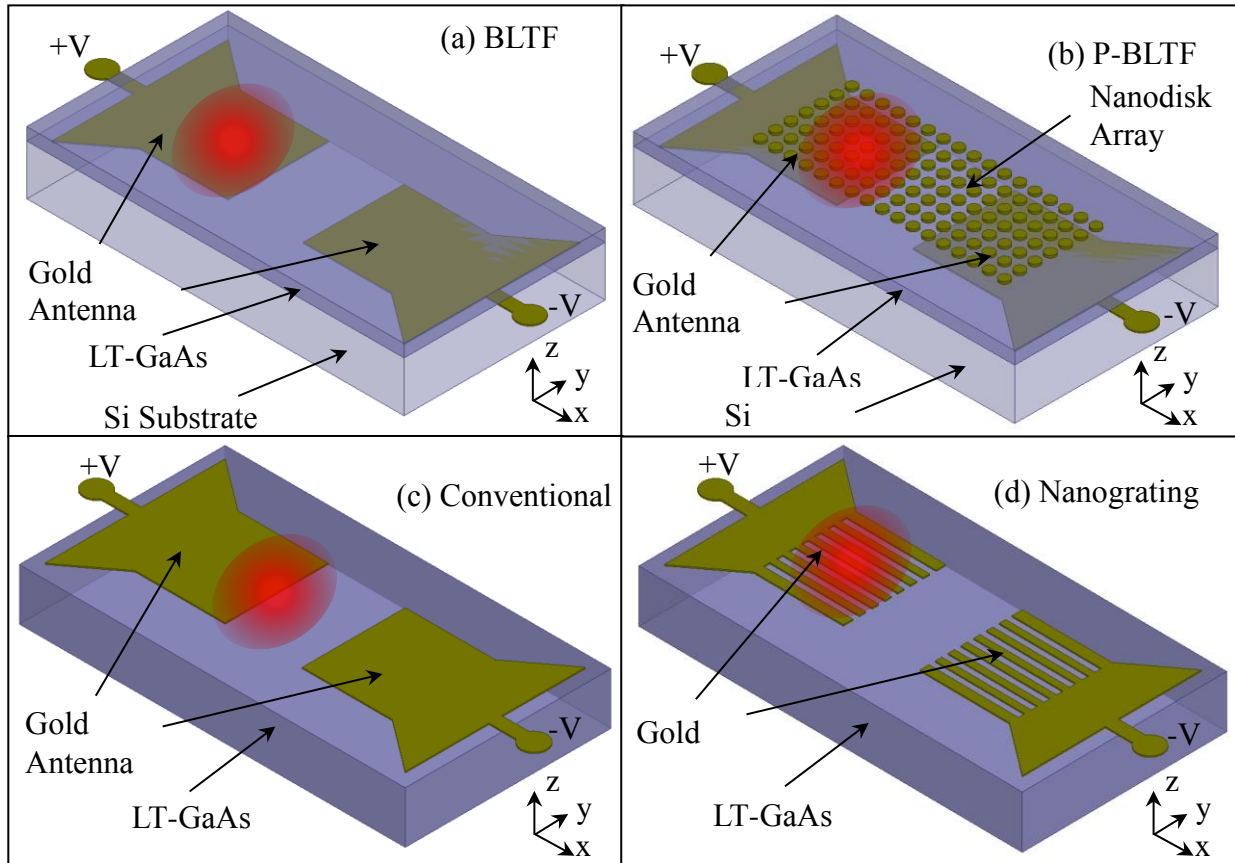


Figure 2.8.2: Illustrations of the various THz-PCA electrode designs considered in this work. (a) bottom-located-thin-film, (b) plasmonic bottom-located-thin-film, (c) plasmonic nanograting [71] top-located electrodes, and (d) conventional top-located electrodes.

For all four antenna designs, the gap between the anode and cathode was $20\ \mu\text{m}$ and a $0.5\ \mu\text{m}$ air layer was included above the photoconductor. For the conventional and nanograting, the LT-GaAs layer had a $0.5\ \mu\text{m}$ depth. For the BLTF and P-BLTF designs, a $0.5\ \mu\text{m}$ dielectric substrate layer was included under the antenna and LT-GaAs. For both these designs, the thickness of the

thin-film LT-GaAs layer was set to 120 nm. For the P-BLTF design, the nanodisk array geometry is optimized such that the average electric field strength inside the LT-GaAs layer is maximized at an 800 nm incident optical wavelength. Details of the optimization are discussed in Section 2.10. The array dimensions are set to a diameter of 200 nm, center-to-center spacing of 520 nm, and a total height of 75 nm. The nanodisks are comprised of a 5 nm Ti adhesion layer, followed by a 70 nm Au layer. The frequency dependent optical properties ϵ_r and σ are taken from Aspnes et al. for GaAs [185], Johnson and Christy for Ti [183], and Rakić et al. for Au [184]. Table 2.8.1 summarizes the values of the model parameters used in this study for Equations 2.4.7-2.5.4.

Table 2.8.1: Optical Properties and Constants of Equations 2.4.7-2.5.4 for Comparison Study of the BLTF, P-BLTF, Nanograting and Conventional PCA Designs.

Symbol	Description	Units	Value
λ	Free Space Wavelength	nm	800
P_{ave}	Average Laser Power	mW	10
f_p	Laser Pulse Repetition Rate	MHz	76
x_o	(conventional)	μm	0
x_o	(BLTF, P-BLTF and nanograting)	μm	-2.5
t_o	Pulse Center Location (time)	ps	0
D_x	Pulse HPBW (x-direction)	μm	5
D_y	Pulse HPBW (y-direction)	μm	5
D_t	Pulse FWHM (time)	fs	100
V_{bias}	DC Bias Voltage	V	40
ϵ_r	Ti [183]	None	-6.21
ϵ_r	Au [184]	None	-24.1
ϵ_r	LT-GaAs [185]	None	13.6
σ	Ti [183]	S/m	$42 \cdot 10^3$
σ	Au [184]	S/m	$2.5 \cdot 10^3$
σ	LT-GaAs [185]	S/m	$1.0 \cdot 10^3$
μ_r	Magnetic Permeability (all regions)	None	1
k_{PC}	Photoconductor Extinction Coefficient of LT-GaAs [185]	1/cm	0.086
\hat{a}_e	(conventional)	None	\hat{a}_x
\hat{a}_e	(BLTF, P-BLTF and nanograting)	None	\hat{a}_y

2.9. Numerical Convergence

The numerical accuracy of the new models is assured by testing the convergence of the model for increasing total number of mesh elements. The results of this study are illustrated in Figure 2.9.1. Here, the current at the anode was calculated versus time in the P-BLTF model for different numbers of mesh elements (inside the semiconductor region), ranging from 6k to 426k. This model was utilized since it had the smallest geometric features of the four models, therefore it was expected to be the most sensitive to the total number of mesh elements. The results show the shape of the induced current pulse increasing and reaching a converged value for mesh elements of 203.9k and above.

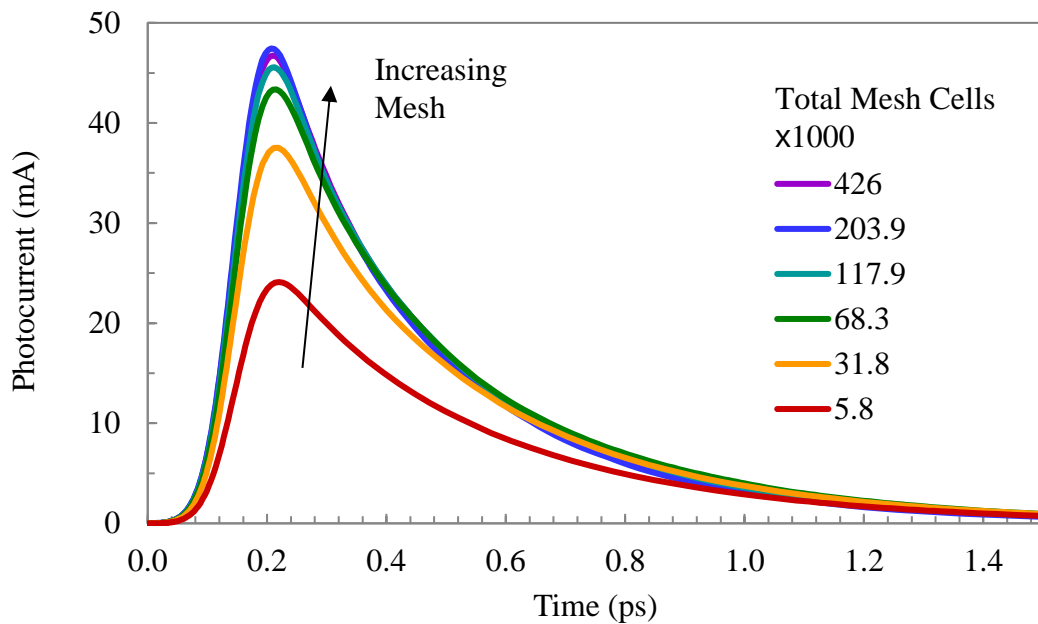


Figure 2.9.1: Anode photocurrent vs. time for the P-BLTF as a function of total number of mesh cells utilized in the FEM solution.

A more quantitative view of the model convergence is illustrated in Figure 2.9.2. Here, the FWHM and peak in the anode current pulse was determined and plotted as a function of total

number of mesh elements. At the 4th to 5th iteration the total number of mesh elements was increased from 117.9k to 203.9k and the relative errors in the FWHM and peak photocurrent were 6.5% and 4.1%, respectively. As the 6th iteration the total number of mesh elements was increased to 426.0k, the relative errors in the FWHM and peak photocurrent decreased further to 0.43% and 1.5%, respectively. In order to maintain low numerical error (<5%), the meshing parameters that yielded 426k mesh elements in the P-BLTF configuration were utilized in all other PCA configurations in this work.

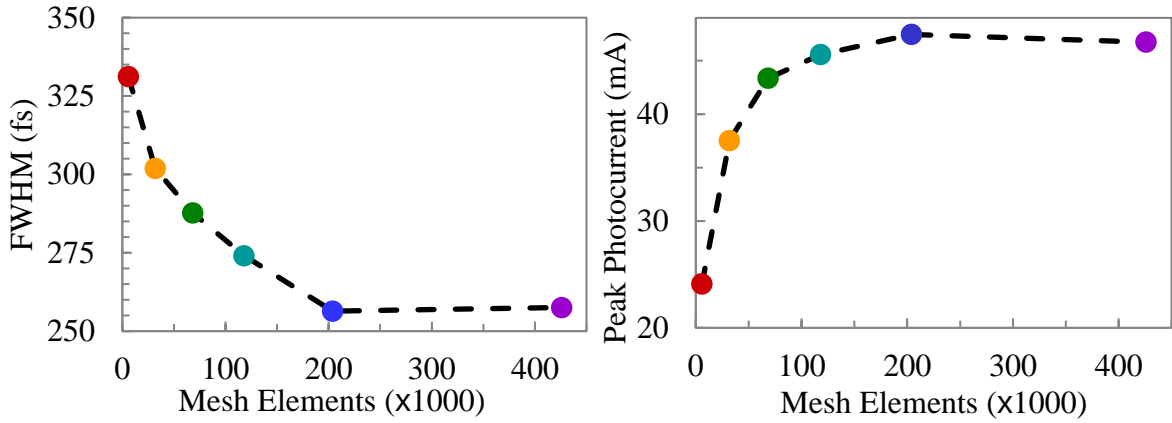


Figure 2.9.2: Anode current pulse FWHM (left) and peak (right) for the P-BLTF design as a function of total number of mesh elements.

2.10. Optimization of Nanodisk Array Geometry

The geometry of the nanodisk array utilized in the P-BLTF configuration was optimized to maximize the average electric field inside the LT-GaAs layer as defined by,

$$|\vec{E}_{ave}| = \int |\vec{E}| dV_{LT-GaAs} / dV_{LT-GaAs}. \quad (\text{Equation 2.10.1})$$

The advantage of maximizing $|\vec{E}_{ave}|$ rather than the optically induced photocurrent is that a one-quarter unit cell of the nanodisk array can be analyzed rather than the much larger computational domain described earlier in this chapter. This reduces the computational expense

of the study, allowing for more variations of the nanodisk geometry to be analyzed in a shorter time. The methodology of this analysis follows that which was described in the author's Master's Thesis [187] and previous publications [136], [137] and as such will not be discussed in detail here.

The nanodisk array consists of an infinite square array of cylinders, with radius R , height $h + 5$ nm and edge-to-edge spacing d . The cylinders are comprised of Au and Ti layers, with the Ti being located between the Au and LT-GaAs and having a fixed height of 5 nm. Prior to optimizing the dimensions of the nanostructure array, the thickness of the LT-GaAs layer was determined. It was desired to keep the thickness as close to 100 nm as possible, since this was approximately the sub-picosecond electron drift distance in the presence of the maximum allowable bias field in GaAs [71]. Using the computational domain described in Figure 2.10.1, only without including the nanodisks, the average electric field in the LT-GaAs layer was calculated as a function of LT-GaAs thickness T .

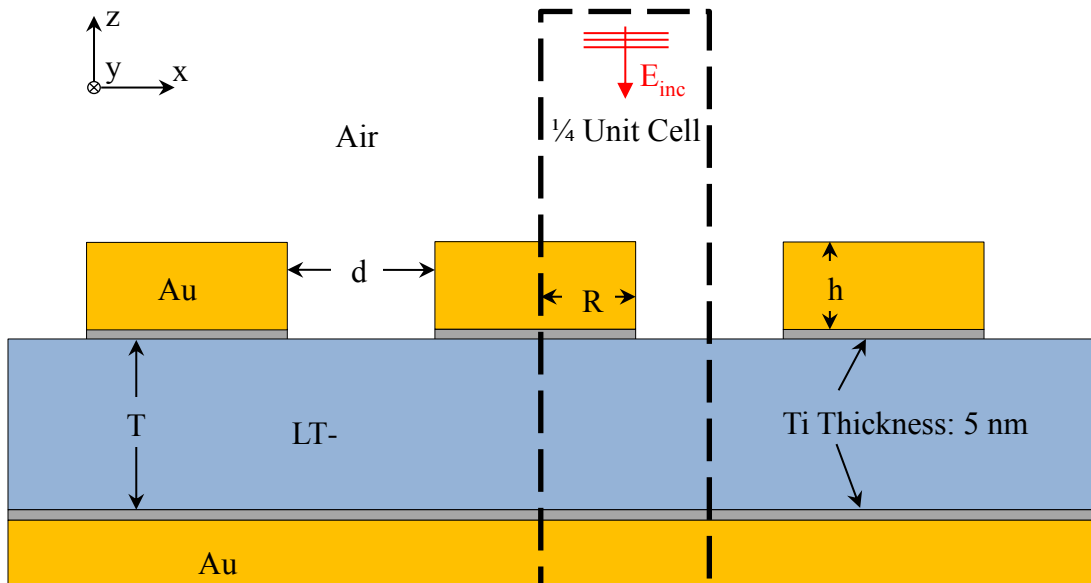


Figure 2.10.1: Cross section illustration of the computational domain utilized in the nanodisk array optimization.

The result of this study is shown in Figure 2.10.2. Peaks in the electric field were observed at $T = 40, 140,$ and 250 nm, while minimums were observed around $T = 90, 200,$ and 300 nm. As the incident optical pulse interacts with the LT-GaAs, multiple internal Fresnel reflections occur, leading to net constructive or destructive interference. Thicknesses corresponding to destructive interference were observed at the average electric field minimum values, while constructive interference was observed at the average electric field maximum values. Choosing the thickness to be used in the device design was a matter of balancing the average electric field with the decreased mechanical stability of the thin film layer at lower T values and the increased recombination losses at higher T values. Ultimately, $T = 120$ nm was chosen since it provided an average electric field value approximately equal to the peak at 40 nm, yet not being so thick as to fall in the high recombination loss region.

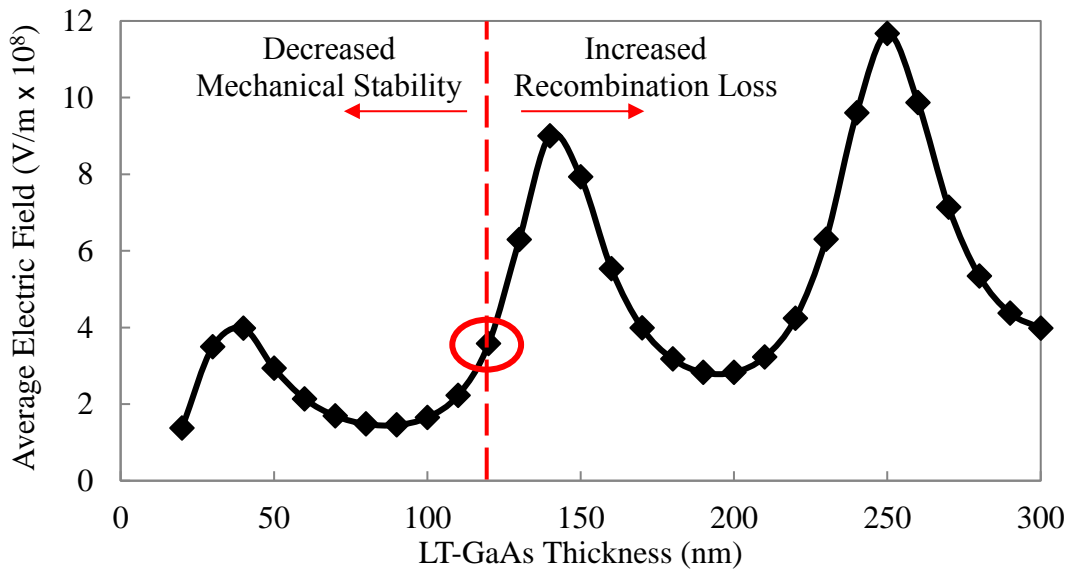


Figure 2.10.2: Average electric field in the LT-GaAs layer without nanodisks as a function of thickness T .

As previously described by many works [134], ordered arrays of nanostructures will exhibit strong and spectrally narrow resonant behavior. This resonance can be tuned in spectral location,

peak amplitude, and geometric location within the nanostructure. This allows the local optical field to be maximized at a desired wavelength and location within the structure, such as inside the nanostructure, gaps between adjacent nanostructures, or inside the photoconductive substrate (as desired in this work). This is illustrated in Figure 2.10.3 for the nanodisk array of this work.

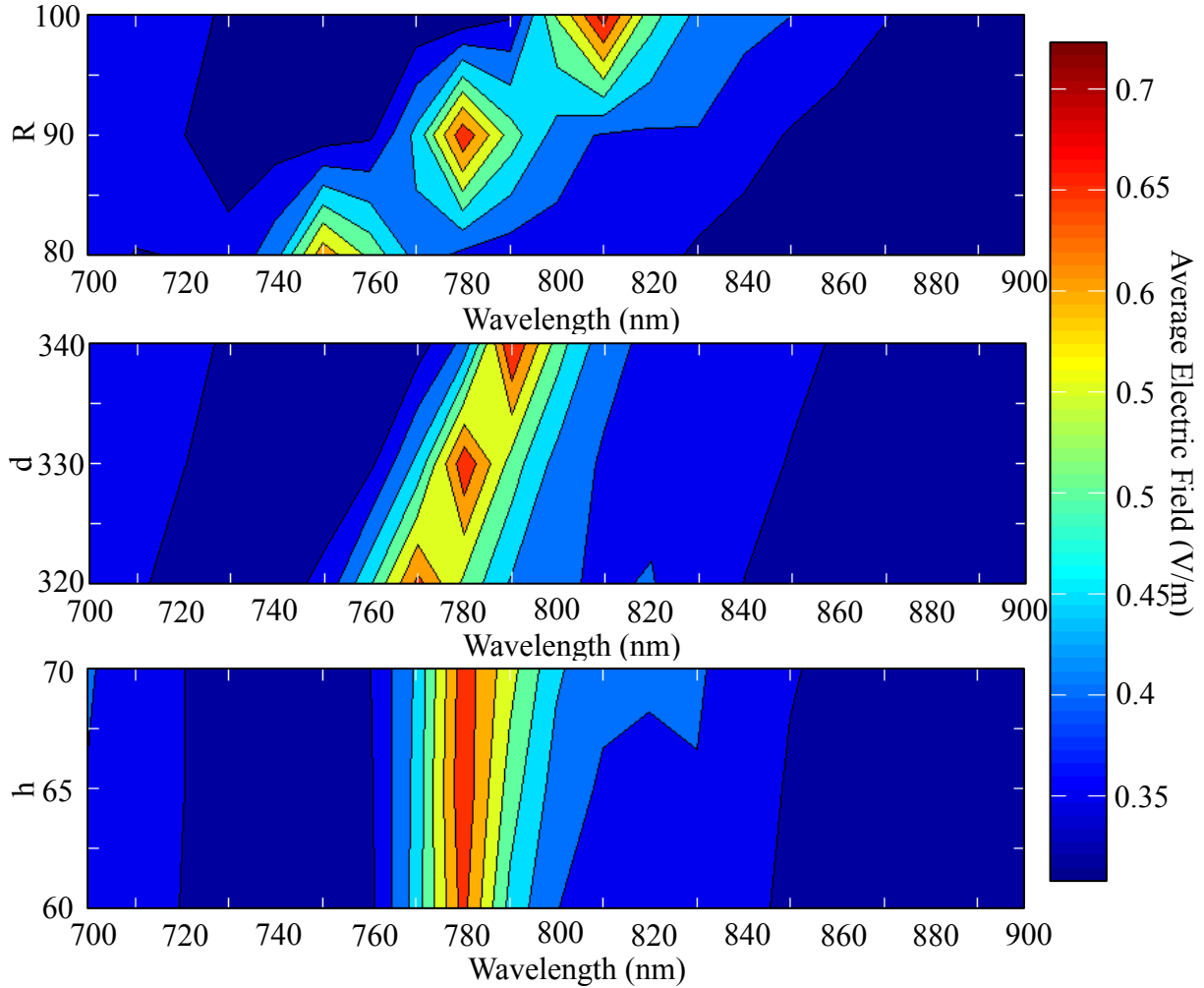


Figure 2.10.3: 2D plots of the average electric field inside the LT-GaAs layer as a function of incident wavelength and (top) radius R , (middle) edge-to-edge spacing d , and (bottom) height h of the gold nanodisks.

In each of the three plots, the horizontal axis represents the incident optical wavelength ranging from 700 nm to 900 nm, the vertical axis represents the nanodisk array geometry

parameters R (top), d (middle), and h (bottom). The color corresponds to $|\vec{E}_{ave}|$ in the LT-GaAs calculated by Equation (Equation 2.10.1) for a 1 V/m incident optical field excitation.

For the parameter ranges shown in Figure 2.10.3 the relationship between nanodisk array geometry and resonance peak spectral location, λ_{peak} was observed. Nominally optimized parameter values were $R = 90$ nm, $d = 330$ nm, and $h = 65$ nm. The nanodisk radius had the strongest influence on λ_{peak} , with a 10 nm increase in R corresponding approximately to a 30 nm increase in λ_{peak} . The nanodisk spacing had a weaker influence on λ_{peak} , with a 10 nm increase in R corresponding approximately to a 10 nm increase in λ_{peak} . Over the range of 20 nm, h had no notable influence on λ_{peak} . Over the parameter range of $80 \text{ nm} \leq R \leq 100$ nm, $320 \text{ nm} \leq d \leq 340$ nm, and $60 \text{ nm} \leq h \leq 70$ nm it was found that $|\vec{E}_{ave}|$ had a maximum value at $R = 100$ nm, $d = 320$ nm, and $h = 70$ nm.

In order to observe the effect of varying the nanodisk height, the average electric field at the spectral peak, $|\vec{E}_{ave}|_{peak}$ was calculated across a range of $20 \text{ nm} \leq h \leq 80$ nm for fixed values $R = 100$ nm and $d = 320$ nm. The results of this study are illustrated in Figure 2.10.4.

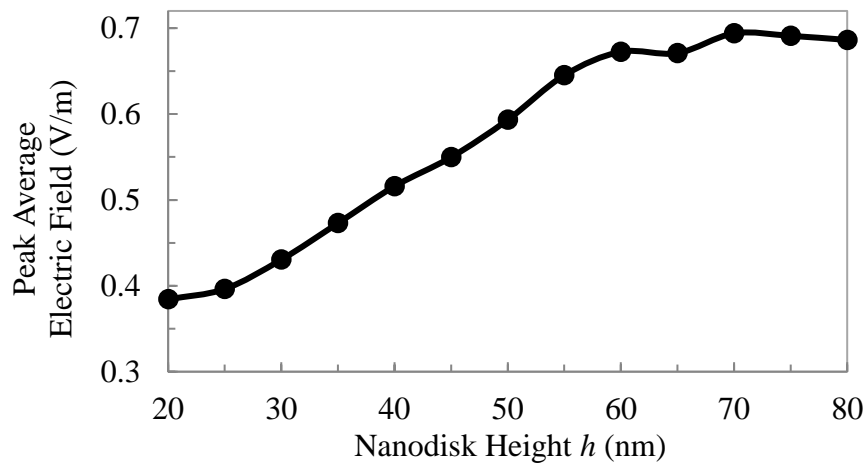


Figure 2.10.4: Average peak electric field in the LT-GaAs layer as a function of nanodisk height for constant $R = 100$ nm and $d = 320$ nm.

Here, it was observed that a steady increase in $|\vec{E}_{ave}|_{peak}$ occurs from $h = 20$ nm to around $h = 60$ nm. For higher values of h , relatively little change in $|\vec{E}_{ave}|_{peak}$ was observed. Important to note is that $|\vec{E}_{ave}|_{peak}$ was taken from the highest values of $|\vec{E}_{ave}|$ across a spectral range of 700 nm to 900 nm. As such, the variation in $|\vec{E}_{ave}|_{peak}$ does not occur from spectral shifting of the resonance peak, but truly represents the maximum strength of the plasmonic resonance regardless of excitation wavelength. This is important to note because there is relatively minor shifting in the spectral location of the resonance peak, as shown in Figure 2.10.5. Across the range $20 \text{ nm} \leq h \leq 60 \text{ nm}$ the peak shifts by a relatively small amount of 5 nm. However, in the saturation region above $h = 60$ nm the shift of the peak is greater, at 10 nm across the $60 \text{ nm} \leq h \leq 80 \text{ nm}$ range.

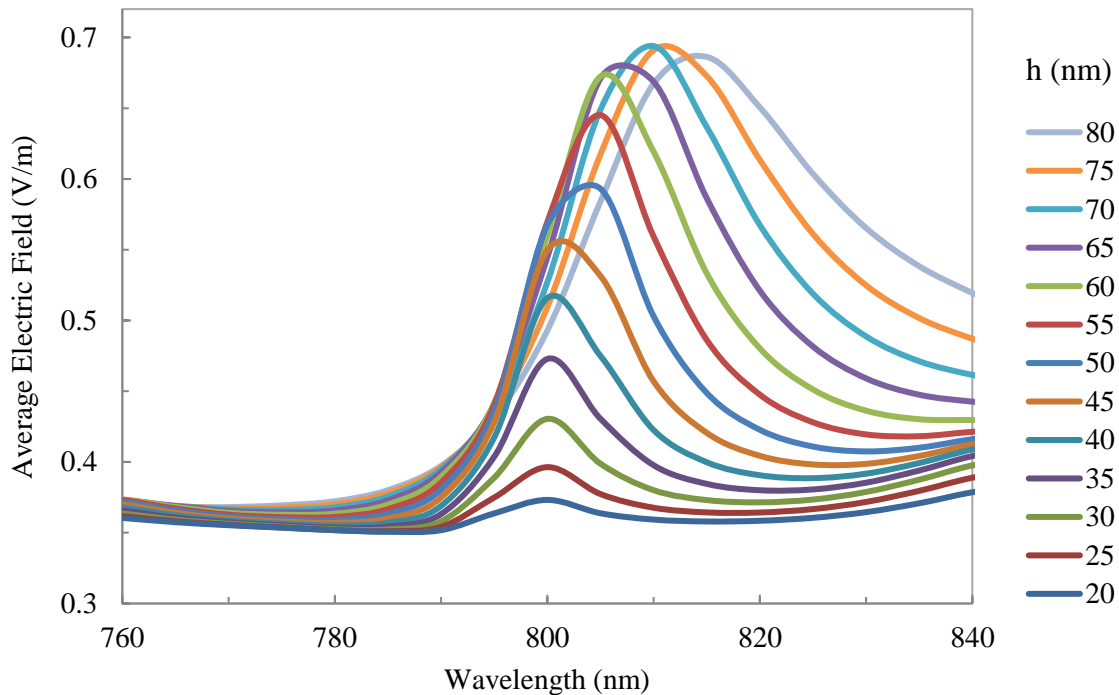


Figure 2.10.5: Average peak electric field in the LT-GaAs layer as a function of incident wavelength and nanodisk height for constant $R = 100$ nm and $d = 320$ nm.

The plasmonic behavior of the nanodisks is illustrated and compared to the non-plasmonic BLTF structure in Figure 2.10.6. In Figure 2.10.6(a), the average electric field inside the LT-GaAs layer is calculated as a function of excitation wavelength for two proposed designs. For the P-BLTF design, a peak in the average electric field was observed at 800 nm. This is characteristic of a plasmonic resonance in the nanostructures efficiently coupling the incident electromagnetic energy into the LT-GaAs thin-film layer. At the 800 nm excitation wavelength, the average electric field is 0.70 and 0.35 V/m for the P-BLTF and BLTF designs, respectively. This indicates a two times increase in the average optical field due to the addition of the plasmonic nanostructures. In addition to the LT-GaAs absorption spectra, the power reflectance spectra for the BLTF and P-BLTF designs are shown in Figure 2.10.6(b).

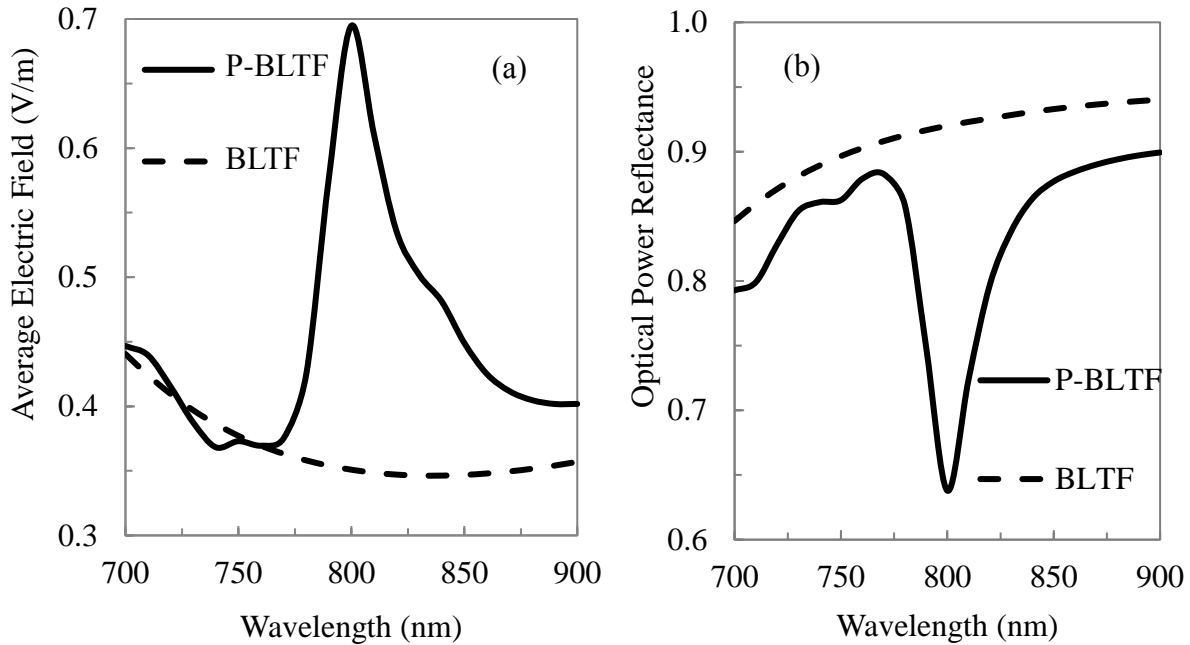


Figure 2.10.6: (a) Average electric field absorbed in the LT-GaAs layer under 1 V/m optical excitation as a function of excitation wavelength and (b) optical power reflectance spectrum. Dashed and solid lines represent the BLTF and P-BLTF designs, respectively.

Power reflectance is found by calculating the average z component of the Poynting vector at the top x-y boundary of the computational domain and dividing it by the average incident optical

power. For the P-BLTF, the peak in the plasmonic resonance is observed at 800 nm. Interesting to note is that in the reflection spectrum for the P-BLTF and BLTF, the minimum reflectance observed at 800 nm is 64% and 92%, respectively.

2.11. Optical Field Comparison of THz PCA Electrode Configurations

With the nanodisk geometry of the P-BLTF design optimized, the full electro-optical model was solved for each of the four electrode configurations shown in Figure 2.8.2. In Figure 2.11.1 2D cross sections of the optical field distribution calculated by solving Maxwell's wave equation (Equation 2.4.8) are illustrated for each of the electrode configurations. In each cross section, the horizontal axis spans a spatial region of around 1040 nm centered at the optical pulse center location. The electric fields plotted in Figure 2.11.1 correspond to the magnitude of the peak optical field, occurring at the pulse center time t_0 . Each of the four plots share a common scale for the electric field, ranging from 0 to 2×10^8 V/m. In the conventional design, it was seen that there was negligible optical field in the LT-GaAs region underneath the anode at $x < 0$. The majority of the incident optical pulse in this region was lost due to reflection from the antenna metallization. In the LT-GaAs region in the gap at $x > 0$, the optical field was significant at around $0.2\text{--}0.4 \times 10^8$ V/m. However, due to the short carrier lifetime, the majority of the carriers generated by this field would recombine before they reached the anode. The nanograting design had optical field values in the LT-GaAs region comparable to the values observed in the $x > 0$ region of the conventional design. Unlike the conventional design, the nanograting had a greater effective anode edge, allowing for significantly more of the optical beam area to be incident in a region of the LT-GaAs that is around 100 nm or less from the antenna anode.

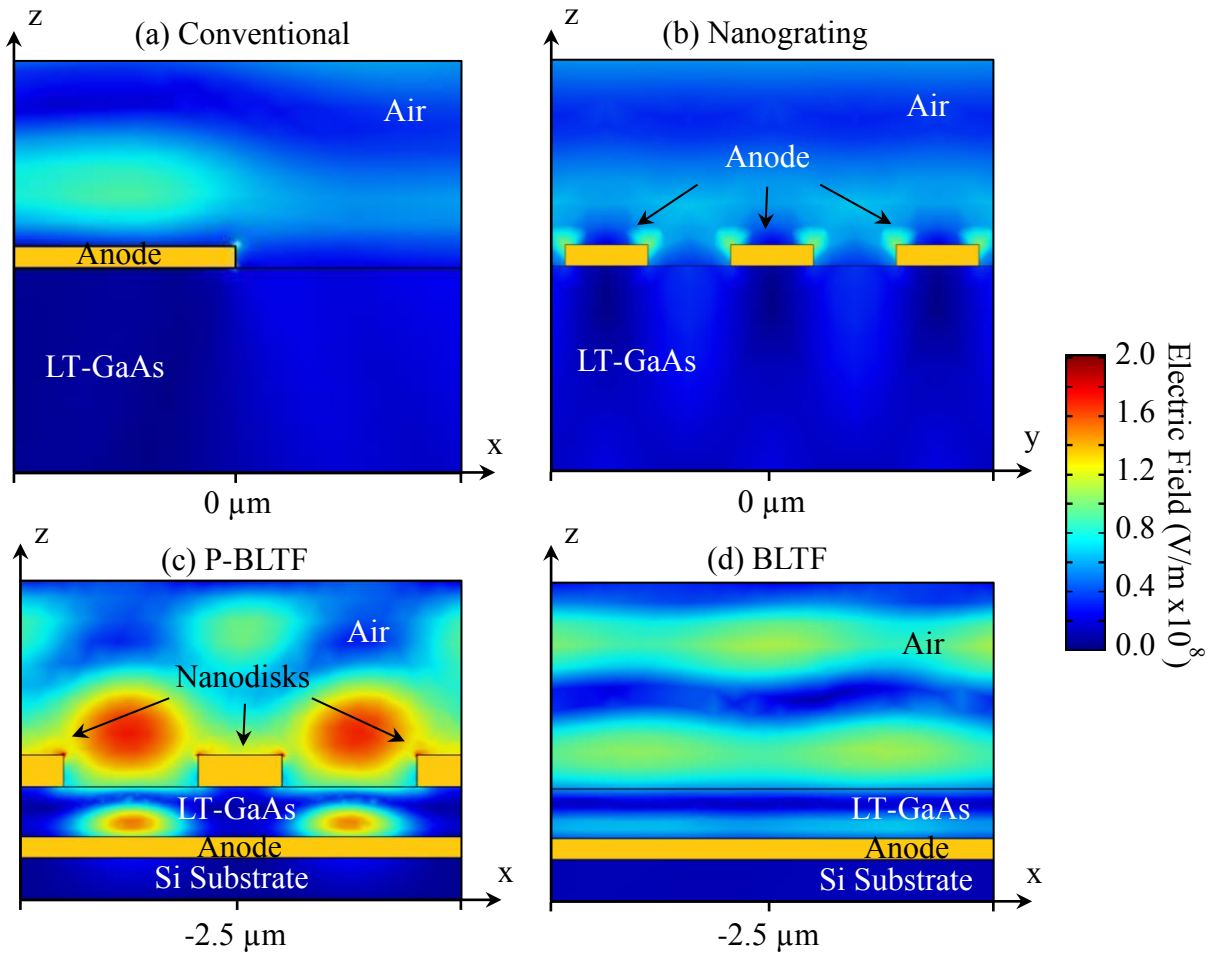


Figure 2.11.1: Electric field distribution at partial 2D cross sections of the computational domain for the conventional (a), nanograting (b), P-BLTF (c) and BLTF (d) designs. Cross sections centered at the focus of the optical excitation.

The P-BLTF and BLTF designs are shown in Figure 2.11.1(c) and Figure 2.11.1(d), respectively. Compared to the conventional and nanograting designs, both the P-BLTF and BLTF designs had higher optical field values in the LT-GaAs layer at around 1.6×10^8 V/m and 0.8×10^8 V/m, respectively. In the BLTF design, the optical field in the LT-GaAs was uniform along the x-axis and sinusoidal along the y-axis. On the y-axis, it was observed that the optical field was strongest near the LT-GaAs/electrode interface, weakest at the middle of the LT-GaAs and beginning to increase again at the air/LT-GaAs interface. This was due to Fresnel

interference in the LT-GaAs, which produces a standing wave pattern with minimum and maximum field values. The optical field distribution in the LT-GaAs layer of the P-BLTF device was more complex. Here, the field was strongest at regions centered in the LT-GaAs and in between adjacent nanodisks. With the electric field polarization in the x-direction, the incident optical field will polarize the nanodisks along the x-direction as well. Therefore, for two adjacent nanodisks the edges facing the gap would have opposing charge, inducing the strong electric field that was observed in the gap.

2.12. Comparison of Optically Induced Photocurrent in the THz PCA Configurations

The time dependent photocurrent of each of the four anode geometries is calculated under similar conditions to study each design's ability to convert the incident optical pulse to collectable photocurrent. The results are shown in

Figure 2.12.1, which covers a range greater than four orders of magnitude.

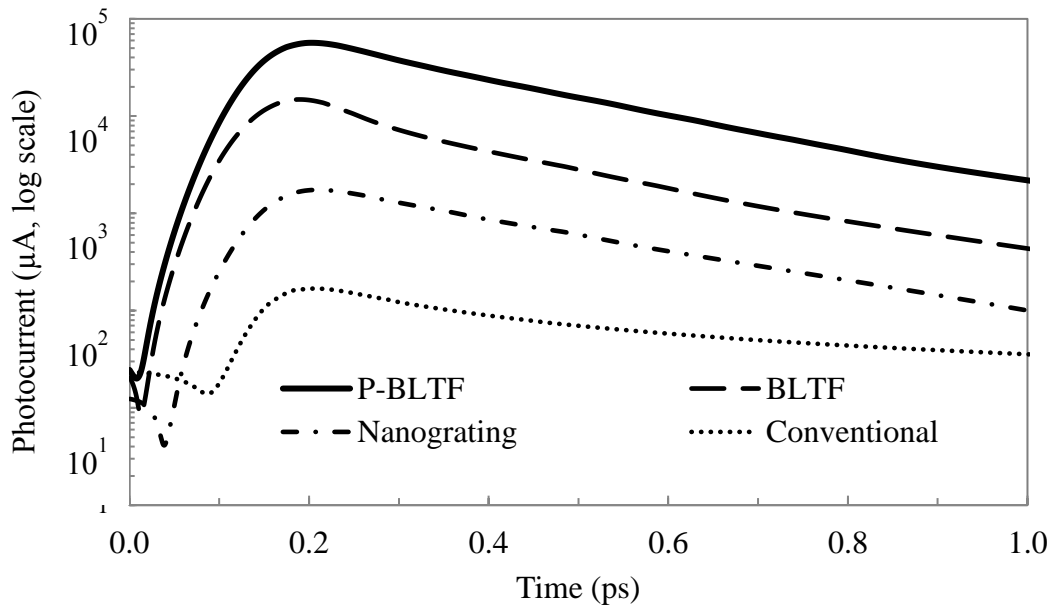


Figure 2.12.1: Anode photocurrent response versus time for each of the four THz-PCA electrode designs.

The conventional anode design has the lowest overall photocurrent response, followed by the nanograting, BLTF, and finally P-BLTF design which has the strongest response. Peak photocurrent of each design is 0.17, 1.7, 14.8 and 56.8 mA for the conventional, nanograting, BLTF, and P-BLTF designs, respectively. In addition to peak photocurrent, the FWHM of the current pulse is another performance factor to consider since smaller FWHM translates to increased power at higher THz frequencies. The FWHM is found from the data in

Figure 2.12.1 by measuring the time span between the half-maximum values for each curve and is 170, 221, 258 and 280 fs for the BLTF, P-BLTF, conventional, and nanograting designs, respectively.

Numerical methods currently exist that allow the output power of a THz-PCA to be calculated, once the optically induced photocurrent is known [44], [46], [181], [188]–[190]. However, in [71] it has been reported that regardless of electrode design and incident optical power, the output THz power is linearly proportional to the photocurrent. The results in

Figure 2.12.1 show that the peak photocurrent enhancement for the P-BLTF as compared to conventional design is approximately 300x. Therefore, the expected output THz power of the P-BLTF could be 300 times larger than the output power of a conventional emitter. Since conventional emitters generally have optical-to-THz conversion efficiencies on the order of 10^{-5} – 10^{-4} , the P-BLTF design would provide output power of $\sim 30 - 300 \mu\text{W}$ versus the conventional emitter that would provide $\sim 0.1 - 1 \mu\text{W}$.

The final study considered in this work examines the effect of increasing the Schottky-Read-Hall carrier recombination time. Physically, this would represent utilizing higher temperature grown GaAs photoconductive layer, since the growth temperature is the main factor dictating carrier recombination time [49]. The carrier lifetime $\tau_n = \tau_p$ is varied across values of 0.48, 4.8,

and 48 ps and the anode photocurrent is calculated for each of the four designs, similar to the results shown in

Figure 2.12.1. The peak photocurrent versus carrier lifetime is shown in Figure 2.12.2. For all designs, with the exception of the conventional electrode, the peak photocurrent increases slightly with increasing carrier lifetime. Across the 0.48 to 48 ps range there is a peak photocurrent increase of 56.8 to 65.1 mA for the P-BLTF, 14.8 to 17.6 mA for the BLTF, 1.7 to 2.0 mA for the nanograting, and a decrease of 0.17 to 0.13 mA for the conventional design. In the first three designs, the full area of the optical excitation is utilized regardless of carrier recombination time. Although the majority of generated photocarriers are collected before being recombined, in the $\tau_{n,p} = 0.48$ ps case there is still a minority that recombine before being reaching the anode. Increasing $\tau_{n,p}$ minimizes this minor recombination, resulting in the slight increase in peak photocurrent that is observed.

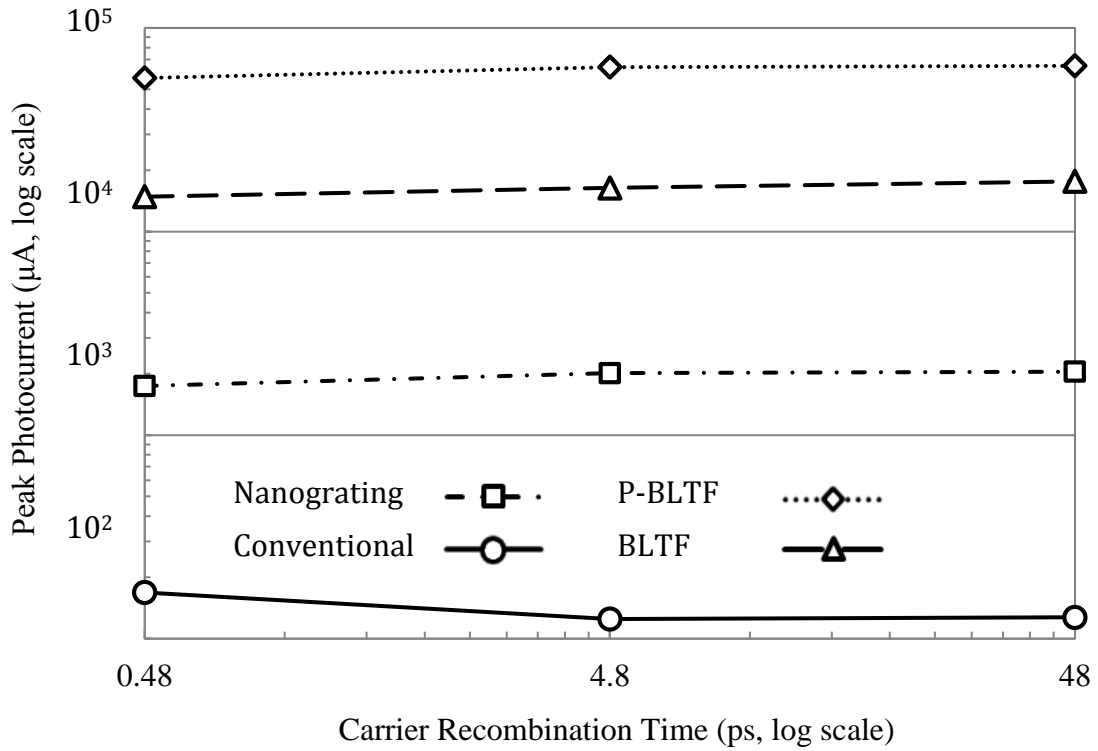


Figure 2.12.2: Peak anode photocurrent of each of the four electrode designs as a function of carrier recombination time $\tau_{n,p}$.

The FWHM versus carrier recombination time is shown in Figure 2.12.3. The FWHM is observed to increase with carrier recombination time for all designs, from 221 to 569 fs for the P-BLTF, 170 to 264 fs for the BLTF, 280 to 876 fs for the nanograting, and 258 to 552 fs for the conventional.

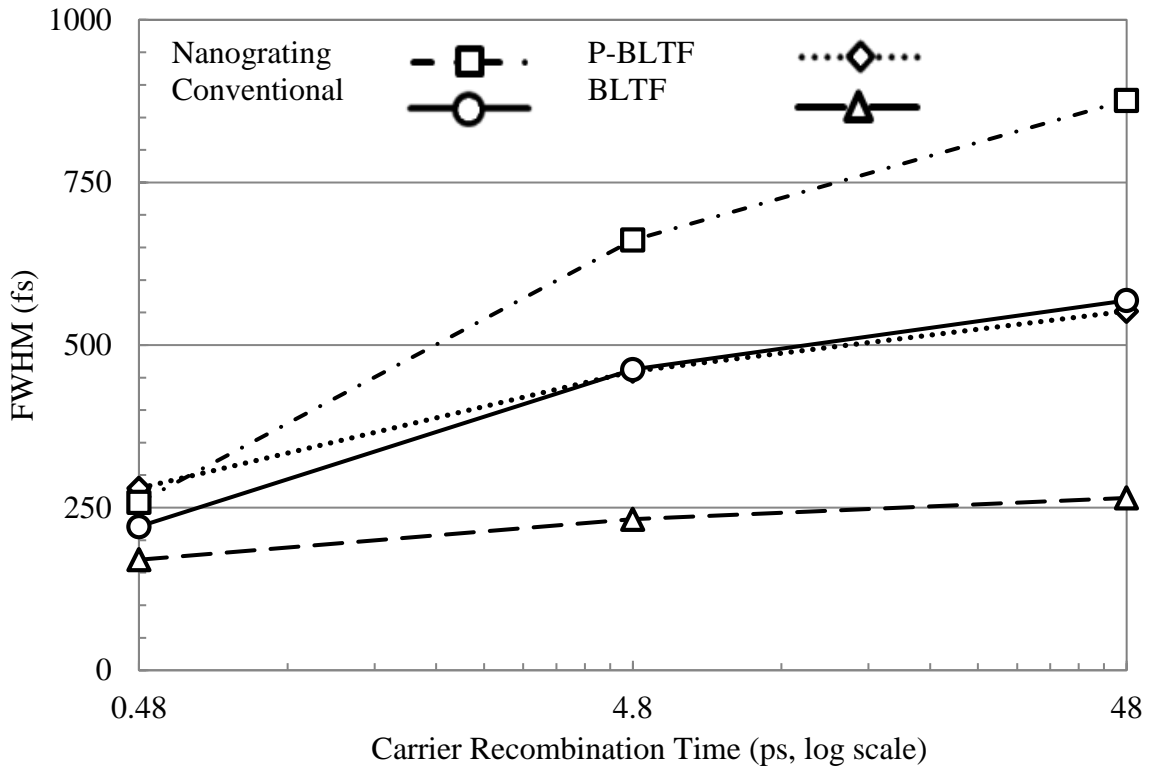


Figure 2.12.3: FWHM of each of the four electrode designs as a function of carrier recombination time $\tau_{n,p}$.

For the conventional anode, the increase in FWHM can be attributed to the increased contribution from the carriers more than 100 nm from the electrode generated at the excitation peak. These carriers take longer to reach the anode and therefore broaden the current pulse. Similarly, in the P-BLTF there is observed a significant concentration of optical energy at the air/LT-GaAs interface. This region was 120 nm from the anode, and increasing the recombination time increases the total number of carriers generated in the region that are able to reach the anode before recombining. In contrast, the increase in FWHM was lowest for the BLTF. This is due to the fact that the optical energy localized at the air/LT-GaAs interface was less as compared to the P-BLTF design. There is a greater percentage of generated photocarriers near the anode, thereby resulting in a lower FWHM at high carrier recombination times as

compared to the P-BLTF. The FWHM is highest and has the most drastic increase with recombination time for the nanograting design. Here, the LT-GaAs layer was 500 nm, over four times the thickness in the P-BLTF and BLTF designs. Although the nanograting design does induce plasmonic localization of the optical field near the anode, much of the photocarriers are generated deeper in the LT-GaAs leading to a broadening of the collected current pulse.

2.13. Discussion of the Carrier Screening Effect

Carrier screening is the nonlinear increase in optical reflection loss at the air/LT-GaAs interface due to increasing carrier density at higher optical pump power. As discussed in Section 2.6, this carrier screening effect has not been taken into account in any of the results here. However, it is possible to estimate the average effect on the optical power transmittance, and consequently the induced photocurrent [191]. First note that the optical conductivity is proportional to the total free carrier concentration, $N_{\text{tot}} = N_{\text{D}} + N_{\text{opt}}$. Here, N_{opt} is the concentration of optically generated carriers. For low incident optical power, $N_{\text{opt}} \ll N_{\text{D}}$ and our approximation of a constant optical conductivity is reasonable. As the incident optical power increases with time there eventually comes a point when $N_{\text{opt}} \geq N_{\text{D}}$ and the optical conductivity and surface reflectance will increase. In all cases, N_{tot} remained on the order of 10^{16} cm^{-3} with less than an order of magnitude variation between the device geometry.

To analyze this effect, the spatial and temporal average in N_{tot} is calculated at the air/LT-GaAs surface and is used to estimate the expected increased optical conductivity σ_{E} , power reflectance $(R_{\text{E}})^2$ and expected overestimation in optical power transmittance $(1-R^2)/(1-(R_{\text{E}})^2)-1$ in the current model. These estimated data are shown in Table 2.13.1. Here, R^2 represents the reflectance in the current model (i.e. without the carrier screening effect). Neglecting the carrier

screening effect leads to overestimation of the optical power transmittance by ~5.8% for the P-BLTF design. This is due to the large optical fields at the LT-GaAs surface generated by the plasmonic nanostructures. In addition, it is important to note that calculated carrier screening effect is higher in the nanograting design as compared to the conventional one. This is consistent with the validation of our model with experimental data in Figure 2.7.3, where the observed 20% overestimation in the calculated and experimental photocurrent enhancement is consistent with the observed difference in the carrier screening effect of the nanograting and conventional configurations. It is important to note that this simplified model underestimates the reflectance of the BLTF and P-BLTF designs, as can be seen by comparing Table 2.13.1 to the reflectance spectra of Figure 2.10.6(b). The simplified model used to calculate the values of Table 2.13.1 considers only the change in surface reflection of the air/LT-GaAs interface and does not include the effects of the nanodisk array and bottom electrode.

Table 2.13.1: Summary of the Expected Carrier Screening Effect

Model	σ (S/m)	σ_E (S/m)	R^2	R_E^2	$\frac{1 - R^2}{1 - R_E^2} - 1$
Conventional		$3.55 \cdot 10^3$		14.0%	3.2%
Nanograting	$1.10 \cdot 10^3$	$4.54 \cdot 10^3$	11.3%	15.0%	4.3%
BLTF		$2.74 \cdot 10^3$		12.1%	1.7%
P-BLTF		$5.83 \cdot 10^3$		16.2%	5.8%

2.14. Terahertz Emission from the Calculated Optically Induced Photocurrent

In order to fully examine the performance of the various devices configurations as THz emitters, a final model was developed to translate the calculated optically induced photocurrent to THz electric field emission. Using the RF Module of COMSOL[®], a transient study was performed of the computational domain illustrated in Figure 2.14.1. Illustrated in Figure

2.14.1(c) is a quarter domain representation of the geometry. The external x-z boundary at $y = 0$ was a perfect electrical conductor (PEC) symmetry boundary, the y-z boundary at $x = 0$ was a perfect magnetic conductor (PMC) symmetry boundary and all other boundaries were scattering boundaries. The electromagnetic properties of the top layer were set to air. The antenna electrode pattern was set to a 2D PEC sheet. The first substrate layer represented the adhesive layer, with variable thickness, d_{ad} , and electromagnetic properties set to the measured THz band properties of either JB Weld epoxy or cured SU-8 photoresist. The second substrate layer, d_{sub} , was set to 500 μm thickness with electromagnetic properties set to either SI-GaAs, 0.65 $\Omega\text{-cm}$ Si, 50 $\Omega\text{-cm}$ Si, or high-resistivity float zone silicon (HRFZ Si). The final substrate layer d_{lens} was set to 250 μm thick HRFZ Si to represent the transition from the device substrate to the HRFZ Si THz focusing lens. The domain width dimensions w_x and w_y were set to 500 μm . The antenna electrode was a parallel microstrip based bowtie dipole with dimensions described in Figure 2.14.1(e). The excitation current was described via a spatially uniform surface current density across a 2D sheet defined in the antenna gap region and oriented in the +y direction. The time-profile of the surface current was taken from the calculation of the current density in

Figure 2.12.1. The radiated THz field was calculated by taking the surface average of the y component of the electric field across a one-quarter circle surface of 65 μm diameter in the x-y plane centered at $x = y = 0$ and at various z depth values.

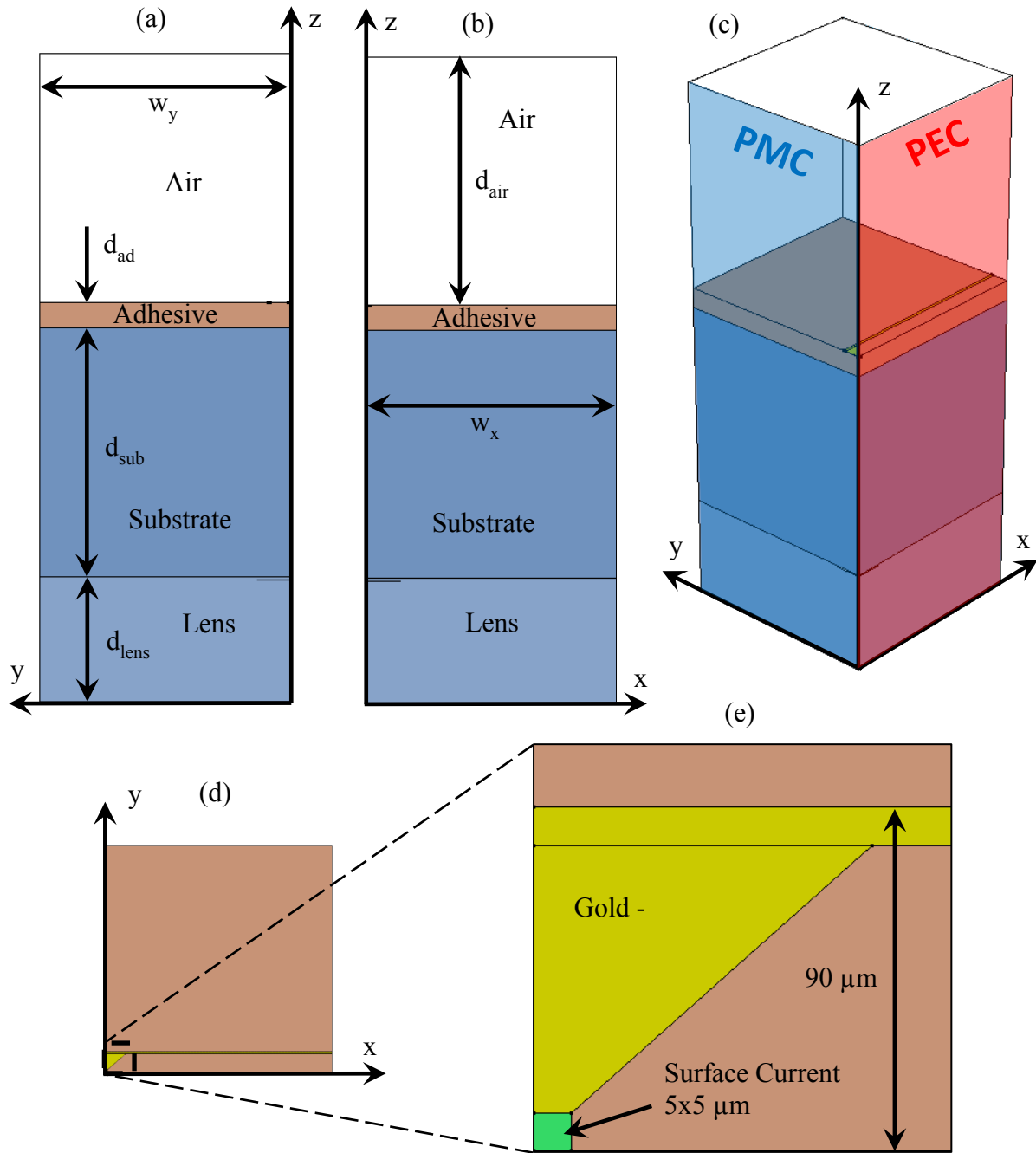


Figure 2.14.1: Illustration of the computational domain representation of the THz PCA. (a) y-z plane, (b) x-z plane, (c) isometric view, (d) full x-y plane, and (e) expanded x-y plane view of the dipole antenna.

Several comparative studies were performed to validate the model. The configuration considered in the following validation studies consisted of the domain described in Figure 2.14.1,

with no adhesive layer, no lens layer, and the electric field calculation plane placed at 250 μm below the antenna inside the substrate layer. The substrate was set to LT-GaAs. Convergence of the time step size dt was observed by decreasing dt from 0.1 ps to 0.01 ps. The results of this study are shown in Figure 2.14.2.

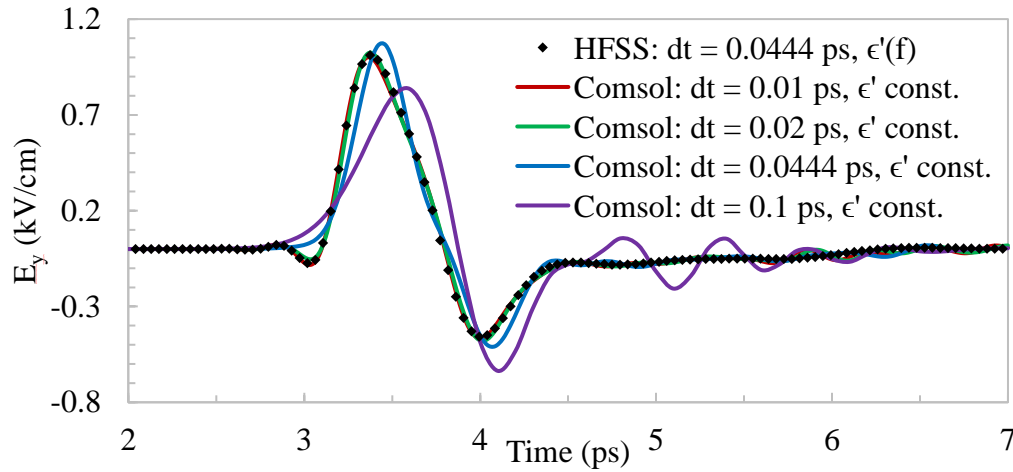


Figure 2.14.2: Time step convergence of the emitted THz electric field and comparison between COMSOL® Multiphysics and ANSYS® HFSS.

Convergence of the results was observed for values of $dt \leq 0.02$ ps. Also shown in Figure 2.14.2 is the same geometry solved using a second computation software, ANSYS® HFSS. These results are shown as the trace of black dots in Figure 2.14.2. Both the converged COMSOL results and the HFSS results overlap exactly, thus supporting that error arising from the numerical solvers and geometric configuration in both solvers were minimized. In addition, it was important to note that for HFSS the frequency dependence of the material electrical permittivity was taken into account, while for COMSOL the electrical permittivity of the LT-GaAs was fixed to its corresponding value at 1 THz. This indicated that the frequency dependence did not have a significant impact in these time-domain calculations. This model was utilized for examining the initial round of fabrication and experimental results, which will be discussed in depth in Chapter 3 of this dissertation.

Chapter 3. Fabrication Process of the Plasmonic Thin-Film THz Emitter

This chapter will discuss the various fabrication processes used in the creation of the plasmonic thin-film emitter prototypes. To better understand the next two chapters, it is important to consider the overall timeline of this work. After the computational design of the proposed THz emitter, the next step was to fabricate the devices using fabrication methods hypothesized to have a high yield of working devices. Each step was attempted to be optimized and at the end of the first fabrication round, approximately 35 expected working devices were produced. The first round of experimental measurements and testing took place during a visit to the facilities of Teraview LTD, a UK based company specializing in the manufacture and development of commercial THz systems. However, the overall results of the trip indicated that several flaws in the first round fabrication processes were preventing the devices from working as designed. Suggestions were made to modify the fabrication process in order to overcome these issues, which lead to a second round of fabrication.

The following chapter is organized into four parts. First, an overview of the general fabrication methodology is given, since this remained the same between both rounds. Second, the first fabrication round will be discussed in detail. Third, an analysis and discussion will be given over the preliminary experimental results and the conclusion that a flawed first-round fabrication approach was the cause of the non-working devices. Finally, the updated second-round fabrication process will be presented. The measurement results will be presented in Chapter 4.

3.1. Overview of the Fabrication Process

The fabrication process was divided into five main steps; molecular beam epitaxial growth of the LT-GaAs, photolithographic patterning of the antenna electrodes, flip-mounting to a resistive

Si carrier wafer, removal of the GaAs wafer substrate, and electron beam lithography (EBL) of the nanodisk array. Illustrations of the steps are shown in Figure 3.1.1.

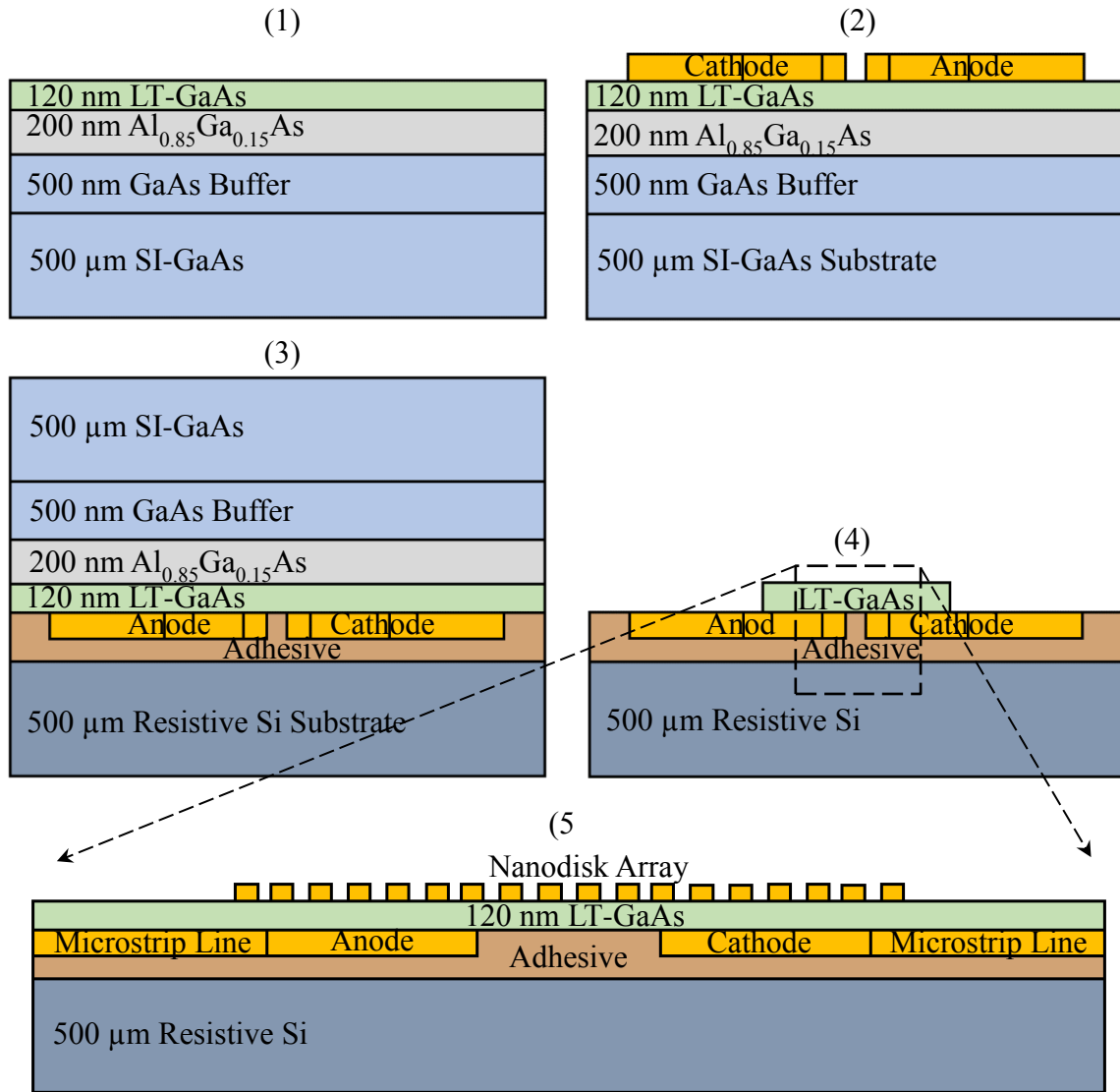


Figure 3.1.1 Illustrative overview of the plasmonic thin-film THz emitter fabrication. (a) MBE wafer growth, (b) antenna electrodes patterning, (c) flip-mounting to Si carrier, (d) substrate removal, and (e) electron beam lithography patterning of metal nanodisk array.

First, a system of epitaxial layers is grown on a SI-GaAs substrate using molecular beam epitaxy (MBE), as shown in Figure 3.1.1(a). The first layer is a 500 nm thick GaAs “buffer” layer, which provides a high quality, low defect surface for the subsequent layer growths. The

second layer is a 200 nm thick $\text{Al}_{0.85}\text{Ga}_{0.15}\text{As}$ layer, which will be used as an etch-stop during the substrate removal process. The Al fraction determines the etching selectivity. The final layer is the 120 nm thick LT-GaAs active layer. The second step, shown in Figure 3.1.1(b), is the patterning of the THz antenna metallization. Standard processes consisting of photolithographic patterning of a photoresist, electron-beam metal evaporation and photoresist-metal liftoff are used to produce the bias pads, microstrip lines and anode/cathode of the antennas. Figure 3.1.1(c) shows the third step, which is the flip-mounting of the antenna to a resistive Si carrier wafer. This flip-mounting is necessary for the substrate removal process, shown in Figure 3.1.1(d).

Removal of the substrate leaves only the thin 120 nm LT-GaAs layer and antenna metallization. As such, the resistive Si substrate is needed to provide mechanical support for the device. Removal of the substrate consists first of a mechanical polishing of the SI-GaAs to reduce its thickness from 500 μm to less than 100 μm . Next, a chemical etchant such as an ammonia hydroxide/hydrogen peroxide solution is used to chemically etch the remaining SI-GaAs material, down to the $\text{Al}_{0.85}\text{Ga}_{0.15}\text{As}$ etch stop layer. As long as the fractional Al concentration x is sufficiently high, the etching rate of the SI-GaAs can be several orders of magnitude greater than $\text{Al}_x\text{Ga}_{1-x}\text{As}$, allowing the LT-GaAs layer to be protected during the SI-GaAs removal. The $\text{Al}_x\text{Ga}_{1-x}\text{As}$ can then be removed using diluted hydrochloric acid (HCl), which will not affect the LT-GaAs layer. The final step, shown in Figure 3.1.1(e), is the electron beam lithography (EBL) patterning of the metal nanodisk array.

The process steps of the three design variations for the THz PCAs described in this dissertation are summarized in Figure 3.1.2. All three designs shared the same first and final steps, while the bottom-located thin-film (BLTF) and plasmonic bottom-located thin-film (P-BLTF) both required the substrate removal step.

THz PCA Design

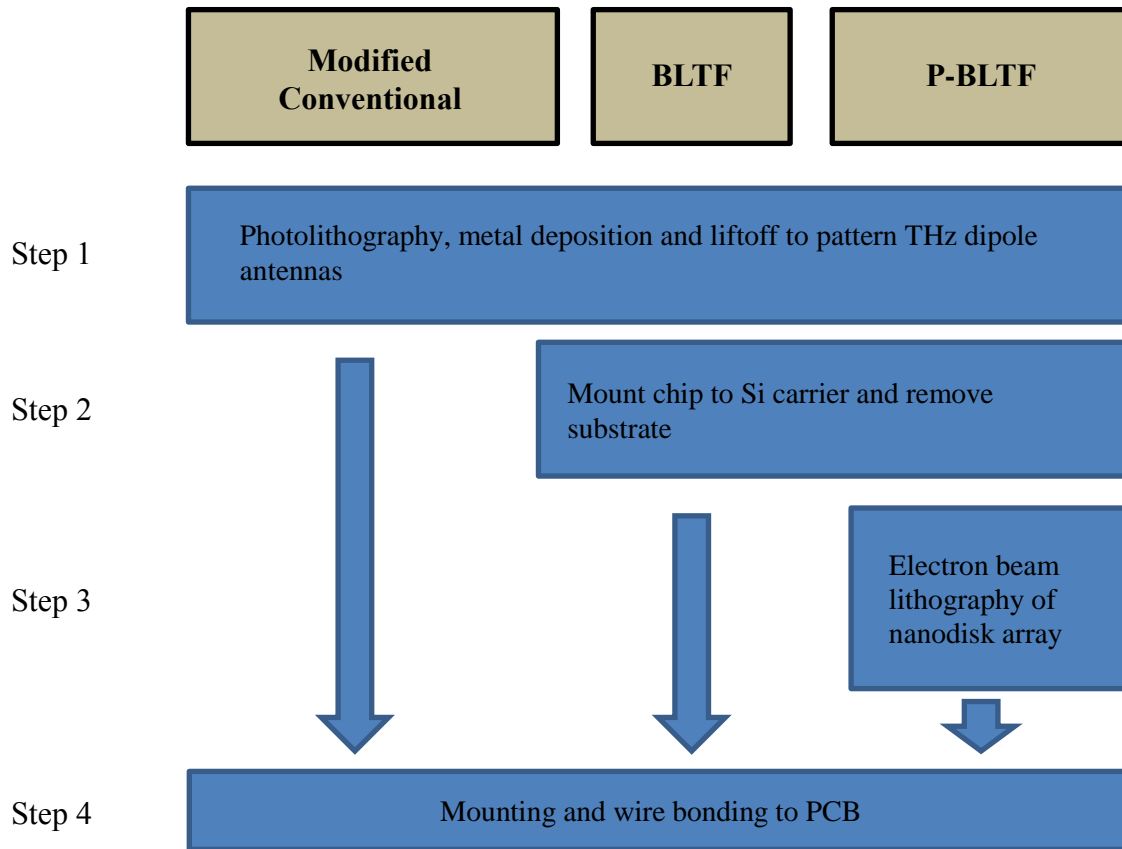


Figure 3.1.2: Summary of process steps required for each of the three THz PCA designs.

In addition, the P-BLTF required an EBL step to pattern the metal nanodisk arrays. Important to note was that the devices produced without performing the substrate removable process were really “modified conventional” devices. In standard conventional THz emitters as described in the literature, the substrate/photoconductor layer consists of a SI-GaAs substrate with around 1 μm or more LT-GaAs grown on the surface. The antenna electrodes were then patterned on the LT-GaAs layer. The modified conventional devices described in this dissertation differ from this conventional architecture, in that the LT-GaAs layer was around an order of magnitude reduced

in thickness at 120 nm. Additionally, there was a 200 nm $\text{Al}_{0.85}\text{Ga}_{0.15}\text{As}$ etch stop layer between the LT-GaAs and the substrate.

3.2. First-Round of Plasmonic Thin-Film THz Emitter Fabrication

3.2.1. MBE Wafer Growth

The wafer used in the first round of fabrication was grown at the University of Arkansas Institute for Nanoscience and Engineering MBE facility by Dr. Vasyl Kunets. The wafer was a 2" diameter SI-GaAs wafer, 515 μm thick. A 500 nm GaAs buffer layer was grown at 588 °C, followed by a 200 nm $\text{Al}_{0.85}\text{Ga}_{0.15}\text{As}$ etch stop grown at 609 °C, and lastly, the 120 nm LT-GaAs layer grown at 290 °C. For the LT-GaAs layer growth, the As_2/Ga beam equivalent pressure ratio was approximately 20. No post-growth anneal was performed for the first round of fabrication.

3.2.2. Photolithography Patterning of the Antenna Electrodes

As previously mentioned, the patterning of the antenna electrodes on the LT-GaAs layer utilized standard photolithography processes. For this, a positive photomask was designed and purchased. Four different general patterns were considered, three of which are illustrated in Figure 3.2.2.1. These are a parallel microstrip (M), simple face-to-face dipole (D), and bowtie dipole (B) with variable dipole length L and gap size G . The fourth pattern, not shown, is a copy of the bowtie dipole antenna described in [71]. Each pattern consists of five replications arranged vertically, with the text at the top indicating the antenna type (M, D or B), length (L) and gap (G) in microns.

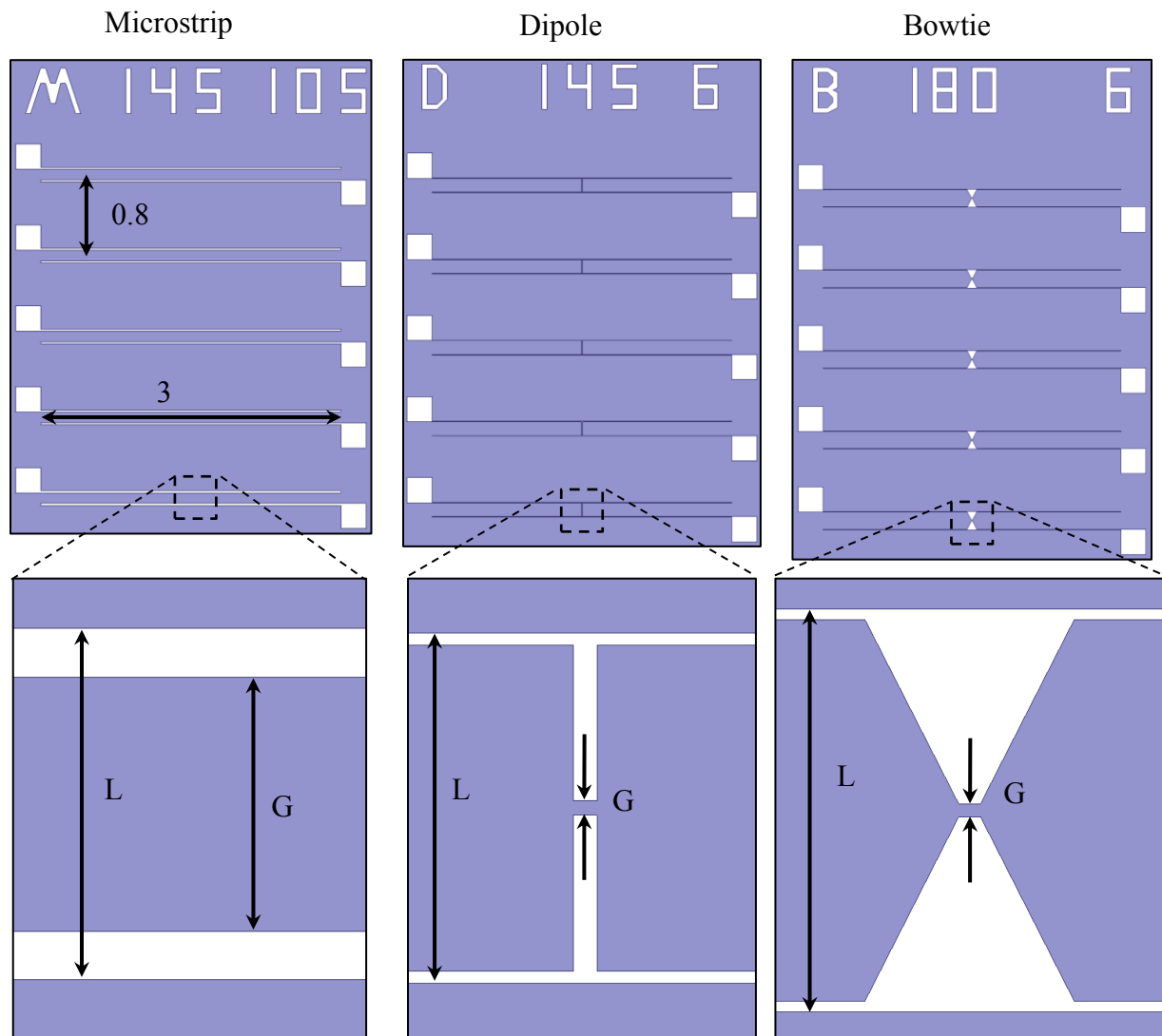


Figure 3.2.2.1: Layouts of the microstrip, dipole, and bowtie (white color represents metal).

The arrangement of the patterns on the full mask layout is shown in Figure 3.2.2.2. Each white square represents the location of the antenna patterns described by the text above. There were 20 total different antenna design variations (not shown in Figure 3.2.2.2), five microstrips, six face-to-face dipoles, six bowties, and one bowtie (UCLA) based on reference [71]. The first round photomask was designed to provide this large number of different THz antenna designs to allow for potential experiments to be conducted later to study the effect of varying the antenna geometry.

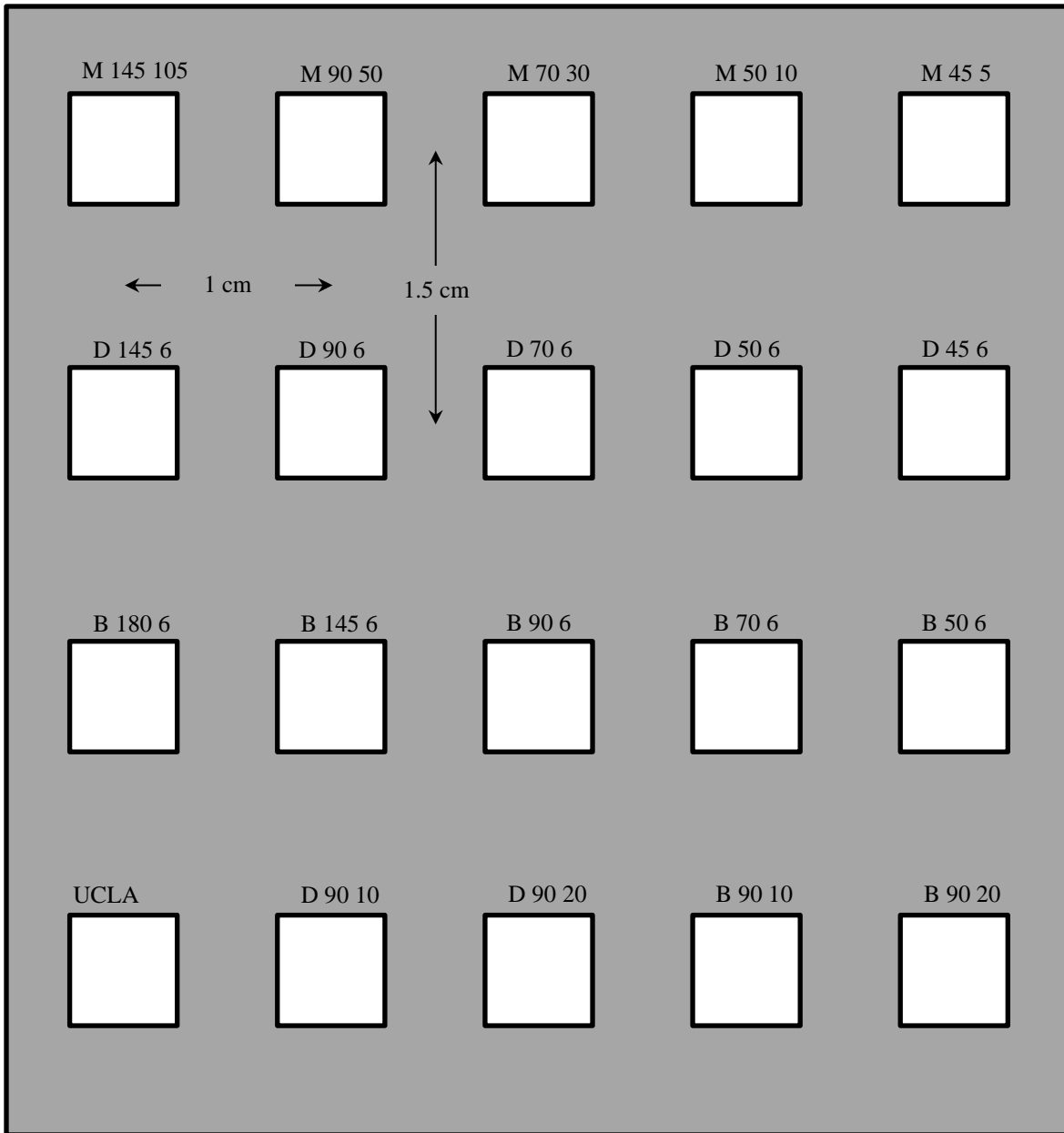


Figure 3.2.2.2: Pattern layout of the first round photomask.

A positive photolithography process was developed for the antenna electrode patterning. Some of the processes in this step were later determined to be unnecessary and removed from the second round fabrication. However, all processes will be explained from the perspective of their original reasoning. The process is illustrated in Figure 3.2.2.3.

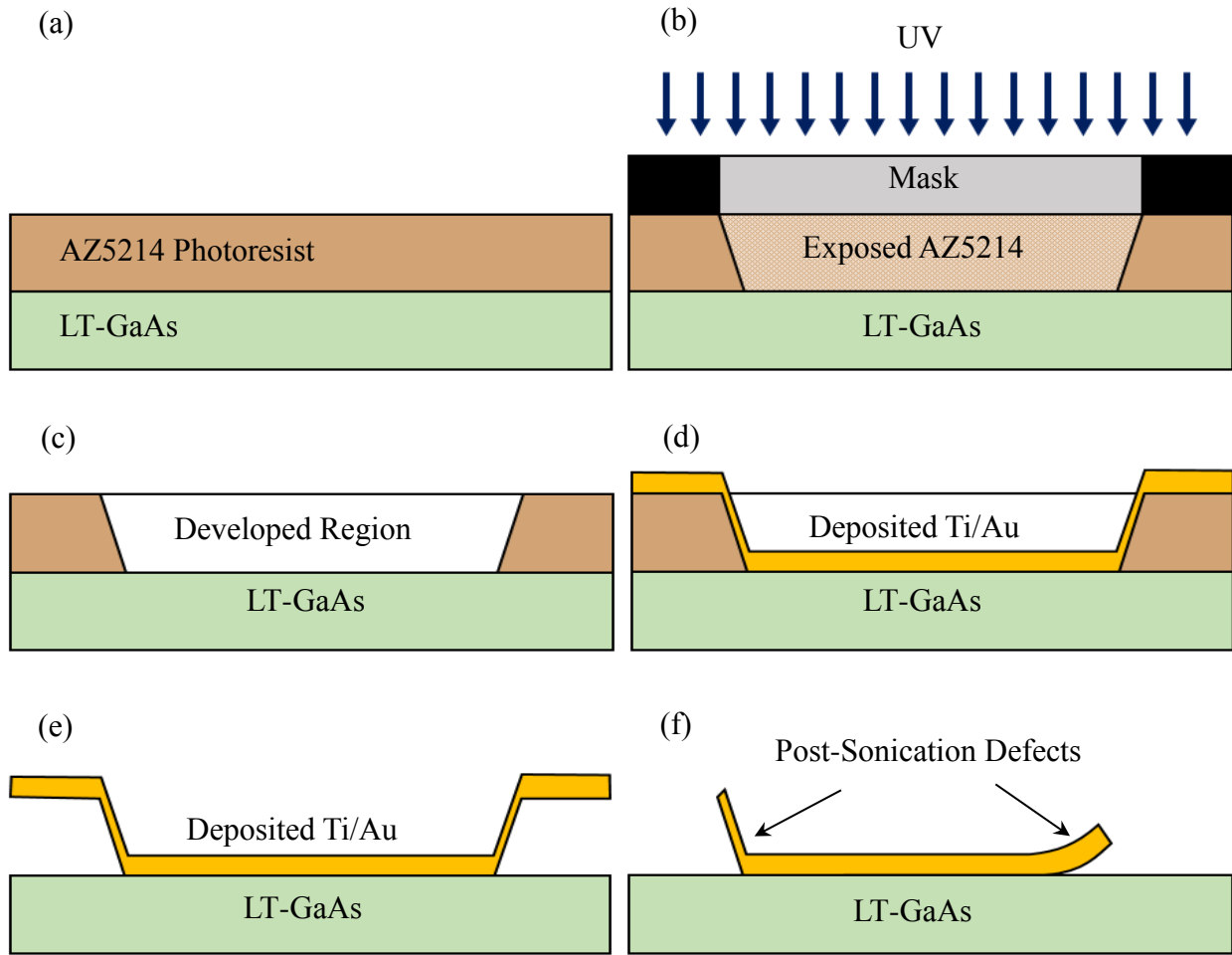


Figure 3.2.2.3: Illustrated overview of the first round photolithography process.

After cleaning the sample with acetone, IPA, and DI-H₂O and dehydrating at 100 °C for 5 min, AZ 5214 photoresist was spun on at 3000 RPM for 30 seconds, Figure 3.2.2.3(a). After a 95 °C, 90 s pre-exposure bake, the sample was placed in the mask aligner and the pattern was exposed in UV light for 18 s, Figure 3.2.2.3(b). Images of the exposed and developed photoresist for exposure times of 14, 18 and 22 s are shown in Figure 3.2.2.4. For the 14 s exposure, residual photoresist is left behind due to incomplete exposure. In the 22 s exposure, the pattern is slightly overexposed as can be seen by the broadening of the microstrip line in the upper left hand corner. As such, 18 s exposure was chosen as the optimized exposure time.

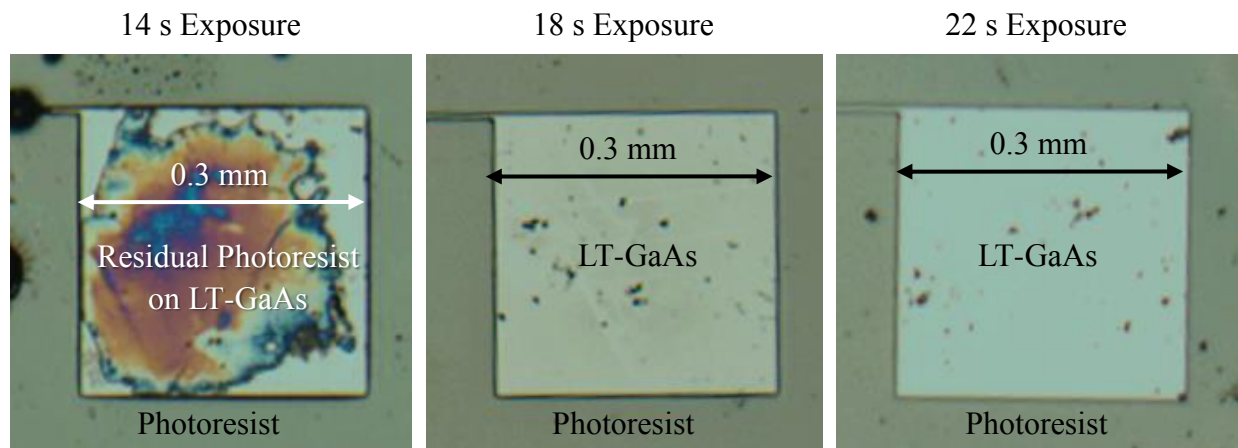


Figure 3.2.2.4: Microscope images of the developed photoresist on LT-GaAs for varying exposure time. Image is taken over the bias pad of the antenna pattern.

After exposure, the sample was developed in AZ 300MIF for 100 s, Figure 3.2.2.3(c). Here it was critical to consistently agitate the sample, either by lightly spraying the surface with developer or holding the sample with tweezers and swirling it in the developer. This ensured that the full pattern was developed in 100 s. Note in Figure 3.2.2.3(c) that due to diffraction of light at the mask edge, a positive slope was created in the photoresist sidewall. After developing, the sample was immediately rinsed in DI-H₂O for 60 s, blown dry with N₂, and baked for 95 °C for 60 s. The surface of the exposed region was then further cleaned by descumming in a plasma cleaner (PE-50 Plasma Cleaner) [192], 200 sccm O₂ rate, 30 W power for 15 s and the GaAs native oxide layer is removed by a 30 s soak in 3:10 ratio HCl:DI-H₂O. After this soak, the sample was held under a continuous rinse of DI-H₂O for 5 min and kept in DI-H₂O until ready for metal evaporation. This prevented re-oxidization of the exposed LT-GaAs surface.

The next step was to deposit the metal for the antenna electrodes via e-beam evaporation. The sample was removed from the DI-H₂O, blown dry with N₂, and baked at 100 °C for 60 s for dehydration. The sample was immediately loaded into the e-beam evaporation chamber (Edwards 306 [193]) and pumped down. This evaporator included a pre-deposition Ar plasma

cleaning process, which was utilized for all samples. After pumping to $< 4 \times 10^{-6}$ mTorr, the electrode metallization consisting of 5/400 nm Ti/Au were evaporated at rates of < 0.1 nm/s and < 0.4 nm/s, respectively (see Figure 3.2.2.3(d)). After metal evaporation, the sample is soaked in acetone to dissolve the photoresist layer (see Figure 3.2.2.3(e)). Due to the positive sidewall profile, a continuous layer of Ti/Au connected the metallization on the LT-GaAs surface with the floating metallization where the photoresist was removed. This required sonication to remove the unwanted metallization, which had the negative impact of causing defects in the antenna metallization as illustrated in Figure 3.2.2.3(f). An example of this sort of defect is shown in the microscope image of Figure 3.2.2.5.

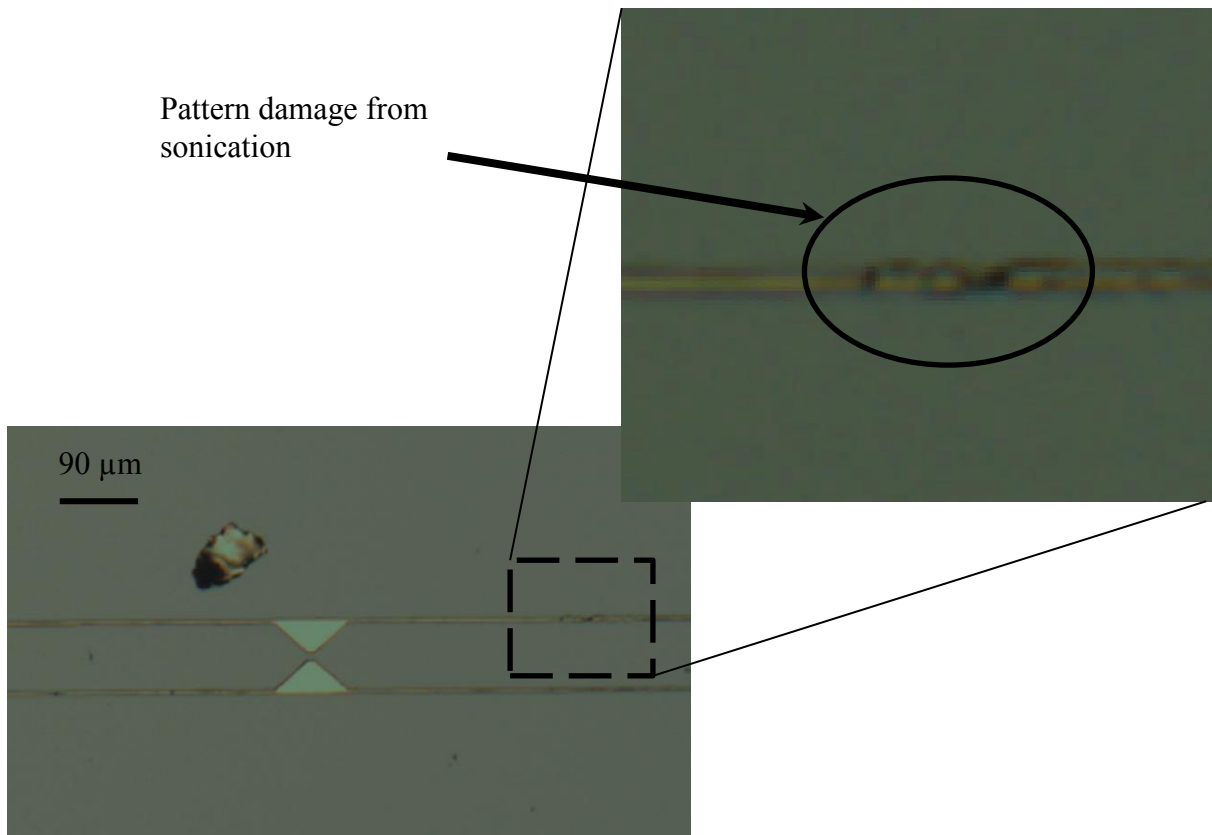


Figure 3.2.2.5: Microscope image of bowtie antenna pattern after metallization and liftoff. Zoomed images shows sonication induced damage to the microstrip line.

3.2.3. Wafer Mounting and Substrate Removal

After patterning of the antenna electrodes, the next step was to remove the wafer substrate and $\text{Al}_{0.85}\text{Ga}_{0.15}\text{As}$ layer. This was accomplished through a combination of mechanical lapping and selective chemical etching. First, the sample was flip-mounted to a 515 μm thick Si carrier substrate and bonded using an off-the-shelf epoxy as shown in Figure 3.2.3.1. Uniform pressure was applied to reduce the thickness of the epoxy layer and ensure that the sample mounted level with respect to the Si carrier substrate. Ensuring that the sample was mounted level was a critical step, for reasons that will be discussed later in this section.

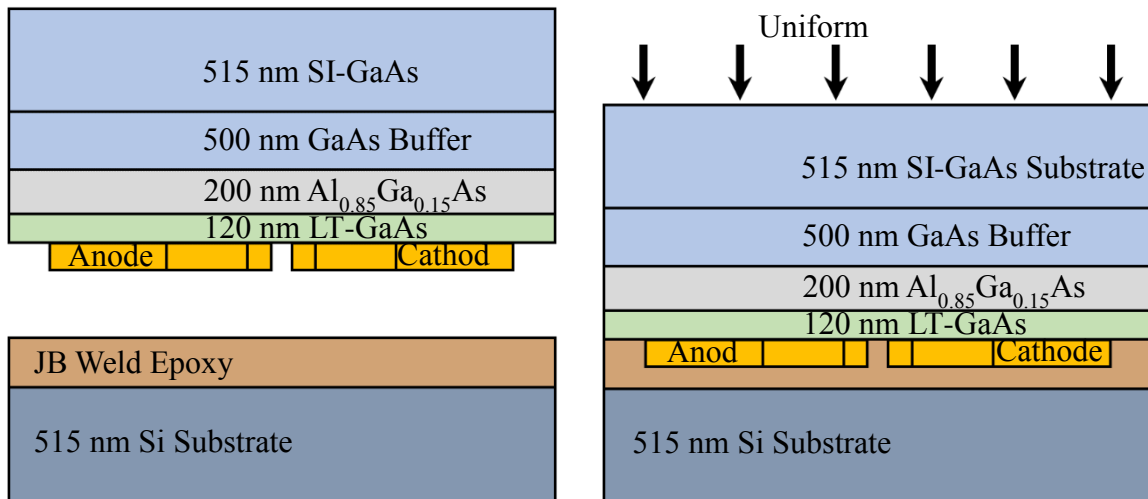


Figure 3.2.3.1: Illustrate of flip-mounting of the sample to the Si carrier substrate.

After the epoxy was allowed to cure for 24 hours, the sample was mounted to a glass carrier plate using bonding wax (heated to 80 $^{\circ}\text{C}$) and placed in the Logitech PM5 Lapping and Polishing System [194]. The system is illustrated in Figure 3.2.3.2. A mixture of 3 μm Al_2O_3 powder and DI- H_2O was dripped onto a rotating glass plate. The sample was mounted to a spring-loaded sample chuck which applied an even pressure between the sample and plate

surface. Thinning of the sample was achieved through the mechanical polishing of the sample surface by the Al_2O_3 solution. Four variables were able to be controlled in this setup; slurry concentration, slurry drop rate, plate RPM, and sample pressure. As shown in the work of Prakash, Tyagi and Gupta, slurry concentration and drop rate do not have significant influence on the sample lapping rate [195]. This was confirmed for slurry concentration and drop rates varying from 4% to 20% and 15 min^{-1} and 45 min^{-1} , respectively, where the variation in lapping rate across these variable ranges was less than 2%.

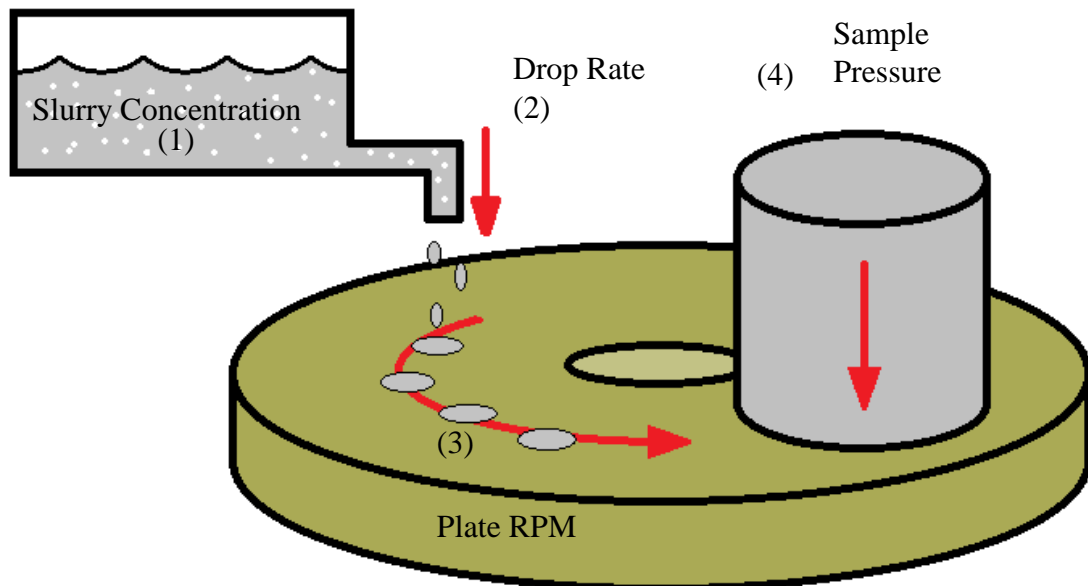


Figure 3.2.3.2: Illustration of the Logitech PM5 Lapping and Polishing System.

Due to the difficulty in controlling the sample pressure, this variable was held constant at a comparatively low value and the plate RPM was varied to achieve different lapping rates. For most cases, plate RPM of around 5 was used to achieve a lapping rate of approximately 5-10 $\mu\text{m}/\text{min}$. It is important to note that the lapping rate varied slightly from sample to sample, even if all other factors were kept constant. Therefore, it was critical that the sample thickness be

checked periodically to confirm the sample lapping rate. The samples were lapped to reduce the GaAs wafer thickness to below 100 μm .

After lapping, the sample was removed from the glass plate and residual wax on the backside of the Si carrier was removed with heat and an acetone soaked cleanroom wipe. To remove the remainder of the GaAs substrate a 3:19 selective etch solution of $\text{NH}_4\text{OH}:\text{H}_2\text{O}_2$ ($\text{NH}_4\text{OH} = 30\%$ solution in water, $\text{H}_2\text{O}_2 = 35\%$ solution in water) was used [196]. The selectivity, defined as the ratio of etch rate for two materials, is as high as 200 for GaAs to AlGaAs for this solution. To increase the etch rate the samples were initially agitated in a sonicator for approximately 20 min to remove the remaining GaAs wafer. However, it was later considered that the agitation may have been too aggressive and caused damage to the LT-GaAs thin film later. As such, later work adopted a gentle agitation by hand to prevent damage to the LT-GaAs.

Figure 3.2.3.3 shows photographs of the samples at points during the selective etching process just as the $\text{Al}_{0.85}\text{Ga}_{0.15}\text{As}$ layer begins to be exposed (left) and after the GaAs substrate is completely removed (right). On the left image it can be seen that once the $\text{Al}_{0.85}\text{Ga}_{0.15}\text{As}$ layer is exposed it is visible as a glossy, semi-transparent green-purple layer, whereas the GaAs substrate is less glossy, opaque and grey. In the image on the right, it is seen that once the GaAs substrate layer is fully removed, the antenna electrodes can be observed through the semi-transparent LT-GaAs and $\text{Al}_{0.85}\text{Ga}_{0.15}\text{As}$ layers. After the GaAs substrate was completely removed, the sample was rinsed continuously for 5 min in DI- H_2O . It is critical that any residual etchant is removed from the sample, since the next step is to remove the $\text{Al}_{0.85}\text{Ga}_{0.15}\text{As}$ etch stop layer. If residual etchant is left on the sample, it can react with and damage the LT-GaAs layer after the $\text{Al}_{0.85}\text{Ga}_{0.15}\text{As}$ is removed. Once the sample was cleaned of etchant, it was placed in a 30% HCl solution for approximately 30 s to remove the $\text{Al}_{0.85}\text{Ga}_{0.15}\text{As}$ layer. Provided there is no

residual oxidizer on the sample surface from the previous etching step, HCl will not etch the LT-GaAs.

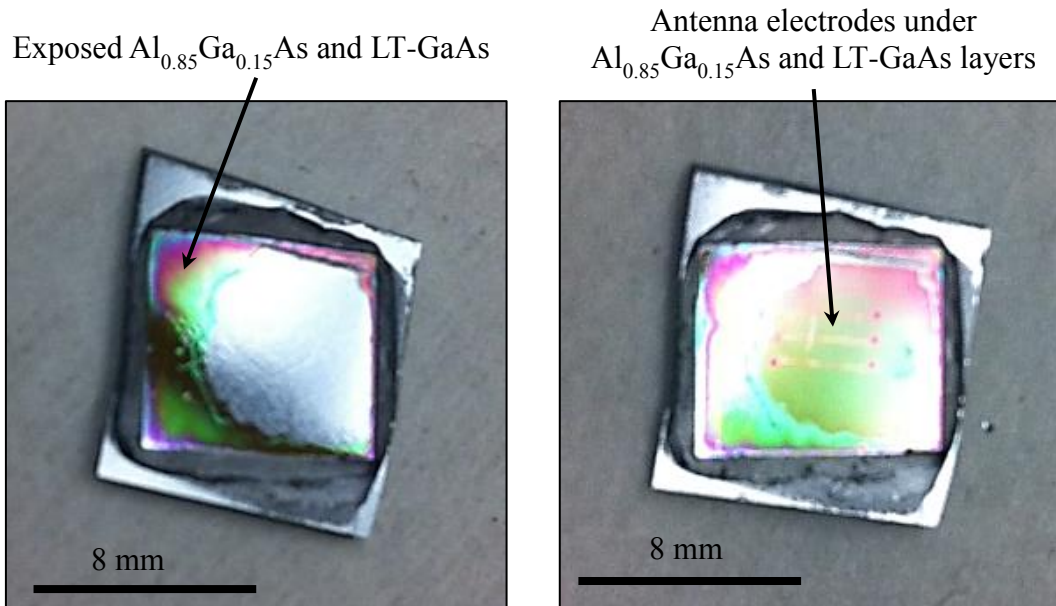


Figure 3.2.3.3: MBE GaAs wafer sample flip mounted onto an Si carrier wafer just as the $\text{Al}_{0.85}\text{Ga}_{0.15}\text{As}$ layer is starting to be exposed (left) and just after the $\text{Al}_{0.85}\text{Ga}_{0.15}\text{As}$ is fully exposed (right).

As previously discussed, level mounting of the GaAs sample to the Si carrier wafer is critical. The problem that can be caused by non-level mounting is illustrated in Figure 3.2.3.4. When the sample is mounted to the Si carrier with some tilt, the mechanical lapping process will induce a non-uniform thickness to the GaAs substrate. As the sample is etched in $\text{NH}_4\text{OH}:\text{H}_2\text{O}_2$ the GaAs on the thinner side of the sample will be removed first, as shown in Figure 3.2.3.4(c). Since the etchant selectivity is finite, the $\text{Al}_{0.85}\text{Ga}_{0.15}\text{As}$ layer effectively slows the etching, it does not completely halt it. If the tilt is great enough, the $\text{Al}_{0.85}\text{Ga}_{0.15}\text{As}$ layer on the thin side can become fully etched before the GaAs substrate on the thick side is completely removed, shown in Figure 3.2.3.4(d). If this happens, the LT-GaAs in the exposed areas will be immediately removed.

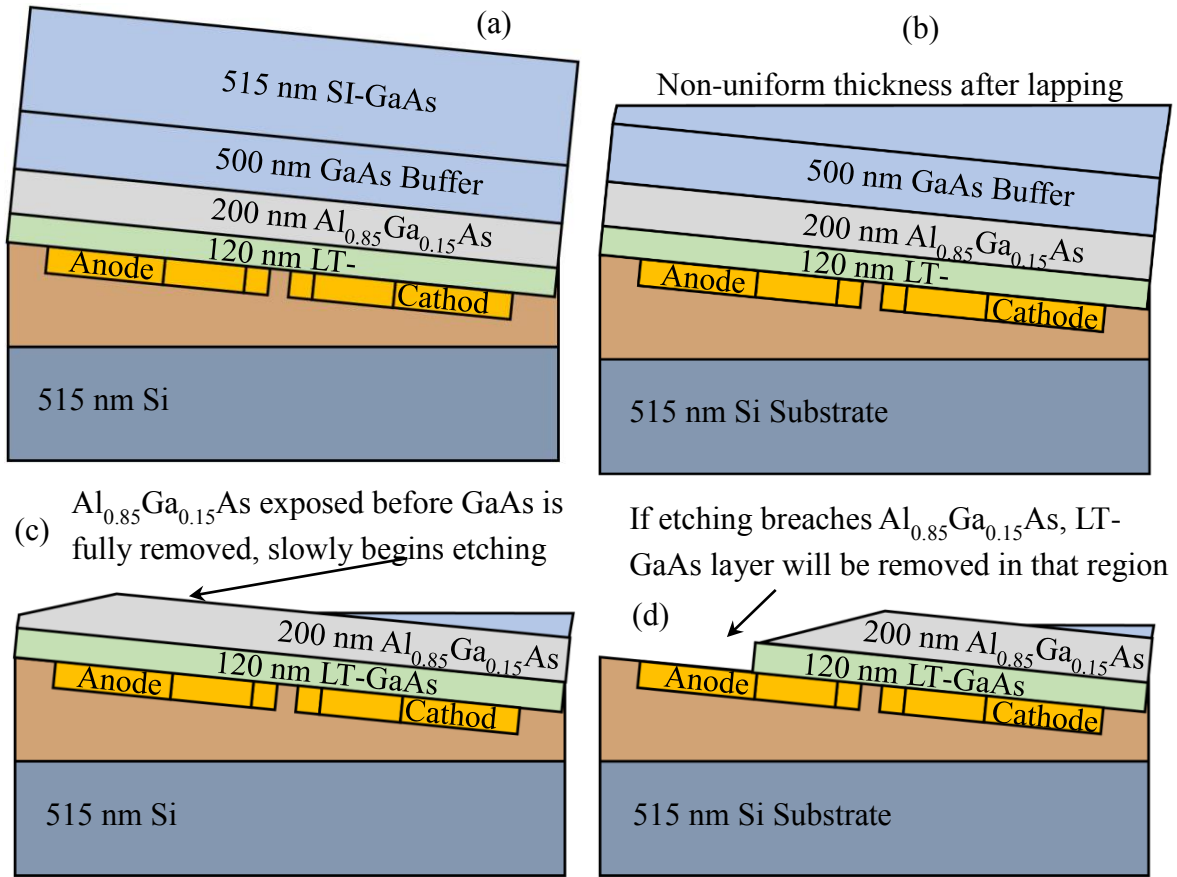


Figure 3.2.3.4: Illustration of a non-level mounted GaAs sample and the non-uniform lapping and etching it causes.

An example of this effect is shown in the photograph in Figure 3.2.3.5. Here, an MBE GaAs sample was mounted to glass without considering the necessity of level mounting. It was observed that on the left the $\text{Al}_{0.85}\text{Ga}_{0.15}\text{As}$ and LT-GaAs layers became fully etched, while on the right there is still remaining GaAs substrate. In between, there is a region where the protective $\text{Al}_{0.85}\text{Ga}_{0.15}\text{As}$ remains. Once this effect was observed, samples were mounted with $< 10 \mu\text{m}$ vertical displacement across a 5-10 mm horizontal displacement. The mounting was achieved by first mounting the Si carrier wafer to the lapping system's glass mounting plate using bonding wax. Epoxy was then placed on the Si carrier and the MBE GaAs samples were placed LT-GaAs side down onto the epoxy with moderate pressure. Using digital calipers, the

total thickness (glass plate + Si carrier + epoxy + MBE GaAs wafer) was measured at various points around the edge of the sample. Pressure was applied to the sample as needed to produce the necessary minimized vertical displacement.

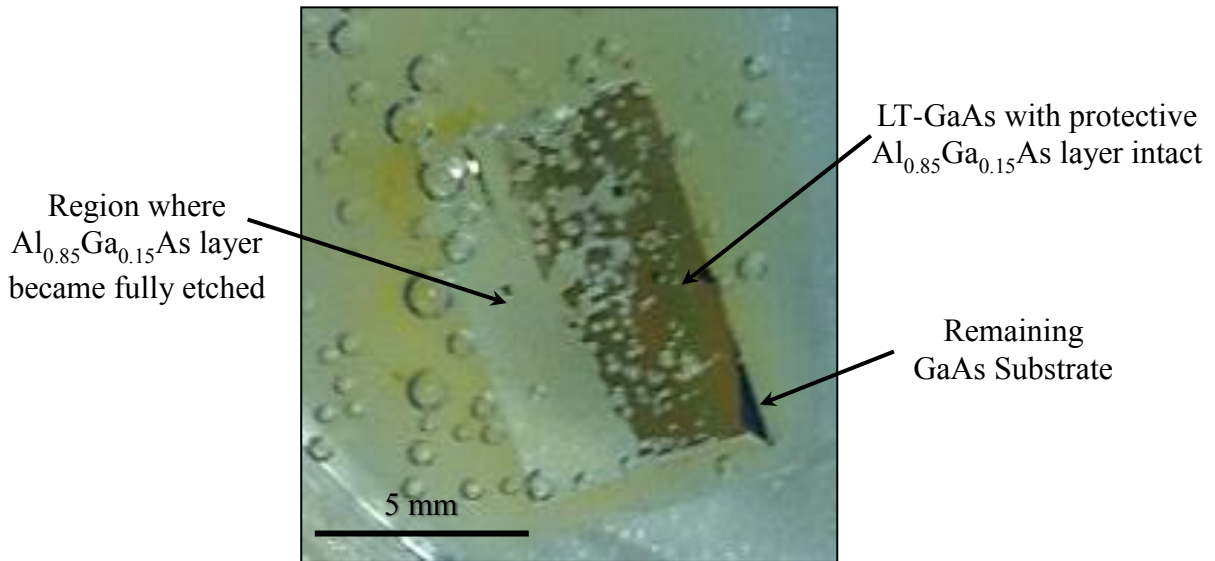


Figure 3.2.3.5: Photograph of a non-level mounted MBE GaAs sample on glass during the substrate removal etching process.

After the GaAs substrate and Al_{0.85}Ga_{0.15}As layers were removed, a final photolithography step was required to remove the LT-GaAs over the bias pad regions to allow for electrical connection to the device. AZ 5214 photoresist was spin coated on the surface at 3000 RPM for 30 s. There was a concern that excessive heating and cooling of the sample could cause damage to the LT-GaAs layer due to differences in thermal expansion coefficients of the epoxy and LT-GaAs layer. Therefore, no pre-exposure bake was performed. The sample was then placed in the mask aligner and a simple positive photomask was used to block the UV in a rectangular strip region over the dipole antennas. The sample was overexposed for 22 s since this process did not have critical dimensions to consider. After exposure, the sample was baked at 90 °C for 60 s, then developed in AZ300MIF for approximately 100 s. After development the sample was rinsed

in DI-H₂O for 2 min and blown dry with N₂. This process left a vertical strip of photoresist on the LT-GaAs surface, centered over the dipole antennas and approximately 1 mm wide. The sample was then placed in 3:19 NH₄OH:H₂O₂ solution for < 30 s to etch the LT-GaAs layer in the regions over the bias pads that were not protected by the photoresist. The sample was again rinsed in DI-H₂O for 5 min (critical to completely remove etchant), rinsed in acetone to remove the photoresist, rinsed in IPA and DI-H₂O, blown dry with N₂, and baked for 60 s at 95 °C to remove any residual water from the surface.

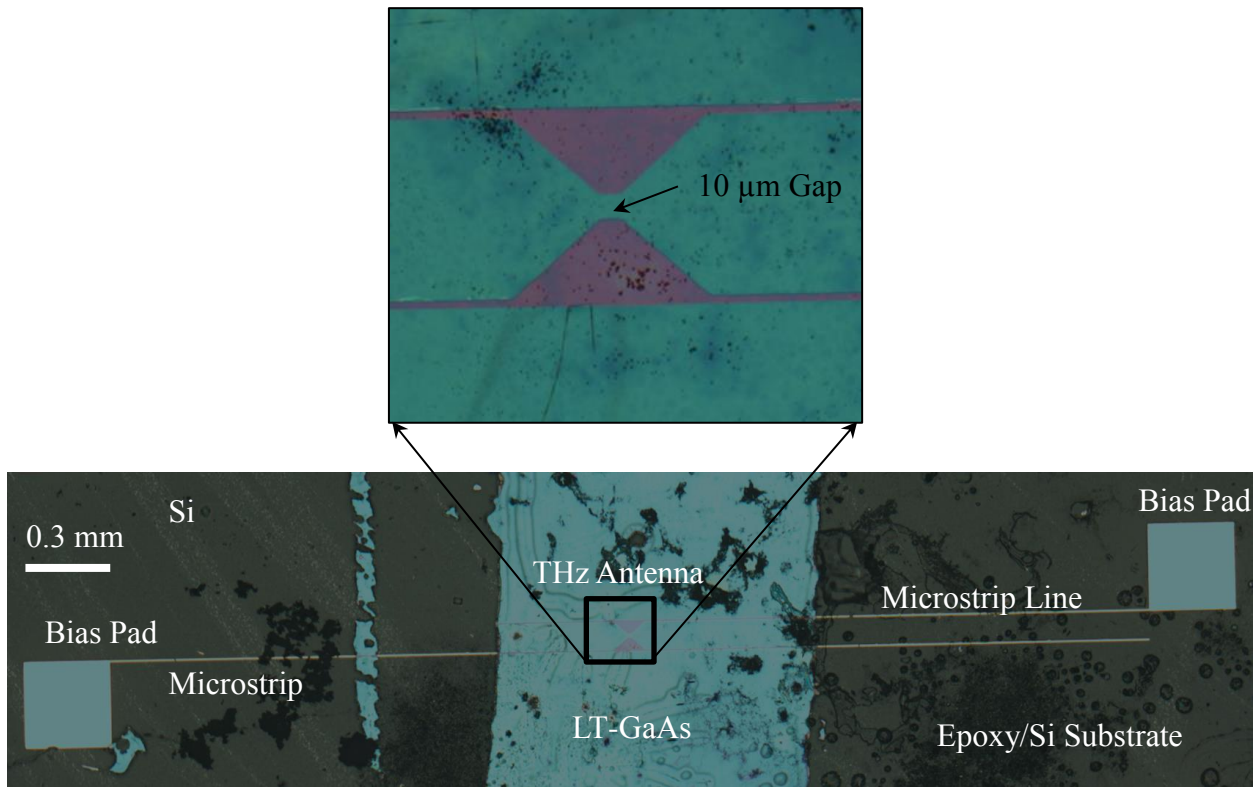


Figure 3.2.3.6: Microscope image of a BLTF THz PCA fabricated using the first round fabrication methods.

A microscope image of a typical device fabricated with this method is shown in Figure 3.2.3.6. The LT-GaAs thin film layer can be seen at the center as the blue-green vertical strip. The dipole antenna is visible through this semi-transparent layer, as shown by the zoomed image

at the top. It is important to note the defects and debris across the sample. In the LT-GaAs layer there are cracks and defects throughout the surface. However, only the region in the antenna gap is utilized for generation of photocarriers. Therefore, defects and debris in the LT-GaAs in other regions should not affect the device performance.

3.2.4. Electron Beam Lithography

The difference between the fabrication processes of the BLTF and P-BLTF designs is the addition of an EBL step to produce the metallic nanodisk arrays on the LT-GaAs surface. Before fabricating the nanodisks on the processed samples, several parameters were optimized to ensure consistency in the size and shape of the array. Optimization was performed on scrap GaAs wafer material and all EBL patterning was performed on the FEI XL-30 Environmental Scanning Electron Microscope [197] at the University of Arkansas Nano and Bio Materials Characterization Facility. This instrument is fitted with the Nanometer Pattern Generation System (NPGS) from JC Nability Lithography Systems [198], which allows for the EBL patterning to be performed. For all EBL processes, the following sample preparation procedure was performed. The sample surface was cleaned with acetone and IPA, then blown dry with N₂. The EBL photoresist 495 PMMA A4 [199] was spun on to the GaAs surface at 3000 RPM for 45 s, followed by a 180 °C bake for 75 s.

In this EBL system, two critical factors required optimization in order to produce the desired nanodisk array patterns: the pattern magnification scale (MS) and pattern exposure dose (ED). The MS dictates the uniform overall uniform size of the pattern while the ED dictates the total electrical charge per unit area deposited into the pattern in units of $\mu\text{C}/\text{cm}^2$. Another factor, the working distance, determines the physical distance between the sample surface and the e-beam

source. For the nanodisk arrays there were two defining geometric parameters, the disk center-to-center spacing S and the disk diameter d . For a fixed input array size, the actual produced S depends on the MS, while the produced d depends on both MS and ED. Shown in Figure 3.2.4.1 is the result of a study of the effects of MS on S . Here, a pattern consisting of a 10×10 array of nanodisks with input geometry parameters $S_{\text{input}} = 520 \text{ nm}$ and $d_{\text{input}} = 200 \text{ nm}$ was patterned at MS values ranging from 88,000 to 94,000. Here, the measured S_{actual} of the array (top) and absolute error $(S_{\text{actual}} - S_{\text{input}})/S_{\text{input}}$ (bottom) after 5/40 nm Ti/Au metallization and liftoff is plotted as a function of MS. The error was below 1% and minimum between MS = 91,000 and 92,000. MS = 92,000 was utilized for the remaining work in this dissertation.

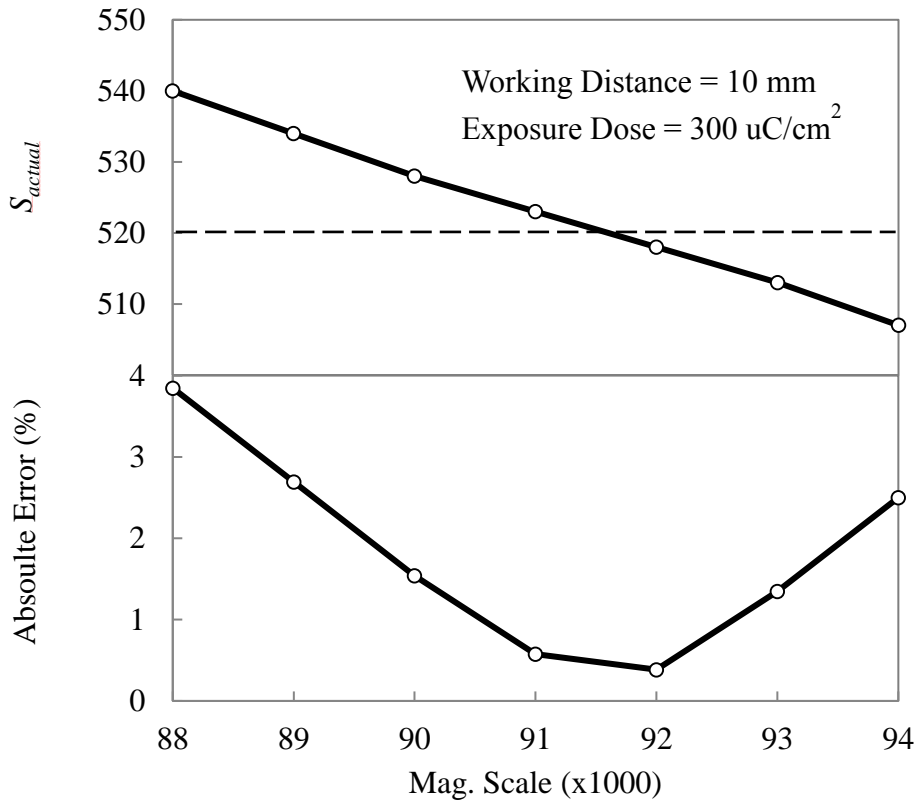


Figure 3.2.4.1: Measured nanodisk spacing S_{actual} for an array with input nanodisk spacing of 520 nm (top vertical axis) and absolute error (bottom vertical axis) as a function magnification scale (horizontal axis).

Several optimization trials were performed in order to determine the optimum ED. The first study considered varying d_{input} between 100, 150, and 200 nm and varying ED between 200, 300, 400, 500, and 600 $\mu\text{C}/\text{cm}^2$. After 5/40 nm Ti/Au metallization and liftoff, the samples were imaged in the SEM and d_{actual} was measured. Figure 3.2.4.2 illustrates the results of this study in terms of the difference in d_{actual} and d_{input} (Δd) as a function of ED for varying d_{input} . It was observed that Δd was near zero only when $d_{\text{input}} = 150$ and 100 nm and ED = 200 $\mu\text{C}/\text{cm}^2$. When $d_{\text{input}} = 200$, the lowest Δd observed was around 100 nm for both ED = 200 and 300 $\mu\text{C}/\text{cm}^2$.

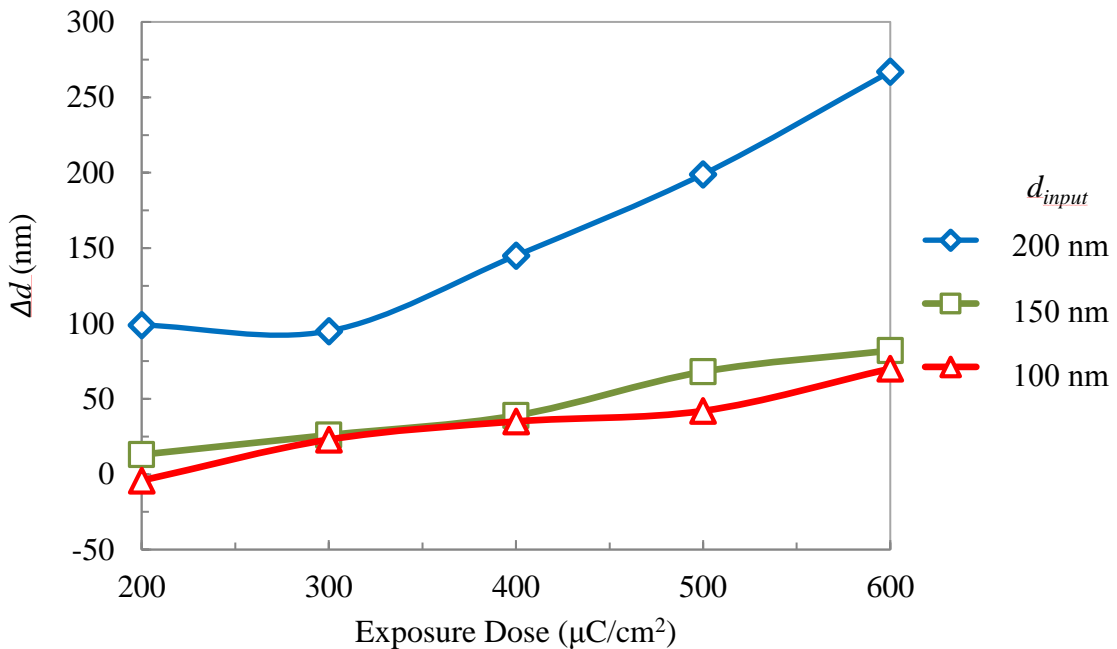


Figure 3.2.4.2: Difference in d_{actual} and d_{input} for d_{input} varying from 100 to 200 nm as a function of ED.

SEM images of nanodisk arrays patterned using $d_{\text{input}} = 150$ nm and ED = 600, 300, and 200 $\mu\text{C}/\text{cm}^2$ are shown in Figure 3.2.4.3. Notice that for ED = 600 and 300 $\mu\text{C}/\text{cm}^2$, the disks are all of uniform size. When ED = 200 $\mu\text{C}/\text{cm}^2$, it was observed that the disk diameter varies between

160 and 200 nm. This effect of nonuniform disk size was observed for all arrays patterned with $ED < 300 \mu\text{C}/\text{cm}^2$. To avoid this, $ED = 300 \mu\text{C}/\text{cm}^2$ was utilized in all other EBL work.

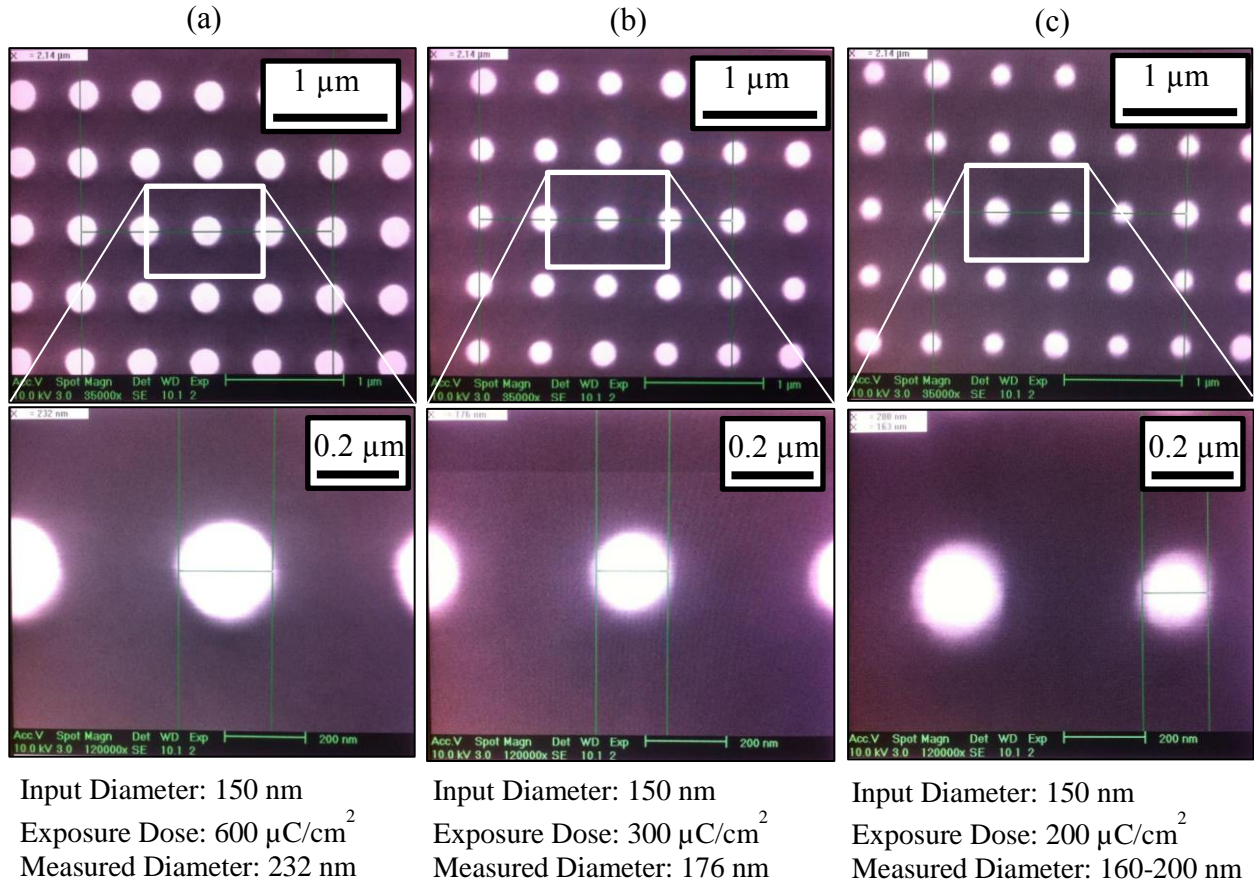


Figure 3.2.4.3: SEM images of Ti/Au nanodisk arrays fabricated on GaAs using EBL. $d_{\text{input}} = 150 \text{ nm}$ and (a) $ED = 600 \mu\text{C}/\text{cm}^2$, (b) $ED = 300 \mu\text{C}/\text{cm}^2$, and (c) $ED = 200 \mu\text{C}/\text{cm}^2$.

In order to achieve the desired $d_{\text{actual}} = 200 \text{ nm}$, the patterning factors MS and ED were kept constant at 92,000 and $300 \mu\text{C}/\text{cm}^2$, respectively. d_{input} was varied to determine the value which would yield $d_{\text{actual}} = 200 \text{ nm}$. Additionally, it was recommended that the working distance be changed from 10 mm to 7 mm, as this was the value other users of the EBL system had been using for patterning [200]. Due to the change in working distance, it was not certain if the S_{input} would yield the desired 520 nm. Therefore, 10x10 nanodisk arrays were patterned with a range

of input geometry values varying $d_{\text{input}} = 75, 80, 85,$ and 90 nm and $S_{\text{input}} = 500, 510, 520,$ and 530 nm. After patterning, $5/40$ nm Ti/Au metallization and liftoff was performed, followed by SEM imaging of the sample to acquire values of S_{actual} and d_{actual} . The results are summarized in Table 3.2.4.1. Here, it was observed that the desired $S_{\text{actual}} = 520$ nm and $d_{\text{actual}} = 200$ nm occurred at $S_{\text{input}} = 500$ nm and $d_{\text{input}} = 150$ nm.

Table 3.2.4.1: Measured S_{actual} and d_{actual} as a function of S_{input} and d_{input} . Optimum parameters are highlighted in bold.

		S_{input} (nm)			
		500	510	520	530
d_{input} (nm)	150	520	540	555	565
		200	200	200	200
	160	520	540	555	565
		210	215	210	210
170	520	540	555	565	
	225	225	220	225	
180	520	540	555	565	
	230	235	230	230	

With the EBL parameters optimized to yield the desired nanodisk array geometry, the next step was to pattern the nanodisk arrays on the LT-GaAs layer of the fabricated BLTF devices. Initially, there were concerns with how well the nanodisk patterns optimized on the scrap GaAs would pattern on the LT-GaAs thin-film layer. The reason for this is that with SEM imaging, the surface to be imaged needs to have some electrical conductivity to prevent charge buildup from the electrons. Since the LT-GaAs thin-film is separated from the bulk Si substrate by an epoxy layer, it was uncertain if the epoxy would prevent dissipation of the electron charge and have a negative effect of the EBL patterning. However, after testing the pattern on a sample of 120 nm LT-GaAs epoxy bonded to Si, there were no notable differences in the pattern as compared to those on scrap GaAs.

The P-BLTF samples were prepared for EBL patterning in the same manner as the previously described scrap GaAs samples. One of the main considerations with this process was the alignment of the nanodisk pattern with the antenna electrodes. The goal was to have the array patterned, at a minimum, over the antenna anode, gap, and cathode. The method for alignment and orientation of the sample is illustrated in Figure 3.2.4.4.

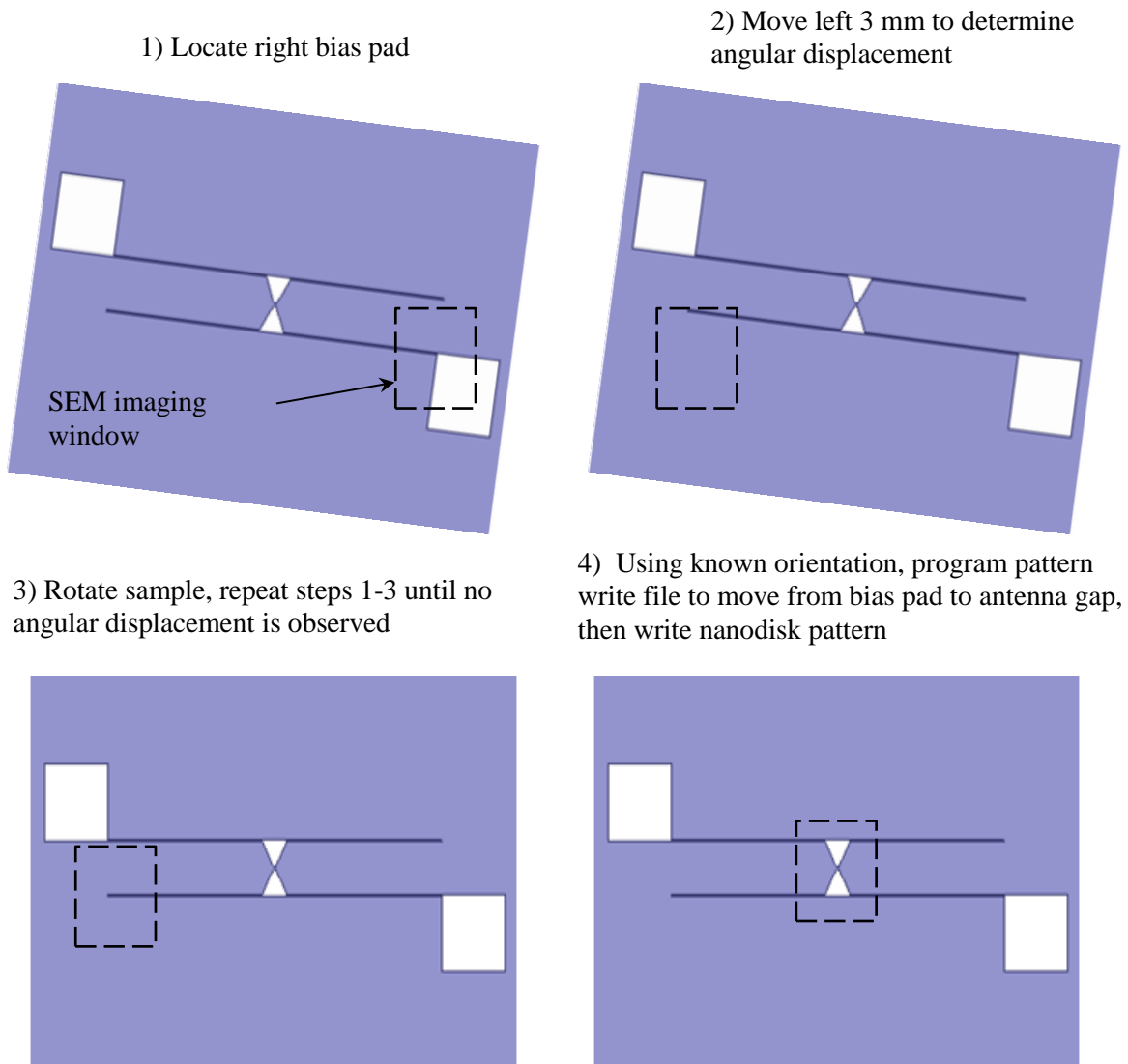


Figure 3.2.4.4: Illustration of the method used for aligning the THz-PCA pattern with the EBL system.

With the SEM in imaging mode, the right side bias pad was located and the imaging window was centered over the junction of the bias pad with the microstrip line. The window was blanked, and moved to the left a distance of 3 mm (the length of the microstrip line). It was important to ensure that the SEM imaging window never passed over the area where the nanodisk array was intended to be patterned without first being blanked. The reason for this is to avoid exposing the PMMA resist in this area and affecting the pattern. If the sample was mounted with no angular tilt, the viewing window should have been centered at the left end of the bottom microstrip line. Any displacement of this from the center indicated that the sample was not aligned, so the sample stage was rotated accordingly to correct for this. This process was repeated until no sample tilt was observed.

After the sample was oriented, the viewing window was centered over some known reference point (for example, the junction of the bias pad with the microstrip line). From here, the pattern writing program was set to blank the imaging window, move from the reference point to the center of the antenna dipole gap, pattern the nanodisk array, and move back to the starting reference point. Since the alignment accuracy was not well known, a relatively large $80 \times 80 \mu\text{m}^2$ nanodisk array was utilized to ensure that all three regions (anode, gap, and cathode) were covered. After patterning development, 5/40 nm Ti/Au was evaporated and lifted off in acetone to produce the metallic array structures. Figure 3.2.4.5 shows optical microscope and SEM images of the fabricated nanodisk arrays on the LT-GaAs thin-film antenna. In both the optical microscope and SEM images, the antenna electrodes, located under the 120 nm LT-GaAs layer, could be observed. The nanodisk array had the desired dimensions of $d = 200 \text{ nm}$ and $S = 520 \text{ nm}$. In most cases, it was observed that the added process of patterning the nanodisks induced cracks and defects to the LT-GaAs thin-film layer. An example is shown in the optical

microscope image of Figure 3.2.4.5, where a vertical crack in the LT-GaAs was observed on the left side.

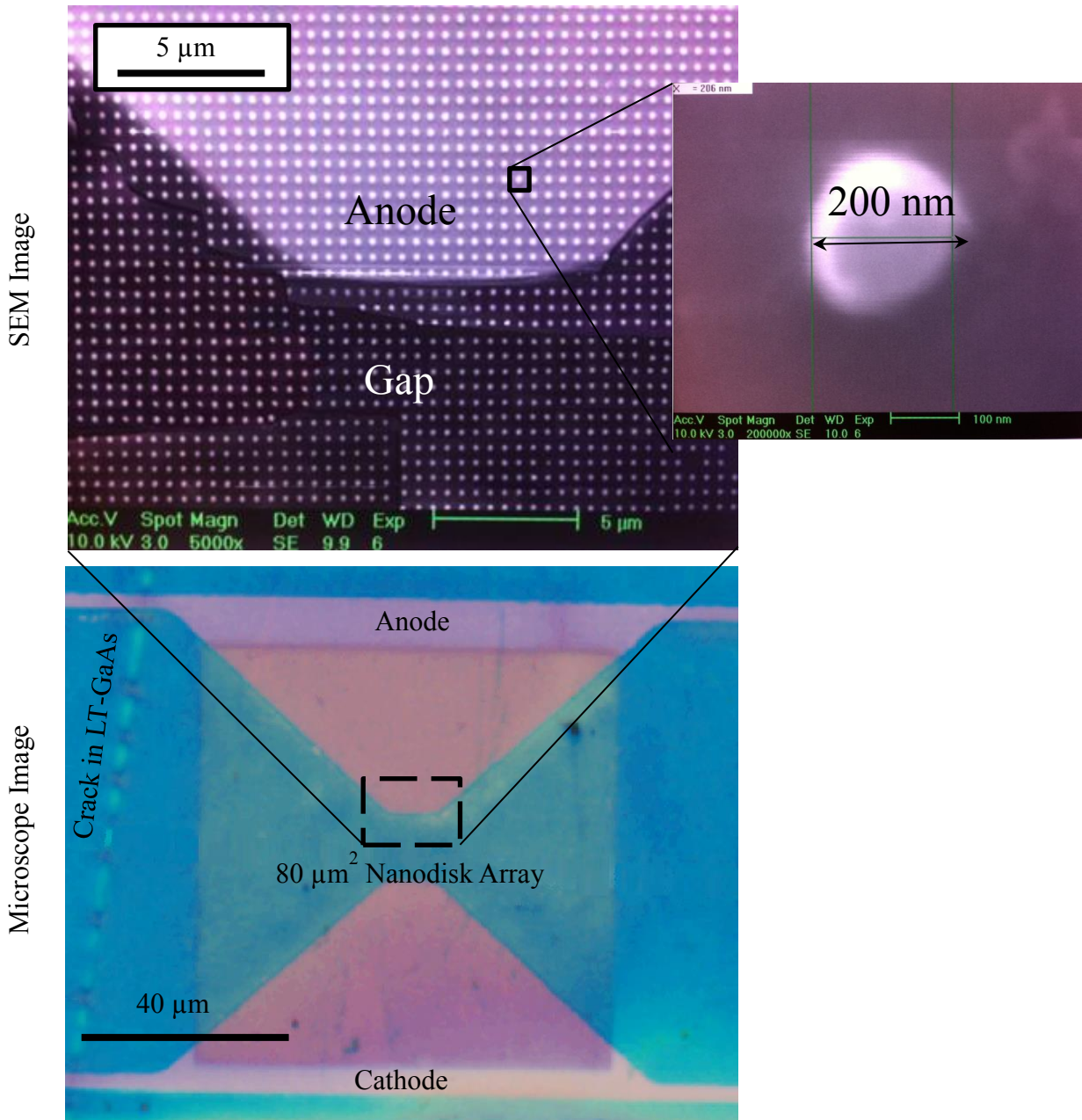


Figure 3.2.4.5: Microscope and SEM image of P-BLTF anode after nanodisk array fabrication.

3.2.5. Device Packaging

After the individual chips were fully processed, the final step was to package the devices for later testing. In order to easily connect to the individual devices electrically, the electrodes of the antennas needed to be connected to a larger conductor that could be connected to by hand. Therefore, a simple copper clad FR4 printed circuit board (PCB) was designed with five separate traces for the anode of each device and a single ground trace for the cathodes. The traces were soldered to a custom 6-pin cable designed to easily connect to a custom-made switching box. The PCB and switching box are shown in Figure 3.2.5.1. The switching box had a single coax output and allowed the DC bias voltage to be easily switched between devices.

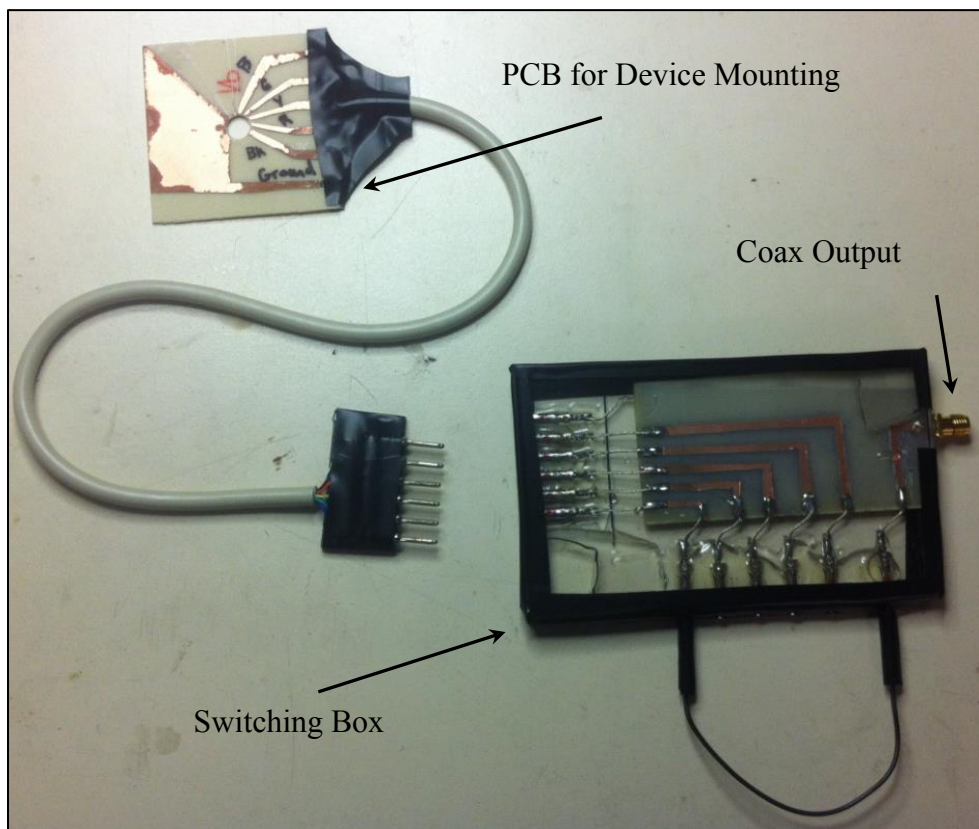


Figure 3.2.5.1: PCB and switching box for device packaging and testing.

A separate PCB was fabricated for each of the THz PCA chips. The devices were mounted to the non-copper side of the PCB using the same JB Weld epoxy used to bond the thin-film LT-GaAs to the Si substrate. A cross section illustration of the THz PCA mounted to the PCB is shown in Figure 3.2.5.2. One problem that arose was the electrical connection to the antenna electrodes. Originally, the plan was to utilize wire bonding to connect from the PCB copper to the antenna bias pads. Wedge bonding was attempted first, and was found to work fairly well for the modified conventional devices. However, for the BLTF and P-BLTF devices, the JB Weld epoxy under the bias pad metallization did not provide enough mechanical support to allow wire bonding. Every attempt to bond to the bias pads would effectively break through the bias pad and deform the underlying epoxy layer without bonding. Ball bonding was attempted as well with the help of University of Arkansas High Density Electronics Center staff member Mike Steiger. Here, it was observed that bonds that did appear to be successful would easily pull the metallization away from the surface under very little force. This was likely due to the poor adhesion between the antenna metallization and the underlying epoxy layer.

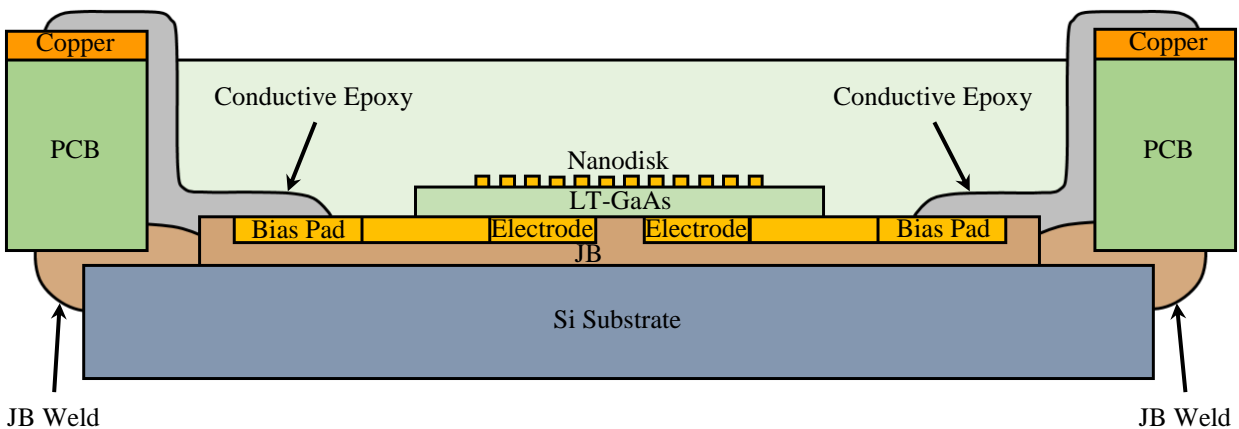


Figure 3.2.5.2: Cross section illustration of the device mounted to the PCB.

In order to electrically connect to the device, a less than conventional method was utilized. As shown in Figure 3.2.5.2, a conductive epoxy Epotek P1011 [201] was manually applied to create an electrical bridge from the antenna bias pads to the PCB metallization. Due to the scale and vicinity of the bias pads to one another, the conductive epoxy traces needed to be applied in sub-millimeter widths. This required looking at the sample surface through a microscope while manipulating the epoxy on the end of a fine point needle to “draw” the epoxy traces. After applying the epoxy, the samples were oven baked at 150 °C for 30 min to cure and activate the epoxy. After baking, the resistance across the epoxy was checked using a probe station and found to be $< 5 \Omega$ for the majority of connections. This was considered to be a negligible resistance when considering that the gap resistance of the antenna was expected to be on the order of $10^9 \Omega$. With the mounting and electrical connection to the PCB, the fabrication process for the first round of devices was complete. Seven total samples were fabricated, each with five devices patterned, two modified conventional, three BLTF, and two P-BLTF. A preliminary experimental check of the devices was performed in which each was connected to a DC 10 V bias and the anode current was measured under dark and light (broadband white light) conditions. The purpose here was to observe a current increase under illumination to check for device photoresponsivity and potential electrical faults. The results of this test are shown in Table 3.2.5.1. “Pass” indicated that when measuring the device current, a significant increase was observed under broadband white light illumination. “Fail” indicated that no photocurrent increase was observed.

Table 3.2.5.1: Dark and light photocurrent measurements of the first round devices under a DC 10 V bias.

Chip Name	Device Number	Dark Current (μA)	Light Current (μA)	Pass/Fail
Modified Conventional 1	1	0.1	12.3	Pass
	2	0.1	10.9	Pass
	3	0.1	11.1	Pass
	4	0.1	12.3	Pass
	5	<0.1	6.0	Fail
Modified Conventional 2	1	0.7	14.4	Pass
	2	0.7	14.5	Pass
	3	0.9	16.4	Pass
	4	0.7	17.5	Pass
	5	26.1	40.4	Fail
BLTF 1	1	140	264	Pass
	2	∞	∞	Fail
	3	∞	∞	Fail
	4	16	31	Fail
	5	110	287	Pass
BLTF 2	1	75	209	Pass
	2	80	258	Pass
	3	81	242	Pass
	4	80	242	Pass
	5	0	0	Fail
BLTF 3	1	52	116	Pass
	2	37	100	Pass
	3	43	120	Pass
	4	36	93	Pass
	5	37	81	Pass
P-BLTF 1	1	47	140	Pass
	2	40	138	Pass
	3	45	145	Pass
	4	44	165	Pass
	5	N/A	N/A	Fail
P-BLTF 2	1	116	232	Pass
	2	120	280	Pass
	3	N/A	NA	Fail
	4	144	390	Pass
	5	∞	∞	Fail

3.3. Failure Analysis of First-Round Prototype Devices

Experimental analysis of the first round of the THz PCA devices revealed several unexpected problems with the devices. After fabrication, the devices were taken to Teraview LTD., a

company located in the United Kingdom that is manufacturing terahertz technology [202]. There, several tests were conducted and although THz emission was observed in the modified conventional emitters, it was several orders of magnitude weaker than anticipated. Additionally, no THz emission was observed from the BLTF or P-BLTF emitters. This section will present the theoretical and experimental analysis of the first round devices that was performed to determine their modes of failure.

3.3.1. I-V Characteristics

When discussing the fabrication process of the BLTF and P-BLTF devices with Michael Evans, staff member at Teraview LTD., there was an immediate concern over the epoxy bond of the LT-GaAs thin film to the Si substrate. This was before the first testing was even performed that concluded that these devices did not generate measureable THz radiation. As illustrated in Figure 3.3.1.1, when the LT-GaAs thin film layer is bonded to the Si substrate with epoxy, there are two contributions to the gap resistance that exist in parallel with each other; $R_{\text{LT-GaAs}}$ and R_{epoxy} .

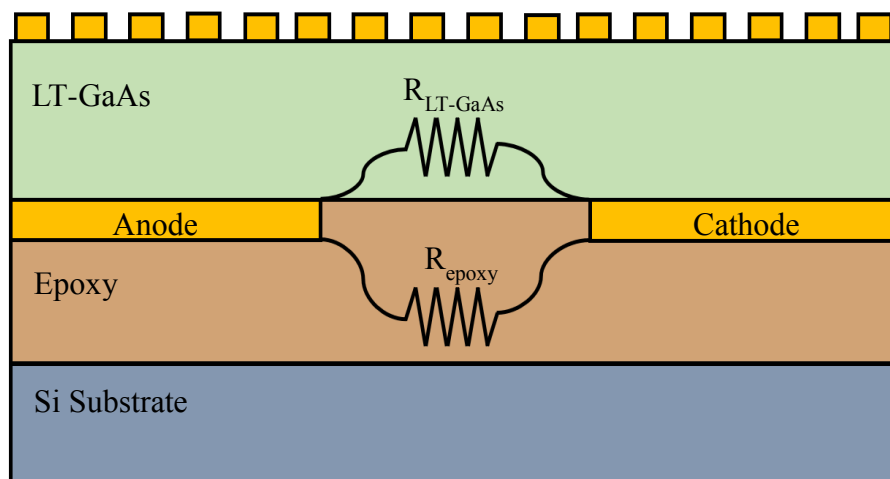


Figure 3.3.1.1: Hypothesized gap resistance contributions in the P-BLTF device.

If $R_{\text{epoxy}} > R_{\text{LT-GaAs}}$, the total device resistance of the BLTF and P-BLTF devices will be lower than the modified conventional devices. This introduced an unwanted conduction path in close proximity to the photoconductive gap of the device, which could reduce the device capacitance and interfere with THz generation mechanisms.

After the initial measurement attempts concluded that the BLTF and P-BLTF devices did not produce measurable THz radiation, the first step was to analyze the dark I-V characteristics of the devices. Current was measured for each device as a function of bias voltage from 0 to 2 V. Higher voltage ranges, some as high as 100 V, were also measured for select devices and confirmed the same linear trends observed in the 0 to 2 V range. Measurement results for the average I-V characteristics of each design are shown in Figure 3.3.1.2.

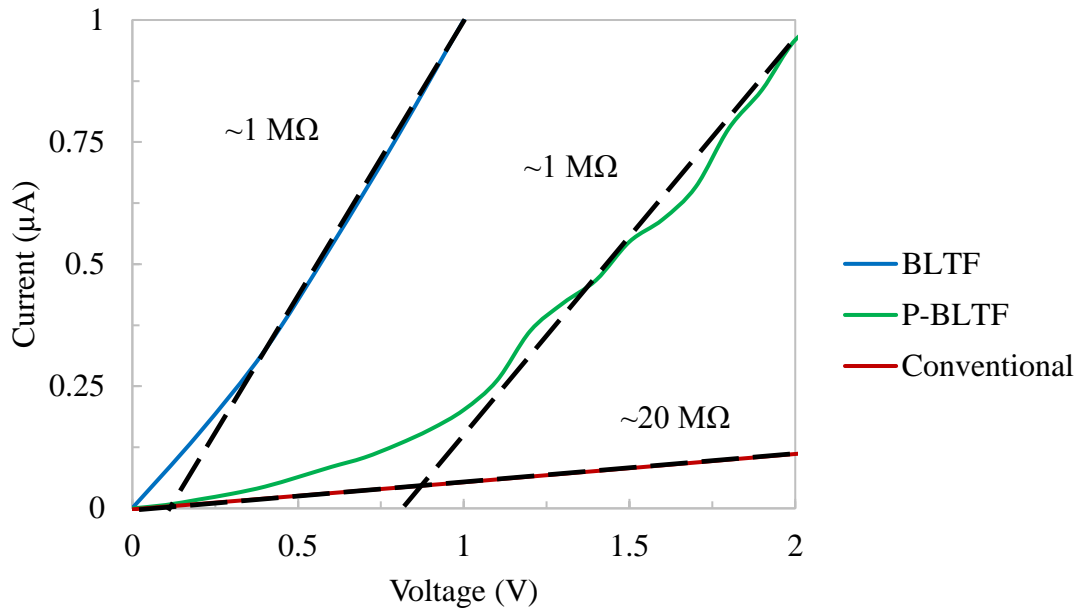


Figure 3.3.1.2: Average I-V characteristics of the first round fabricated devices.

For each of these traces, black dashed lines are included as a guide to the eye to illustrate the linear behavior of each device. From these measurement results it was possible to extrapolate gap resistance values of approximately 1 MΩ for the BLTF and P-BLTF devices while it was 20

MΩ for the modified conventional devices. Assuming that the resistance of the modified conventional emitter is approximately the resistance of the LT-GaAs and following the resistance model described by Figure 3.3.1.1, the resistance values were $R_{\text{LT-GaAs}} = 20 \text{ M}\Omega$ and $R_{\text{epoxy}} = (1/R_{\text{BLTF}} - 1/R_{\text{LT-GaAs}})^{-1} = (1/1 - 1/20)^{-1} \text{ M}\Omega = 1.05 \text{ M}\Omega$. Low resistance of the gap would effectively lower the capacitance of the gap, decreasing the amount of stored energy able to be released as a THz pulse.

3.3.2. THz Transmission Characterization of Substrate and Adhesive Materials

Another potential contributor to the poor performance in the first round devices was THz absorption loss in the substrate and adhesive materials. In the modified conventional emitters, THz is generated at the electrodes and propagates through the GaAs substrate before transmitting into the Si lens. In the BLTF and P-BLTF, THz is generated at the electrodes, propagates through the thin layer of adhesive, transmit into and propagates through the Si substrate, and transmits into the Si lens. Since the I-V measurements of the previous measurements indicated higher gap conductivity than expected, there was a concern that absorption losses in these layers could be occurring.

In order to quantify the absorption loss in these materials, THz time-domain spectroscopy was performed on various samples of the materials. The system utilized was a Teraview TPS Spectra 3000, shown in Figure 3.3.2.1 [202]. THz spectroscopy was performed on six different samples; the unprocessed GaAs MBE wafer, JB Weld Epoxy, SU-8 2000.5 photoresist and three difference Si samples; the Si wafer used in the first round of fabrication (assumed to be high resistivity), a 50 Ω-cm wafer, and 0.65 Ω-cm wafer. SU-8 2000.5 was investigated as an alternative adhesive material due to its high post-cure strength and low electrical resistance.

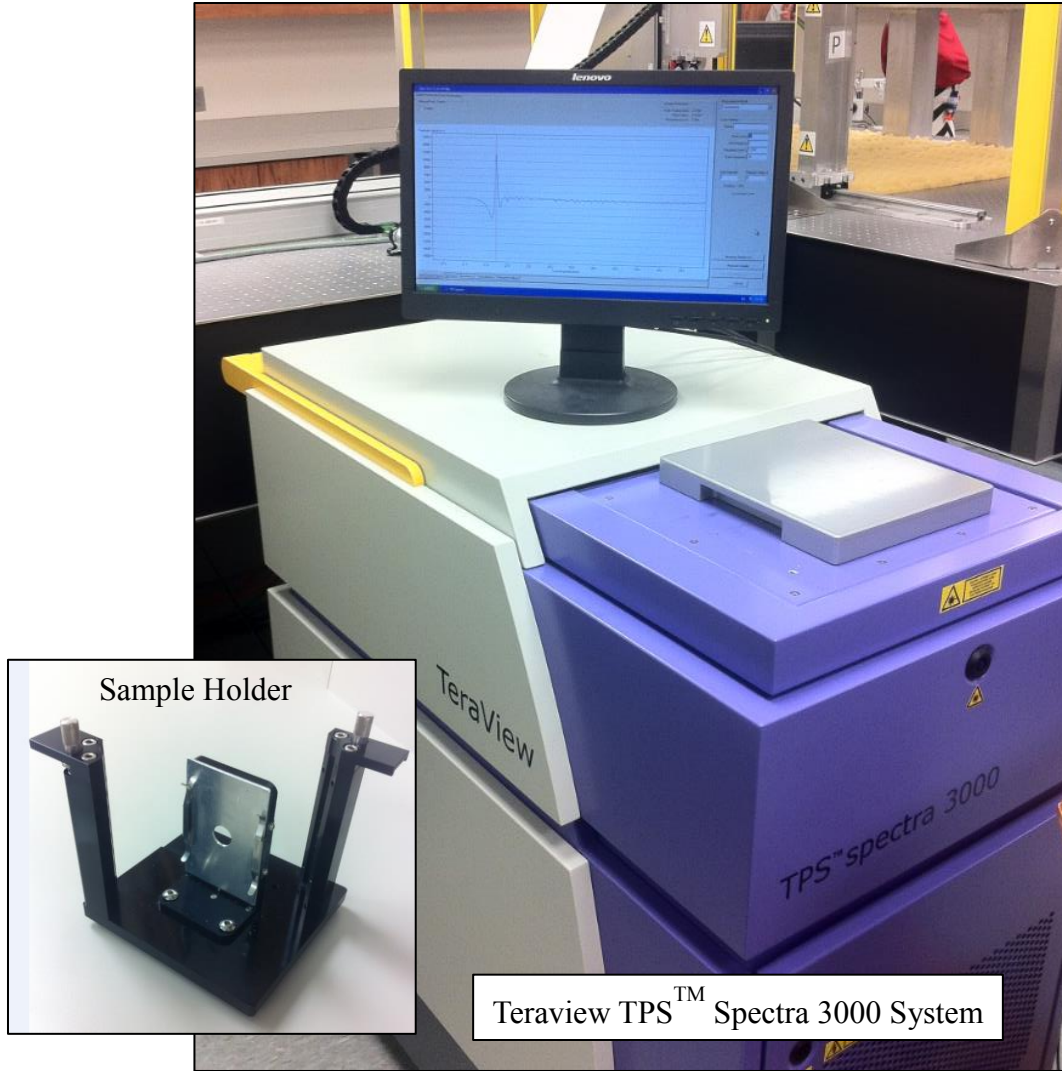


Figure 3.3.2.1: Photograph of the Teraview TPS Spectra 300 system utilized to characterized the THz properties of the antenna materials.

The system measures the magnitude and phase of the THz field transmitted through the sample, which is related to the refractive index n and absorption coefficient by,

$$\left(\frac{E_s}{E_r}\right) = T(n) \exp\left(-\frac{\alpha d}{2} + \frac{i n \omega d}{c_0}\right) \quad \text{Equation (3.3.2. 1).}$$

Here, E_s and E_r are the sample and reference complex electric field values, $T(n)$ is the transmission coefficient, d is the sample thickness, ω is angular frequency, α is the material absorption coefficient, n is the refractive index, and c_0 is the free space speed of light. For the

GaAs and Si samples, the reference measurements were taken as transmission through the nitrogen gas (N_2) purged chamber with nothing in the beam path.

For the JB Weld Epoxy and SU-8 2000.5 measurements, the samples needed to be mounted to some supporting medium, which would then be taken as the reference. Figure 3.3.2.2 shows a photograph of the SU-8 2000.5 and JB Weld sample preparation.

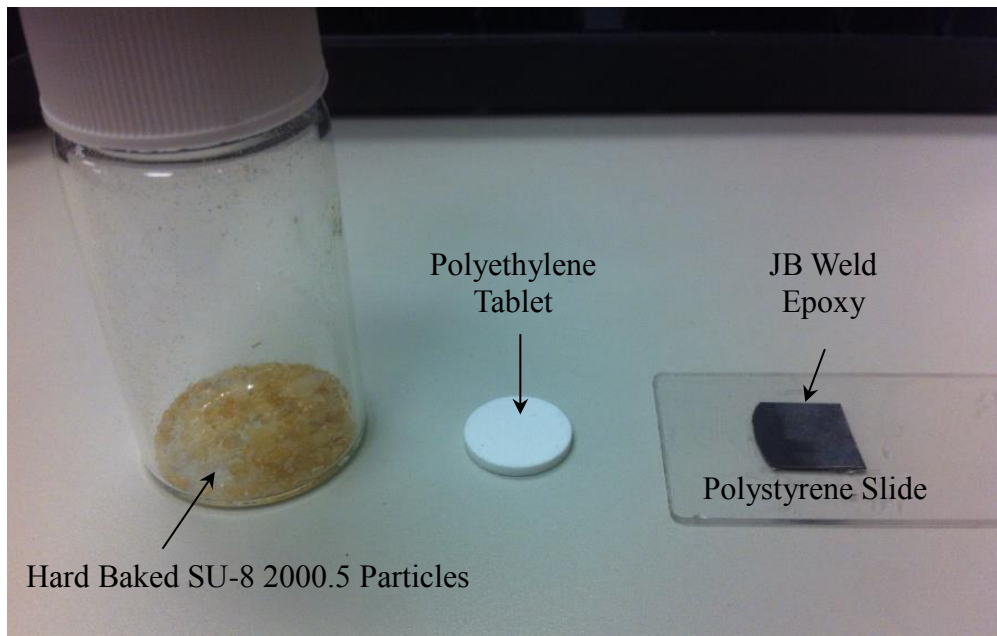


Figure 3.3.2.2: Photograph of the JB Weld and SU-8 2000.5 sample preparation for THz spectroscopic characterization.

The JB Weld Epoxy was prepared on a polystyrene slide to yield a uniform $285\ \mu\text{m}$ thickness. E_r was taken at a point through the slide only and E_s was taken through both the slide and epoxy layer. For the SU-8 2000.5 sample preparation, it was not possible to produce a uniform sample layer on a polystyrene slide. This material exists in a liquid form that must be baked at $150\ ^\circ\text{C}$ to solidify. This temperature is high enough to cause the polystyrene slide to significantly deform. Therefore, an alternative method of sample preparation was used in which the SU-8 2000.5 was hard baked on a glass slide (glass has poor THz transmission, making it

unsuitable for THz transmission spectroscopy), scraped off as small flakes, ground to a fine particle size, and incorporated into a polyethylene tablet. Two tablets were made, one reference tablet containing 500 mg of polyethylene and one sample tablet containing 500 mg of polyethylene and 112 mg of the SU-8 2000.5 particles. The difference in tablet thickness corresponds to the thickness d of the SU-8 2000.5 material, since the background polyethylene material mass was kept the same. The derived values of n and k from the sample measurements are shown in Figure 3.3.2.3.

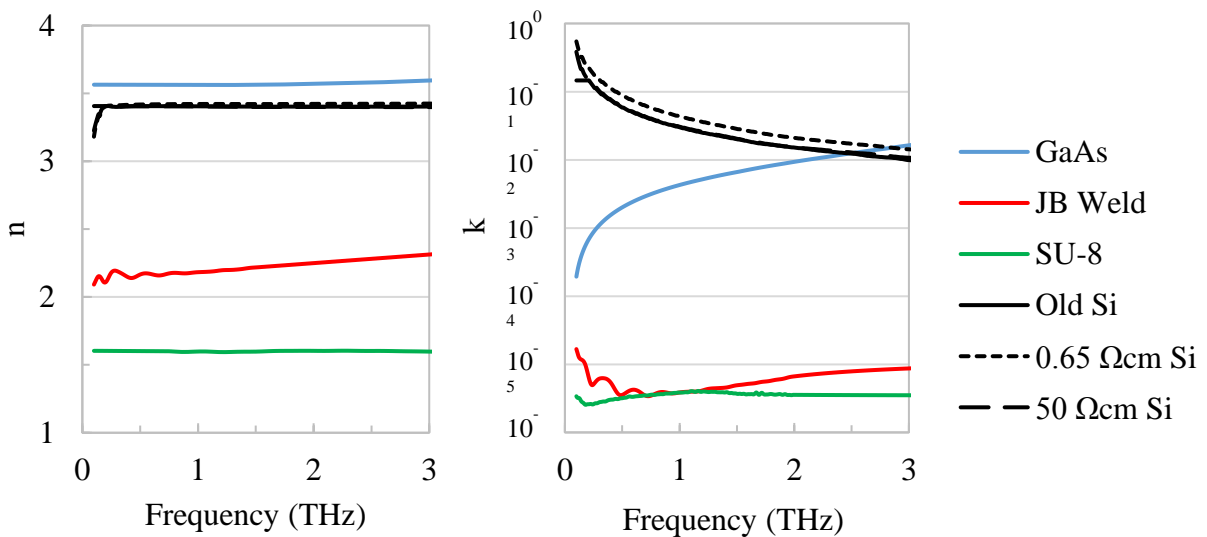


Figure 3.3.2.3: Real and imaginary refractive index values calculated from THz TDS transmission measurements of the various substrate materials.

THz refractive index values have been reported for SU-8 [203], Si, and GaAs [204] and the measured values matched the reported values within less than 10% difference. Both adhesives studied showed two to three orders of magnitude lower k than the Si and GaAs substrate materials. This indicated that absorption loss in the adhesive layer was an unlikely cause of the failure of the BLTF and P-BLTF devices. However, there was a significant difference in the

values of the n of the JB Weld Epoxy and Si substrates. It is possible that losses could have occurred through reflections at the JB Weld/Si interface due to mismatch.

3.3.3. Modeling of THz Transmission Through PCA Substrate

In order to more accurately understand the THz wave propagation through the THz antenna structure, two models were developed and considered. The first was a simplified analysis of the reflection and absorption losses in a 1-dimensional multi-layered system. The second was a full-wave FEM analysis of the antenna structure using COMSOL® Multiphysics. To analytically study the effects of the adhesive layer and substrate material on THz transmission a multi-layered model was based on the geometry illustrated in Figure 3.3.3.1. In this model a steady state plane wave is assumed as the excitation, which begins just to the right of the antenna electrode inside the adhesive layer.

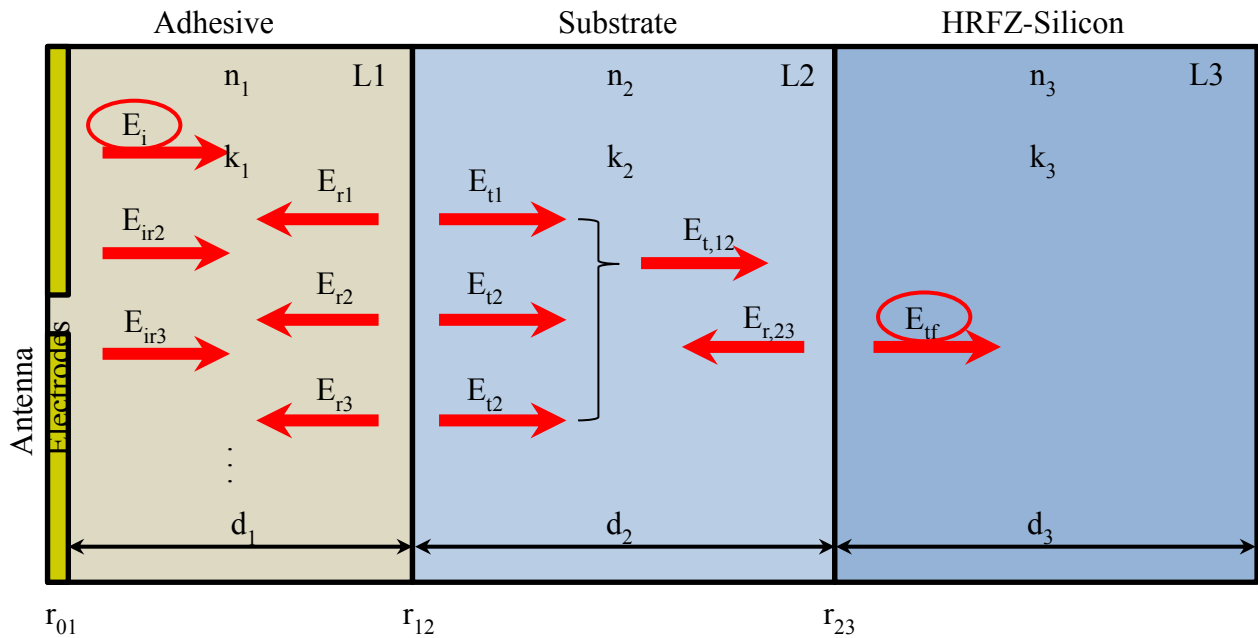


Figure 3.3.3.1: Geometry of the multi-layer transmission analysis of the THz PCA structure using the simple model.

At the left surface is the antenna electrode metallization, where the THz pulse E_i is generated. This interface has a reflection coefficient r_{01} , which for a dielectric/metal interface is -1. The pulse propagates to the right through the adhesive layer a distance d_1 before reaching the adhesive/substrate interface. Here, an approximation is made that the adhesive thickness $d_1 \ll D_p$, where D_p is the spatial width of the pulse ($D_p = 150 \mu\text{m}$ for a 500 fs pulse), while the substrate thickness $d_2 > D_p$. Under this approximation, multiple reflections were accounted for in the adhesive layer while only the single pass through the substrate was considered. This approximation arose from the need to model the time-domain pulse using simplified steady-state equations. Since the adhesive layer is thin with respect to the pulse duration, the multiple internal reflections of the pulses were considered to overlap, leading to either a net constructive or destructive interference in the transmitted pulse. In the substrate layer, the thickness was great enough that the additional internal reflections would be separated in time enough to not lead to interference in the primary pulse.

Following the described model, the electric field transmitted into the silicon lens $\hat{E}_{t,f}$ can be written in terms of the incident electric field \hat{E}_i as shown in Equation 3.3.3.1 [164].

$$\hat{E}_{t,f} = \hat{E}_i \exp\left(\frac{i2\pi f \hat{n}_1 d_1}{c}\right) t_{12} \dots \sum_{j=1}^{\infty} \left[r_{01} r_{12} \exp\left(\frac{i4\pi f \hat{n}_1 d_1}{c}\right) \right]^j \exp\left(\frac{i2\pi f \hat{n}_2 d_2}{c}\right) t_{23} \quad \text{Equation (3.3.3.1)}$$

Here, \hat{n} is the complex index of refraction of each layer, t_{jk} and r_{jk} are the transmission and reflection coefficients from layer j to k , f is the THz frequency, and c is the speed of light in vacuum. The first exponential term represents the first pass of the THz pulse from the antenna electrodes through the adhesive layer. The summation represents the attenuation and phase shift

from the infinite sum of pulses reflecting internally in the adhesive. Each term in the summation represents one round of the internal reflection, where part of the pulse is reflected from surface r_{12} , travels backwards through the adhesive layer, reflects from surface r_{01} , travels forward through the adhesive, and reflects/transmits through surface r_{12}/t_{12} . The final exponential term and transmission coefficient t_{23} represents the attenuation and phase shift from the pulse propagation through the substrate layer and reflection loss at the substrate/lens interface.

For comparison, modeling of the modified conventional antenna structure was simpler, since there were no thin layers with internal reflections to account for. This simplified solution is shown in Equation 3.3.3.2, where only the attenuation and phase shift of a single, forward propagation through the substrate layer followed by transmission at surface t_{23} are considered.

$$\hat{E}_{t,f} = E_i \exp\left(\frac{i2\pi f \hat{n}_2 d_2}{c}\right) t_{23} \quad \text{Equation (3.3.3.2)}$$

In order to check that the internal reflections of Equation 3.3.3.1 are properly accounted for, a comparison was made between the solution of this equation with that of Equation 3.3.3.2 as the adhesive layer thickness was decreased. Conceptually, as $d_1 \rightarrow 0$ these two solutions should converge, since they would then be modeling the same effective geometry. For this test, the material properties used for the substrate layer was GaAs and the adhesive was SU-8. The adhesive thickness d_1 was decreased from 50 μm down to 0.1 μm . The results of this comparison are shown in Figure 3.3.3.2. The solution of Equation 3.3.3.2 is shown in the dotted black trace, and the colored solid traces show the solutions of Equation 3.3.3.1. Here, it was observed that once the adhesive thickness is reduced to 1 μm , the two solutions converge and remain converged for a lower thickness of 0.1 μm .

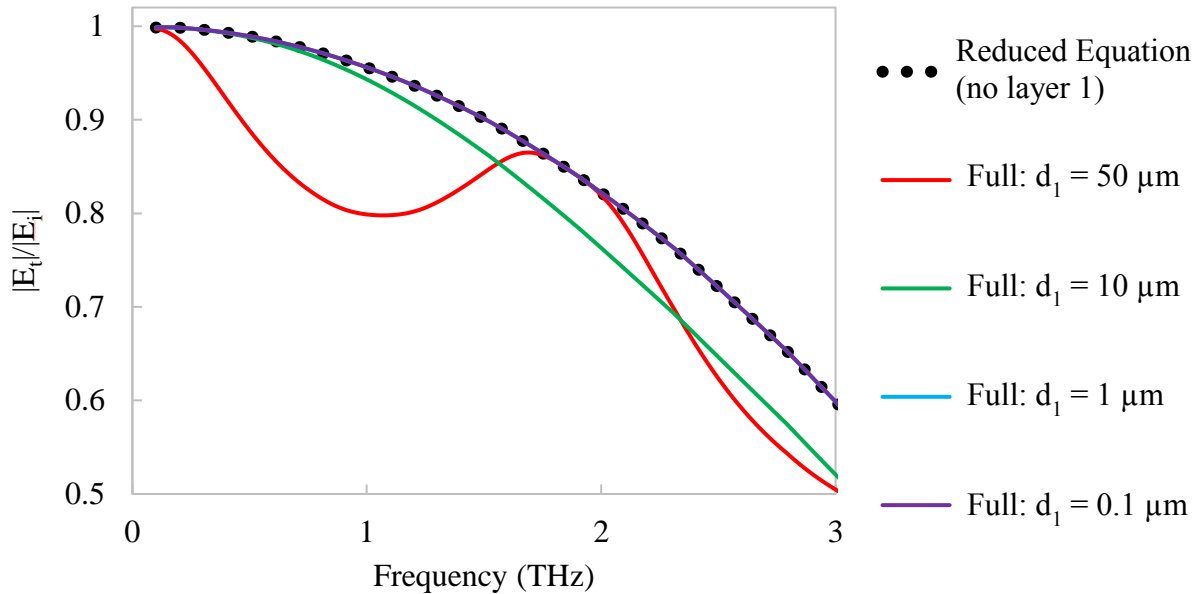


Figure 3.3.3.2: Convergence of Equation (3.3.3.1) to Equation (3.3.3.2) as d_1 is decreased.

Using Equation 3.3.3.2 the effect of changing the substrate material with no adhesive layer present was observed. GaAs, 0.65 Ωcm Si, 50 Ωcm Si, HRFZ Si, and the Si used in the first round fabrication were the materials considered here. The results of the THz transmission as a function of frequency are shown in Figure 3.3.3.3. The lower resistivity Si samples all showed a uniform loss of around 27% for the 50 $\Omega\text{-cm}$ Si and 37% for the 0.65 $\Omega\text{-cm}$ Si. Since the loss was uniform across the frequency range, it indicated that this loss was primarily due to reflection loss at the substrate/lens interface. In contrast, when the substrate material was HRFZ Si there was no notable loss, since the substrate and lens material were matched in their refractive indices and have low absorption coefficients. On the other hand, the GaAs had a notable non-uniform loss that was negligible at 0.1 THz but increased to around 41% at 3 THz. This was likely due to the increased absorption coefficient at higher THz frequencies that arises from the phonon vibration mode at around 8 THz [127].

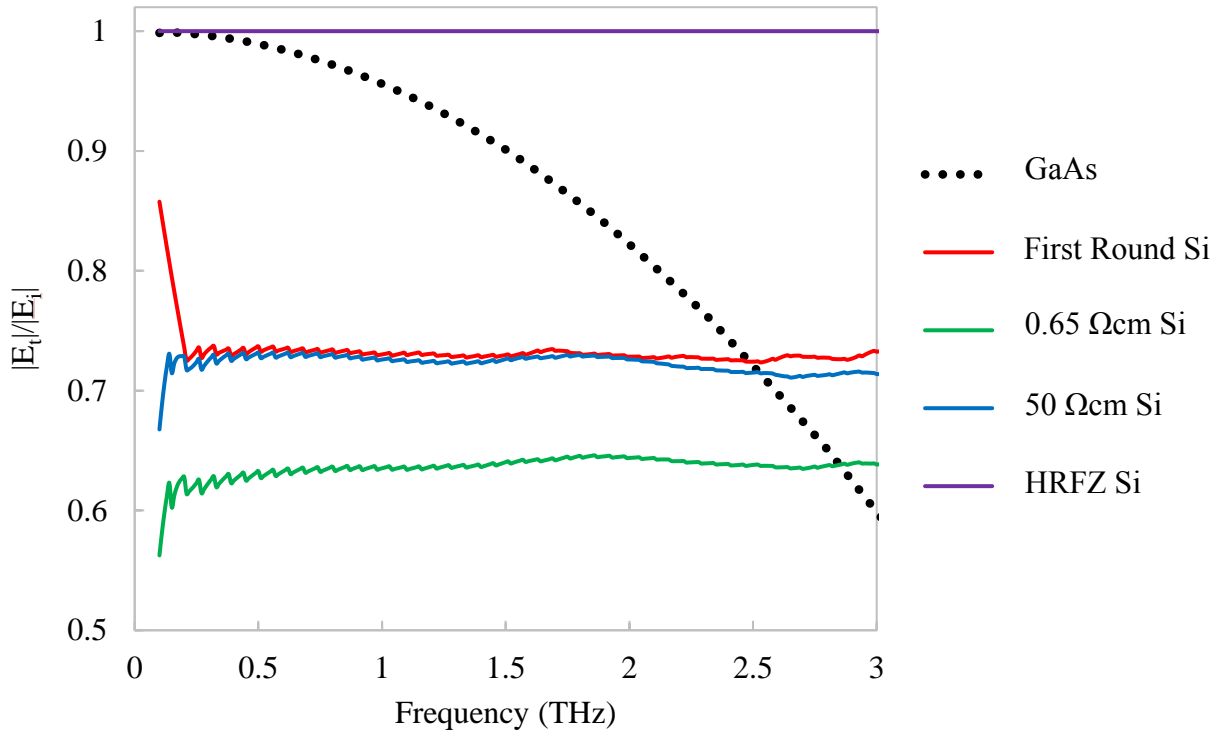


Figure 3.3.3.3: Effect of changing the PCA substrate material with no adhesive layer present.

Next, the effect of adding the adhesive layers to each of the various substrate materials was studied. Figure 3.3.3.4 shows the results of the THz transmission through the THz PCA substrate and adhesive layers, where the adhesive is JB Weld Epoxy and the layer thickness is varied from 1 μm to 50 μm . As a reference, the transmission through a GaAs substrate with no adhesive layer (NA) was included in all plots. For JB Weld thickness of 1 μm , no difference was observed between the GaAs with and without the adhesive and only minor change was observed for $d_1 = 5 \mu\text{m}$. At $d_1 = 10 \mu\text{m}$ there is slightly more decrease in the transmission at certain frequencies, though this was always below 5%. At the highest JB Weld thickness observed of $d_1 = 50 \mu\text{m}$, notable resonant oscillations are observed. These arise from the interference from the multiple internal reflections in the adhesive layer. However, the loss induced from these oscillations was still relatively low, less than 10%. The results indicated that absorption losses in the adhesive

layer was not a significant contributor to the BLTF and P-BLTF device failure for the first round of fabrication.

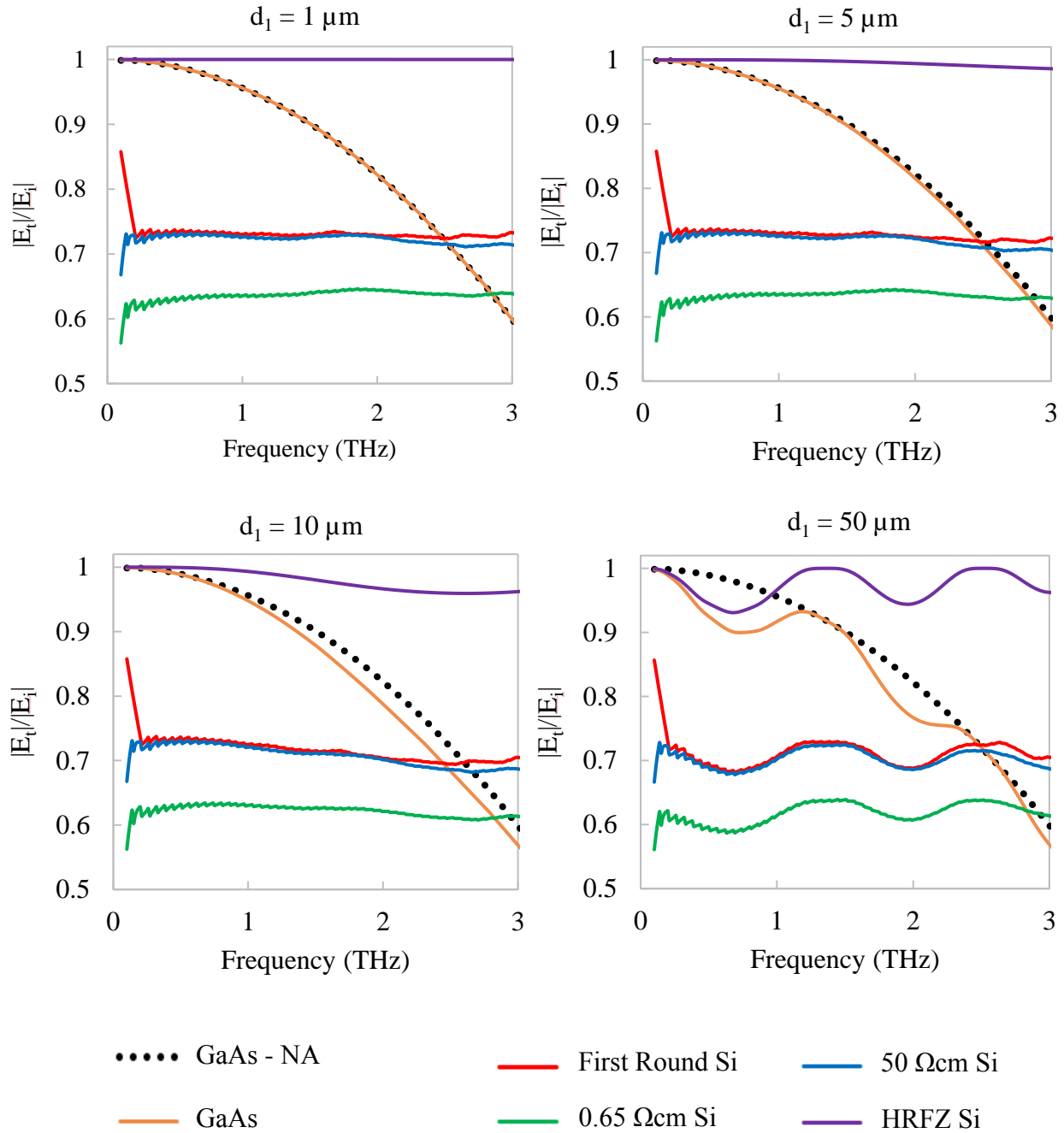


Figure 3.3.3.4: THz transmission through various substrate materials with addition of 1, 5, 10 and 50 μm thick JB Weld Epoxy layers.

In addition to investigating the JB Weld adhesive used in the first round of device fabrication, it was important to also analyze the effect of replacing the JB Weld with SU-8 2000.5 as this was the adhesive proposed to be utilized in the second round of fabrication. Similar to the JB Weld analysis, the SU-8 2000.5 adhesive layer was varied in thickness from 1 μm to 50 μm and the THz transmission was calculated for each. The results of this study are shown in Figure 3.3.3.5.

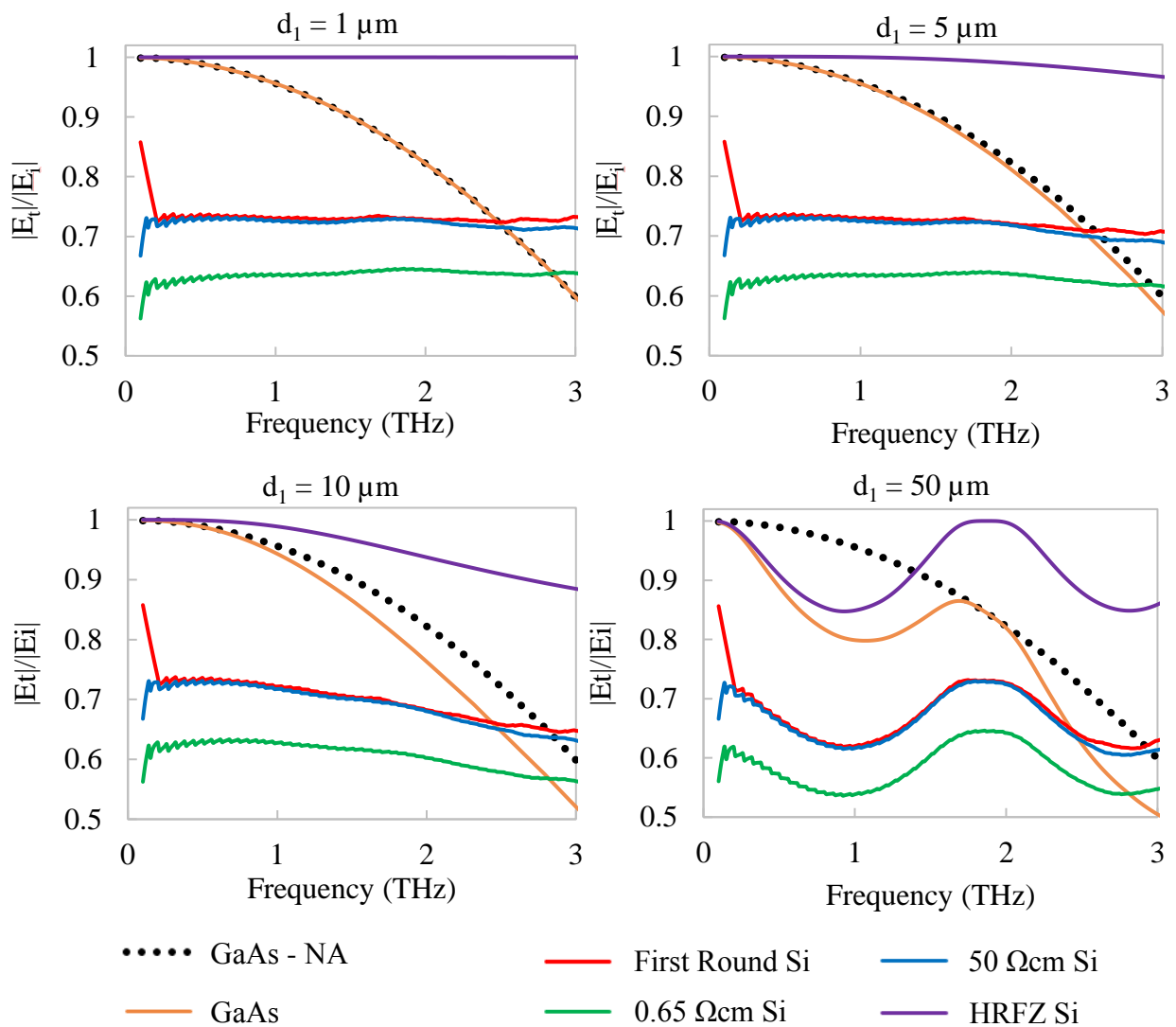


Figure 3.3.3.5: THz transmission through various substrate materials with addition of 1, 5, 10 and 50 μm thick SU-8 2000.5 adhesive layers.

Similar to the JB Weld, no effect is noticed for $d_1 = 1 \mu\text{m}$, but as the thickness is increased resonant oscillation losses begin to increase. For thicknesses of $5 \mu\text{m}$ and above, the losses were notably greater in the SU-8 2000.5 than in the JB Weld, around 15% at some frequencies. This is likely due to the increased mismatch in refractive index of the SU-8 2000.5 as compared to the JB Weld.

The THz property characterization of the materials shown in Figure 3.3.2.2 show that the refractive indices of the substrate materials were 3.4 and 3.56 for the Si and GaAs while the adhesive materials were 2.2 and 1.6 for the JB Weld and SU-8 2000.5, respectively. Since both adhesives had lower refractive indices than the substrates and the SU-8 2000.5 was the lower of the two, it is expected that this increased mismatch in refractive index would contribute to the higher loss in the SU-8 2000.5. However, in addition to having a higher resistivity the SU-8 2000.5 has the added benefit of being much less viscous than the JB Weld. This meant that the SU-8 2000.5 adhesive layer could be made much thinner than the JB Weld, on the order of $1 \mu\text{m}$. Therefore, it was concluded that utilizing SU-8 2000.5 as the adhesive material in the second fabrication round would not contribute to significant THz transmission losses.

In order to verify the conclusions of this simplified model, the COMSOL model described in Section 2.14 of this dissertation was used to also study the effect of varying the substrate material, adhesive material and adhesive thickness. For these studies, the $250 \mu\text{m}$ thick HRFZ Si lens layer was included under the substrate, with the quarter circle electric field evaluation plane placed at a depth of $5 \mu\text{m}$ below the substrate, inside the HRFZ Si lens layer. Since COMSOL is not readily capable of accounting for material dispersion in time domain calculations, the complex electrical properties for the various materials were taken from the measured properties at 1 THz.

Comparison of varying the substrate material with no adhesive (NA) layer present is shown in Figure 3.3.3.6. These results are the frequency spectrum of the pulse transmitted into the Si lens layer, calculated by taking the Fourier transform of the time domain pulse. Across the full 0 to 3 THz range, there is insignificant difference between the HRFZ and LT-GaAs substrates. Between approximately 0.25 and 1 THz the transmitted signal is around 30% lower for the 50 Ω -cm Si substrate and 33% lower for the 0.65 Ω -cm Si substrate. These results are confirmed with those shown in Figure 3.3.3.3 using the analytical model.

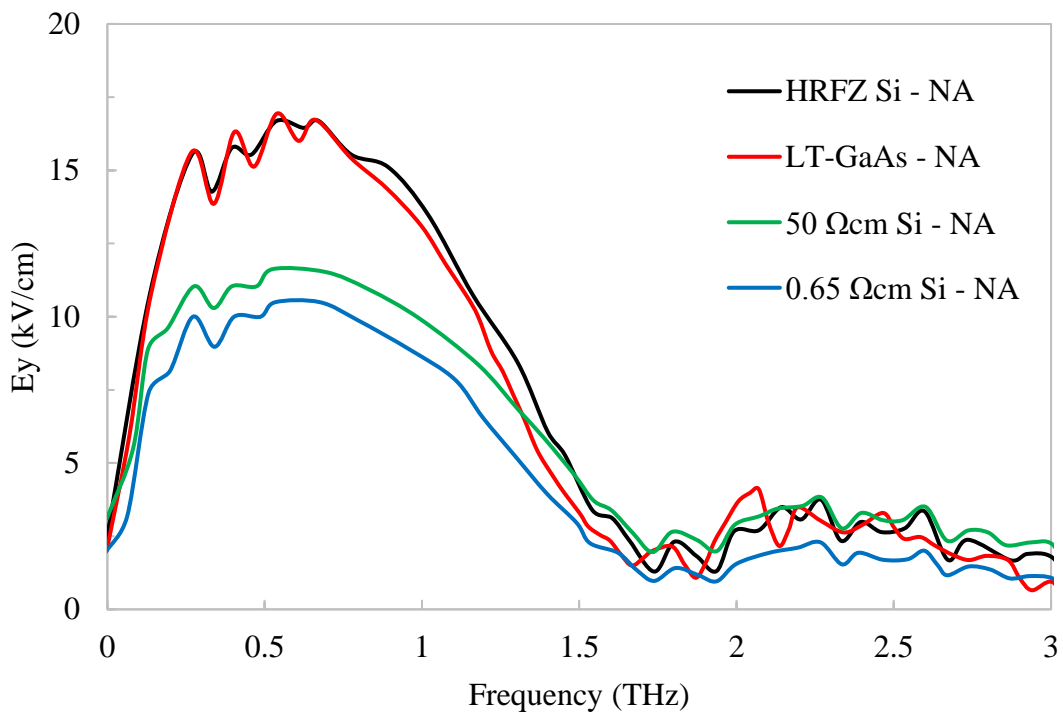


Figure 3.3.3.6: Fourier transform of the electric field transmitted into the Si lens layer calculated using COMSOL[®] for the various substrate materials without adhesive layers.

The model was also used to calculate the transmitted THz spectra for each substrate material while including 5 and 50 μ m thick JB Weld and SU-8 adhesive layers. The results of these calculations are summarized in Figure 3.3.3.7.

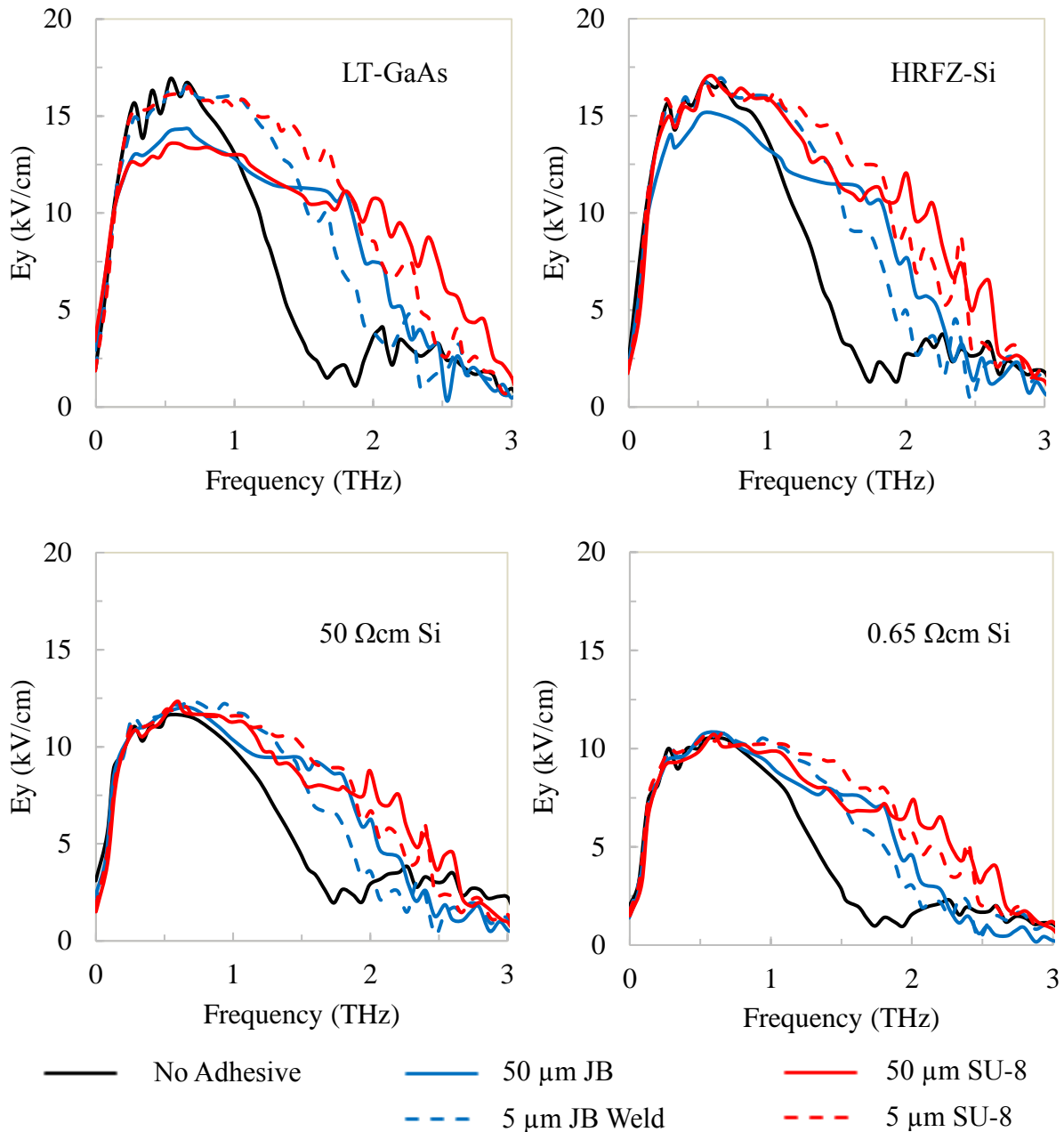


Figure 3.3.3.7: Fourier transform of the electric field transmitted into the Si lens layer calculated using COMSOL[®] for the various substrate materials, with and without 5 (dashed) and 50 (solid) μ m JB Weld (blue) and SU-8 (red) adhesive layers.

Each plot represents a different substrate material, with the black curve indicating the substrate with no adhesive layer, the color indicating the adhesive type, and the line type (solid or dashed) indicating the adhesive thickness. From the results, several trends were observed.

With all substrates, addition of the almost all adhesive layers, regardless of thickness, increased or did not degrade THz transmission across the observed frequency range. The exceptions to this were for the LT-GaAs substrates with both JB Weld and SU-8 adhesives at 50 μm thickness, as well as the HRFZ-Si substrate with JB Weld adhesive at 50 μm thickness. Here, both 50 μm adhesives degraded the transmission for frequencies below 1 THz by about 12% for the LT-GaAs, while the 50 μm JB Weld adhesive on the HRFZ-Si substrate reduced this transmission by about 9%. The increased transmission observed was likely due to the adhesive layers acting as refractive index matching layers. Matching layers are often used to increase transmission at low to high refractive index interfaces. Since the THz refractive index of both adhesives lay between the substrate's refractive indices and air, they could provide the increased transmission observed in the model. Most importantly, these modeled results indicated that THz losses from the adhesive layers was not a likely mode of failure for the first round devices.

In conclusion, the mode of failure analysis indicates that primary mode of failure was the conduction losses in the JB Weld epoxy, due to its lower resistivity as compared to LT-GaAs. Therefore, the remaining devices utilized cured SU-8 2000.5 photoresist as the adhesive due to its high electrical resistivity as compared to LT-GaAs.

3.4. Second-Round of Plasmonic Thin-Film THz Emitter Fabrication

3.4.1. MBE Wafer Growth

The LT-GaAs MBE wafer for the second fabrication found was grown by Dr. John Prineas at the University of Iowa Optical Science and Technology Center. The architecture of the second round MBE wafer and comparison to the original first round wafer is shown in Figure 3.4.1.1. The structure of the growth varied slightly as compared to the first round, mainly in that 10/1 nm AlAs/HT-GaAs was added between the $\text{Al}_{0.85}\text{Ga}_{0.15}\text{As}$ and LT-GaAs layers, as well as increasing

the thickness of the $\text{Al}_{0.85}\text{Ga}_{0.15}\text{As}$ from 200 nm to 300 nm. The AlAs was added as an electrical barrier layer between the LT-GaAs and $\text{Al}_{0.85}\text{Ga}_{0.15}\text{As}$, while the 1 nm HT-GaAs was added to provide a smooth, high quality surface for the LT-GaAs growth. The $\text{Al}_{0.85}\text{Ga}_{0.15}\text{As}$ layer was increased from 200 nm to 300 nm thickness to better protect the LT-GaAs layer during the substrate removal process.

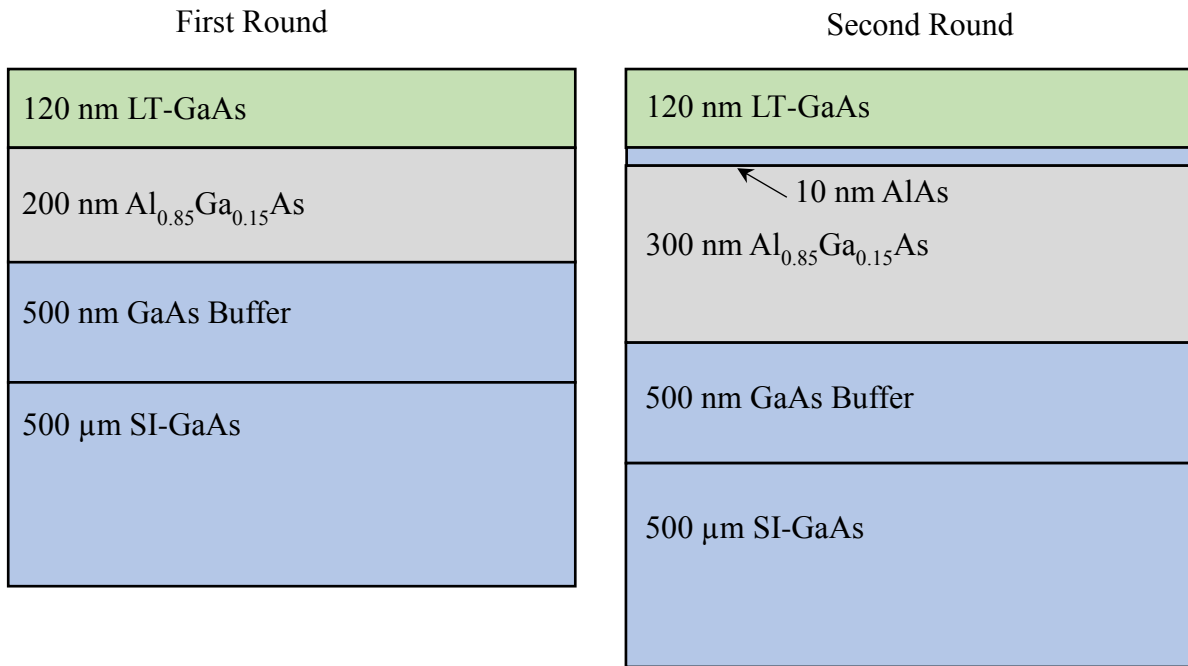


Figure 3.4.1.1: Comparison of the second round MBE wafer structure with the original first round structure.

The LT-GaAs growth temperature was 250 °C with the temperature being controlled/monitored using a thermocouple with a ± 15 °C variation. Post-growth annealing was performed to increase the LT-GaAs resistivity. As discussed in [205], the post-growth annealing of LT-GaAs allows the high resistivity of SI-GaAs to be recovered while maintaining a sub-picosecond carrier lifetime, so long as the anneal temperature is not excessively high. In order to determine the anneal temperature for each wafer, an anneal test was performed. 6 pieces of the LT-GaAs

wafer were cleaved and each was annealed at different temperatures using an AG Associates Heatpulse 610 Rapid Thermal Processor [206]. For all samples the process included a 1-min ramp from room temperature to the anneal temperature, 10-mins steady state hold at the anneal temperature followed by a passive return to room temperature, requiring approximately 10 min. For all samples, there was a maximum 10-30 °C overshoot following the 1-min ramp, which returned to the steady state anneal temperature value after less than 1 min. The anneal was performed in a nitrogen purged environment with the sample LT-GaAs surface placed against a SI-GaAs wafer surface. This was to prevent surface oxidation and outgassing of the As⁺³ precipitates in the LT-GaAs during annealing. For the six samples, anneals were performed at 350, 400, 450, 500, 550, and 600 °C.

Following the annealing, 4 μm gap bowtie dipole antennas were patterned on each sample using the process described in the next section of this dissertation. After patterning, the resistance across the 4 μm gap of each was measured using a HP 4140B picoammeter and voltage source [207]. The I-V characteristics were obtained from 0 to 50 V and the resistance of each was extrapolated by applying a linear fit to each curve. The R² coefficient of determination of the linear fits were >99%, indicating highly linear behavior. Figure 3.4.1.2 illustrates the results of this study. Similar devices have shown the 100-1000 MΩ region to provide the necessary balance between gap resistance and carrier lifetime needed for THz PCA emitters. As such, 525 °C was chosen as the anneal temperature for the remainder of the LT-GaAs wafer.

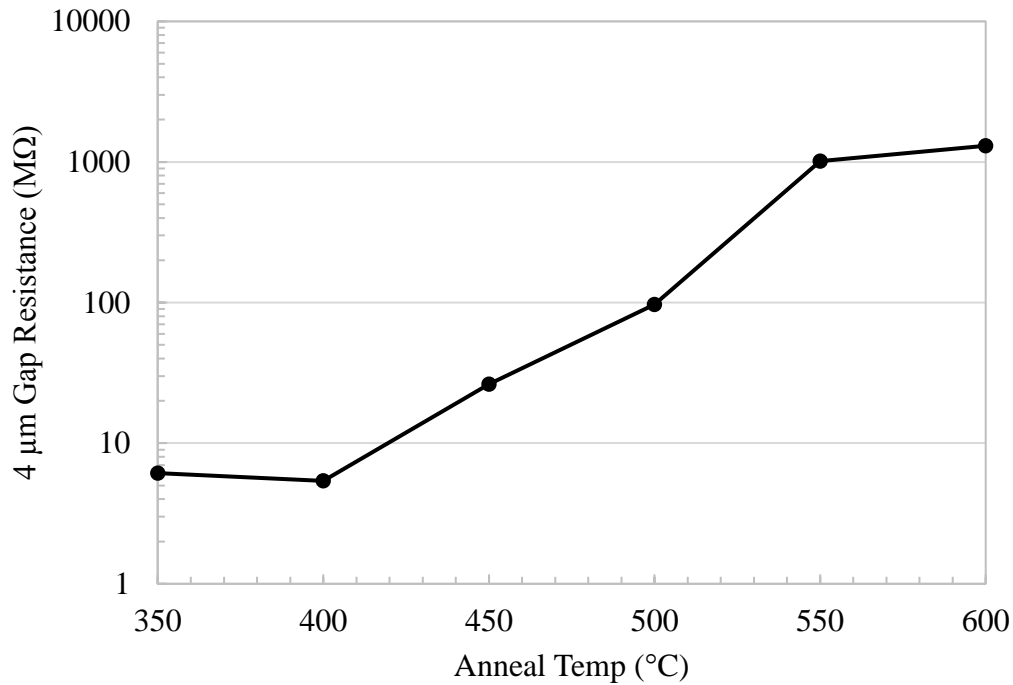


Figure 3.4.1.2: 4 μm gap resistance as a function of 10 min duration anneal temperature.

3.4.2. Photolithography Patterning of the Antenna Electrodes

An improved photolithography process was adopted for the second round of fabrication to address several issues that arose in the first round of fabrication and testing. During testing of the first round devices, one concern was that there could be interference between adjacent devices on the same chip. Therefore, for the second round only, one device was patterned per chip. Since this reduces the total number of devices per wafer, it was important to improve upon the original photolithography process to improve the photolithography success rate. The process that was utilized required a negative photomask, which is illustrated in Figure 3.4.2.1.

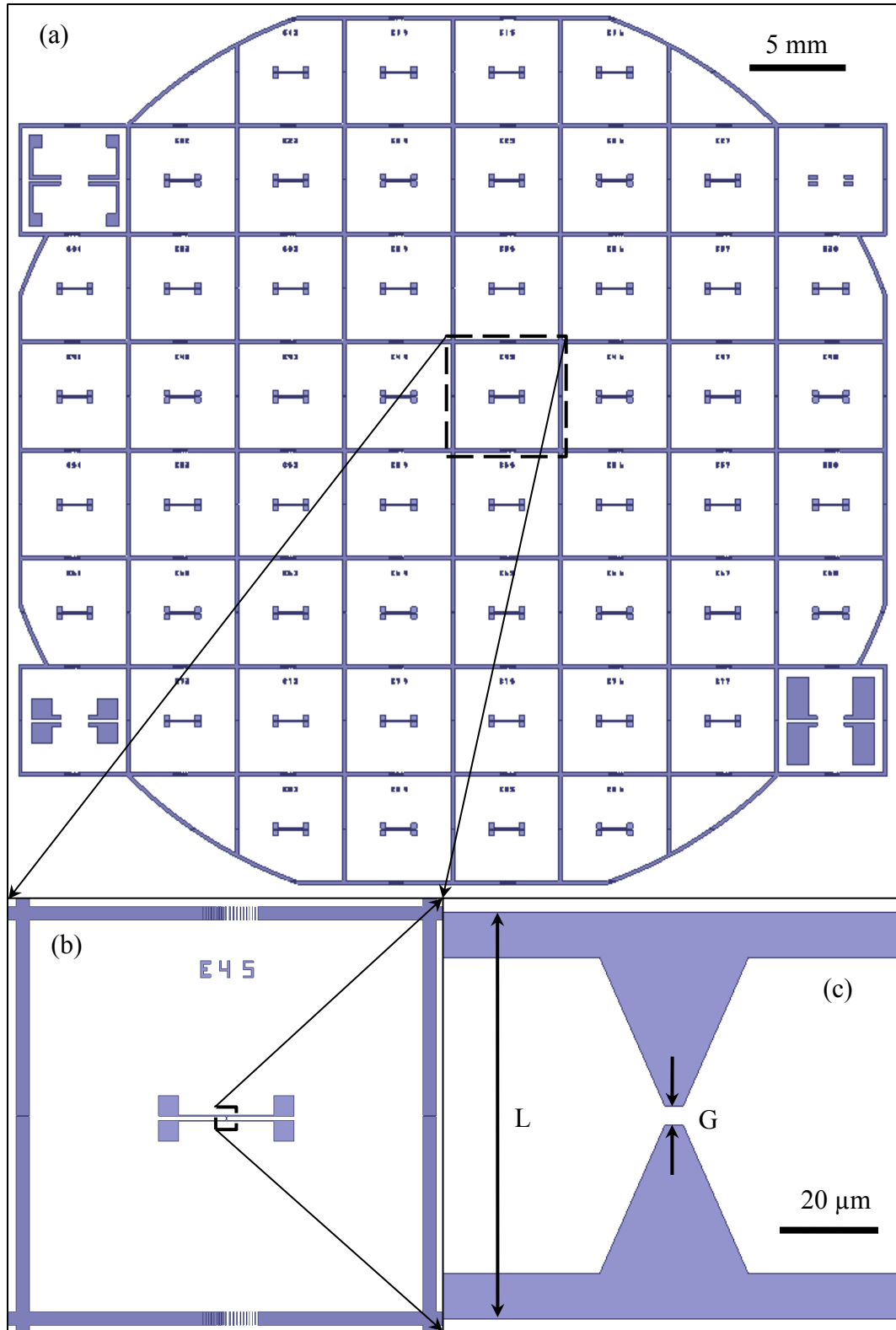


Figure 3.4.2.1: Photomask of the second generation fabrication process. (a) full photomask, (b) single device, and (c) dipole antenna structure.

The structure is similar to the B-90-10 design used in the first round. However, the dipole gap G is reduced to $4\ \mu\text{m}$ and four bias pads are included, two for each electrode. Each device is noted “E-R-C” where “E” stands for “Emitter” (uniform for this mask), “R” stands for the row number (1 through 8) and “C” stands for the column number (1 through 8). For example, Figure 3.4.2.1(b) is notated as “Emitter, Row 4, Column 5”. The mask contains 52 repetitions of the same antenna pattern, plus four other patterns shown in the corners. These additional patterns are for etching through the LT-GaAs to expose the electrode bias pads and four different variations of this pattern were included to potentially add a second metallization process to allow improved success of wire bonding.

As previously discussed, the first round photolithography process led to defects in the pattern due to the positive sidewalls in the photoresist. To prevent this in the second round of fabrication, an image reversal process was utilized to create negative sidewalls in the photoresist. The process is illustrated in Figure 3.4.2.2. If the sample surface required cleaning, a 1-min acetone rinse, 1 min IPA rinse, N_2 blow dry, and $200\ ^\circ\text{C}$ 5 min hotplate bake was performed. AZ5214E was spin-coated at 6000 RPM for 30 s, followed by a 50 s, $90\ ^\circ\text{C}$ hotplate bake. The sample was then placed in the mask aligner and exposed for a time requiring optimization, approximately with half the dose needed for full exposure. The sample was then baked to reverse the image, shown in Figure 3.4.2.2(c). This bake caused the exposed regions of the photoresist to become cross-linked, while the unexposed regions remain unchanged. The baking time was constant at 2 min, and the temperature of the bake required optimization and was critical to the process. The sample was then flood exposed in UV for 20 s, exposing the non-crosslinked region of the resist while leaving the crosslinked region unchanged, shown in Figure 3.4.2.2(d).

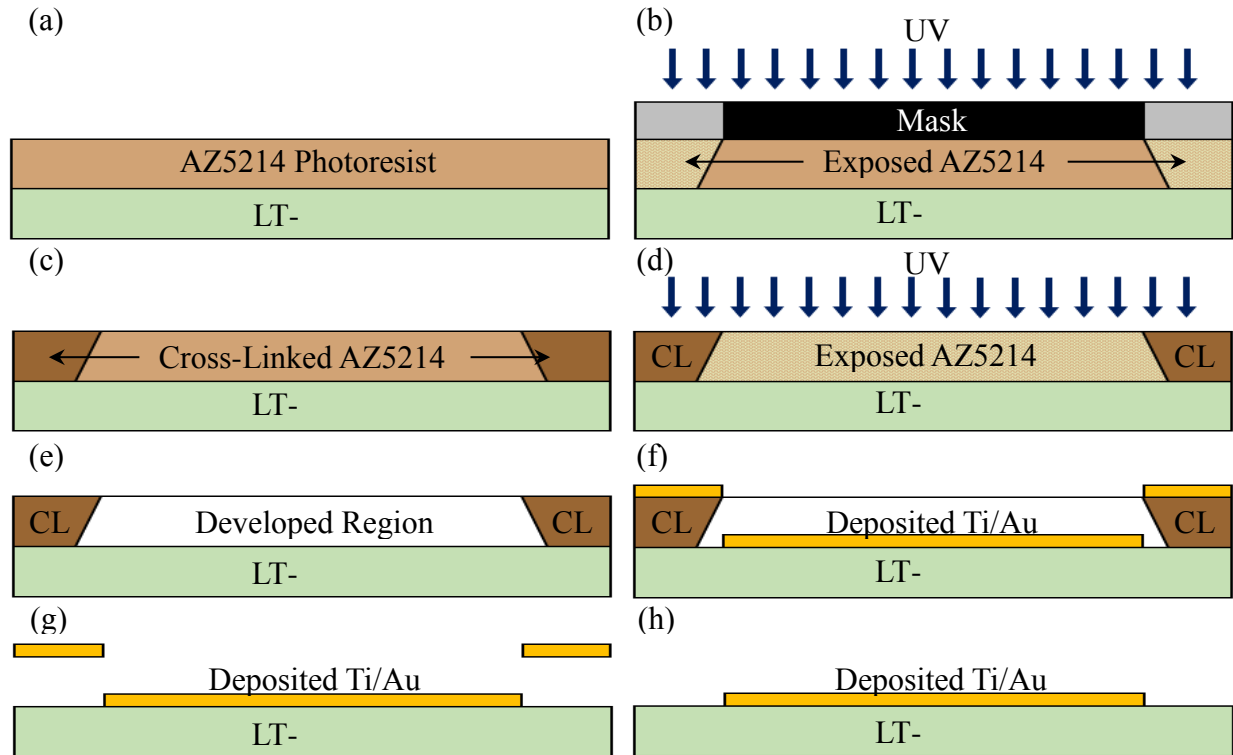


Figure 3.4.2.2: Second round photolithography process implementing the image reversal process to generate negative photoresist sidewalls.

The sample was developed in AZ300MIF for 100 s, shown in Figure 3.4.2.2(e). Here, it was noted that for complete development to occur in 100 s or less, the sample/developer must not remain stagnant. Two methods were observed to work equally well; holding the sample with tweezers and swirling it in developer or using a pipette to regularly spray the sample surface with developer. After development, the sample was continuously rinsed in DI-H₂O for 1 min, blown dry with N₂, and hotplate baked at 90 °C for 60 s. An optional post-development descum in the PE-50 Plasma Cleaner was performed at 200 sccm O₂ and 30 W power for 10 s [192]. The sample was then placed in the Edwards 306 e-beam evaporator and 15/120 nm Ti/Au was deposited at a <0.4 nm/s rate. As shown in Figure 3.4.2.2(f), if a negative sidewall profile was produced and there was no continuity between the metal deposited in the developed (LT-GaAs) and undeveloped (cross linked AZ5214) surfaces. After evaporation, the sample was placed in

acetone to dissolve the cross-linked photoresist, shown in Figure 3.4.2.2(g). If desired, the acetone could be heated to 70 °C for several minutes to speed up the process. Here, it was critical that: 1) the sample was not sonicated, since requiring sonication to lift-off the metal indicates a negative sidewall profile was not obtained; and, 2) the sample was not allowed to dry before complete liftoff, since lifted off metal that has collapsed to the sample surface was very difficult to remove. The sample (still immersed in acetone) could be sprayed with acetone as needed to lift off the metal.

In the above described photolithography process, there were three critical parameters to investigate and optimize; image exposure dose, image reversal bake temperature, and post-development plasma clean. This study included a full factorial optimization study of 6 and 8 s exposure dose, 120, 123, and 125 °C image reversal bake and 0 (none) and 10 s plasma clean time. Samples were prepared as described above, including metallization and liftoff. After liftoff, samples were determined to pass/fail depending on if complete liftoff could be achieved. The results of this optimization are summarized in Table 3.4.2.1. Four of the twelve samples had successful liftoff (pass), while the remainder did not (fail).

Table 3.4.2.1: Optimization results of the second round photolithography process.

Sample Number	Exposure Dose (s)	Image Reversal Bake (°C)	Plasma Time (s)	Results
1	6	120	0	Pass
2	6	120	10	Fail
3	6	123	0	Fail
4	6	123	10	Fail
5	6	125	0	Fail
6	6	125	10	Fail
7	8	120	0	Pass
8	8	120	10	Pass
9	8	123	0	Fail
10	8	123	10	Fail
11	8	125	0	Pass
12	8	125	10	Fail

3.4.3. Wafer Mounting and Substrate Removal

For the second round of device fabrication, the JB Weld epoxy adhesive was replaced with an SU-8 2000.5 photoresist adhesive. SU-8 can be baked at high temperatures in order to cure and raise the glass transition temperature of the polymer. After cleaning with acetone and IPA the HRFZ Si substrates were brought to 100 °C via hotplate, followed by deposition of the SU-8 to the surface as shown in Figure 3.4.3.1 (left).

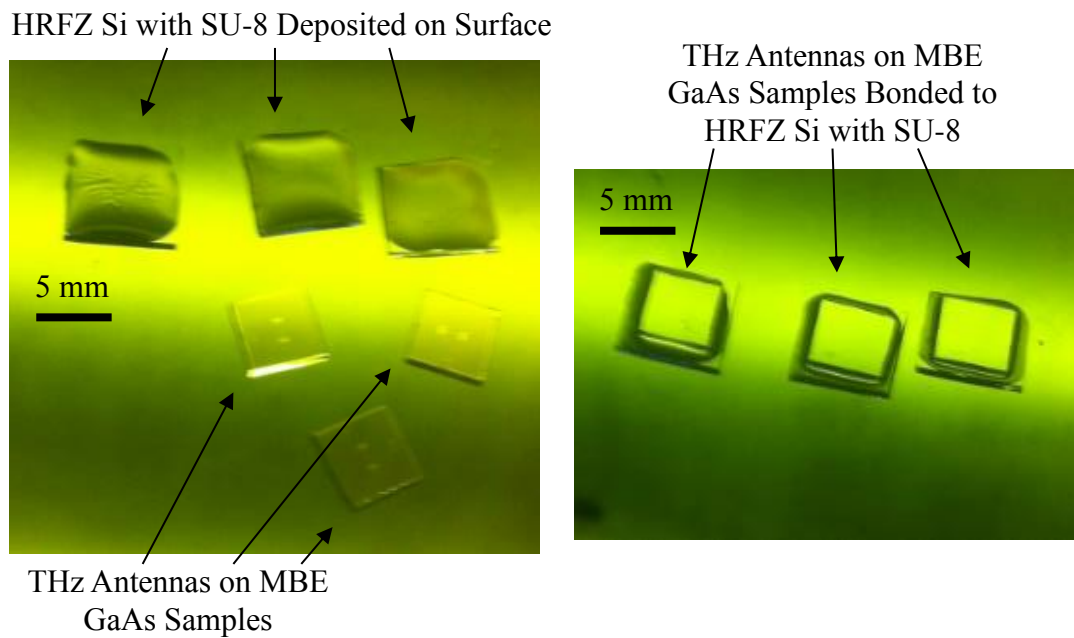


Figure 3.4.3.1: Photograph of the bonding of THz antennas on MBE GaAs sample to the HRFZ Si substrates prior to GaAs substrate removal.

The SU-8 was pre-cured at this temperature for 15 min, during which time the THz antennas on the MBE GaAs samples were cleaned and brought to 100 °C temperature. The THz antenna samples were then placed antenna side down onto the SU-8 coated HRFZ Si substrates as shown

in Figure 3.4.3.1 (right), with slight tweezer pressure used to ensure contact. The temperature was then raised to 180 °C and held there for 30 min to fully cure the SU-8. Finally, the hot plate temperature was lowered and the samples were allowed to gradually return to room temperature. Differential micrometer measurements before and after bonding indicated an SU-8 bonding layer thickness of approximately 5 μm.

Following wafer bonding, the SI-GaAs substrate, Al_{0.85}Ga_{0.15}As etch stop, and AlAs isolation layers were removed. Previously this was accomplished by a combination of mechanical lapping to thin the wafer to <100 μm, followed by chemical etching with NH₄OH:H₂O₂ and HCl. However, trials using only the chemical etching to remove the SI-GaAs layer demonstrated that this could be accomplished without mechanical lapping and in a shorter time period of less than one hour. Therefore, the process for the substrate removal was the same as the first round devices, only with no mechanical lapping and a longer NH₄OH:H₂O₂ chemical etching time.

3.4.4. Device Packaging

In order to provide an electrical connection to the antenna electrodes with enough mechanical strength to support wire bonding, a second lithography and metal evaporation process was included to extend the SU-8 supported electrodes to the Si substrate surface. Prior to this step, the antenna electrodes were located on a 5 μm thick cured SU-8 layer. This SU-8 layer did not provide enough support for the wedge bonding used to electrically connect to the device. This was the same problem in the first round of devices that led to using conductive epoxy to connect to the devices. Therefore, an alternative solution was developed.

First, the SU-8 and LT-GaAs layer were removed by hand from all of the regions surrounding the device, thus exposing the Si substrate surface in these regions. Using the same

photolithography process described in Section 3.4.2, photoresist was spin coated, exposed, and developed to produce the pattern on the sample surface shown in Figure 3.4.4.1. Here, all of the sample surface is covered in photoresist except for the dark blue regions. These regions would become the extensions of the antenna electrodes off of the SU-8 and onto the Si surface. Before the metal was evaporated to produce the electrode extensions, the sample was submersed in the $\text{NH}_4\text{OH}:\text{H}_2\text{O}_2$ etch solution to remove the LT-GaAs in the exposed (dark blue) regions. If this step were not done, there would be a layer of LT-GaAs in between the antenna electrodes and electrode extensions. After the etching, 25/300 nm of Ti/Au was evaporated followed by acetone liftoff to produce the desired electrode extensions.

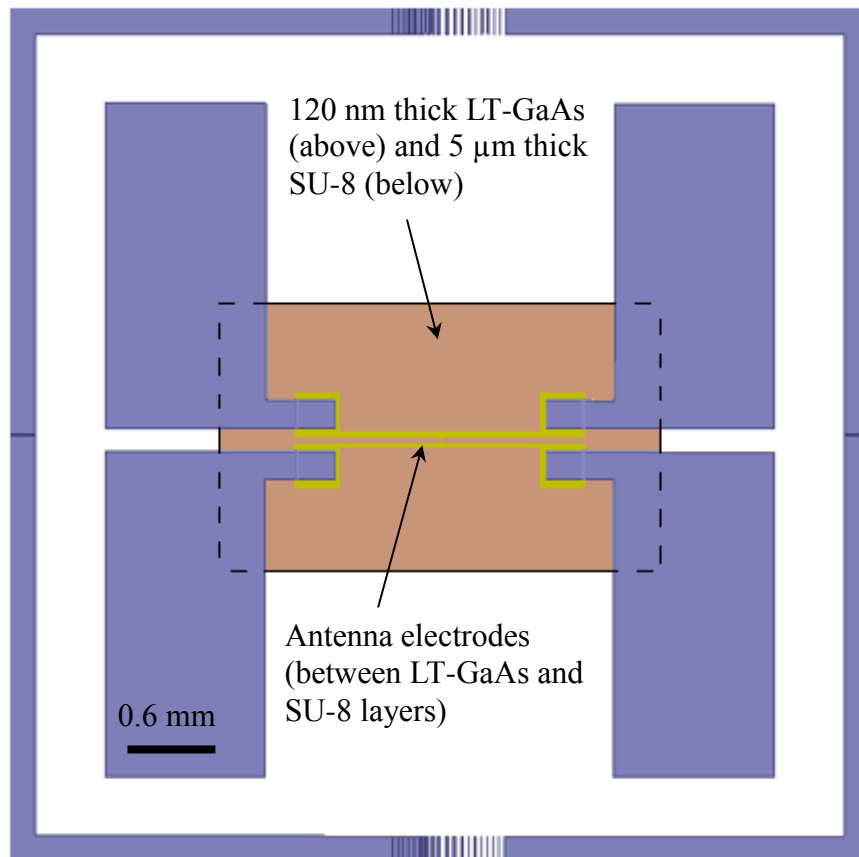


Figure 3.4.4.1: Illustration of the photolithography pattern utilized to extend the antenna electrodes onto the Si surface of the sample.

The devices were then mounted with epoxy antenna side down to the back side of standard leadless chip carriers (LCC) with 5 mm center cut holes. Wire bonding using a wedge bonder was performed to connect from the device surface to the LCC electrodes. Images of the final packaged P-BLTF device are shown in Figure 3.4.4.2.

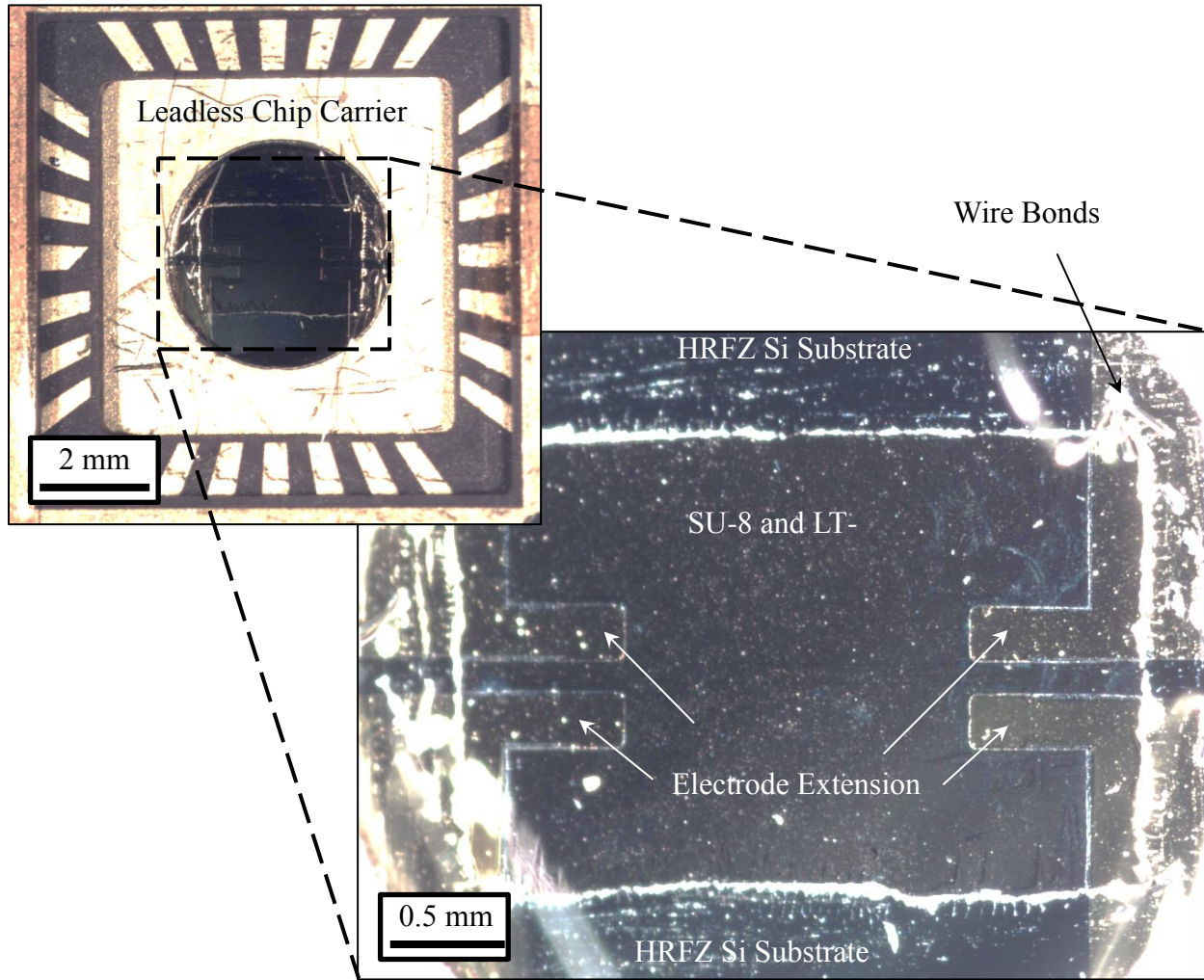


Figure 3.4.4.2: Image of the final device mounted to the leadless chip carrier and zoomed image of the device surface. Antenna electrodes under the LT-GaAs layer are not visible due to limitations of the microscope used to acquire this image.

Chapter 4. Experimental Characterization of the Fabricated Devices

This chapter presents the experimental characterization of the second round of fabricated THz PCA emitters. Several devices of different types were fabricated, each being designated C# for the modified convention, T# for the thin-film without plasmonics, and P# for the thin-film with plasmonics. Here, “#” represents the device number. 20 total devices were fabricated, 7 “C” devices, 7 “T” devices, and 6 “P” devices. Devices C1-5, T1-5 and P1-4 were shipped to Teraview LTD for spectral characterization. Devices C6, C7, T6, T7, P6 and P7 were tested at the University of Arkansas in Dr. Shui-Qing Yu’s optoelectronics lab using the experimental setup by the candidate to measure their total THz output power, as will be discussed in the following section.

4.1. Pyroelectric Detection of Relative Emitted THz Power

Characterization of the average output THz power of the fabricated devices was performed using pyroelectric detection. The experimental configuration is illustrated and photographed in Figure 4.1.1. A wavelength tunable pulsed Ti:Sapph laser with a 100 fs pulse duration was tuned to 800 nm to excite the THz PCA under test. The laser pulse was chopped at a 25 Hz rate and 50% duty cycle to allow lock-in detection with the pyroelectric detector. The beam passed through a neutral density filter (NDF) to attenuate the beam power. A beam expander was then implemented using a plano-concave and plano-convex lens system with focal lengths $F = -27.0$ mm and $F = 125$ mm, respectively. Adjustable pinholes before and after the beam expander allowed the beam size to be adjusted as well as allowing unwanted secondary reflections to be removed from the beam path to the device.

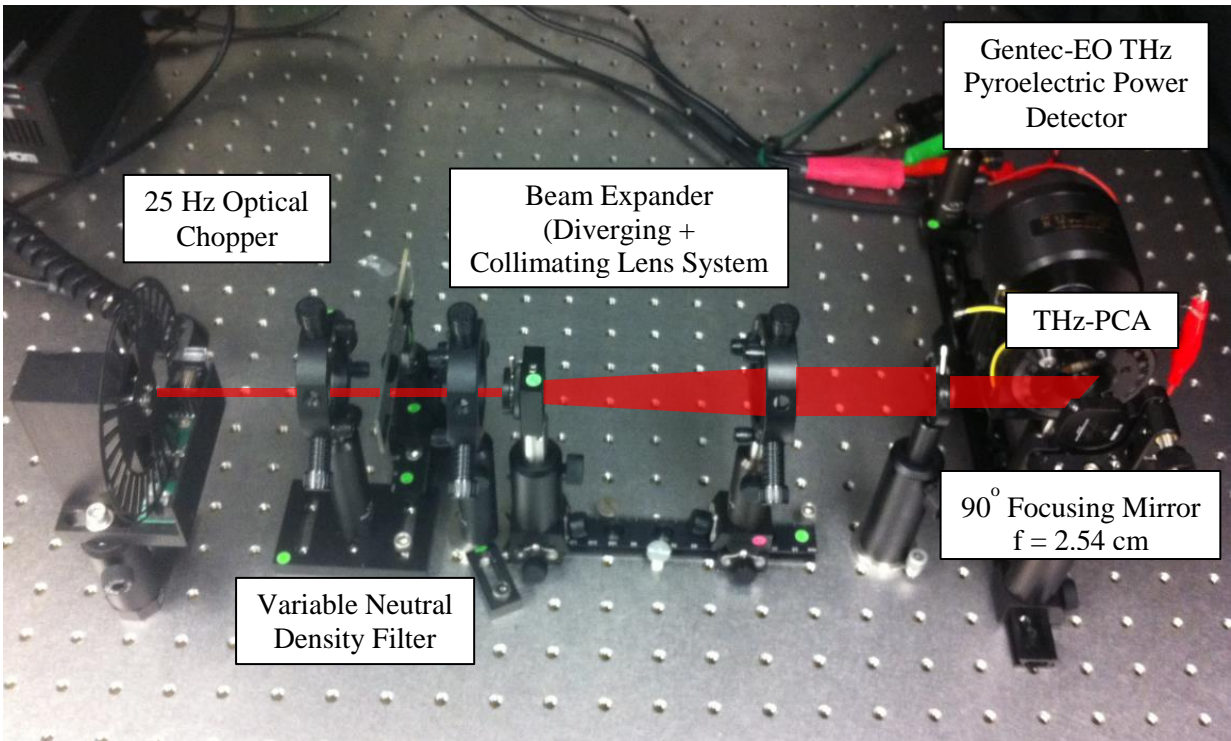
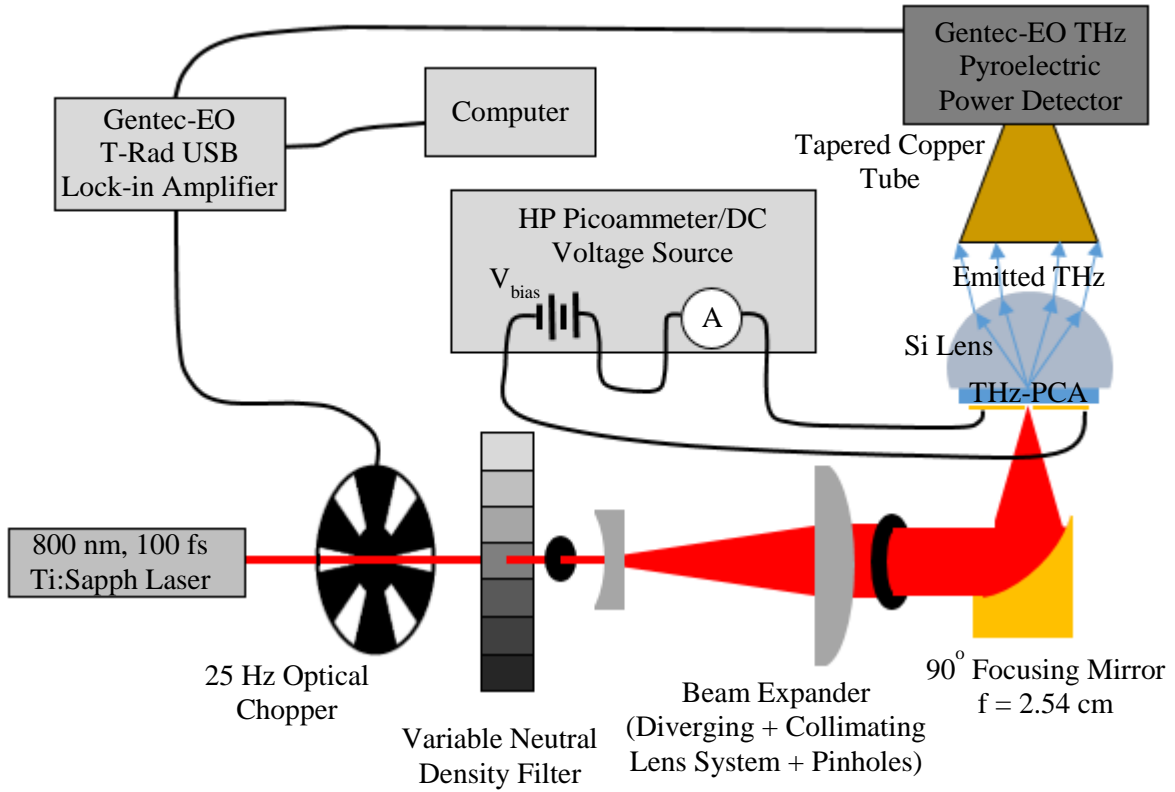


Figure 4.1.1: Illustration (top) and photograph (bottom) of the experimental setup for pyroelectric detection of the average output THz power of the devices.

An off-axis 90° parabolic focusing mirror with $F = 25.4$ mm focused the beam to a diffraction limited spot with a diameter that could be varied by changing the beam width at the second pinhole. The THz PCA sample was mounted to an x-y-z translation stage to allow the focused optical beam to be aligned to the device gap. The radiation emitted from the THz PCA was collected by a HRFZ Si lens and collected by a tapered copper tube, which reflected the THz radiation onto the active area of the pyroelectric power detector. The detector, a Gentec-EO THz Pyroelectric Power Detector, was connected to a Gentec-EP T-Rad USB digital lock-in amplifier interface [208]. This allowed for direct connection of the interface to a laptop computer so that the emitted THz power levels could be directly measured. Voltage biasing and photocurrent measurements of the THz PCAs were performed simultaneously using an HP Picoammeter/DC Voltage Source [207].

Alignment of the optical beam to the THz antenna gap was not trivial as the beam size at the focal point was around $5 \mu\text{m}$ and the antenna gap size was $4 \mu\text{m}$ by $4 \mu\text{m}$. In order to align the beam, a method was implemented to visualize the surface of the THz PCA using the back reflection of the optical beam. This is illustrated in Figure 4.1.2. Here it was noted that at the THz PCA surface part, of the incident optical beam will be reflected backwards towards the parabolic mirror. By placing a glass plate in the beam path to split the beam, the reflected component of the beam can be aligned off the optical axis and imaged onto another surface. Using an IR viewer this allowed the magnified image of the reflected surface to be visualized. Higher reflectivity of the antenna electrodes provided the necessary contrast to locate the dipole and align the focused optical beam to the dipole gap.

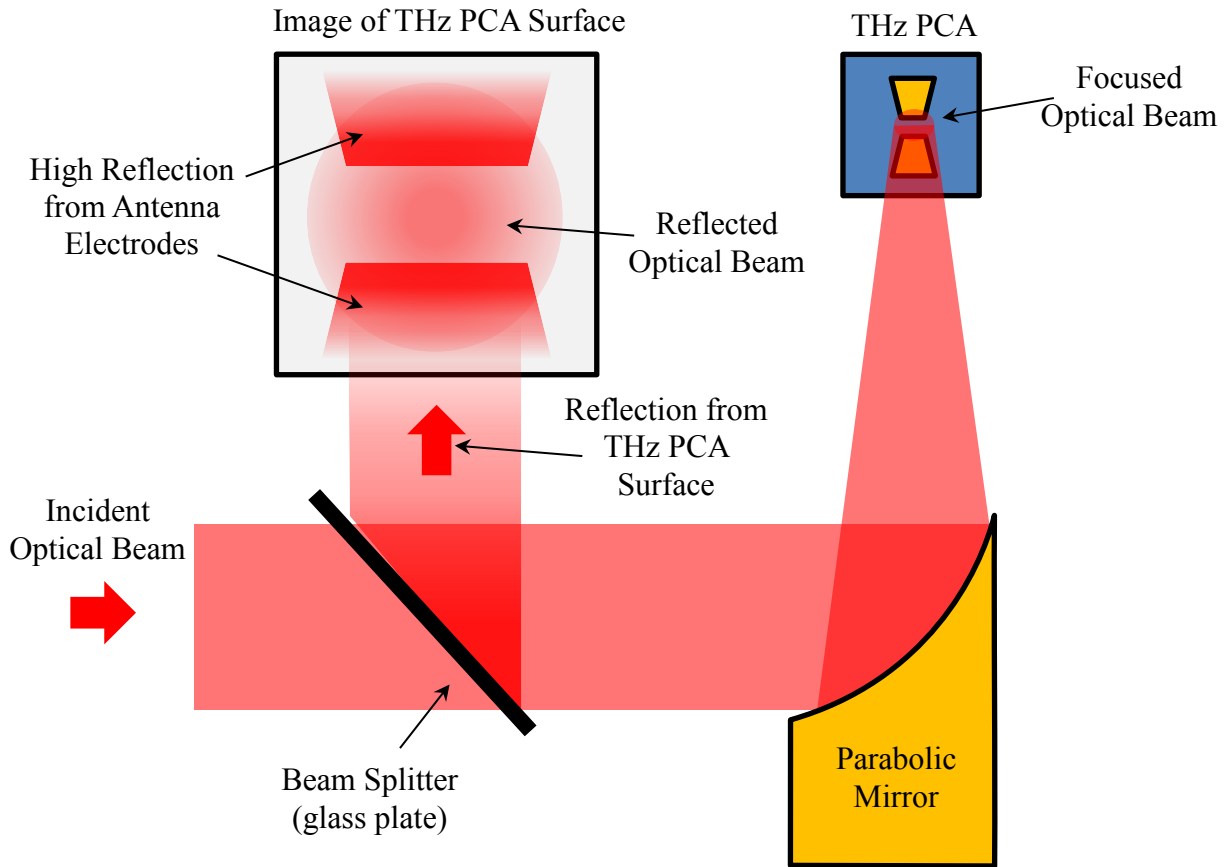


Figure 4.1.2: Illustration of the method utilized for visualizing the focused optical excitation beam location on the THz PCA surface.

The output THz power of each of the three device designs measured by pyroelectric detection is shown in Figure 4.1.3. Devices C6, T6, and P6 are shown as C7, T7, and P7 did not provide measureable THz power above the 20 nW noise floor of the detector, likely due to device failure at some point in the fabrication or packaging. Measurements were taken at 50 V bias voltage with the optical beam aligned to the dipole gap and tuned to maximize the output THz power. The measurement results showed peak THz power of 0.58 μW for C6 and 2.43 μW for both T6 and P6, all at the highest tested optical pump power of 13.4 mW. All devices demonstrated significant saturation of the measured THz power with increasing optical pump power.

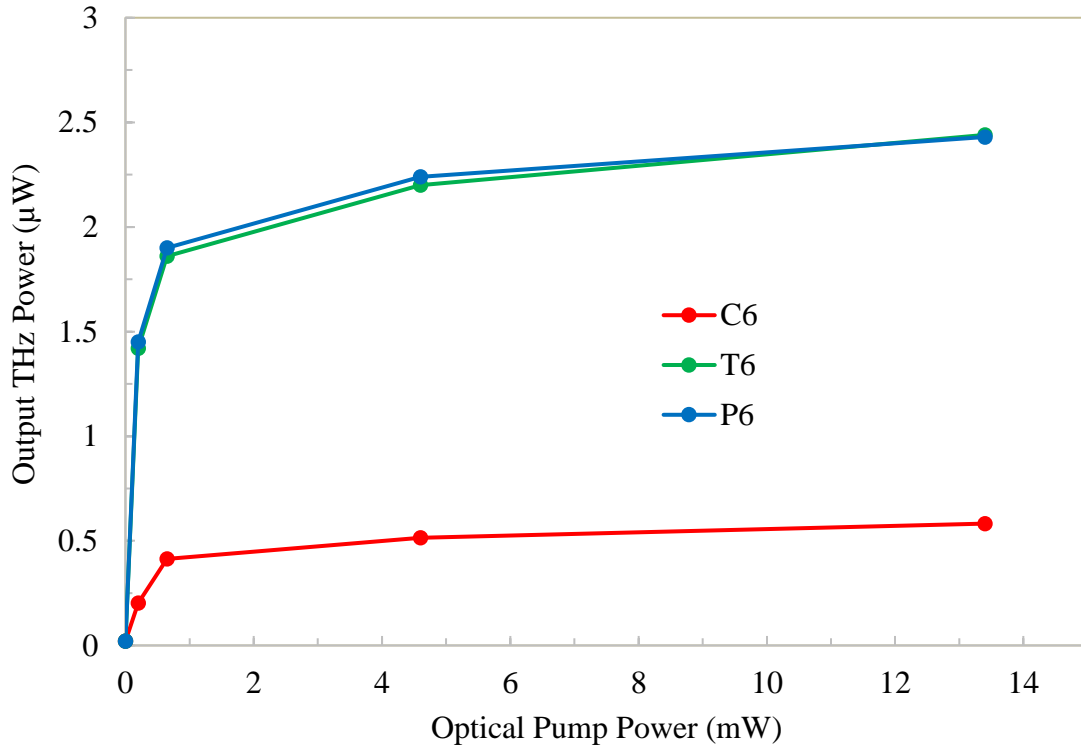


Figure 4.1.3: Output THz power versus optical pump power for devices C6 (red), T6 (green) and P6 (blue).

From the output THz power measurements, the optical to THz conversion efficiency was calculated by taking the ratio of the THz power to optical pump power. The result of this analysis is shown in Figure 4.1.4. Again, the performance of T6 and P6 nearly overlap, while C6 was significantly lower. The highest conversion efficiency of around 0.73% was observed in devices P6 and T6 at the lowest optical pump power of 0.2 mW. The highest conversion efficiency of C6 was 0.1% and also occurred at the lowest optical pump power. The increase in conversion efficiency with decreasing optical pump power occurred due to the reduction in carrier screening. As discussed in Section 2.13 of this dissertation, optically induced carriers increase the total carrier concentration of the material. This leads to a change in the complex refractive index, which in turn increases the reflection from an air-photoconductor interface. At the higher optical

pump powers, this surface reflection loss was greater as indicated by the low conversion efficiency.

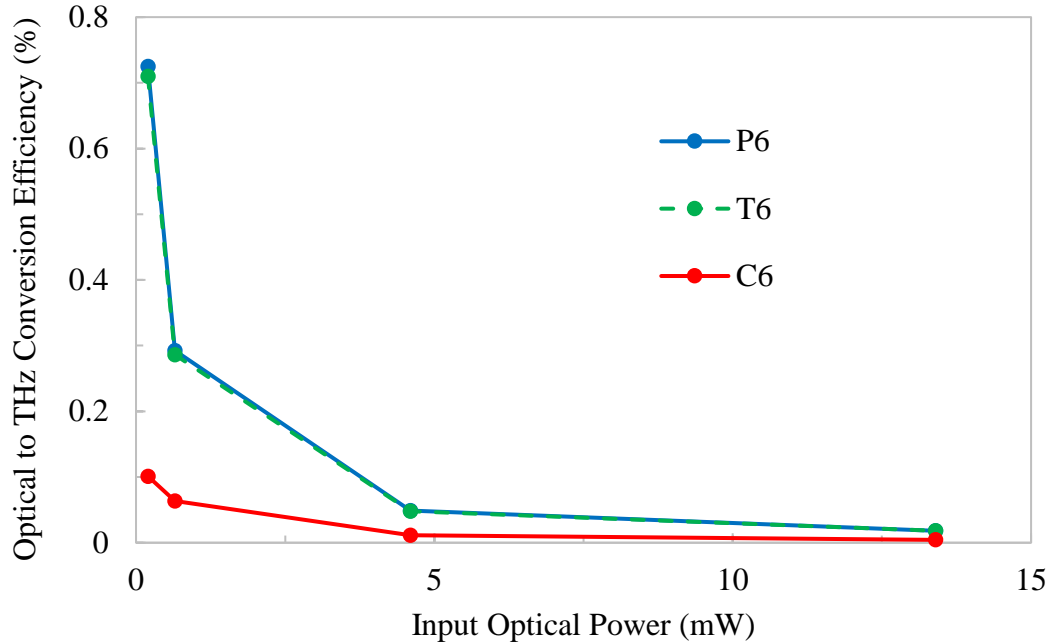


Figure 4.1.4: Optical to THz conversion efficiency versus optical pump power devices C6 (red), T6 (green) and P6 (blue).

4.2. Methods for Analyzing the THz Spectral Characteristics

THz spectral characterization of the fabricated devices was performed at Teraview LTD in a standard THz time-domain spectroscopy configuration, such as that illustrated in Figure 1.1.2.2. In all cases, the optical pump was a 780 nm wavelength, 100 fs pulse width beam focused to a 5 μm spot size. The bias voltage was a variable magnitude AC 1000 kHz square wave, which allowed the antenna to be driven at a bias higher than the DC breakdown voltage. The detector was a conventional 2 μm gap bowtie dipole antenna on LT-GaAs, one of Teraview's own fabricated devices. The optical pump power for gating the detector was 5 mW. This configuration allowed the time-dependent emitted THz field to be directly measured and the

Fourier transform frequency spectrum to be calculated, as shown in the example measurement of device C2 in Figure 4.2.1.

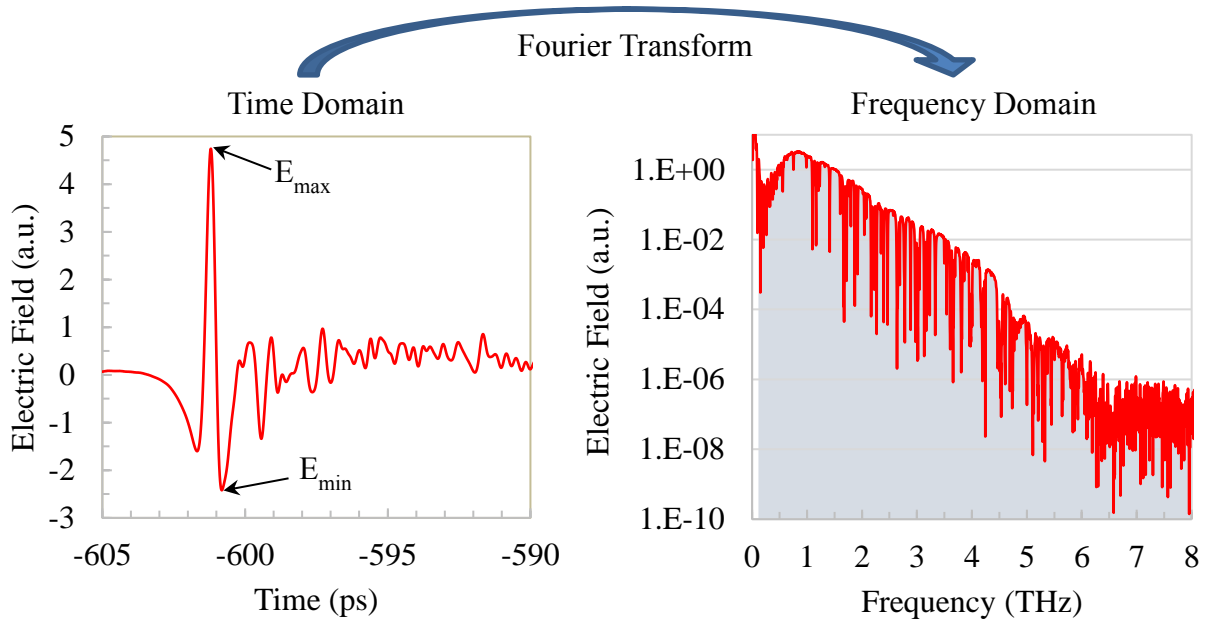


Figure 4.2.1: Measured time-dependent electric field waveform of a THz pulse emitted from device C2 (left) and frequency spectrum acquired from the Fourier transform (right).

In order to quantify the strength of the emitted THz signals, two methods were considered. The first method was measurement of the peak-to-peak THz electric field time-domain signal defined as,

$$E_{pp} = E_{max} - E_{min}. \quad (\text{Equation 4.2.1})$$

E_{max} and E_{min} were the maximum and minimum values of the measured pulse electric field from the time domain data, as indicated in Figure 4.2.1. In addition to E_{pp} , the total THz power was evaluated from the Fourier transform spectra and is defined here by,

$$P_{THZ} = \int_{0.1 \text{ THz}}^{8 \text{ THz}} |E(f)|^2 df. \quad (\text{Equation 4.2.2})$$

Here, $E(f)$ was the frequency dependent Fourier transform of the measured time-domain data. The spectra were integrated from 0.1 THz to the maximum frequency of 8 THz, as shown in the grey shaded area in Figure 4.2.1. 0.1 THz was chosen as the minimum of the integration range since this is often referred to as the beginning of the THz band. Starting the integration at 0.1 THz therefore removed any low frequency contributions to the calculation. Important to note was that all measured values were not calibrated, therefore will be designated in terms of arbitrary units (a.u.).

Since the measurements were obtained in an open air THz TDS configuration, water absorption lines were present in all measured data. When comparing multiple spectra on the plot, the water lines made differentiating between curves visually difficult. This issue was addressed by considering only the top profile of the spectra, as illustrated in Figure 4.2.2. In addition to removing the water absorption lines, the approximate system noise region is illustrated in the shaded gray.

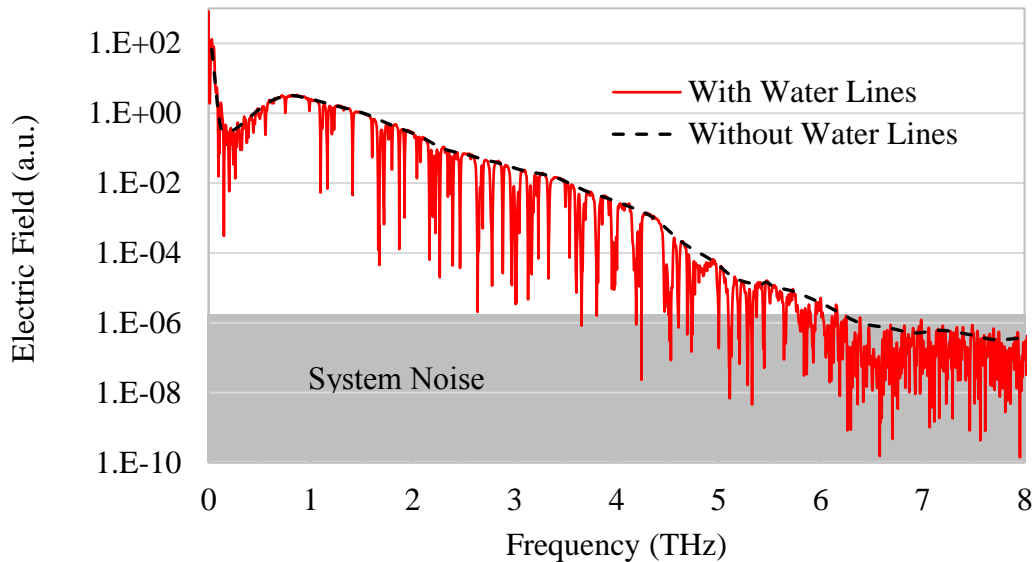


Figure 4.2.2: Frequency spectrum of the measured time-dependent electric field waveform of a THz pulse emitted from device C2 with (red solid) and without (dashed black) water absorption lines present in the trace.

The final consideration for characterization of the fabricated THz emitter devices was alignment in the THz TDS setup. The main issue addressed is illustrated in Figure 4.2.3.

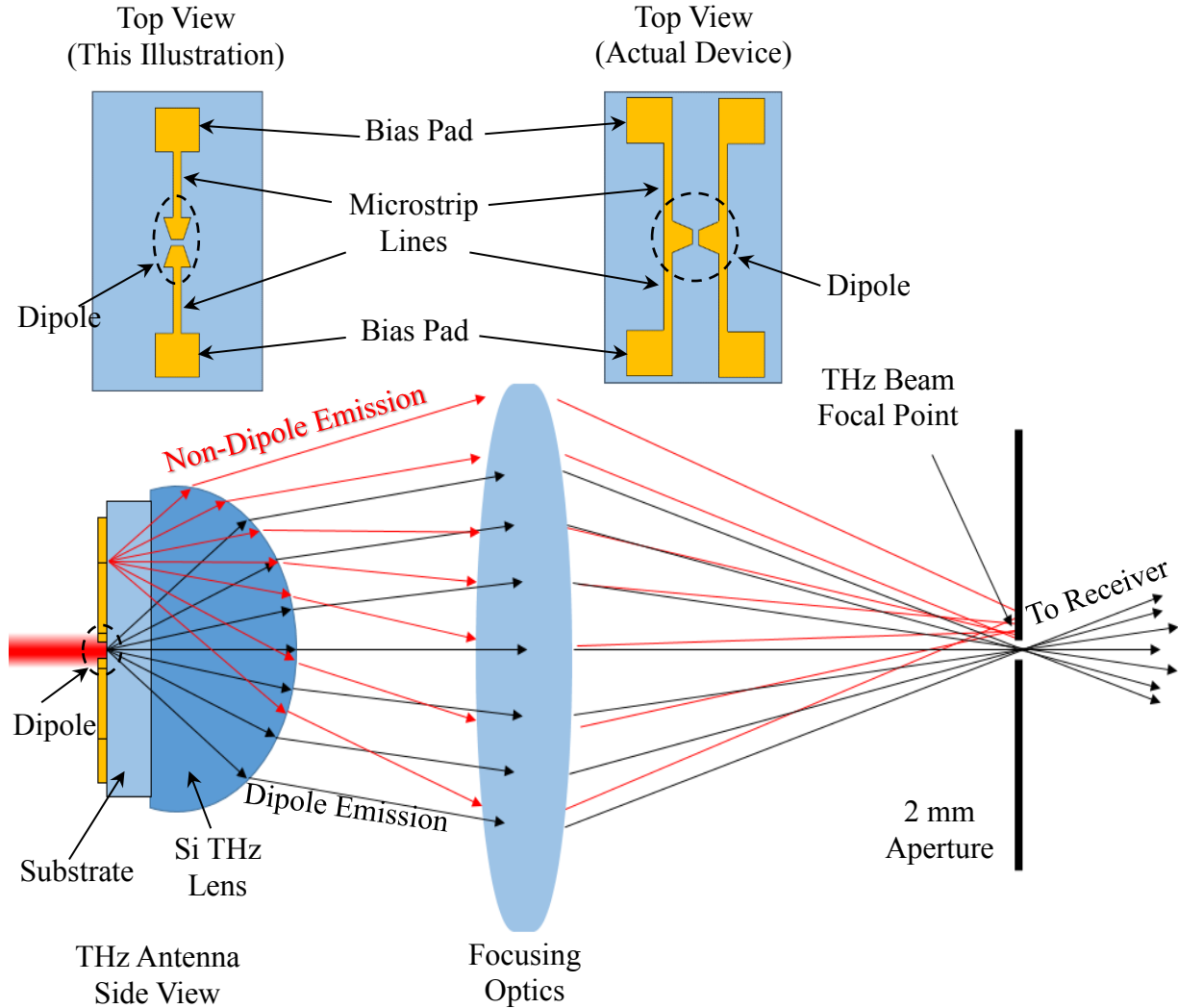


Figure 4.2.3: Illustration of the method for utilizing a 2 mm aperture to prevent non-dipole THz emission from reaching the receiver.

First, consider the top views for this illustration (left) and the actual device (right). This illustration considered a THz dipole antenna that is in line with the microstrip bias lines, while the actual devices had THz dipoles perpendicular to the microstrip bias lines. This difference was made for this illustration so that in the device side view, the location of the dipole with respect to

the microstrip and bias pads could be observed. In the THz antenna side view, the incident optical pulse is focused on the antenna dipole, which then emitted THz radiation from this point (black traces) through the substrate, lens, THz focusing optics, and into the THz receiver (not shown). However, since the optical pulse excites surface currents in the metal, radiation can be emitted from regions elsewhere on the antenna electrodes, illustrated by the non-dipole emission (red trace). The illustration shows how THz emission from non-dipole regions will be out of focus with respect to the dipole emission. This out of focus, non-dipole emission can lead to interference when attempting to align the THz focusing optics to the dipole emission.

Additionally, inclusion of non-dipole emission has the potential for causing phase interference at the receiver. To overcome this, some measurements were taken with a 2 mm aperture at the THz beam focal point. As shown in Figure 4.2.3, the aperture will block much of the out-of-focus THz emission, ensuring that the majority of the received emission comes from the dipole.

4.3. Spectral Characterization in a THz Time-Domain Spectroscopy System

The following section provides a presentation and analysis of the measured THz spectra of each device in the approximate chronological order in which they were obtained. The analysis started with the characterization of devices C2, T2 and P2. The measurements of the time-domain THz pulses of each device are shown in Figure 4.3.1. For all devices the optical pump power was 5 mW, the bias voltage was 50 V, and no aperture was utilized. Comparing E_{pp} , C2 was the lowest at 7.16, T2 was 2.34 times higher at 16.73, and P2 was 4.77 times higher than C2 and 2.04 times higher than T2, at a value of 34.15. All devices had similar waveform shapes with sub-picosecond pulse widths.

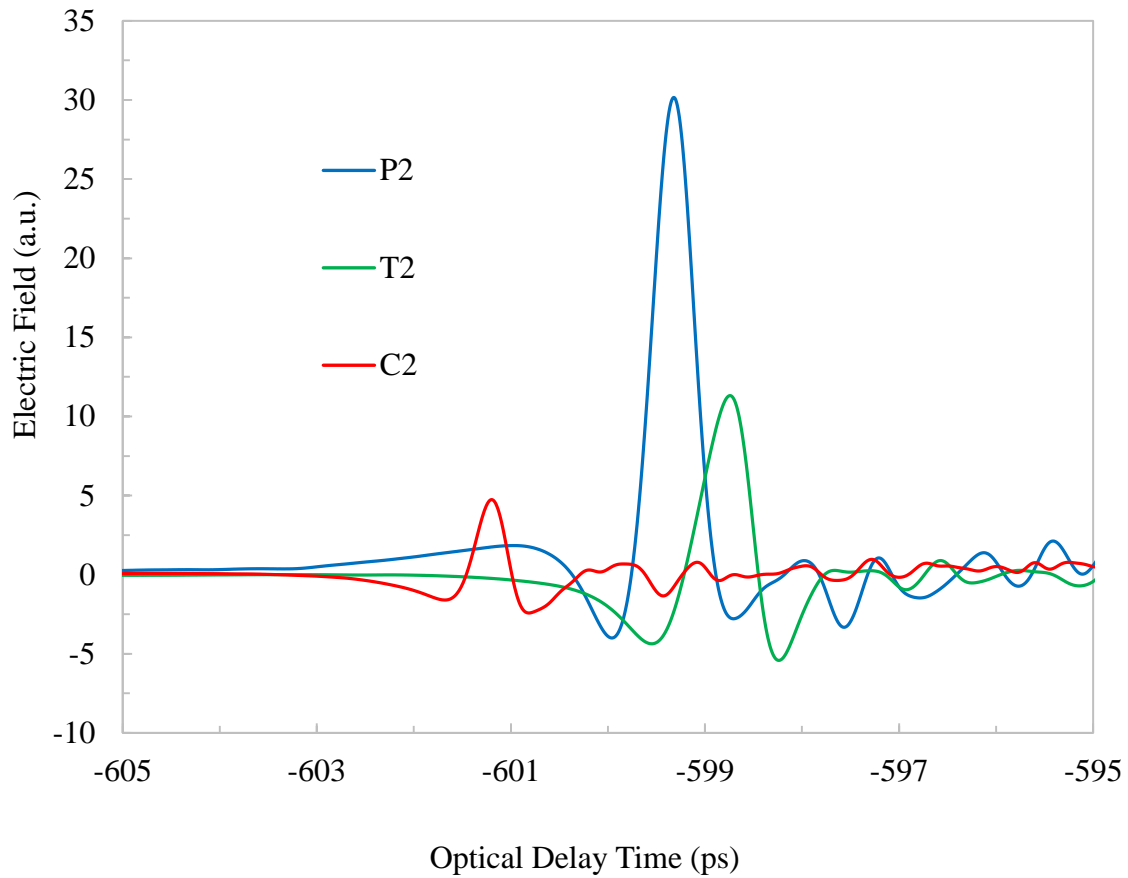


Figure 4.3.1: Time-domain measurements of the emitted THz pulses from devices C2 (red), T2 (green) and P2 (blue) under 5 mW optical excitation and 50 V bias voltage.

The Fourier transform spectra of the time-domain data of Figure 4.3.1, with water absorption lines removed are shown in Figure 4.3.2. All devices had measurable THz signal above the system noise floor up to or beyond 5 THz. In the lower THz frequency range, the trend follows that which was observed in the time-domain data with C2 having the lowest THz field and P2 having the highest. The peak THz field (not including the sharp low frequency increase) was around 3.0 for C2, 22.4 for T2, and 83.6 for P2. At higher frequency, P2 remained greater than T2, however, the THz field of C2 surpassed that of T2 and P2 at frequencies above 1.51 THz and 2.2 THz, respectively.

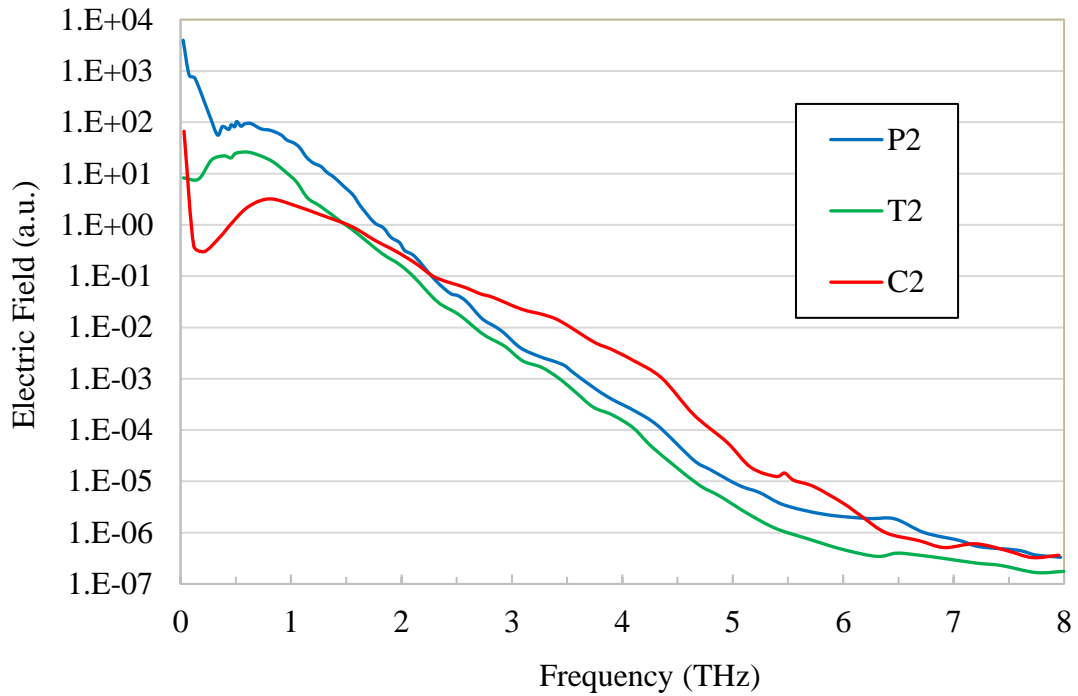


Figure 4.3.2: Fourier transform spectra of the time-domain measurements of the emitted THz pulses from devices C2 (red), T2 (green) and P2 (blue) under 5 mW optical excitation and 50 V bias voltage.

Next, the THz time-domain signals and frequency-domain spectra of devices C2, T2, and P2 were measured as a function of optical pump power at fixed bias voltages. The time-domain signals and frequency-domain spectra of device C2 for optical pump power varied from 2.5 mW to 10 mW at 75 V bias voltage are shown in Figure 4.3.3. At 2.5, 7.5, and 10 mW the spectra had similar trends, with the 7.5 and 10 mW spectra both being greater than the 2.5 mW spectra, but no notable difference between 7.5 and 10 mW. The 5 mW spectrum differed from the others in that below around 2.3 THz the spectrum was nearly identical to that of 2.5 mW, while above 2.3 THz the spectrum increased significantly, surpassing the other three. At optical powers 2.5, 7.5, and 10 mW the signal reached to just above 5 THz before falling to the system noise level while

at 5 mW the signal reached up to 6 THz. The shape of the measured signals in the time-domain did not have notable variation with varied optical pump power.

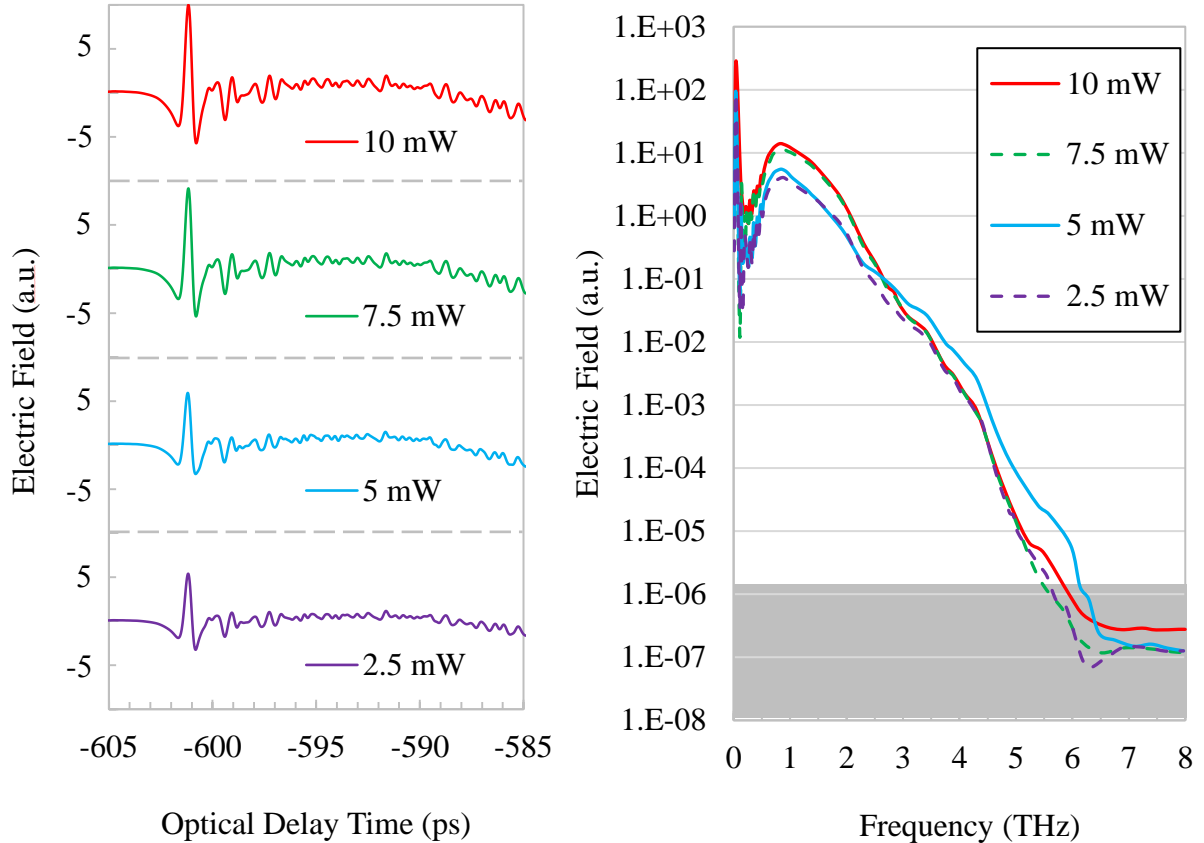


Figure 4.3.3: Time-domain measurements (left) and Fourier transform spectra (right) of the emitted THz pulses from device C2 as a function of optical pump power.

The THz time-domain signals and frequency-domain spectra of device T2 are shown in Figure 4.3.4 for optical pump power varied from 2.5 to 15 mW at 50 V bias voltage. Here there was uniform increase in the THz spectrum across all frequencies as the incident optical pump power was increased. For all optical powers, the THz signal fell to the system noise level at frequencies between 5 and 6 THz. Similar to device C2, the shape of the measured signals in the time-domain did not have notable variation with varied optical pump power.

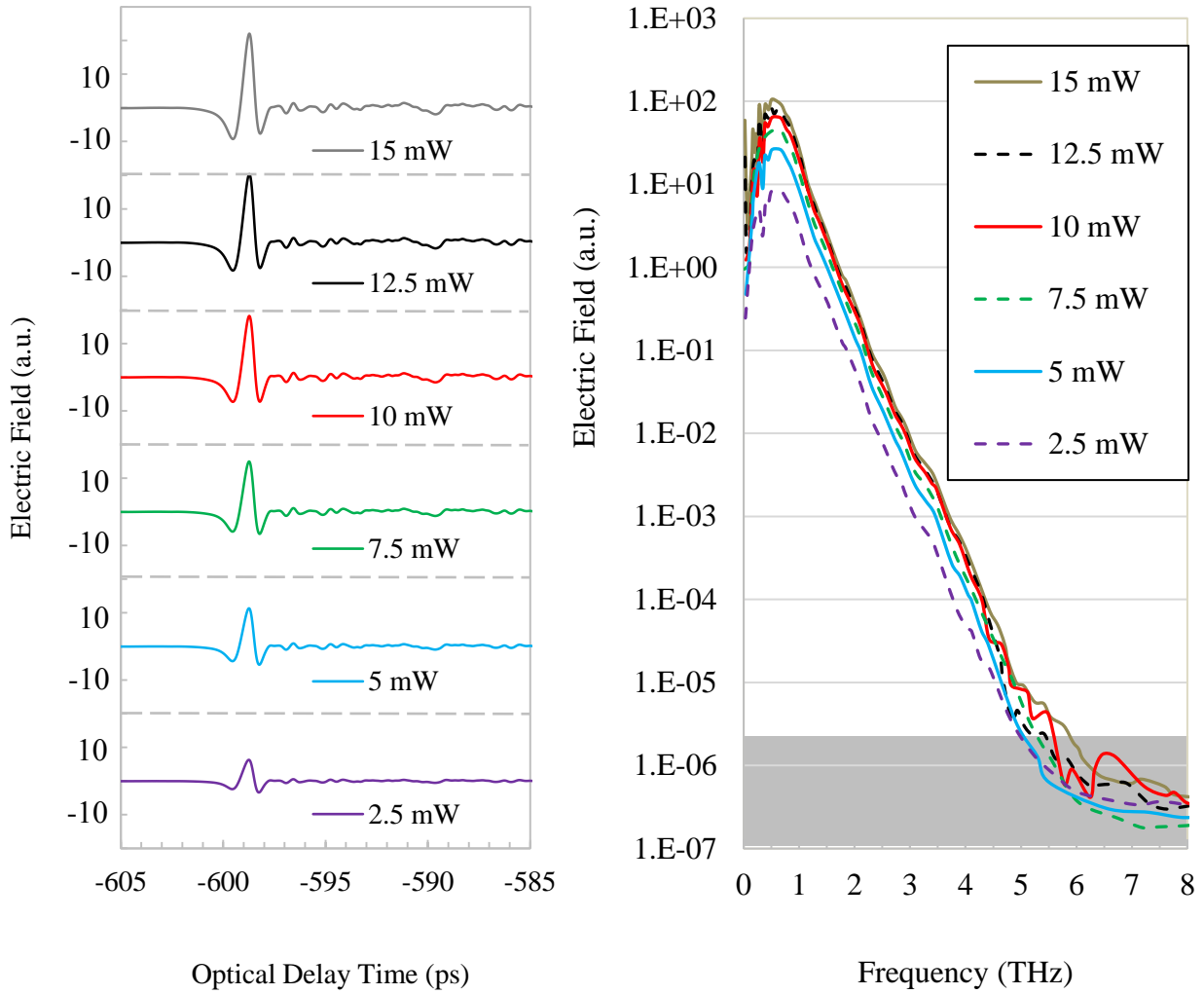


Figure 4.3.4: Time-domain measurements (left) and Fourier transform spectra (right) of the emitted THz pulses from device T2 as a function of optical pump power.

The THz time-domain signals and frequency-domain spectra of device P2 are shown in Figure 4.3.5 for optical pump power varied from 2.5 to 15 mW at 50 V bias voltage. Similar to T2, there was uniform increase in the THz spectrum across all frequencies as the incident optical pump power was increased. For all optical powers, the THz signal fell to the system noise level at frequencies around 5 THz. Again, all devices had a consistent shape of the time-domain signal waveforms regardless of incident optical pump power.

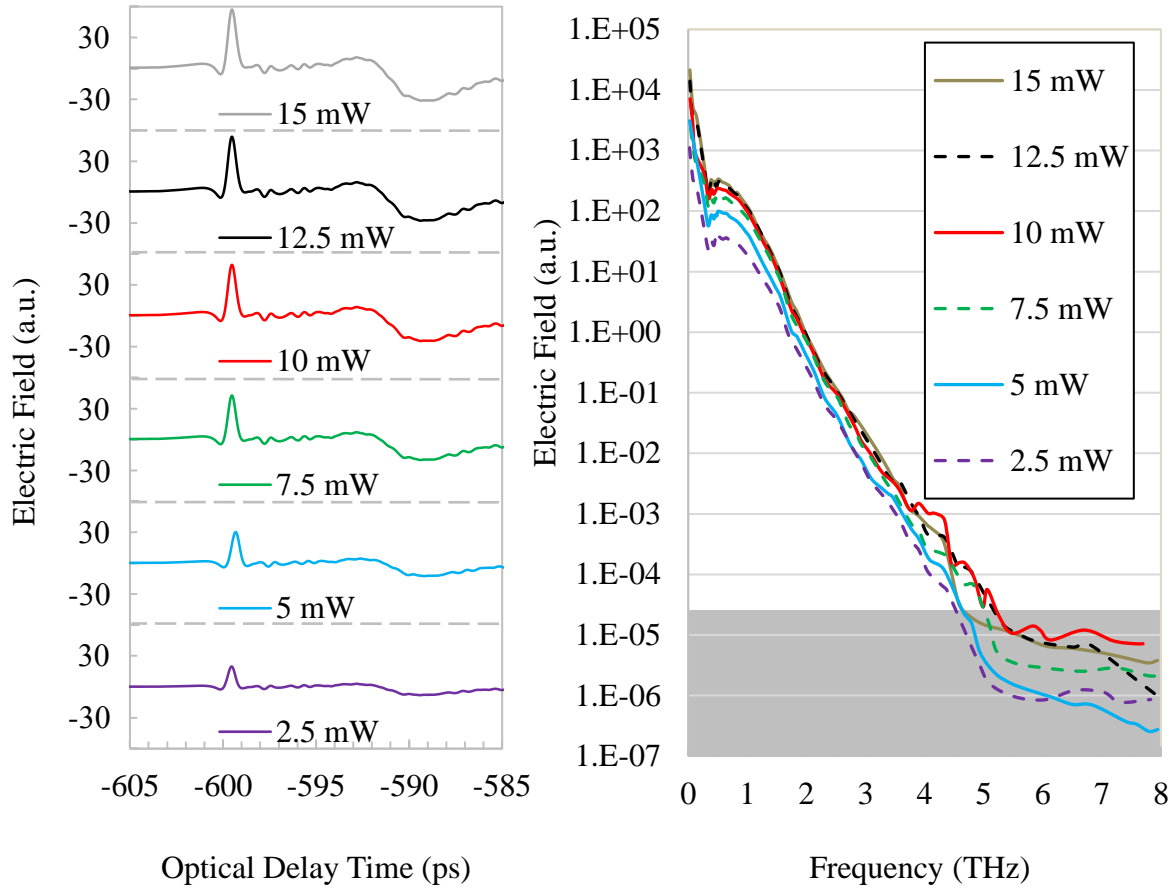


Figure 4.3.5: Time-domain measurements (left) and Fourier transform spectra (right) of the emitted THz pulses from device P2 as a function of optical pump power.

From the time-domain measurements of the devices C2, T2, and P2 operated under various optical pump power, the peak-to-peak THz field was extrapolated using Equation 4.2.1. The results of this analysis are shown in Figure 4.3.6. All devices showed an increase in E_{pp} with increasing optical pump power. At 10 mW optical pump power, the E_{pp} of C2, T2, and P2 were 14.5, 21.5, and 47.2, respectively. From 2.5 to 15 mW, the E_{pp} increased from 22.2 to 62.9 for P2 and 9.7 to 31.3 for T2. From 2.5 to 10 mW, the E_{pp} power increased from 8.6 to 15.7 for C2. The saturation effect could be seen in all devices in the nonlinear response of E_{pp} with increasing optical pump power.

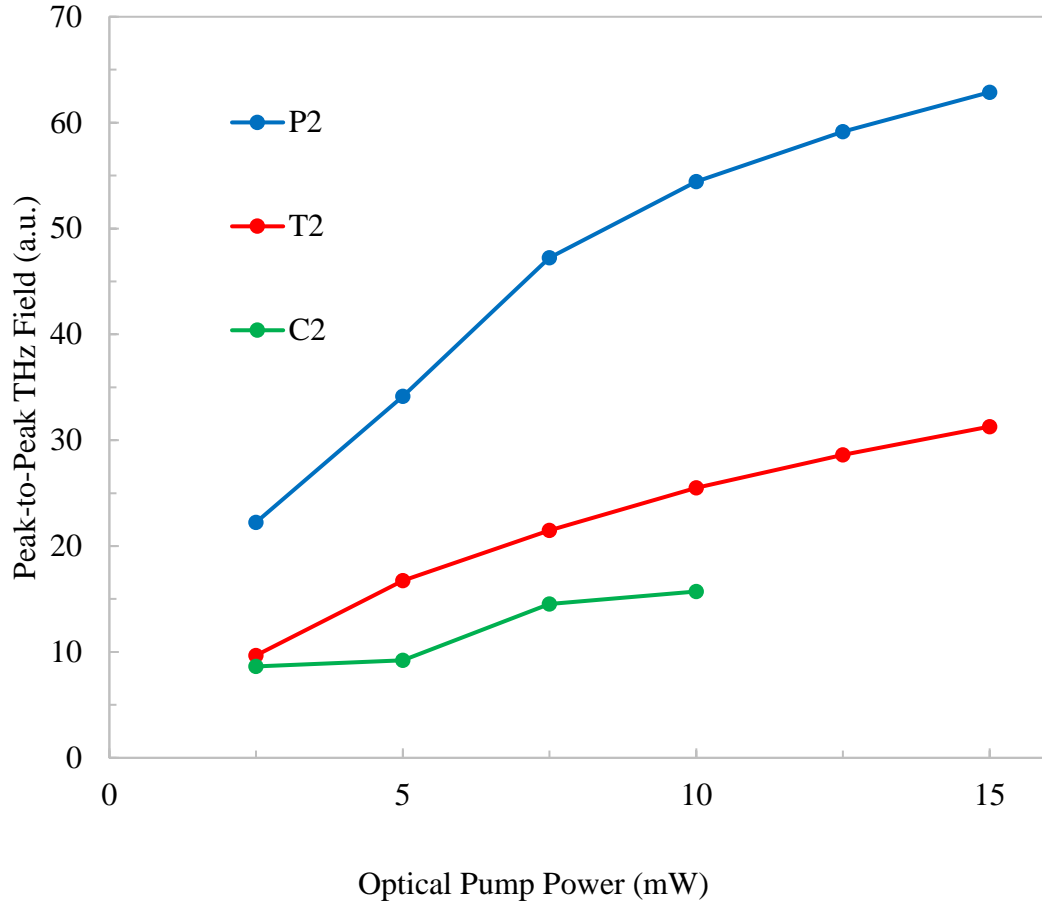


Figure 4.3.6: Peak-to-peak THz field extrapolated from time-domain measurements as a function of optical pump power for devices C2 (red), T2 (green) and P2 (blue).

From the spectral measurements of the devices C2, T2, and P2 operated under various optical pump power, the THz TSP was extrapolated using Equation 4.2.2. The results of this analysis are shown in Figure 4.3.7. All devices showed a linear increase in THz power with increasing optical pump power. At 10 mW optical pump power, the output THz powers of C2, T2 and P2 were 0.043, 0.58 and 82.2, respectively. From 2.5 to 15 mW, the output THz power increased from 2.4 to 433 for P2 and 0.019 to 2.7 for T2. From 2.5 to 10 mW the output THz power increased from 0.005 to 0.063 for C2.

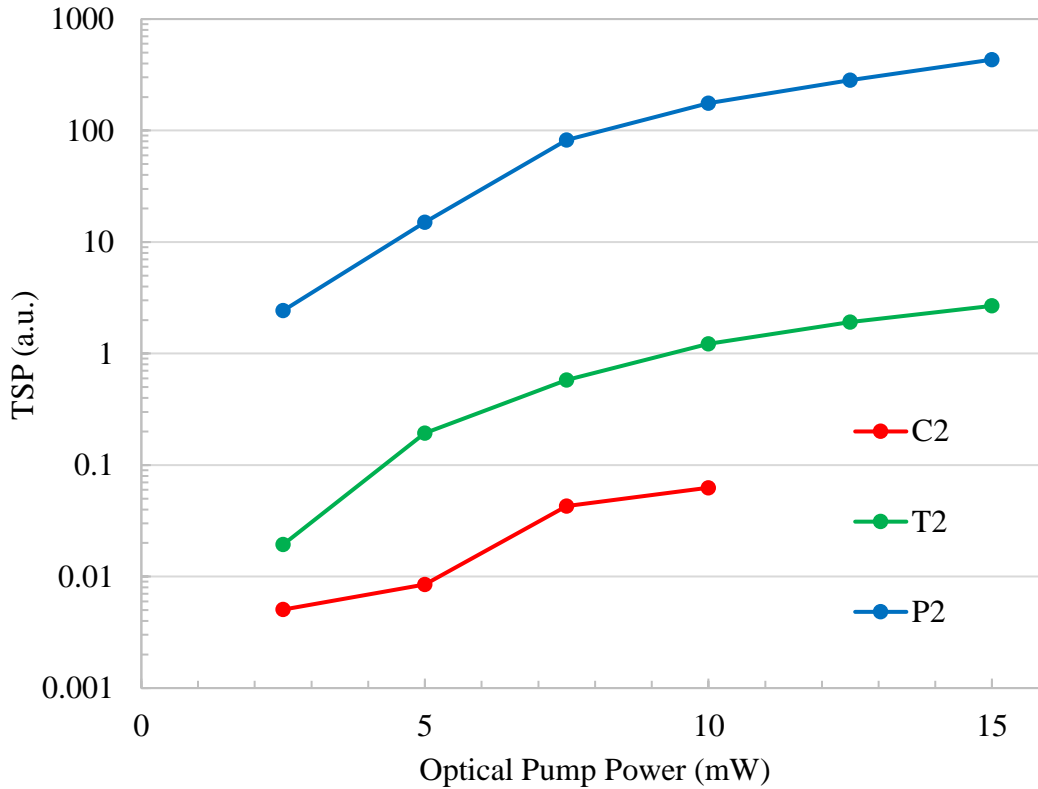


Figure 4.3.7: THz TSP extrapolated from frequency-domain spectrum as a function of optical pump power for devices C2 (red), T2 (green) and P2 (blue).

After characterization of the optical power dependence of these first three devices, the remaining devices were characterized. At this point, the previously described alignment issues were observed. As such, all remaining measurements were taken with a 2 mm aperture in place at the THz beam focal point, as illustrated in Figure 4.2.3. Of the remaining devices, several failed during initial testing and/or packaging, leaving devices C2, C4, T1, T2, T4, T5, P1, P2, and P3 available for measurement. In addition, a conventional emitter fabricated by Teraview was also characterized. This device represented the current industry standard for conventional THz emitter devices.

In order to observe the effect of adding the 2 mm aperture, THz spectra were obtained for devices C2, T2, P2, and one of Teraview’s reference conventional devices, first with the aperture

in place and again with the aperture removed. The results for device C2 are shown in Figure 4.3.8.

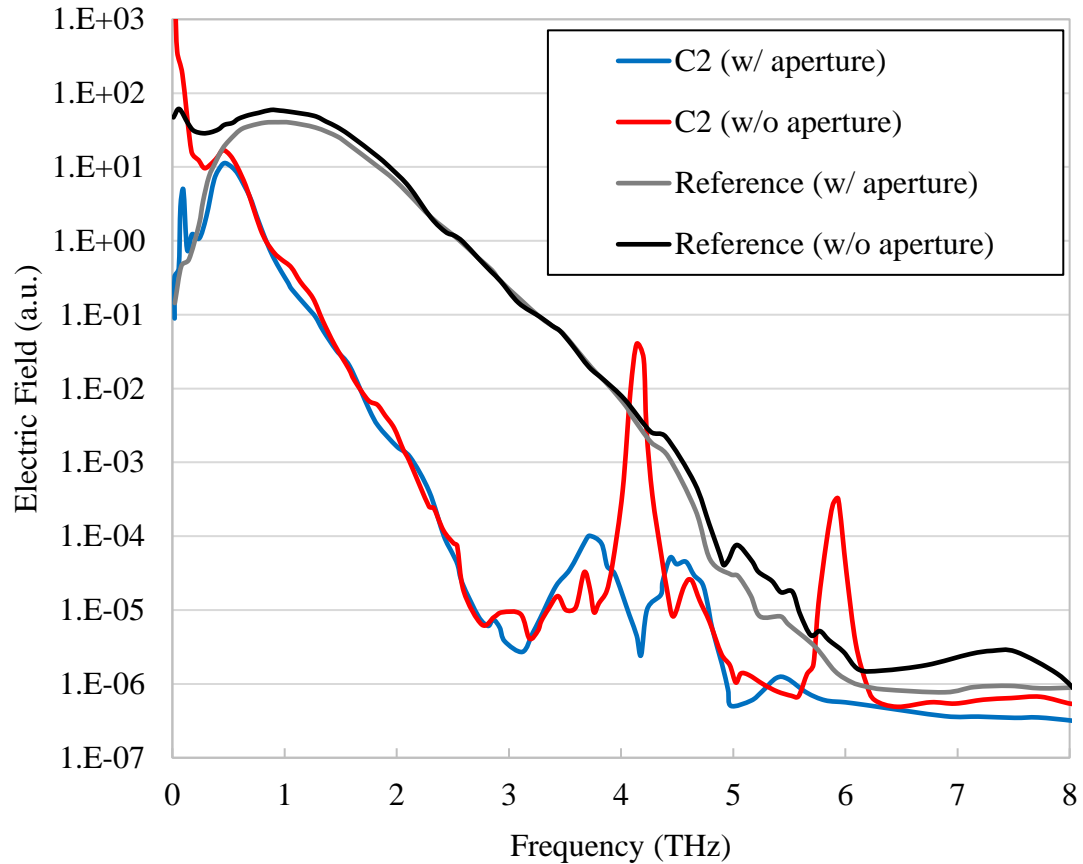


Figure 4.3.8: Fourier transform spectra of the time-domain measurements of devices C2 (blue and red) and reference (black and gray) both with (blue and gray) and without (red and black) 2 mm aperture.

In the reference device, minimal change was observed in the spectrum above 1 THz. At lower THz frequencies, a sharp cutout was observed with the 2 mm aperture present. This was also observed in device C2. Additionally, in the spectra of C2, the high frequency peaks at 4.2 and 5.9 THz were drastically reduced. Similarly, for device T2, the spectra with and without 2 mm aperture are shown in Figure 4.3.9.

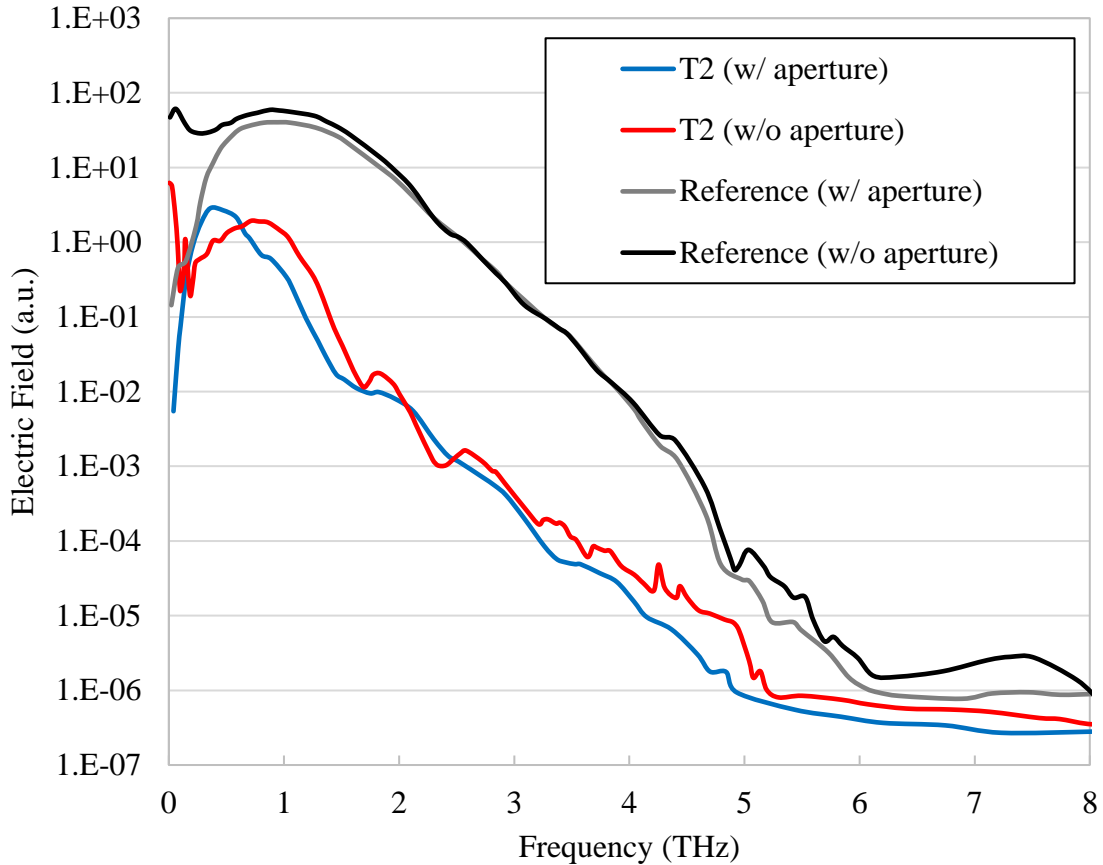


Figure 4.3.9: Fourier transform spectra of the time-domain measurements of devices T2 (blue and red) and reference (black and gray) both with (blue and gray) and without (red and black) 2 mm aperture.

Similar to device C2, reduction in the lower frequency range below around 0.2 THz was observed in device T2 with the addition of the 2 mm aperture. Another notable change in the spectrum of T2 was the “smoothing” of the spectral dips at around 1.7 and 2.4 THz. As previously discussed, any non-dipole emission from the antenna would be out of phase with the dipole emission. This would cause phase interference at the detector, which could have led to the periodic dips observed without the aperture present. Similar reduction of spectra dips as well as reduction of a high frequency peak at around 4.1 THz were observed in the spectra of device P2, as shown in Figure 4.3.10.

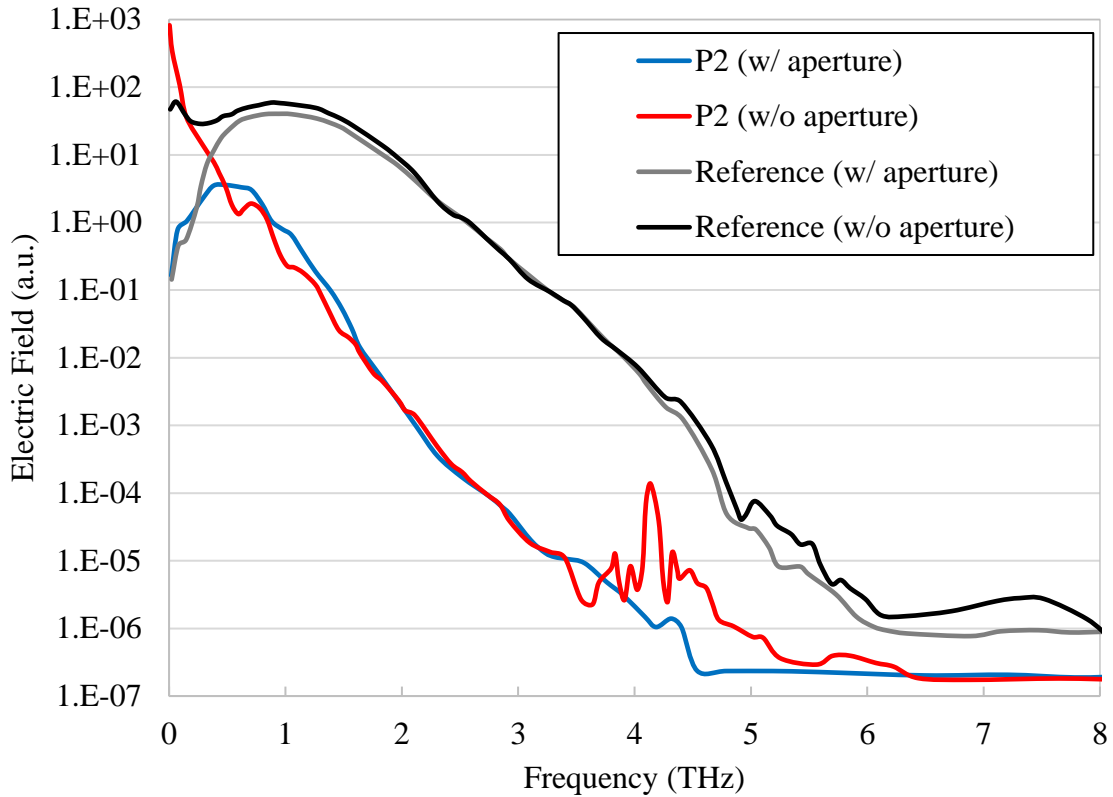


Figure 4.3.10: Fourier transform spectra of the time-domain measurements of devices P2 (blue and red) and reference (black and gray) both with (blue and gray) and without (red and black) 2 mm aperture.

The measured time-domain signals from devices C2, C4, and Reference under 50 V bias voltage, 10 mW optical pump power and 2 mm aperture are shown in Figure 4.3.11. The E_{pp} was 33.0 for the reference device, 7.0 for C2 and 5.2 for C4. All devices showed sub-picosecond pulse widths, with the reference device having the lowest pulse width around 0.3 ps. However, the time location of the pulse varied across devices. The peak locations of C2 and C4 were shifted +4.5 ps and +3.8 ps, respectively, compared to the peak location of Reference. Shifting in the peak location could be attributed to several things, including changes in the THz PCA substrate thickness or refractive index. If the substrate thickness increases, the optical pulse will be delayed since it will have a greater optical path length inside a slower phase velocity material.

A change in substrate thickness (with respect to the reference device) could also place the THz PCA dipole out of the focus of the backside mounted HRFZ Si THz lens. A shift in the optical delay time of 4.5 ps corresponds to a shift in optical path length of around 1.35 mm. Since the thickness of the substrates varied by less than 10-20 μm , it is likely that the observed shift in the pulse peak location was due to focusing issues rather than phase delay from extra substrate material.

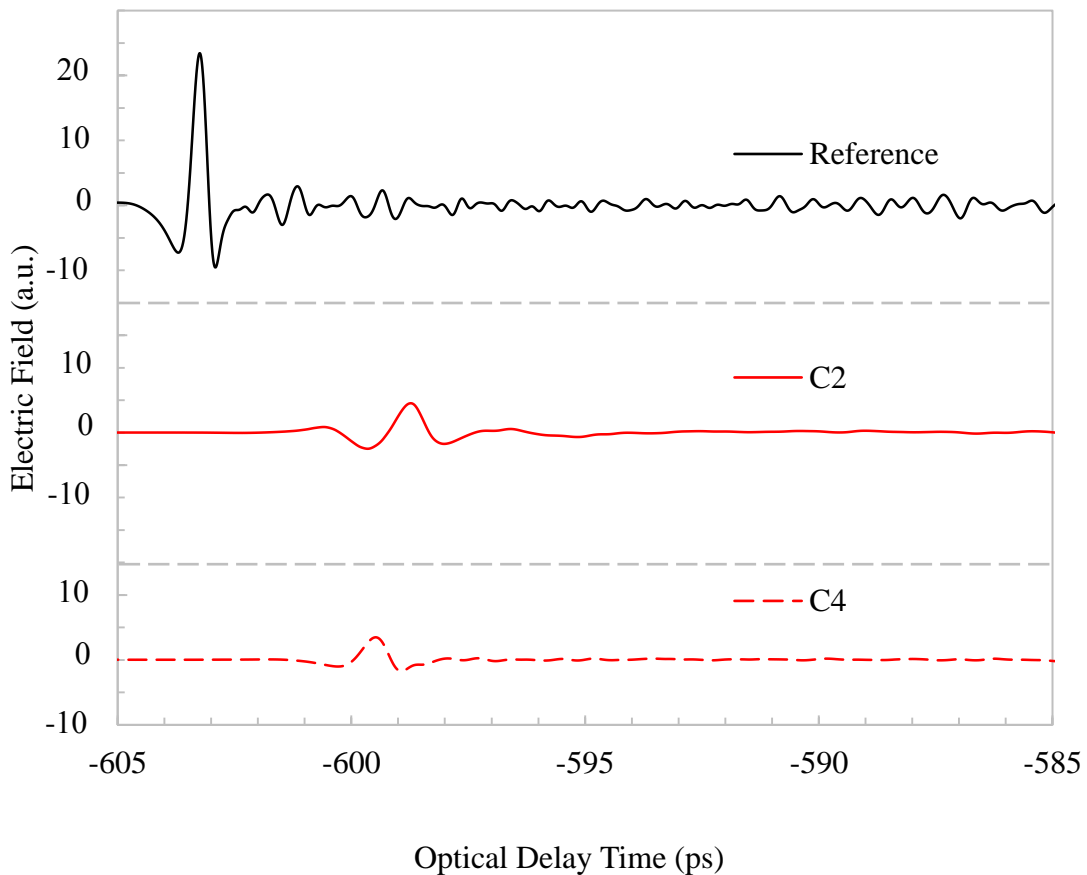


Figure 4.3.11: Time-domain measurements of the emitted THz pulses from devices Reference (black), C2 (solid red) and C4 (dashed red).

The measured time-domain signals from devices T1, T2, T4, T5, and Reference under 50 V bias voltage, 10 mW optical pump power, and 2 mm aperture are shown in Figure 4.3.12. The

E_{pp} was 33.0 for the reference device, 24.8 for T1, 4.9 for T2, 15.0 for T4, and 2.8 for T5. Again, all “T” devices had pulse widths below 1 ps and had a positive time shift with respect to the reference. The time shift varied significantly for these devices, with the peak locations occurring at -597.7 ps, -600.0 ps, -599.9 ps, and -590.8 ps for T1, T2, T4, and T5, respectively. Although all devices have the LT-GaAs thin-film layers transferred onto HRFZ Si substrates of identical thickness, the adhesive layer used to connect the thin-films to the substrates could introduce greater variance in the total device thickness than what is observed in the modified conventional devices.

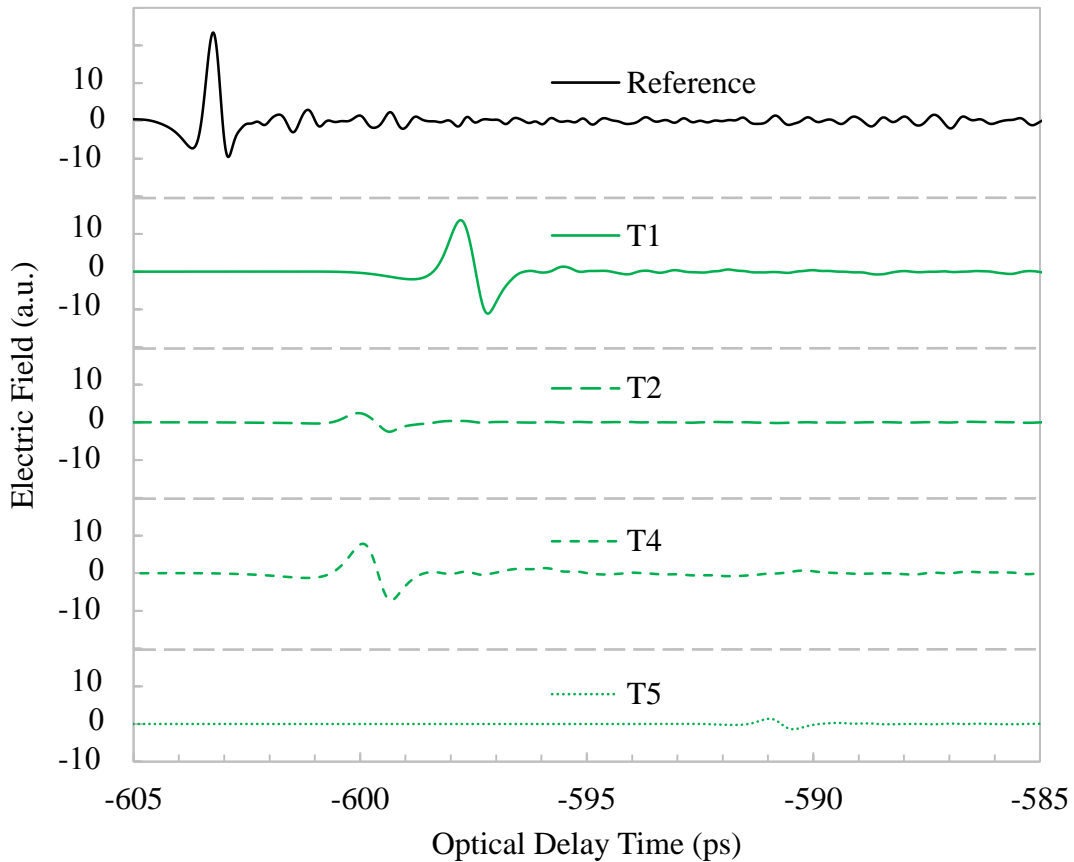


Figure 4.3.12: Time-domain measurements of the emitted THz pulses from devices Reference (black), T1 (solid green), T2 (large dash green), T4 (medium dash green) and T5 (small dash green).

As with the other devices, the measured time-domain signals from devices P1, P2, P3, and Reference under 50 V bias voltage, 10 mW optical pump power and 2 mm aperture are shown in Figure 4.3.13. The E_{pp} was 33.0 for the reference device, 14.5 for P1, 5.9 for P2, and 5.0 for P3. Again, all “T” devices had pulse widths below 1 ps and had a positive time shift with respect to the reference. The time shift varied significantly for these devices, with the peak locations occurring at -597.6 ps, -598.9 ps, and -599.3 ps for P1, P2 and P3, respectively.

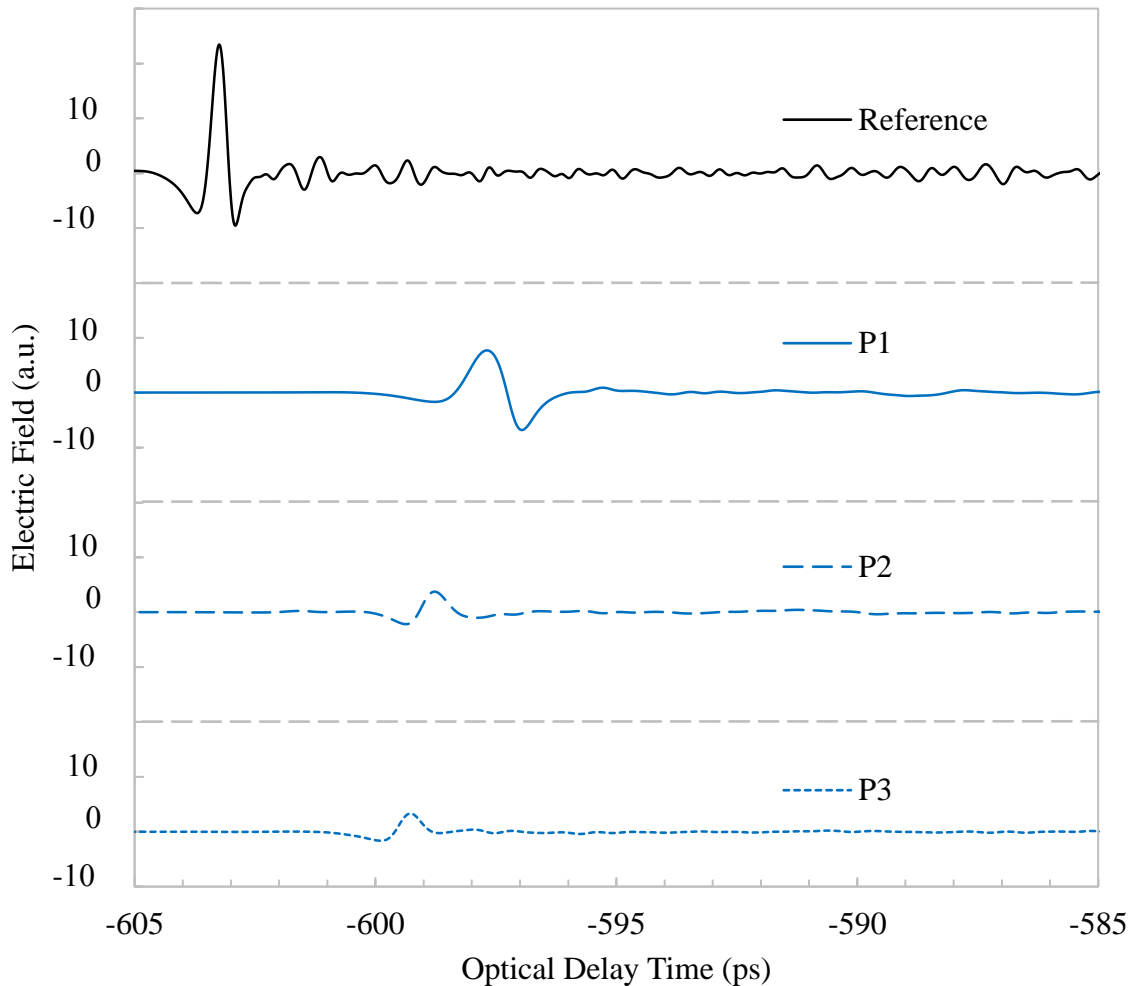


Figure 4.3.13: Time-domain measurements of the emitted THz pulses from devices Reference (black), P1 (solid blue), P2 (large dash blue) and P3 (medium dash blue).

Considering all time-domain data, several observations were made. First, the best performing devices of each type in terms of E_{pp} were C2, T1, and P1 with E_{pp} values of 7.0, 24.8, and 14.5, respectively. These were all less than the E_{pp} of the reference device, which was 33.0. Comparing these results to the previous measurements of devices C2, T2, and P2, it was observed that after addition of the aperture no performance improvement was achieved in the plasmonic thin-film device as compared to the non-plasmonic thin-film. However, both of these devices did have higher E_{pp} values than the best performing modified conventional device. Considering all devices together, it was observed that the greatest E_{pp} values occurred in devices that had pulses centered around -598 ps, with E_{pp} reducing the further the pulse center location was from -598 ps. This could indicate that the variation in performance in the thin-film devices occurred due to variation in the adhesive layer thickness, since this would potentially alter the location of the antenna dipole with respect to the HRFZ Si THz lens focal point.

Comparison of the Fourier transform spectra of the measured emitted THz pulses of each device are shown in Figure 4.3.14. Again, the bias voltage was 50 V, the optical pump power was 10 mW, and a 2 mm aperture was included at the THz beam focal point. The reference device had the broadest spectrum, reaching nearly 6 THz before falling to the system noise level. Nearly all of the thin-film devices have bandwidth exceeding the modified conventional devices, with device T4 reaching nearly 5 THz. In device C2, it should be noted that the higher frequency peaks observed around 3.8 THz and 4.6 THz did not constitute usable THz signal, since none of the water absorption peaks were distinguishable in these regions. Therefore, those peaks were not included when considering the device bandwidth. T1, T4, and P1 provided higher output THz power than the reference device at frequencies below 0.82 THz for T1 and 0.51 THz for T4

and P1. At all higher frequencies for these devices, the reference device provided higher output THz power.

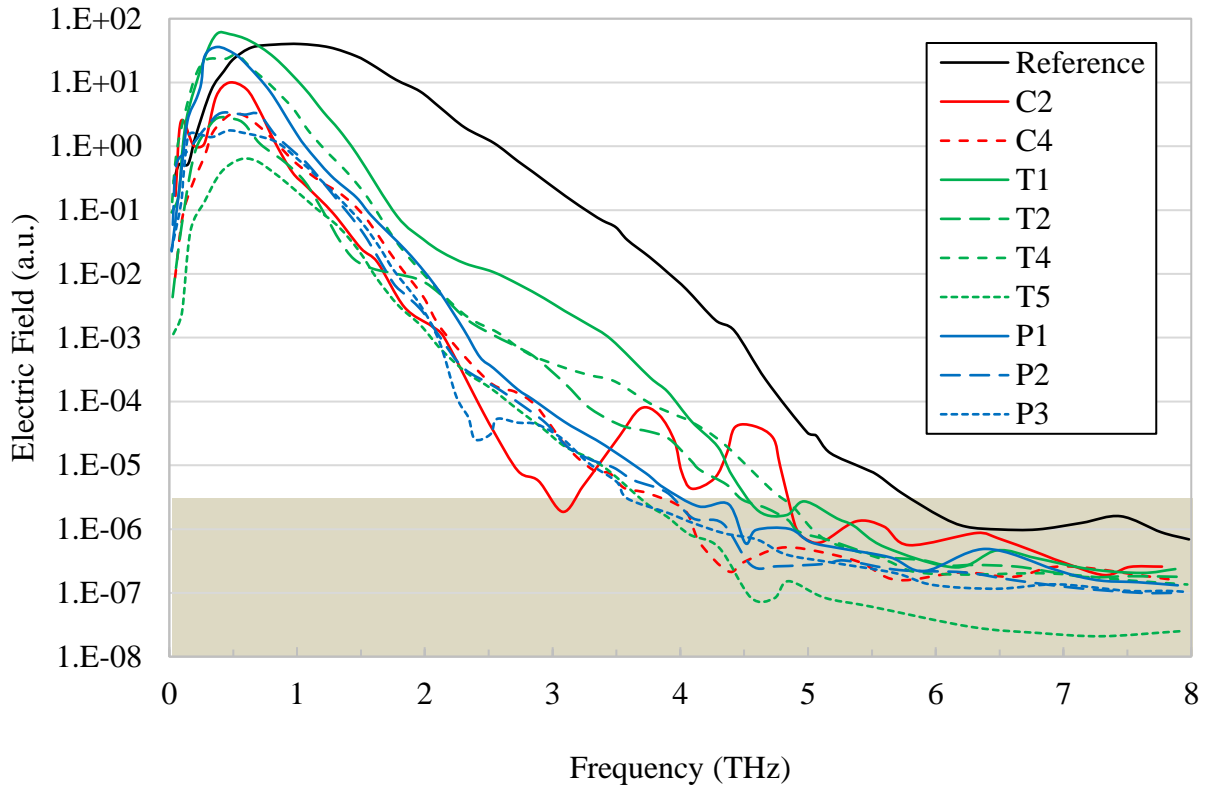


Figure 4.3.14: Fourier transform spectra of the time-domain measurements of the emitted THz pulses from devices Reference (black), C2 (solid red), C4 (dashed red), T1 (solid green), T2 (large dash green), T4 (medium dash green), T5 (small dash green), P1 (solid blue), P2 (large dash blue) and P3 (small dash blue). All measurements taken at 50 V bias voltage and 10 mW optical pump power.

The total THz power taken from the Fourier transform spectra of each of the devices were summarized in Figure 4.3.15. All designs showed significant variance with the “C” devices varying from 2020 to 15,400, “T” devices varying from 220 to 131,000 and “P” devices varying from 1130 to 8400. Considering only the best performing devices, these measurements both support and contrast the previously discussed single device measurements taken without an aperture, shown in Figure 4.3.3 to Figure 4.3.5. Here, the best thin-film devices still provide

higher output power than the best modified conventional device. However, the result did not illustrate any performance improvement in the thin-film devices due to the presence of plasmonic nanostructures. Since high variation was observed in the device performance, a larger number of samples would need to be produced in order to draw sound statistical conclusions.

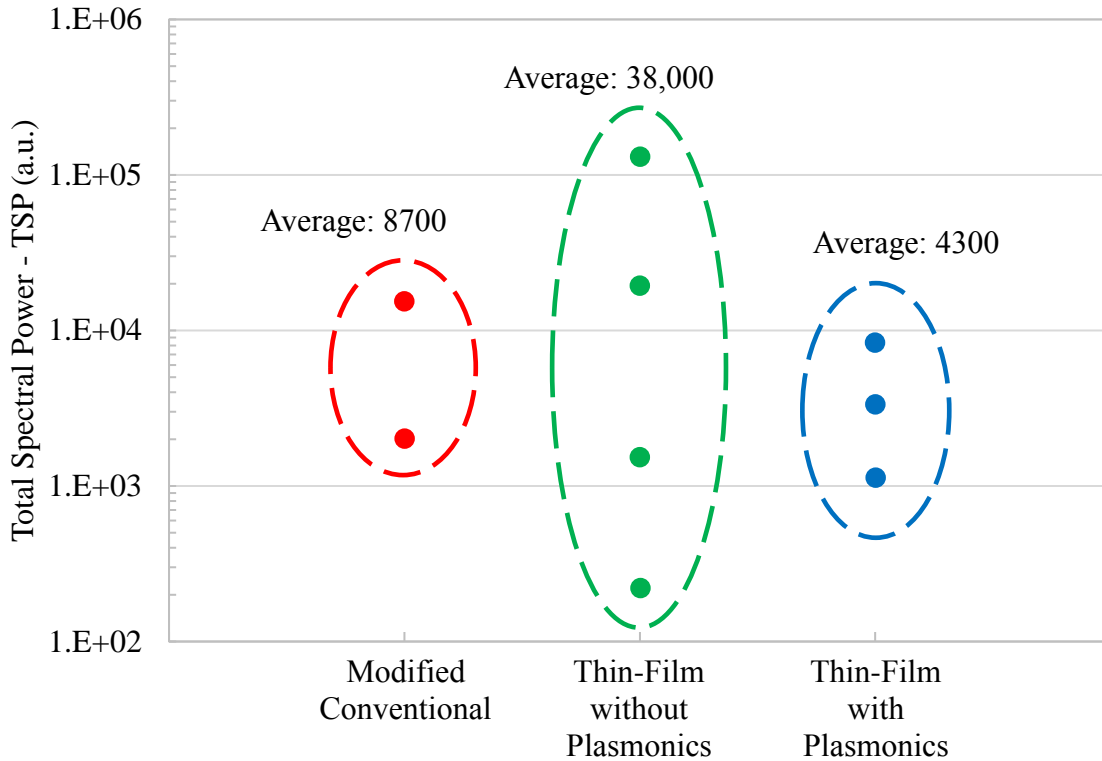


Figure 4.3.15: Total output THz power for all devices.

A final set of measurements was performed to observe the dependence of output THz power on bias voltage under 10 mW optical excitation and with a 2 mm aperture in place. The results of this study are shown in Figure 4.3.16. The bias voltage was varied from 12.5 V to 75 V for device C2, C4, T2, T4, P2, and P3. For all devices, the relationship between P_{THz} and V_{bias} matched approximately a second order polynomial relation, indicating linear dependence of E_{THz} on V_{bias} . However, a few outliers occurred around a bias voltage of 50 V for devices C2, T2, and

P2. Each of these devices had a peak in output THz power at this voltage, followed by a decrease in power at the next higher measured bias voltage of 62.5 V. This behavior was also observed in some of the devices that had failed due to being driven too close to their breakdown voltage. As the bias electric field in the LT-GaAs layer increases, a nonlinear response in the carrier drift velocity can occur due to carrier screening, as well as other factors [186]. Since this nonlinear response is not observed in all devices, it could be attributed to material damage during fabrication, natural variation of the LT-GaAs growth across the wafer, or previously induced defects from being driving at high bias voltages or optical pump powers.

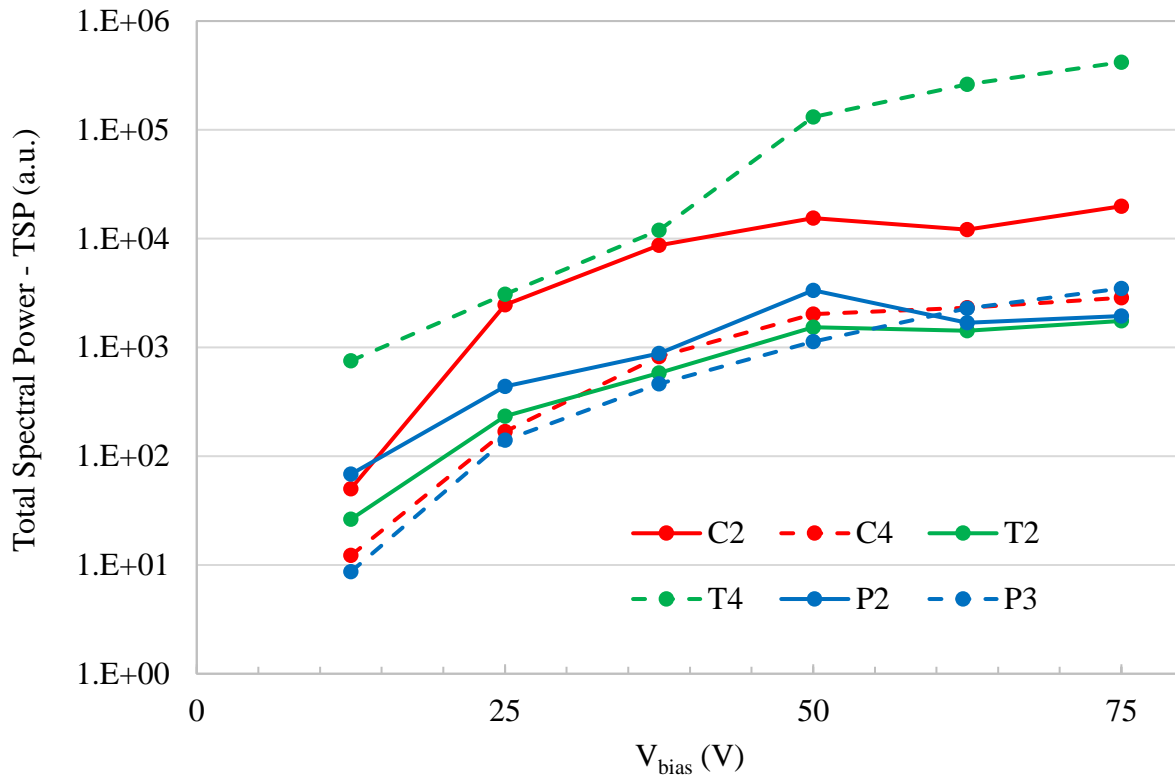


Figure 4.3.16: Output THz power versus bias voltage for devices C2 (solid red), C4 (dashed red), T2 (solid green), T4 (dashed green), P2 (solid blue) and P3 (dashed blue).

From the experimental characterization of the fabricated devices it was seen that although broadband THz emission was achieved in all device types, significant performance variation

occurred between the same types of devices. Considering average performance of all devices, the thin-film devices demonstrated over an order of magnitude improvement in the output THz power as compared to the modified conventional devices. Considering average behavior, no improvement was seen in the thin-film devices due to the addition of the plasmonic nanostructures. However, when considering best performing devices only, clear order of magnitude improvement was observed comparing the thin-film without plasmonics device to the modified conventional, as well as another order of magnitude improvement comparing the thin-film devices with and without plasmonics. Additionally, it was important to note that the LT-GaAs thickness and nanodisk array geometry was optimized for 800 nm excitation wavelength, while the spectral characterization was performed at 780 nm. This, along with fabrication and LT-GaAs material growth variation, could explain the wide range observed in the device performance.

Chapter 5. Summary and Conclusions

This work computationally and experimentally investigated the feasibility of a plasmonic enhanced THz photoconductive antenna. A computational model utilizing the commercial finite element method (FEM) package COMSOL[®] Multiphysics was developed, combining optical field distribution calculations with time-dependent carrier dynamics in order to quantify the optically induced photocurrent in various THz PCA designs. The computational modeling revealed several observations. First, the optical field distribution for the thin film devices, both with and without the plasmonic structures, was found to be visibly greater than both the conventional and nanograting devices of Berry et al. [71]. In the BLTF device, the enhanced optical field was the result of constructive interference of internal Fresnel reflections inside the LT-GaAs layer. For the P-BLTF device, the enhanced optical field was a result of the Fresnel reflections and the plasmonic resonances of the nanostructures, which effectively localized the incident optical fields into the sub-wavelength LT-GaAs layer. Calculation of the optically induced time-dependent photocurrent showed 87 and 329 times enhancement of the peak photocurrent in the BLTF and P-BLTF devices, respectively, as compared to the conventional device. These were both greater than the enhancement in the nanograting device, which was 10 times greater than the conventional device. In calculating the width of the optically induced current pulse, it was found that the BLTF device had the lowest increase in pulse width with increasing carrier lifetime of 55% when increasing the carrier lifetime across two orders of magnitude. By comparison, the conventional, P-BLTF, and nanograting devices had increases of 157%, 97%, and 240%, respectively. This indicated that the BLTF design could potentially be implemented with longer carrier lifetime photoconductors without compromising response time and bandwidth.

Fabrication of the proposed plasmonic thin-film devices was demonstrated by utilizing a number of micro and nanofabrication techniques. Photolithography recipes were developed to pattern the antenna electrodes. Devices were flip-mounted to silicon carrier wafers and lapping and chemical etching procedures were developed to remove the GaAs substrate and sacrificial layers. Electron beam lithography writing of plasmonic nanodisk array patterns was optimized, yielding 200 nm diameter Au nanodisk arrays with 520 nm center-to-center spacing on the LT-GaAs thin-film surface. Two rounds of device fabrication were performed, with the first round devices showing no measureable THz emission. This was attributed to the conductivity of the epoxy adhesive used to bond the LT-GaAs thin-films to their silicon carrier wafers. After identifying this issue, an alternative high resistivity adhesive was implemented, along with several other process improvements to generate a second round of THz devices.

The fabrication process revealed several key insights. First, although the methods to remove the LT-GaAs thin-film from the GaAs carrier substrate resulted in the substrate being destroyed, it had the advantage of being more practical than alternative substrate-conserving epitaxial liftoff methods. Additionally, although mechanical lapping was initially utilized to thin the devices before chemical etching, it was found that chemical etching of the entire 500 μm thick GaAs substrate was just as, if not more, effective. In addition to the substrate removal process, the photolithography process was improved upon by implementing an image reversal process in the photoresist. This allowed the exposed regions of photoresist to produce negative, recessed sidewalls, reducing defects in the metallization due to ineffective liftoff.

The experimental results of the second round of fabricated devices demonstrated measurable emission of sub-picosecond width THz pulses from the three device designs (modified conventional, BLTF, and P-BLTF). This corresponded to around 5 THz bandwidth in each

device. First results of single devices of each type alluded to promising support for the theorized enhancement, with around one and two order of magnitude increase in the THz power of the BLTF and P-BLTF devices as compared to a modified conventional device. Later measurements were obtained from multiple other devices implementing apertures to improve the THz beam alignment. From these results, no improvement in the thin-film devices was observed comparing those with and without plasmonic nanostructures. However, comparing all of the thin-film devices to the modified conventional devices demonstrated an average of over an order of magnitude higher THz power in the thin-film devices.

While the thin-film devices outperformed the modified conventional devices, the thin-film devices also demonstrated greater performance deviation, with output powers varying from 0.049 to 375.7. This large deviation was attributed to the added steps needed to fabricate the thin-film devices. For each added fabrication step, the probability of device defects increases. Additionally, thermal strain mismatch between the adhesive layer and LT-GaAs thin-film layer could induce cracks in the LT-GaAs any time the device experiences a temperature change. It may be possible to reduce this performance deviation by improving the repeatability of the fabrication process.

THz PCA technology is still relatively young, with many opportunities and avenues for performance improvement to be realized. By designing THz PCA devices with high optical-to-THz conversion efficiency, THz time-domain imaging and spectroscopy systems with high milliwatt level THz power could be possible. Additionally, by increasing the efficiency the amount of laser power needed to excite each device can be reduced. This would potentially allow the development of multipixel time-domain THz detectors, which could open the door for the practical implementation of many THz imaging and nondestructive evaluation applications.

References

- [1] C. Fattinger and D. Grischkowsky, "Terahertz beams," *Appl. Phys. Lett.*, vol. 54, no. 6, pp. 490–492, 1989.
- [2] L. A. Samoska, "An overview of solid-state integrated circuit amplifiers in the submillimeter-wave and THz regime," *IEEE Trans. Terahertz Sci. Technol.*, vol. 1, no. 1, pp. 9–24, 2011.
- [3] P. Dean, A. Valavanis, J. Keeley, K. Bertling, Y. L. Lim, R. Alhathloul, A. D. Burnett, L. H. Li, S. P. Khanna, D. Indjin, T. Taimre, A. D. Rakić, E. H. Linfield, and A. G. Davies, "Terahertz imaging using quantum cascade lasers—a review of systems and applications," *J. Phys. D: Appl. Phys.*, vol. 47, no. 37, p. 374008, 2014.
- [4] A. Nahata, A. S. Weling, and T. F. Heinz, "A wideband coherent terahertz spectroscopy system using optical rectification and electro-optic sampling," *Appl. Phys. Lett.*, vol. 69, no. 16, p. 2321, 1996.
- [5] J. A. Fülöp, L. Pálfalvi, G. Almási, and J. Hebling, "Design of high-energy terahertz sources based on optical rectification," *Opt. Express*, vol. 18, no. 12, pp. 12311–12327, 2010.
- [6] M. D. King, W. D. Buchanan, and T. M. Korter, "Understanding the terahertz spectra of crystalline pharmaceuticals: terahertz spectroscopy and solid-state density functional theory study of (S)-(+)-ibuprofen and (RS)-ibuprofen," *J. Pharm. Sci.*, vol. 100, no. 3, pp. 1116–29, 2011.
- [7] L. Ho, M. Pepper, and P. Taday, "Terahertz spectroscopy: Signatures and fingerprints," *Nat. Photonics*, vol. 2, no. September, pp. 541–543, 2008.
- [8] A. Grange, "Terahertz Spectroscopy : An investigation into the use of terahertz radiation to detect/sense drugs , pharmaceuticals and polymorphs," *e-Engineering, Univ. Leeds*, vol. 2, no. 3, pp. 1–12, 2010.
- [9] M. C. Kemp, P. F. Taday, B. E. Cole, J. A. Cluff, A. J. Fitzgerald, and W. R. Tribe, "Security Applications of Terahertz Technology," in *Proc. SPIE 5070*, 2003, vol. 5070, pp. 44–52.
- [10] J. F. Federici, B. Schulkin, F. Huang, D. Gary, R. Barat, F. Oliveira, and D. Zimdars, "THz imaging and sensing for security applications—explosives, weapons and drugs," *Semicond. Sci. Technol.*, vol. 20, no. 7, pp. S266–S280, 2005.
- [11] H.-B. Liu, H. Zhong, N. Karpowicz, Y. Chen, and X.-C. Zhang, "Terahertz Spectroscopy and Imaging for Defense and Security Applications," *Proc. IEEE*, vol. 95, no. 8, pp. 1514–1527, 2007.

- [12] T. I. Jeon and D. Grischkowsky, "Characterization of optically dense, doped semiconductors by reflection THz time domain spectroscopy," *Appl. Phys. Lett.*, vol. 72, no. 23, pp. 3032–3034, 1998.
- [13] D. Hashimshony, I. Geltner, G. Cohen, Y. Avitzour, a. Zigler, and C. Smith, "Characterization of the electrical properties and thickness of thin epitaxial semiconductor layers by THz reflection spectroscopy," *J. Appl. Phys.*, vol. 90, no. 11, p. 5778, 2001.
- [14] T. Kiwa, M. Tonouchi, M. Yamashita, and K. Kawase, "Laser terahertz-emission microscope for inspecting electrical faults in integrated circuits.," *Opt. Lett.*, vol. 28, no. 21, pp. 2058–2060, 2003.
- [15] N. Hasegawa, T. Loffler, M. Thomson, and H. G. Roskos, "Remote identification of protrusions and dents on surfaces by terahertz reflectometry with spatial beam filtering and out-of-focus detection," *Appl. Phys. Lett.*, vol. 83, no. 19, pp. 3996–3998, 2003.
- [16] M. Yamashita, C. Otani, K. Kawase, K. Nikawa, and M. Tonouchi, "Noncontact inspection technique for electrical failures in semiconductor devices using a laser terahertz emission microscope," *Appl. Phys. Lett.*, vol. 93, no. 4, pp. 2008–2010, 2008.
- [17] I. Javaid, "Terahertz Time of Flight Detection for Absolute Thickness," M.S. Thesis, Dept. Elect. Eng., Univ. North Carolina, Charolette, NC, 2010.
- [18] M. Yamashita, C. Otani, T. Matsumoto, Y. Midoh, K. Miura, K. Nakamae, K. Nikawa, S. Kim, H. Murakami, and M. Tonouchi, "THz emission characteristics from p/n junctions with metal lines under non-bias conditions for LSI failure analysis.," *Opt. Express*, vol. 19, no. 11, pp. 10864–10873, 2011.
- [19] L. Minkevičius, R. Suzanovičienė, S. Balakauskas, G. Molis, a. Krotkus, G. Valušis, and V. Tamošiūnas, "Detection of tab wire soldering defects on silicon solar cells using terahertz time-domain spectroscopy," *Electron. Lett.*, vol. 48, no. 15, p. 932, 2012.
- [20] N. M. Burford, M. O. El-Shenawee, C. B. O. Neal, and K. J. Olejniczak, "Terahertz Imaging for Nondestructive Evaluation of Packaged Power Electronic Devices," *Int. J. Emerg. Technol. Adv. Eng.*, vol. 4, no. 1, pp. 395–401, 2014.
- [21] P. C. Ashworth, E. Pickwell-MacPherson, E. Provenzano, S. E. Pinder, A. D. Purushotham, M. Pepper, and V. P. Wallace, "Terahertz pulsed spectroscopy of freshly excised human breast cancer.," *Opt. Express*, vol. 17, no. 15, pp. 12444–12454, 2009.
- [22] A. M. Hassan, D. C. Hufnagle, M. El-shenawee, and G. E. Pacey, "Terahertz Imaging for margin assessment of breast cancer tumors," *Proc. IEEE IMS*, Montreal, 2012.
- [23] C. Yu, S. Fan, Y. Sun, and E. Pickwell-Macpherson, "The potential of terahertz imaging for cancer diagnosis: A review of investigations to date.," *Quant. Imaging Med. Surg.*, vol. 2, no. 1, pp. 33–45, 2012.

- [24] T. C. Bowman, M. El-shenawee, and L. K. Campbell, "Terahertz Imaging of Excised Breast Tumor Tissue on Paraffin Sections," *IEEE Trans. Antennas Propag.*, vol. 63, no. 5, pp. 2088–2097, 2015.
- [25] R. M. Woodward, B. E. Cole, V. P. Wallace, R. J. Pye, D. D. Arnone, E. H. Linfield, and M. Pepper, "Terahertz pulse imaging in reflection geometry of human skin cancer and skin tissue.," *Phys. Med. Biol.*, vol. 47, pp. 3853–3863, 2002.
- [26] C. S. Joseph, A. N. Yaroslavsky, V. A. Neel, T. M. Goyette, and R. H. Giles, "Continuous wave terahertz transmission imaging of nonmelanoma skin cancers," *Lasers Surg. Med.*, vol. 43, no. 6, pp. 457–462, 2011.
- [27] C. S. Joseph, R. Patel, V. A. Neel, R. H. Giles, and A. N. Yaroslavsky, "Imaging of ex vivo nonmelanoma skin cancers in the optical and terahertz spectral regions," *J. Biophotonics*, vol. 7, no. 5, pp. 295–303, 2014.
- [28] Z. D. Taylor, R. S. Singh, M. O. Culjat, J. Y. Suen, W. S. Grundfest, H. Lee, and E. R. Brown, "Reflective terahertz imaging of porcine skin burns," *Opt. Lett.*, vol. 33, no. 11, pp. 1258–1260, 2008.
- [29] P. Tewari, C. P. Kealey, D. B. Bennett, N. Bajwa, K. S. Barnett, R. S. Singh, M. O. Culjat, A. Stojadinovic, W. S. Grundfest, and Z. D. Taylor, "In vivo terahertz imaging of rat skin burns," *J. Biomed. Opt.*, vol. 17, no. 4, p. 40503, 2012.
- [30] M. H. Arbab, D. P. Winebrenner, T. C. Dickey, A. Chen, M. B. Klein, and P. D. Mourad, "Terahertz spectroscopy for the assessment of burn injuries in vivo.," *J. Biomed. Opt.*, vol. 18, no. 7, p. 77004, 2013.
- [31] P. U. Jepsen, D. G. Cooke, and M. Koch, "Terahertz spectroscopy and imaging - Modern techniques and applications," *Laser Photonics Rev.*, vol. 5, no. 1, pp. 124–166, 2011.
- [32] J. F. O'Hara, W. Withayachumnankul, and I. Al-Naib, "A review on thin-film sensing with terahertz waves," *Journal of Infrared, Millimeter, and Terahertz Waves*, vol. 33, no. 3, pp. 245–291, 2012.
- [33] A. Redo-Sanchez, N. Laman, B. Schulkin, and T. Tongue, "Review of terahertz technology readiness assessment and applications," *Journal of Infrared, Millimeter, and Terahertz Waves*, vol. 34, no. 9, pp. 500–518, 2013.
- [34] M. Haaser, K. C. Gordon, C. J. Strachan, and T. Rades, "Terahertz pulsed imaging as an advanced characterisation tool for film coatings - A review," *International Journal of Pharmaceutics*, vol. 457, no. 2, pp. 510–520, 2013.
- [35] S. K. Mathanker, P. R. Weckler, and N. Wang, "Terahertz (THz) Applications in Food and Agriculture: A Review," *Trans. ASABE*, vol. 56, no. 3, pp. 1213–1226, 2013.

- [36] A. Abina, U. Puc, A. Jeglič, and A. Zidanšek, “Applications of Terahertz Spectroscopy in the Field of Construction and Building Materials,” *Appl. Spectrosc. Rev.*, vol. 50, no. 4, pp. 279–303, 2014.
- [37] X. Yang, X. Zhao, K. Yang, Y. Liu, Y. Liu, W. Fu, and Y. Luo, “Biomedical Applications of Terahertz Spectroscopy and Imaging,” *Trends Biotechnol.*, vol. 34, no. 10, pp. 810-824, 2016.
- [38] D. H. Auston, “Subpicosecond electro-optic shock waves,” *Appl. Phys. Lett.*, vol. 43, no. 8, pp. 713–715, 1983.
- [39] D. H. Auston, K. P. Cheung, and P. R. Smith, “Picosecond photoconducting Hertzian dipoles,” *Appl. Phys. Lett.*, vol. 45, no. 3, pp. 284–286, 1984.
- [40] D. H. Auston, K. P. Cheung, J. A. Valdmanis, and D. A. Kleinman, “Cherenkov radiation from femtosecond optical pulses in electro-optic media,” *Phys. Rev. Lett.*, vol. 53, no. 16, pp. 1555–1558, 1984.
- [41] P. R. Smith, D. H. Auston, and M. C. Nuss, “Subpicosecond Photoconducting Dipole Antennas,” *IEEE J. Quantum Electron.*, vol. 24, no. 2, pp. 255–260, 1988.
- [42] M. B. Ketchen, D. Grischkowsky, T. C. Chen, C. C. Chi, I. N. Duling, N. J. Halas, J. M. Halbout, J. a Kash, and G. P. Li, “Generation of subpicosecond electrical pulses on coplanar transmission-lines,” *Appl. Phys. Lett.*, vol. 48, no. May 2015. p. 751, 1986.
- [43] C. Fattinger and D. Grischkowsky, “Point source terahertz optics,” *Applied Physics Letters*, vol. 53, no. 16. pp. 1480–1482, 1988.
- [44] P. U. Jepsen, R. H. Jacobsen, and S. R. Keiding, “Generation and detection of terahertz pulses from biased semiconductor antennas,” *J. Opt. Soc. Am. B*, vol. 13, no. 11, p. 2424, 1996.
- [45] H. Němec, a. Pashkin, P. Kužel, M. Khazan, S. Schnüll, and I. Wilke, “Carrier dynamics in low-temperature grown GaAs studied by terahertz emission spectroscopy,” *J. Appl. Phys.*, vol. 90, no. 3, pp. 1303–1306, 2001.
- [46] E. Moreno, M. F. Pantoja, S. G. Garcia, A. R. Bretones, and R. G. Martin, “Time-domain numerical modeling of THz photoconductive antennas,” *IEEE Trans. Terahertz Sci. Technol.*, vol. 4, no. 4, pp. 490–500, 2014.
- [47] A. C. Warren, N. Katzenellenbogen, D. Grischkowsky, J. M. Woodall, M. R. Melloch, and N. Otsuka, “Subpicosecond, freely propagating electromagnetic pulse generation and detection using GaAs:As epilayers,” *Applied Physics Letters*, vol. 58, no. 14. pp. 1512–1514, 1991.
- [48] S. Gupta, M. Y. Frankel, J. A. Valdmanis, J. F. Whitaker, G. A. Mourou, F. W. Smith, and A. R. Calawa, “Subpicosecond carrier lifetime in GaAs grown by molecular beam epitaxy at low temperatures,” *Appl. Phys. Lett.*, vol. 59, no. 25, pp. 3276–3278, 1991.

- [49] E. S. Harmon, D. D. Nolte, N. Otsuka, and C. L. Chang, "Carrier lifetime versus anneal in low temperature growth GaAs," *Appl. Phys. Lett.*, vol. 63, pp. 2248–2250, 1993.
- [50] M. Tani, K. Sakai, H. Abe, S. Nakashima, H. Harima, M. Hangyo, Y. Tokuda, K. Kanamoto, Y. Abe, and N. Tsukada, "Spectroscopic Characterization of Low-Temperature Grown GaAs Epitaxial Films," *Jpn. J. Appl. Phys.*, vol. 33, no. 9A, pp. 4807–4811, 1994.
- [51] M. Tani, S. Matsuura, K. Sakai, and S. Nakashima, "Emission characteristics of photoconductive antennas based on low-temperature-grown GaAs and semi-insulating GaAs," *Appl. Opt.*, vol. 36, no. 30, pp. 7853–7859, 1997.
- [52] M. R. Stone, M. Naftaly, R. E. Miles, J. R. Fletcher, and D. P. Steenson, "Electrical and radiation characteristics of semilarge photoconductive terahertz emitters," *IEEE Trans. Microw. Theory Tech.*, vol. 52, no. 10, pp. 2420–2429, 2004.
- [53] K. Moon, J. Choi, J. H. Shin, S. P. Han, H. Ko, N. Kim, J. W. Park, Y. J. Yoon, K. H. Park, K. Y. Kang, and H. C. Ryu, "Generation and detection of terahertz waves using low-temperature-grown GaAs with an annealing process," *ETRI J.*, vol. 36, no. 1, pp. 159–162, 2014.
- [54] T. A. Liu, M. Tani, and C. L. Pan, "THz radiation emission properties of multienergy arsenic-ion-implanted GaAs and semi-insulating GaAs based photoconductive antennas," *J. Appl. Phys.*, vol. 93, no. 5, pp. 2996–3001, 2003.
- [55] T. A. Liu, M. Tani, M. Nakajima, M. Hangyo, and C. L. Pan, "Ultrabroadband terahertz field detection by photoconductive antennas based on multi-energy arsenic-ion-implanted GaAs and semi-insulating GaAs," *Appl. Phys. Lett.*, vol. 83, no. 7, pp. 1322–1324, 2003.
- [56] B. Salem, D. Morris, V. Aimez, J. Beerens, J. Beauvais, and D. Houde, "Pulsed photoconductive antenna terahertz sources made on ion-implanted GaAs substrates," *J. Phys. Condens. Matter*, vol. 17, no. 46, pp. 7327–7333, 2005.
- [57] B. Salem, D. Morris, Y. Salissou, V. Aimez, S. Charlebois, M. Chicoine, and F. Schiettekatte, "Terahertz emission properties of arsenic and oxygen ion-implanted GaAs based photoconductive pulsed sources," *J. Vac. Sci. Technol. A Vacuum, Surfaces Film.*, vol. 24, no. 3, pp. 774–777, 2006.
- [58] B. Salem, D. Morris, V. Aimez, J. Beauvais, and D. Houde, "Improved characteristics of a terahertz set-up built with an emitter and a detector made on proton-bombarded GaAs photoconductive materials," *Semicond. Sci. Technol.*, vol. 21, no. 3, pp. 283–286, 2006.
- [59] S. Winnerl, F. Peter, S. Nitsche, A. Dreyhaupt, B. Zimmermann, M. Wagner, H. Schneider, M. Helm, and K. Köhler, "Generation and detection of THz radiation with scalable antennas based on GaAs substrates with different carrier lifetimes," *IEEE J. Sel. Top. Quantum Electron.*, vol. 14, no. 2, pp. 449–457, 2008.

- [60] M. Mikulics, M. Marso, I. C. Mayorga, R. Güsten, S. Stanček, P. Kováč, S. Wu, X. Li, M. Khafizov, R. Sobolewski, E. A. Michael, R. Schieder, M. Wolter, D. Buca, A. Förster, P. Kordoš, and H. Lüth, “Photomixers fabricated on nitrogen-ion-implanted GaAs,” *Appl. Phys. Lett.*, vol. 87, no. 4, pp. 1–3, 2005.
- [61] S. H. Yang, R. Salas, E. M. Krivoy, H. P. Nair, S. R. Bank, and M. Jarrahi, “Characterization of ErAs:GaAs and LuAs:GaAs Superlattice Structures for Continuous-Wave Terahertz Wave Generation through Plasmonic Photomixing,” *J. Infrared, Millimeter, Terahertz Waves*, pp. 1–9, 2016.
- [62] E. Budiarto, J. Margolies, S. Jeong, J. Son, J. Bokor, and S. Member, “High-Intensity Terahertz Pulses at 1 -kHz Repetition Rate,” *IEEE J. Quantum Opt.*, vol. 32, no. 10, pp. 1839–1846, 1996.
- [63] R. Mendis, C. Sydlo, J. Sigmund, M. Feiginov, P. Meissner, and H. L. Hartnagel, “Tunable CW-THz system with a log-periodic photoconductive emitter,” *2003 Int. Semicond. Device Res. Symp. ISDRS 2003 - Proc.*, vol. 48, pp. 318–319, 2003.
- [64] C. D. Wood, O. Hatem, J. E. Cunningham, E. H. Linfield, A. G. Davies, P. J. Cannard, M. J. Robertson, and D. G. Moodie, “Terahertz emission from metal-organic chemical vapor deposition grown Fe:InGaAs using 830 nm to 1.55 μm excitation,” *Appl. Phys. Lett.*, vol. 96, no. 19, pp. 1–4, 2010.
- [65] J. H. Kim, A. Polley, and S. E. Ralph, “Efficient photoconductive terahertz source using line excitation,” *Opt. Lett.*, vol. 30, no. 18, pp. 2490–2492, 2005.
- [66] N. T. Yardimci, S. Yang, C. W. Berry, and M. Jarrahi, “High-Power Terahertz Generation Using Large-Area Plasmonic Photoconductive Emitters,” *IEEE Trans. Terahertz Sci. Technol.*, vol. 5, no. 2, pp. 223–229, 2015.
- [67] S. Yang, M. R. Hashemi, C. W. Berry, and M. Jarrahi, “7.5% Optical-to-Terahertz Conversion Efficiency Offered by Photoconductive Emitters With Three-Dimensional Plasmonic Contact Electrodes,” *Ieee Trans. Terahertz Sci. Technol.*, vol. 4, no. 5, pp. 1–7, 2014.
- [68] T. Hattori, K. Tukamoto, and H. Nakatsuka, “Time-resolved study of intense terahertz pulses generated by a large-aperture photoconductive antenna,” *Japanese J. Appl. Physics, Part 1 Regul. Pap. Short Notes Rev. Pap.*, vol. 40, no. 8, pp. 4907–4912, 2001.
- [69] B. Globisch, R. J. B. Dietz, T. Göbel, M. Schell, W. Bohmeyer, R. Müller, and A. Steiger, “Absolute terahertz power measurement of a time-domain spectroscopy system,” *Opt. Lett.*, vol. 40, no. 15, p. 3544, 2015.
- [70] S. Kono, M. Tani, and K. Sakai, “Ultrabroadband photoconductive detection: Comparison with free-space electro-optic sampling,” *Appl. Phys. Lett.*, vol. 79, no. 7, pp. 898–900, 2001.

- [71] C. W. Berry, N. Wang, M. R. Hashemi, M. Unlu, and M. Jarrahi, “Significant performance enhancement in photoconductive terahertz optoelectronics by incorporating plasmonic contact electrodes,” *Nat. Commun.*, vol. 4, p. 1622, 2013.
- [72] P. K. Benicewicz, J. P. Roberts, and A. J. Taylor, “Scaling of terahertz radiation from large-aperture biased photoconductors,” *J Opt Soc Am B*, vol. 11, no. 12, pp. 2533–2546, 1994.
- [73] M. van Exter and D. R. Grischkowsky, “Characterization of an optoelectronic terahertz beam system,” *IEEE Trans. Microw. Theory Tech.*, vol. 38, no. 11, pp. 1684–1691, 1990.
- [74] J. T. Darrow, B. B. Hu, X.-C. Zhang, and D. H. Auston, “Subpicosecond electromagnetic pulses from large-aperture photoconducting antennas,” *Opt. Lett.*, vol. 15, no. 6, pp. 323–325, 1990.
- [75] I. S. Gregory, C. Baker, W. R. Tribe, I. V. Bradley, M. J. Evans, E. H. Linfield, A. G. Davies, and M. Missous, “Optimization of photomixers and antennas for continuous-wave terahertz emission,” *IEEE J. Quantum Electron.*, vol. 41, no. 5, pp. 717–728, 2005.
- [76] A. Jooshesh, L. Smith, M. Masnadi-Shirazi, V. Bahrami-yekta, T. Tiedje, T. E. Darcie, and R. Gordon, “Nanoplasmonics enhanced terahertz sources,” *Opt. Express*, vol. 22, no. 11, pp. 6255–6259, 2012.
- [77] H. Tanoto, J. H. Teng, Q. Y. Wu, M. Sun, Z. N. Chen, S. a Maier, B. Wang, C. C. Chum, G. Y. Si, a J. Danner, and S. J. Chua, “Nano-antenna in a photoconductive photomixer for highly efficient continuous wave terahertz emission,” *Sci. Rep.*, vol. 3, p. 2824, 2013.
- [78] J. T. Darrow, X. C. Zhang, D. H. Auston, and J. D. Morse, “Saturation Properties of Large-Aperture Photoconducting Antennas,” *IEEE J. Quantum Electron.*, vol. 28, no. 6, pp. 1607–1616, 1992.
- [79] E. R. Brown, “A photoconductive model for superior GaAs THz photomixers,” *Appl. Phys. Lett.*, vol. 75, no. 6, pp. 769–771, 1999.
- [80] S. E. Ralph and D. Grischkowsky, “Trap-enhanced fields in semi-insulators: The role of electrical and optical carrier injection,” *Appl. Phys. Lett.*, vol. 59, no. 16, pp. 1972–1974, 1991.
- [81] D. H. Auston, “Picosecond optoelectronic switching and gating in silicon,” *Appl. Phys. Lett.*, vol. 26, no. 3, pp. 101–103, 1975.
- [82] T.-A. Liu, M. Tani, M. Nakajima, M. Hangyo, K. Sakai, S.-I. Nakashima, and C.-L. Pan, “Ultrabroadband terahertz field detection by proton-bombarded InP photoconductive antennas,” *Opt. Express*, vol. 12, no. 13, pp. 2954–9, 2004.
- [83] L. Hou, W. Shi, and S. Chen, “Noise analysis and optimization of terahertz photoconductive emitters,” *IEEE J. Sel. Top. Quantum Electron.*, vol. 19, no. 1, 2013.

- [84] L. Hou and W. Shi, "An LT-GaAs terahertz photoconductive antenna with high emission power, low noise, and good stability," *IEEE Trans. Electron Devices*, vol. 60, no. 5, pp. 1619–1624, 2013.
- [85] M. Suzuki and M. Tonouchi, "Fe-implanted InGaAs terahertz emitters for 1.56 μm wavelength excitation," *Appl. Phys. Lett.*, vol. 86, no. 5, pp. 1–3, 2005.
- [86] M. Suzuki and M. Tonouchi, "Fe-implanted InGaAs photoconductive terahertz detectors triggered by 1.56 μm femtosecond optical pulses," *Appl. Phys. Lett.*, vol. 86, no. 16, pp. 1–3, 2005.
- [87] N. Chimot, J. Mangeney, L. Joulaud, P. Crozat, H. Bernas, K. Blary, and J. F. Lampin, "Terahertz radiation from heavy-ion-irradiated $\text{In}_{0.53}\text{Ga}_{0.47}\text{As}$ photoconductive antenna excited at 1.55 μm ," *Appl. Phys. Lett.*, vol. 87, no. 19, pp. 1–3, 2005.
- [88] A. Takazato, M. Kamakura, T. Matsui, J. Kitagawa, and Y. Kadoya, "Detection of terahertz waves using low-temperature-grown InGaAs with 1.56 μm pulse excitation," *Appl. Phys. Lett.*, vol. 90, no. 2007, p. 101119, 2007.
- [89] A. Takazato, M. Kamakura, T. Matsui, J. Kitagawa, and Y. Kadoya, "Terahertz wave emission and detection using photoconductive antennas made on low-temperature-grown InGaAs with 1.56 μm pulse excitation," *Appl. Phys. Lett.*, vol. 91, no. 1, pp. 1–4, 2007.
- [90] O. Hatem, J. Cunningham, E. H. Linfield, C. D. Wood, A. G. Davies, P. J. Cannard, M. J. Robertson, and D. G. Moodie, "Terahertz-frequency photoconductive detectors fabricated from metal-organic chemical vapor deposition-grown Fe-doped InGaAs," *Appl. Phys. Lett.*, vol. 98, no. 12, pp. 1–3, 2011.
- [91] R. Salas, S. Guchhait, S. D. Sifferman, K. M. McNicholas, V. D. Dasika, E. M. Krivoy, D. Jung, M. L. Lee, and S. R. Bank, "Growth and properties of rare-earth arsenide InGaAs nanocomposites for terahertz generation," *Appl. Phys. Lett.*, vol. 106, no. 8, pp. 1–3, 2015.
- [92] K. Murakumo, Y. Yamaoka, N. Kumagai, T. Kitada, and T. Isu, "Photoconductivity of Er-doped InAs quantum dots embedded in strain-relaxed InGaAs layers with 1.5 μm cw and pulse excitation," *Jpn. J. Appl. Phys.*, vol. 55, no. 04EH12, pp. 1–5, 2016.
- [93] M. Griebel, J. H. Smet, D. C. Driscoll, J. Kuhl, C. A. Diez, N. Freytag, C. Kadow, A. C. Gossard, and K. Von Klitzing, "Tunable subpicosecond optoelectronic transduction in superlattices of self-assembled ErAs nanoislands," *Nat. Mater.*, vol. 2, no. 2, pp. 122–126, 2003.
- [94] A. Schwagmann, Z. Y. Zhao, F. Ospald, H. Lu, D. C. Driscoll, M. P. Hanson, A. C. Gossard, and J. H. Smet, "Terahertz emission characteristics of ErAs:InGaAs-based photoconductive antennas excited at 1.55 μm ," *Appl. Phys. Lett.*, vol. 96, no. 14, pp. 14–16, 2010.

- [95] H. Roehle, R. J. B. Dietz, H. J. Hensel, J. Böttcher, H. Künzel, D. Stanze, M. Schell, and B. Sartorius, “Next generation 1.5 microm terahertz antennas: mesa-structuring of InGaAs/InAlAs photoconductive layers.” *Opt. Express*, vol. 18, no. 3, pp. 2296–2301, 2010.
- [96] R. J. B. Dietz, M. Gerhard, D. Stanze, M. Koch, B. Sartorius, and M. Schell, “THz generation at 1.55 μm excitation: six-fold increase in THz conversion efficiency by separated photoconductive and trapping regions,” *Opt. Express*, vol. 19, no. 27, p. 25911, 2011.
- [97] S. Preu, M. Mittendorff, H. Lu, H. B. Weber, S. Winnerl, and A. C. Gossard, “1550 nm ErAs:In(Al)GaAs large area photoconductive emitters,” *Appl. Phys. Lett.*, vol. 101, no. 10, pp. 1-3, 2012.
- [98] I. Kostakis, D. Saeedkia, and M. Missous, “Terahertz Generation and Detection Using Low Temperature Grown InGaAs-InAlAs Photoconductive Antennas at 1.55 μm Pulse Excitation,” *IEEE Trans. Terahertz Sci. Technol.*, vol. 2, no. 6, pp. 1–6, 2012.
- [99] M. Mittendorff, M. Xu, R. J. B. Dietz, H. Künzel, B. Sartorius, H. Schneider, M. Helm, and S. Winnerl, “Large area photoconductive terahertz emitter for 1.55 μm excitation based on an InGaAs heterostructure.” *Nanotechnology*, vol. 24, no. 21, p. 214007, 2013.
- [100] R. J. B. Dietz, B. Globisch, M. Gerhard, A. Velauthapillai, D. Stanze, H. Roehle, M. Koch, T. Gobel, and M. Schell, “64 μw pulsed terahertz emission from growth optimized InGaAs/InAlAs heterostructures with separated photoconductive and trapping regions,” *Appl. Phys. Lett.*, vol. 103, no. 6, pp. 1–5, 2013.
- [101] P. Gu, M. Tani, S. Kono, K. Sakai, and X. C. Zhang, “Study of terahertz radiation from InAs and InSb,” *J. Appl. Phys.*, vol. 91, no. 9, pp. 5533–5537, 2002.
- [102] J. Sigmund, C. Sydlo, H. L. Hartnagel, N. Benker, H. Fuess, F. Rutz, T. Kleine-Ostmann, and M. Koch, “Structure investigation of low-temperature-grown GaAsSb, a material for photoconductive terahertz antennas,” *Appl. Phys. Lett.*, vol. 87, no. 25, pp. 1–3, 2005.
- [103] K. Bertulis, A. Krotkus, G. Aleksejenko, V. Pacebutas, R. Adomavicius, G. Molis, and S. Marcinkevicius, “GaBiAs: A material for optoelectronic terahertz devices,” *Appl. Phys. Lett.*, vol. 88, no. 20, pp. 1–3, 2006.
- [104] C. M. Collier, T. J. Stirling, I. R. Hristovski, J. D. A. Krupa, and J. F. Holzman, “Photoconductive terahertz generation from textured semiconductor materials,” *Sci. Rep.*, vol. 6, no. November 2015, p. 23185, 2016.
- [105] S. L. Chuang, *Physics of Photonic Devices*, Wiley, 2009, p.113.
- [106] M. Tani, K. Lee, and X.-C. Zhang, “Detection of terahertz radiation with low-temperature-grown GaAs-based photoconductive antenna using 1.55 μm probe,” *Appl. Phys. Lett.*, vol. 77, no. 9, p. 1396, 2000.

- [107] B. Sartorius, H. Roehle, H. Künzel, J. Böttcher, M. Schlak, D. Stanze, H. Venghaus, and M. Schell, “All-fiber terahertz time-domain spectrometer operating at 1.5 microm telecom wavelengths,” *Opt. Express*, vol. 16, no. 13, pp. 9565–9570, 2008.
- [108] P. Juodawlkis, D. T. McInturff, and S. E. Ralph, “Ultrafast carrier dynamics and optical nonlinearities of low-temperature-grown InGaAs/InAlAs multiple quantum wells,” *Appl. Phys. Lett.*, vol. 69, no. 26, pp. 4062–4064, 1996.
- [109] R. J. B. Dietz, A. Brahm, A. Velauthapillai, A. Wilms, C. Lammers, B. Globisch, M. Koch, G. Notni, A. Tünnermann, T. Göbel, and M. Schell, “Low temperature grown photoconductive antennas for pulsed 1060 nm excitation: Influence of excess energy on the electron relaxation,” *J. Infrared, Millimeter, Terahertz Waves*, vol. 36, no. 1, pp. 60–71, 2014.
- [110] R. J. B. Dietz, B. Globisch, H. Roehle, D. Stanze, T. Göbel, and M. Schell, “Influence and adjustment of carrier lifetimes in InGaAs/InAlAs photoconductive pulsed terahertz detectors : 6 THz bandwidth and 90dB dynamic range,” *Opt. Lett.*, vol. 22, no. 16, pp. 615–623, 2014.
- [111] R. Ascázubi, C. Shneider, I. Wilke, R. Pino, and P. S. Dutta, “Enhanced terahertz emission from impurity compensated GaSb,” *Phys. Rev. B - Condens. Matter Mater. Phys.*, vol. 72, no. 4, pp. 1–5, 2005.
- [112] R. Ascázubi, I. Wilke, K. J. Kim, and P. Dutta, “Terahertz emission from Ga_{1-x}In_xSb,” *Phys. Rev. B*, vol. 74, no. 7, p. 75323, 2006.
- [113] J. T. Darrow, X. C. Zhang, and D. H. Auston, “Power scaling of large-aperture photoconducting antennas,” *Appl. Phys. Lett.*, vol. 58, no. 1, pp. 25–27, 1991.
- [114] D. S. Kim and D. S. Citrin, “Coulomb and radiation screening in photoconductive terahertz sources,” *Appl. Phys. Lett.*, vol. 88, no. 16, pp. 86–89, 2006.
- [115] B. B. Hu, J. T. Darrow, X. C. Zhang, D. H. Auston, and P. R. Smith, “Optically steerable photoconducting antennas,” *Appl. Phys. Lett.*, vol. 56, no. 10, pp. 886–888, 1990.
- [116] N. M. Froberg, B. Bin Hu, X. C. Zhang, and D. H. Auston, “Terahertz Radiation From a Photoconducting Antenna Array,” *IEEE J. Quantum Electron.*, vol. 28, no. 10, pp. 2291–2301, 1992.
- [117] Y. Chen, S. Williamson, T. Brock, F. W. Smith, and A. R. Calawa, “375-GHz-bandwidth photoconductive detector,” *Appl. Phys. Lett.*, vol. 59, no. 16, pp. 1984–1986, 1991.
- [118] S. Y. Chou, Y. Liu, and P. B. Fischer, “Tera-hertz GaAs metal-semiconductor-metal photodetectors with nanoscale finger spacing and width,” *Appl. Phys. Lett.*, vol. 61, no. July, pp. 477–479, 1992.

- [119] E. R. Brown, K. A. McIntosh, F. W. Smith, K. B. Nichols, M. J. Manfra, C. L. Dennis, and J. P. Mattia, “Milliwatt output levels and superquadratic bias dependence in a low-temperature-grown GaAs photomixer,” *Appl. Phys. Lett.*, vol. 64, no. 24, pp. 3311–3313, 1994.
- [120] E. Brown, K. McIntosh, K. Nichols, and Cl, “Photomixing up to 3.8 THz in low-temperature-grown GaAs,” *Appl. Phys. Lett.*, vol. 66, no. 3, pp. 285–287, 1995.
- [121] A. Dreyhaupt, S. Winnerl, T. Dekorsy, and M. Helm, “High-intensity terahertz radiation from a microstructured large-area photoconductor,” *Appl. Phys. Lett.*, vol. 86, no. 12, pp. 1–3, 2005.
- [122] T. Hattori, K. Egawa, S. I. Ookuma, and T. Itatani, “Intense terahertz pulses from large-aperture antenna with interdigitated electrodes,” *Jpn. J. Appl. Phys.*, vol. 45, no. 12–16, pp. 422–424, 2006.
- [123] M. Awad, M. Nagel, H. Kurz, J. Herfort, and K. Ploog, “Characterization of low temperature GaAs antenna array terahertz emitters,” *Appl. Phys. Lett.*, vol. 91, no. 18, pp. 13–15, 2007.
- [124] F. Peter, S. Winnerl, S. Nitsche, A. Dreyhaupt, H. Schneider, and M. Helm, “Coherent terahertz detection with a large-area photoconductive antenna,” *Appl. Phys. Lett.*, vol. 91, no. 8, pp. 1–4, 2007.
- [125] G. Acuna, F. Buergens, C. Lang, M. Handloser, A. Guggenmos, and R. Kersting, “Interdigitated terahertz emitters,” *Electron. Lett.*, vol. 44, no. 3, pp. 229–231, 2008.
- [126] J. Madéo, N. Jukam, D. Oustinov, M. Rosticher, R. Rungsawang, J. Tignon, and S. S. Dhillon, “Frequency tunable terahertz interdigitated photoconductive antennas,” *Electron. Lett.*, vol. 46, no. 9, p. 611, 2010.
- [127] P. J. Hale, J. Madeo, C. Chin, S. S. Dhillon, J. Mangeney, J. Tignon, and K. M. Dani, “20 THz broadband generation using semi-insulating GaAs interdigitated photoconductive antennas,” *Opt. Express*, vol. 22, no. 21, pp. 26358–64, 2014.
- [128] M. Beck, H. Schäfer, G. Klatt, J. Demsar, S. Winnerl, M. Helm, and T. Dekorsy, “Impulsive terahertz radiation with high electric fields from an amplifier-driven large-area photoconductive antenna,” *Opt. Express*, vol. 18, no. 9, pp. 9251–9257, 2010.
- [129] S. Winnerl, “Scalable microstructured photoconductive terahertz emitters,” *J. Infrared, Millimeter, Terahertz Waves*, vol. 33, no. 4, pp. 431–454, 2012.
- [130] G. Klatt, F. Hilser, W. Qiao, M. Beck, R. Gebbs, a Bartels, K. Huska, U. Lemmer, G. Bastian, M. B. Johnston, M. Fischer, J. Faist, and T. Dekorsy, “Terahertz emission from lateral photo-Dember currents,” *Opt. Express*, vol. 18, no. 5, pp. 4939–4947, 2010.
- [131] G. Klatt, D. Stephan, M. Beck, J. Demsar, and T. Dekorsy, “Large-area laser-driven terahertz emitters,” *Electron. Lett.*, vol. 46, no. 26, pp. S24-s26, 2010.

- [132] C. W. Berry, M. R. Hashemi, and M. Jarrahi, "Generation of high power pulsed terahertz radiation using a plasmonic photoconductive emitter array with logarithmic spiral antennas," *Appl. Phys. Lett.*, vol. 104, no. 8, 2014.
- [133] A. Singh and S. S. Prabhu, "Microlensless interdigitated photoconductive terahertz emitters," *Opt. Express*, vol. 23, no. 2, p. 1529, 2015.
- [134] B. Lee, I.-M. Lee, S. Kim, D.-H. Oh, and L. Hesselink, "Review on subwavelength confinement of light with plasmonics," *J. Mod. Opt.*, vol. 57, no. 16, pp. 1479–1497, 2010.
- [135] Y. A. Akimov and W. S. Koh, "Design of Plasmonic Nanoparticles for Efficient Subwavelength Light Trapping in Thin-Film Solar Cells," *Plasmonics*, vol. 6, no. 1, pp. 155–161, 2011.
- [136] N. Burford and M. El-Shenawee, "Plasmonic enhancement of irregular shape nano-patch for thin film silicon solar cells," *Appl. Comput. Electromagn. Soc. J.*, vol. 28, no. 5, pp. 359–373, 2013.
- [137] N. Burford and M. El-Shenawee, "Optimization of Silver Nanotoroid Arrays for the Absorption Enhancement of Silicon Thin-Film Solar Cells," *Plasmonics*, vol. 10, no. 1, pp. 225–232, 2014.
- [138] K. R. Catchpole and a Polman, "Plasmonic solar cells.," *Opt. Express*, vol. 16, no. 26, pp. 21793–800, 2008.
- [139] H. A. Atwater and A. Polman, "Plasmonics for improved photovoltaic devices," *Nat. Mater.*, vol. 9, no. 10, pp. 865–865, 2010.
- [140] X. C. Zhang, X. F. Ma, Y. Jin, T. M. Lu, E. P. Boden, P. D. Phelps, K. R. Stewart, and C. P. Yakymyshyn, "Terahertz optical rectification from a nonlinear organic crystal," *Appl. Phys. Lett.*, vol. 61, no. 26, pp. 3080–3082, 1992.
- [141] S. Varma, J. Spicer, B. Brawley, and J. Miragliotta, "Plasma enhancement of femtosecond laser-induced electromagnetic pulses at metal and dielectric surfaces," *Opt. Eng.*, vol. 53, no. 5, p. 51515, 2014.
- [142] R. N. Singh, M. Gottlieb, N. B. Singh, T. B. Norris, T. Buma, D. Suhre, and J. J. Hawkins, "Properties of nonlinear optical crystals in the terahertz wavelength region," *Opt. Eng.*, vol. 45, no. 9, pp. 94002–94007, 2006.
- [143] G. Welsh and N. Hunt, "Terahertz Emission from Nano-structured Metal Surfaces," 15th International Conference on Ultrafast Phenomena, OSA Technocal Digest Series 2006, pp. 1–3.
- [144] G. H. Welsh, N. T. Hunt, and K. Wynne, "Terahertz-pulse emission through laser excitation of surface plasmons in a metal grating," *Phys. Rev. Lett.*, vol. 98, no. 2, pp. 3–6, 2007.

- [145] G. H. Welsh and K. Wynne, "Generation of ultrafast terahertz radiation pulses on metallic nanostructured surfaces," *Opt. Express*, vol. 17, no. 4, pp. 2470–2480, 2009.
- [146] Y. Gao, M. K. Chen, C. E. Yang, Y. C. Chang, S. Yin, R. Hui, P. Ruffin, C. Brantley, E. Edwards, and C. Luo, "Analysis of terahertz generation via nanostructure enhanced plasmonic excitations," *J. Appl. Phys.*, vol. 106, no. 7, pp. 1-7 2009.
- [147] D. K. Polyushkin, E. Hendry, E. K. Stone, and W. L. Barnes, "THz generation from plasmonic nanoparticle arrays," *Nano Lett.*, vol. 11, no. 11, pp. 4718–4724, 2011.
- [148] G. Ramakrishnan, N. Kumar, G. K. P. Ramanandan, A. J. L. Adam, R. W. A. Hendrikx, and P. C. M. Planken, "Plasmon-enhanced terahertz emission from a semiconductor/metal interface," *Appl. Phys. Lett.*, vol. 104, no. 7, pp. 1-3, 2014.
- [149] G. K. P. Ramanandan, A. J. L. Adam, and P. C. M. Planken, "Enhanced Terahertz Emission from Schottky Junctions Using Plasmonic Nanostructures," *ACS Photonics*, vol. 1, no. 11, pp. 1165–1172, 2014.
- [150] S. Park, K. Jin, J. Ye, and K. H. Jeong, "Nanoplasmonic photoconductive antenna for high power terahertz emission," in *IEEE 2011 16th International Solid-State Sensors, Actuators and Microsystems Conference*, Beijing, 2011, pp. 2498–2501.
- [151] S.-G. Park, Y. Choi, Y.-J. Oh, and K.-H. Jeong, "Terahertz photoconductive antenna with metal nanoislands," *Opt. Express*, vol. 20, no. 23, p. 25530, 2012.
- [152] S. G. Park, K. H. Jin, M. Yi, J. C. Ye, J. Ahn, and K. H. Jeong, "Enhancement of terahertz pulse emission by optical nanoantenna," *ACS Nano*, vol. 6, no. 3, pp. 2026–2031, 2012.
- [153] A. Jooshesh, L. Smith, M. Masnadi-shirazi, V. Bahrami-yekta, T. Tiedje, T. E. Darcie, and R. Gordon, "Nanoplasmonics enhanced terahertz sources," *Opt. Express*, vol. 22, no. 23, pp. 714–719, 2014.
- [154] A. Jooshesh, V. Bahrami-Yekta, J. Zhang, T. Tiedje, T. E. Darcie, and R. Gordon, "Plasmon-Enhanced below Bandgap Photoconductive Terahertz Generation and Detection," *Nano Lett.*, vol. 15, no. 12, pp. 8306–8310, 2015.
- [155] O. Mitrofanov, I. Brener, T. S. Luk, and J. L. Reno, "Photoconductive Terahertz Near-Field Detector with a Hybrid Nanoantenna Array Cavity," *ACS Photonics*, vol. 2, no. 12, pp. 1763–1768, 2015.
- [156] S. Zhong, Y. Shen, H. Shen, and Y. Huang, "FDTD Study of a Novel Terahertz Emitter with Electrical Field Enhancement Using Surface Plasmon Resonance," *PIERS Online*, vol. 6, no. 2, pp. 153–156, 2010.
- [157] C. W. Berry and M. Jarrahi, "Terahertz generation using plasmonic photoconductive gratings," *New J. Phys.*, vol. 14, pp. 1-12, 2012.

- [158] B. Y. Hsieh and M. Jarrahi, “Analysis of periodic metallic nano-slits for efficient interaction of terahertz and optical waves at nano-scale dimensions,” *J. Appl. Phys.*, vol. 109, no. 8, pp. 1-5, 2011.
- [159] S. Yang, R. Watts, X. Li, N. Wang, V. Cojocaru, L. Barry, J. O’Gorman, and M. Jarrahi, “Compact terahertz radiation source using a bimodal laser and plasmonic photomixer,” *SPIE Newsroom*, vol. 1, pp. 2–4, Apr. 2016.
- [160] K. Moon, I.-M. Lee, J.-H. Shin, E. S. Lee, N. Kim, W.-H. Lee, H. Ko, S.-P. Han, and K. H. Park, “Bias field tailored plasmonic nano-electrode for high-power terahertz photonic devices,” *Sci. Rep.*, vol. 5, p. 13817, 2015.
- [161] B. Heshmat, H. Pahlevaninezhad, Y. Pang, M. Masnadi-Shirazi, R. Burton Lewis, T. Tiedje, R. Gordon, and T. E. Darcie, “Nanoplasmonic terahertz photoconductive switch on GaAs,” *Nano Lett.*, vol. 12, no. 12, pp. 6255–6259, 2012.
- [162] S. C. Corzo-Garcia, M. Alfaro, and E. Castro-Camus, “Transit Time Enhanced Bandwidth in Nanostructured Terahertz Emitters,” *Journal of Infrared, Millimeter, and Terahertz Waves*, vol. 35, no. 12, pp. 987-992, 2014.
- [163] N. B. Burford and M. O. El-Shenawee, “Computational modeling of plasmonic thin-film terahertz photoconductive antennas,” *J. Opt. Soc. Am. B*, vol. 33, no. 4, pp. 748–759, 2016.
- [164] C. T. A. Johnk, *Engineering Electromagnetic Fields and Waves*, 2nd ed. Wiley, pp. 342-365, 1988.
- [165] S. Mickan, D. Abbott, J. Munch, X.-C. Zhang, and T. van Doorn, “Analysis of system trade-offs for terahertz imaging,” *Microelectronics J.*, vol. 31, no. 7, pp. 503–514, 2000.
- [166] D. R. Dykaar, B. I. Greene, J. F. Federici, A. F. J. Levi, L. N. Pfeiffer, and R. F. Kopf, “Log-periodic antennas for pulsed terahertz radiation,” *Appl. Phys. Lett.*, vol. 59, no. 3, pp. 262–264, 1991.
- [167] M. M. Gitin, F. W. Wise, G. Arjavalingam, Y. Pastol, and R. C. Compton, “Broadband Characterization of Millimeter-Wave Log-Periodic Antennas by Photoconductive Sampling,” *IEEE Transactions on Antennas and Propagation*, vol. 42, no. 3, pp. 335–339, 1994.
- [168] E. R. Brown, A. Lee, B. Navi, and J. Bjarnason, “Characterization of a Planar Self-Complementary Square-Spiral Antenna in the THz Region,” *Microw. Opt. Technol. Lett.*, vol. 48, no. 3, pp. 524–529, 2006.
- [169] Z. D. Taylor, E. R. Brown, J. E. Bjarnason, M. P. Hanson, and a C. Gossard, “Resonant-optical-cavity photoconductive switch with 0.5% conversion efficiency and 1.0 W peak power,” *Opt. Lett.*, vol. 31, no. 11, pp. 1729–1731, 2006.

- [170] J. Y. Suen, W. Li, Z. D. Taylor, and E. R. Brown, "Characterization and modeling of a terahertz photoconductive switch," *Appl. Phys. Lett.*, vol. 96, no. 14, pp. 2010–2012, 2010.
- [171] S. Liu, X. Shou, and A. Nahata, "Coherent detection of multiband terahertz radiation using a surface plasmon-polariton based photoconductive antenna," *IEEE Trans. Terahertz Sci. Technol.*, vol. 1, no. 2, pp. 412–415, 2011.
- [172] H. Ito, T. Yoshimatsu, H. Yamamoto, and T. Ishibashi, "Broadband photonic terahertz-wave emitter integrating uni-traveling-carrier photodiode and self-complementary planar antenna," *Opt. Eng.*, vol. 53, no. 3, p. 31209, 2014.
- [173] S. Kono, M. Tani, and K. Sakai, "Coherent detection of mid-infrared radiation up to 60 THz with an," *Optoelectron. IEE*, vol. 149, no. 3, pp. 105–109, 2002.
- [174] S. Kono, M. Tani, P. Gu, and K. Sakai, "Detection of up to 20 THz with a low-temperature-grown GaAs photoconductive antenna gated with 15 fs light pulses," *Appl. Phys. Lett.*, vol. 77, no. 25, p. 4104, 2000.
- [175] Y. C. Shen, P. C. Upadhyaya, E. H. Linfield, H. E. Beere, and A. G. Davies, "Ultrabroadband terahertz radiation from low-temperature-grown GaAs photoconductive emitters," *Appl. Phys. Lett.*, vol. 83, no. 15, pp. 3117–3119, 2003.
- [176] Y. C. Shen, P. C. Upadhyaya, H. E. Beere, E. H. Linfield, A. G. Davies, I. S. Gregory, C. Baker, W. R. Tribe, and M. J. Evans, "Generation and detection of ultrabroadband terahertz radiation using photoconductive emitters and receivers," *Appl. Phys. Lett.*, vol. 85, no. 2, pp. 164–166, 2004.
- [177] J. J. Schermer, G. J. Bauhuis, P. Mulder, E. J. Haverkamp, J. van Deelen, a. T. J. van Niftrik, and P. K. Larsen, "Photon confinement in high-efficiency, thin-film III-V solar cells obtained by epitaxial lift-off," *Thin Solid Films*, vol. 511–512, pp. 645–653, 2006.
- [178] G. J. Bauhuis, P. Mulder, E. J. Haverkamp, J. C. C. M. Huijben, and J. J. Schermer, "26.1% thin-film GaAs solar cell using epitaxial lift-off," *Sol. Energy Mater. Sol. Cells*, vol. 93, no. 9, pp. 1488–1491, 2009.
- [179] P. Demeester, I. Pollentier, P. De Dobbelaere, C. Brys, and P. Van Daele, "Epitaxial lift-off and its applications," *Semicond. Sci. Technol.*, vol. 8, pp. 1124–1135, 1993.
- [180] J. Hoffmann, C. Hafner, P. Leidenberger, J. Hesselbarth, and S. Burger, "Comparison of electromagnetic field solvers for the 3D analysis of plasmonic nano antennas," in *Proc. SPIE, Modeling Aspects in Optical Metrology*, vol. 7390, pp. 73900J, 2009.
- [181] E. Moreno, M. F. Pantoja, and S. G. Garc, "On the simulation of carrier dynamics in terahertz photoconductive antennas," 2013 7th European Conference on Antennas and Propagation, Gothenburg, 2013, pp. 749-750.

- [182] M. Sotoodeh, A. H. Khalid, and A. A. Rezazadeh, "Empirical low-field mobility model for III-V compounds applicable in device simulation codes," *J. Appl. Phys.*, vol. 87, pp. 2890–2900, 2000.
- [183] P. Johnson and R. Christy, "Optical constants of transition metals: Ti, V, Cr, Mn, Fe, Co, Ni, and Pd," *Phys. Rev. B*, vol. 9, no. 12, pp. 5056–5070, 1974.
- [184] A. D. Rakic, A. B. Djurišić, J. M. Elazar, and M. L. Majewski, "Optical Properties of Metallic Films for Vertical-Cavity Optoelectronic Devices," *Appl. Opt.*, vol. 37, no. 22, p. 5271, 1998.
- [185] D. E. Aspnes and A. A. Studna, "Dielectric functions and optical parameters of Si, Ge, GaP, GaAs, GaSb, InP, InAs, and InSb from 1.5 to 6.0 eV," *Phys. Rev. B*, vol. 27, no. 2, pp. 985–1009, 1983.
- [186] S. Selberherr, W. Hansch, M. Seavey, and J. Slotboom, "The Evolution of the MINIMOS Mobility Model," *Solid-State Electronics*, vol. 33, no. 11, pp. 1425–1436, 1990.
- [187] N. M. Burford, "Plasmonic Nanostructures for the Absorption Enhancement of Silicon Solar Cells," University of Arkansas, 2013.
- [188] N. Khiabani, Yi Huang, Yao-chun Shen, S. Boyes, and Qian Xu, "A novel simulation method for THz photoconductive antenna characterization," 2013 7th European Conference on Antennas and Propagation, Gothenburg, 2013, pp. 751–754.
- [189] N. Khiabani, Y. Huang, Y. C. Shen, and S. J. Boyes, "Theoretical modeling of a photoconductive antenna in a terahertz pulsed system," *IEEE Trans. Antennas Propag.*, vol. 61, no. 4, pp. 1538–1546, 2013.
- [190] E. Moreno, M. F. Pantoja, F. G. Ruiz, J. B. Roldán, and S. G. García, "On the numerical modeling of terahertz photoconductive antennas," *J. Infrared, Millimeter, Terahertz Waves*, vol. 35, no. 5, pp. 432–444, 2014.
- [191] K. Tsen, *Ultrafast Dynamical Processes in Semiconductors*. Springer, pp. 139-258, 2004.
- [192] "PE-50 Benchtop Plasma Cleaner." Internet: <http://www.plasmaetch.com/pe-50-plasma-cleaner.php>, 2016 [Dec. 5, 2016].
- [193] Edwards Auto 306 Electron Beam Evaporator, BOC Edwards, Crawley, West Sussex, UK.
- [194] PM5 Precision Lapping & Polishing System, Logitech LTD, Glasgow, UK.
- [195] S. J. Prakash, R. Tyagi, and A. Gupta, "Backside thinning of GaAs wafer by lapping using DOE approach," *India Int. Conf. Power Electron. IICPE 2010*, pp. 1–4, 2011.
- [196] A. R. Clawson, "Guide to references on III-V semiconductor chemical etching," *Mater. Sci. Eng. R Reports*, vol. 31, no. 1–6, pp. 1–438, 2001.

- [197] XL-30 Environmental Scanning Electron Microscope, Phillips Electronics, Andover, MA, USA.
- [198] Nanometer Pattern Generation System, JC Nability Lithography Systems, Bozeman, MT, USA
- [199] 495 PMMA A4, MicroChem, Westborough, MA, USA.
- [200] S. J. Bauman, private communication, Jan., 2015.
- [201] EPO-TEK P1011, Epoxy Technology, Inc., Billerica, MA, USA.
- [202] TPS Spectra 3000, Teraview LTD, Cambridge, UK.
- [203] S. Arscott, F. Garet, P. Mounaix, L. Duvillaret, J. Coutaz, and D. Lippens, “All-Optical AND Gate Using Cross-Gain Modulation in Semiconductor Optical Amplifiers,” *Electron*, vol. 35, no. 3, 1999.
- [204] D. Grischkowsky, S. Keiding, M. Van Exter, and C. Fattinger, “Far-infrared time-domain spectroscopy with terahertz beams of dielectrics and semiconductors,” *J. Opt. Soc. Am. B*, vol. 7, no. 10, p. 2006, 1990.
- [205] I. S. Gregory, C. Baker, W. R. Tribe, M. J. Evans, H. E. Beere, E. H. Linfield, A. G. Davies, and M. Missous, “High resistivity annealed low-temperature GaAs with 100 fs lifetimes,” *Appl. Phys. Lett.*, vol. 83, no. 20, pp. 4199–4201, 2003.
- [206] “AG Associates Heatpulse 610 Manual,” Internet: <http://www.ag-rtp.com/heatpulse610-manual.htm>, [Dec. 12, 2016].
- [207] 4140B pA / DC Voltage Source, Hewlett-Packard, Palo Alto, CA, USA.
- [208] THz2.5B-BL-DZ, Gentec Electro-Optics, Inc., Lake Oswego, OR, USA.

Appendix A: Description of Research for Popular Publication

The Final Frontier

Exploring the Last Region of the Electromagnetic Spectrum

How many of us recall a time before wireless communication fit in the palm of your hand? Or when lasers were only found in laboratories, rather than being something you can purchase for \$3 at the supermarket? What about x-rays? Imagine how stressful it must have been to not really know what's going on inside your body when something is definitely wrong, such as having a broken bone. All of these great technologies rose from our study and understanding of various regions of the electromagnetic spectrum. This was made possible by the development of devices that can generate and detect electromagnetic waves at these various frequencies, allowing these applications to be developed.

However, as Captain James T. Kirk of the starship Enterprise would describe it, there is “the final frontier” of the electromagnetic spectrum, a band of frequencies lying between microwaves and infrared light known as the “terahertz gap”. The terahertz gap offers many promising applications in areas of medical imaging, security screening, material characterization and nondestructive quality control. But the problem that has plagued terahertz technology since its discovery has been low power, a few micro Watts at best. Imagine if the strongest lasers in the world were still 1000 times weaker than common classroom laser pointers we have today. It doesn't take much imagination to realize that would severely limit their potential applications, but that's the reality terahertz technology currently faces.

The problem is that generation of terahertz waves is extremely inefficient, since standard antenna technology does not work at these high frequencies. Instead, terahertz waves are generated using a pulsed laser, an antenna, and a photoconductor. Laser pulses that are absorbed in the photoconductor generate pulses of electrical current, similar to how striking a guitar string creates pulses of sound waves. These current pulses feed directly into a terahertz antenna and are emitted as pulses of terahertz light. The problem is that only a tiny amount, less than 0.01%, of the laser power ends up converting to terahertz power, most is reflected or absorbed too far from the antenna.

However, at the University of Arkansas, Microelectronics-Photonics Ph.D. student Nathan Burford and his major professor Dr. Magda El-Shenawee are working to overcome this limitation. Since the laser is made of waves, it can be made to resonate inside of cavities, just like sound waves resonate in an acoustic guitar or a drum. By designing a clever geometry for the photoconductor and antenna of a terahertz source, Mr. Burford and Dr. El-Shenawee have shown using computer modeling that it's possible to force the incident laser pulses to resonate inside the photoconductor. This reduces reflection off the photoconductor surface and allows more of the laser power to be absorbed near the antenna.

“We use computer modeling to design devices before fabricating them,” says Mr. Burford. “This reduces lab time and material costs associated with designing devices by trial and error.”

Modeling of these terahertz antennas have shown up the 300 times increase in the antenna driving current, with preliminary experimental results suggesting similar improvements.

“Although there is a lot of work left, pushing antenna performance to these higher frequencies will be critical to unlocking the many promising applications of the terahertz gap.”

Appendix B: Executive Summary of Newly Created Intellectual Property

The following list of new intellectual property items were created in the course of this research project and should be considered from both a patent and commercialization perspective.

1. A device comprising of a sub-micron thick photoconductive layer, metal electrodes and periodic metal nanostructure array that allows sub-picosecond device response time regardless of the photoconductor carrier lifetime.
2. A fabrication method for transferring and bonding sub-micron thick photoconductor films to other substrates, allowing top-down fabrication process to be implemented on both sides of the thin-films.
3. A computational method for combining frequency domain optical modeling with time domain semiconductor device modeling to study the transient response of photoconductive devices.

Appendix C: Potential Patent and Commercialization Aspects of listed Intellectual Property Items

C.1 Patentability of Intellectual Property (Could Each Item Be Patented)

The three items listed were considered first from the perspective of whether or not the item could be patented.

1. The device design described in item 1 could be patented. This device architecture represent functionality and design not previously described in the literature or prior patents.
2. The fabrication method of item 2 could not be patented. This process is adopted from well-known standard wafer bonding, thinning and selective etching processes. It is unique only in that it has been developed specifically for LT-GaAs thin-films.
3. The computational method of item 3 could not be patented. This method was developed within a commercially available package (COMSOL[®] Multiphysics). It is based off known methods from the literature and unique in the approximations made to simplify the computational model.

C.2 Commercialization Prospects (Should Each Item Be Patented)

The three items listed were considered first from the perspective of whether or not the item should be patented.

1. The device design in item 1 should not, at this time be patented. The experimental results were not conclusive in supporting the hypothesized performance increase over industry standard devices.
2. Not applicable
3. Not applicable

C.3 Possible Prior Disclosure of IP

The following items were discussed in a public forum or have published information that could impact the patentability of the listed IP.

1. The device design described in item 1 was discussed in publications and presentations by the author. The following is a list of publications

N. Burford and M. El-Shenawee, "Computational Modeling of Plasmonic Thin-Film Terahertz Photoconductive Antennas," *J. Opt. Soc. Am. B*, vol. 33, no. 4, pp. 748-759, 2016.

N. Burford and M. El-Shenawee, "Simulation, Fabrication and Measurement of Plasmonic-Enhanced Terahertz Photoconductive Antenna," *Proc. of SPIE Photonics West OPTO 2016*, 15-18 2016.

N. Burford and M. El-Shenawee, "Modeling of Plasmonic Terahertz Antennas using COMSOL Multiphysics," *Proc. of the IEEE Int. Symp. on Antennas and Prop. and North American Radio Science Meeting, Vancouver, Canada, 19-24 July 2015*.

2. Not applicable
3. Not applicable

Appendix D: Broader Impact of Research

D.1 Applicability of Research Methods to Other Problems

The research methods utilized in this work to design and study the proposed THz photoconductive antenna can be applied to many other problems. Often, device designs are considered on a high conceptual level only, before proceeding to fabrication and testing of devices. The described approach of concept, rigorous theoretical modeling, fabrication and testing demonstrates how a strong theoretical background can be used to predict device performance before significant time and financial investment in fabrication and testing is made. This could be applied directly to other optoelectronic devices, such as LEDs, semiconductor photodetectors and solar cells. While this work is focused on LT-GaAs based devices, THz PCAs utilizing other material systems such as InGaAs or multi-quantum-well structures could also be studied using the described methodology.

D.2 Impacts of Research Results on U.S. and Global Society

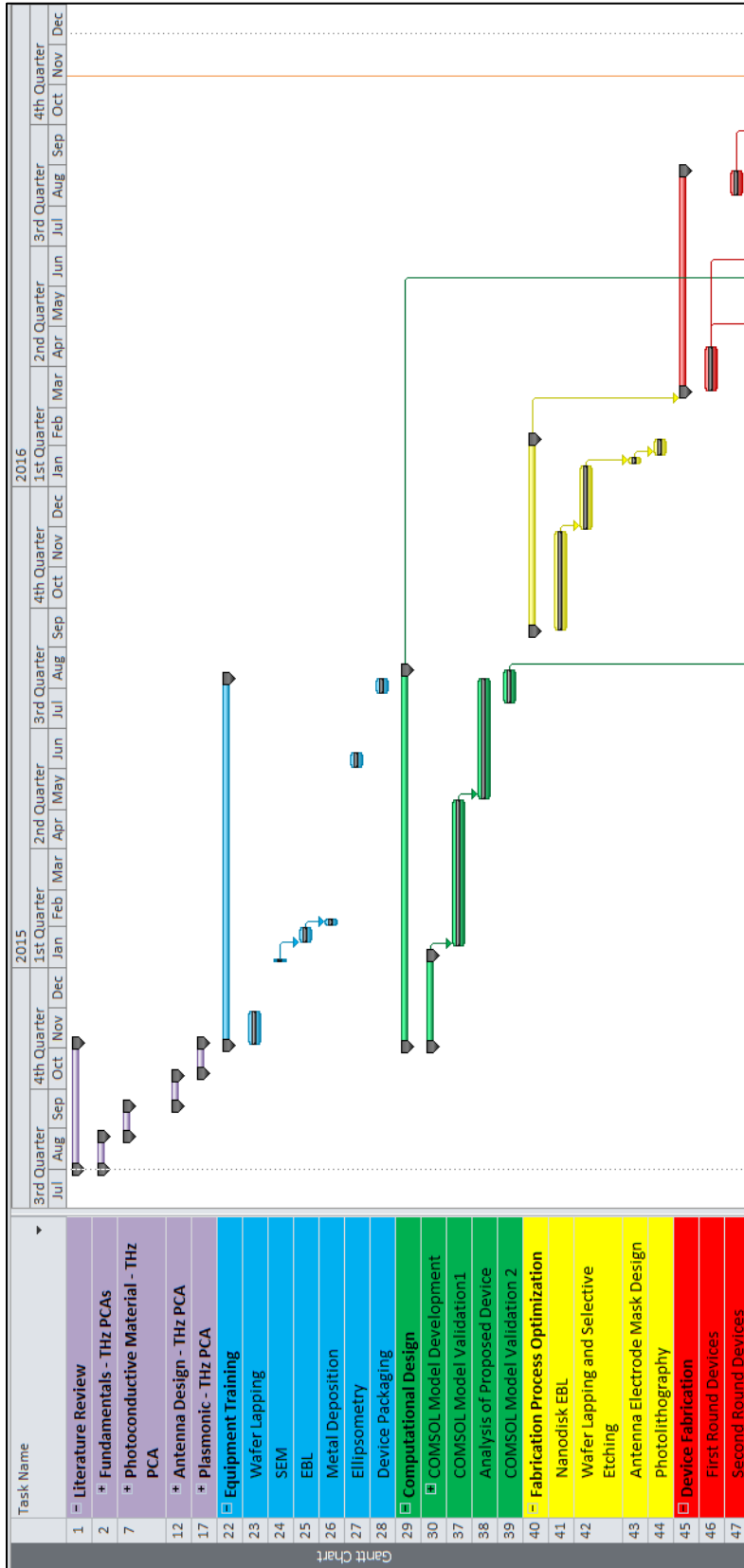
The research results of this dissertation have potential for impacting U.S. and global society. The issue addressed in this work is the low output power of THz frequency devices. This band of the electromagnetic spectrum is not extensively utilized, one of the reasons being this technological limitation. Since THz technology has potential applications in cancer screening, development of high power THz sources could improve human survival rates of certain types of cancers, providing a potential increase in total human population. Other applications of security screening could be realized with such high power THz sources. Although not likely to have

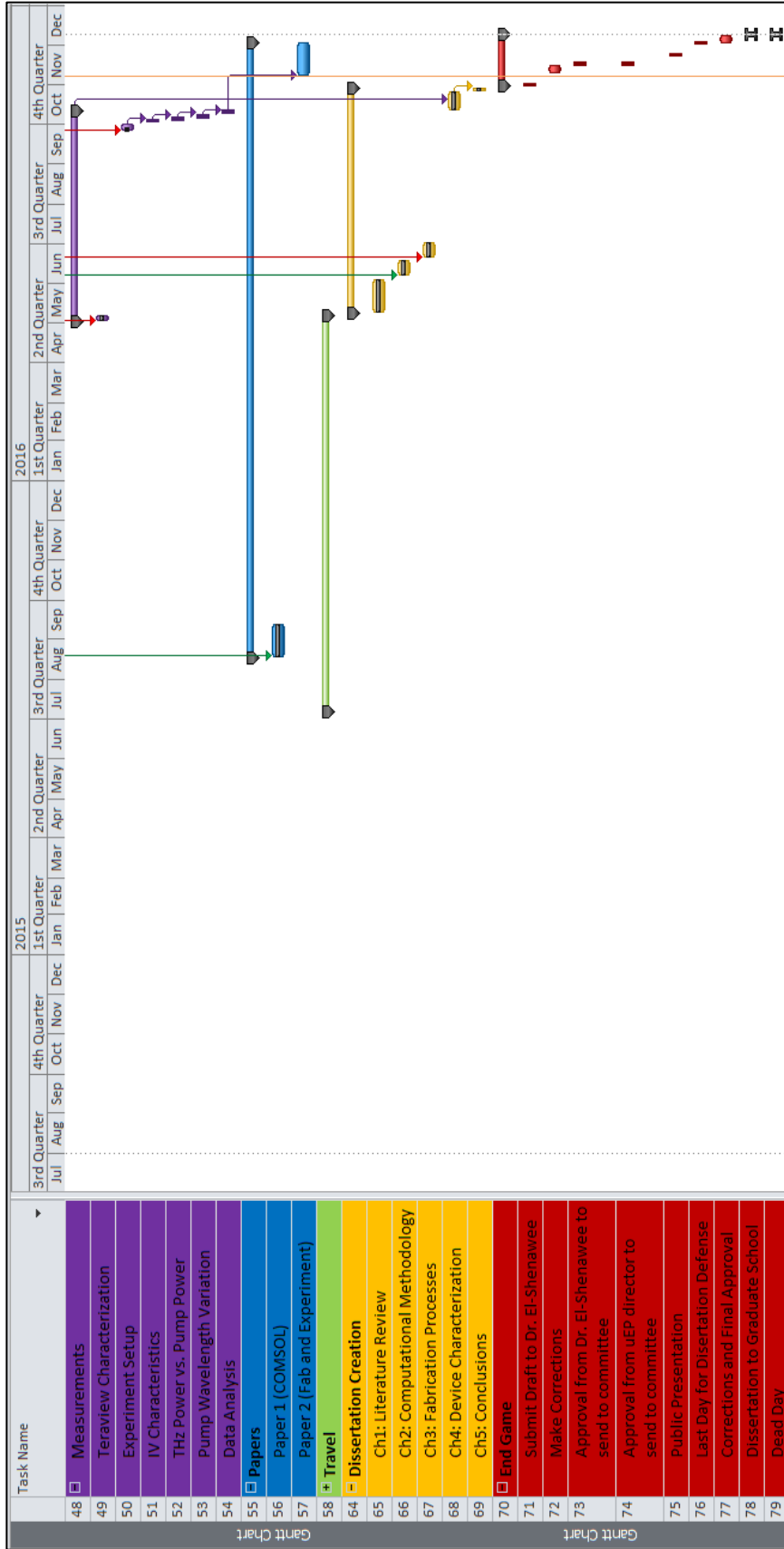
significant effect on total human population density, THz frequency security screening would raise many societal questions in regards to privacy. This is due to the higher resolution achieved in THz imaging allowing a high level of detail of a person's body to be seen when fully clothed. These questions have already been raised with lower resolution millimeter wave imaging currently used in many U.S. airport checkpoints and would only be exaggerated through the implementation of THz technology in these applications.

D.3 Impact of Research Results on the Environment

The research results do not have significant foreseeable adverse effects on the environment. This is mainly due the fact that even under the complete adoption and realization of THz PCA based technology, the total number of THz PCA devices produced would be insignificant compared to production of other semiconductor devices. However, it is possible that medical applications of THz technology could impact the average human life span, indicating that environmental impacts are not completely unreasonable.

Appendix E: Microsoft Project for Ph.D. MicroEP Degree Plan





Appendix F: Identification of All Software Used in Research and Dissertation Generation

Computer #1

Model Number: Dell Optiplex 980
Serial Number: 2Q2MLM1
Location: ENRC 4906
Owner: Dr. Magda El-Shenawee

Software #1

Name: COMSOL® Multiphysics
Owner: Dr. Magda El-Shenawee

Software #2

Name: ANSYS® HFSS
Owner: Dr. Magda El-Shenawee

Software #3

Name: Microsoft Office 2016
Owner: Electrical Engineering Department

Software #4

Name: Matlab vR2013a
Owner: Electrical Engineering Department

Computer #2

Model Number: Dell Latitude E5520
Serial Number: 26082332533
Location: N/A
Owner: Dr. Magda El-Shenawee

Software #1

Name: Microsoft Office 2016
Owner: Electrical Engineering Department

Appendix G: All Publications Published, Submitted and Planned

Journal Publications

- N. Burford and M. El-Shenawee, “Computational Modeling of Plasmonic Thin-Film Terahertz Photoconductive Antennas,” *J. Opt. Soc. Am. B*, vol. 33, no. 4, pp. 748-759, 2016.
- N. Burford and M. El-Shenawee, “Optimization of Silver Nanotoroid Arrays for the Absorption Enhancement of Silicon Thin-Film Solar Cells,” *Plasmonics*, vol. 10, pp. 1-8, 2014
- N. Burford, M. El-Shenawee, C. O’Neal and K. Olejniczak, “Terahertz Imaging for Nondestructive Evaluation of Packaged Power Electronic Devices,” *International Journal of Emerging Technology and Advanced Engineering*, vol. 4, no. 1, pp. 395-401, 2014
- N. Burford and M. El-Shenawee, “Plasmonic Enhancement of Irregular Shape Nano-Patch for Thin Film Silicon Solar Cells,” *Journal of Applied Computational Electromagnetics*, vol. 28, no. 5, pp. 359-373, 2013.
- N. Burford and Y. Zhang, “Experimental Investigation of Polarization Rotation by Multilayer Chiral Metamaterial,” *Journal of Basic and Applied Physics*, vol. 2, no. 4, pp. 205-210, 2013

Conference Proceedings

- N. Burford and M. El-Shenawee, “Simulation, Fabrication and Measurement of Plasmonic-Enhanced Terahertz Photoconductive Antenna,” *Proc. of SPIE Photonics West OPTO 2016*, 15-18 2016.
- N. Smith, L. Rivera, N. Burford, T. Bowman, M. El-Shenawee, and G. DeSouza, “Towards Root Phenotyping in situ Using Terahertz Imaging,” *Proc. of 40th Int. Conf. IRMMW-THz, Hong Kong, 23-28 August 2015*.
- N. Burford and M. El-Shenawee, “Modeling of Plasmonic Terahertz Antennas using COMSOL Multiphysics,” *Proc. of the IEEE Int. Symp. on Antennas and Prop. and North American Radio Science Meeting, Vancouver, Canada, 19-24 July 2015*.
- N. Burford and M. El-Shenawee, “Enhancement of Terahertz Imaging of Packaged Power Electronic Devices,” *Proc. of the IEEE Int. Symp. on Antennas and Prop. and North American Radio Science Meeting, Vancouver, Canada, 19-24 July 2015*.
- M. El-Shenawee, T. Bowman, N. Burford. “Terahertz Imaging and Spectroscopy for Biomedical, Security and Industrial Applications at the University of Arkansas.” *PittCon 2015, New Orleans, 7-12 March 2015*.
- N. Burford and M. El-Shenawee, “Terahertz Investigation of X-Ray Anti-Imaging Coatings: Spectroscopic Characterization and Imaging,” *Proc. 39th Int. Conf. IRMMW-THz, Tucson, AZ, September 14-19, 2014*.
- N. Burford and M. El-Shenawee, “Multiphysics Modeling of THz Photoconductive Antennas,” *Proc. 39th Int. Conf. IRMMW-THz, Tucson, AZ, September 14-19, 2014*.
- H. Tran, N. Burford, S. Ghetmiri, L. Huang, M. El-Shenawee and S. Yu, “Resonant Spectra of Metal Nanotoroids with Various Sizes,” *STEM Posters at the Arkansas State Capitol, Little Rock, AR, March 7, 2014*.

- N. Burford and M. El-Shenawee, “Time-Domain Terahertz Imaging and Spectroscopy of X-Ray Blocking and Scattering Coatings,” Proc. 2014 National Radio Science Meeting, Boulder, USA, January 8-11, 2014.
- N. Burford and M. El-Shenawee, “Terahertz Spectroscopy of Photovoltaic Semiconductors,” Proc. Of the IEEE Int. Symp. on Antennas and Prop. And USNC/URSI Nation Radio Science Meeting, Orlando, USA, Jul 7-13, 2013.
- N. Burford and M. El-Shenawee, “Optimization of Nanotoroid Arrays for Plasmonic Solar Cell Applications,” Proc. Of the IEEE Int. Symp. on Antennas and Prop. And USNC/URSI Nation Radio Science Meeting, Orlando, USA, Jul 7-13, 2013.
- N. Burford and M. El-Shenawee, "Parallel MoM Computation of Localized Field in Silicon due to Finite Array of Nanotoroids," Proc. 29th Annual Review of Progress in Applied Computational Electromagnetics, March 24-28, 2013.
- N. Burford and M. El-Shenawee, "Qualitative Measure of Photocurrent Enhancement in Silicon Solar Cells due to Plasmonic Antennas," Proc. 29th Annual Review of Progress in Applied Computational Electromagnetics, March 24-28, 2013.
- N. Burford, M. El-Shenawee, S. Shumate, D. Hutchings, H. Naseem, “Field enhancement due to surface structuring during aluminum induced crystallization of amorphous silicon,” Proc. of the IEEE Int. Symp. on Antennas and Prop. and USNC/URSI National Radio Science Meeting, Chicago, USA, July 8-13, 2012.
- N. Burford and M. El-Shenawee, “Absorption Enhancement in Silicon Solar Cells due to Surface Plasmons of Nanotoroids,” Proc. of the IEEE Int. Symp. on Antennas and Prop. and USNC/URSI National Radio Science Meeting, Chicago, USA, July 8-13, 2012.
- N. Burford, S. Marsh, Y. Zhang and J. N. Dahiya, “Polarization Rotation by Multilayered Helix Metamaterial,” Proc. of the IEEE Int. Symp. on Antennas and Prop. and USNC/URSI National Radio Science Meeting, Chicago, USA, July 8-13, 2012.
- N. Burford, Y. Zhang and J. N. Dahiya, “Polarization Rotation by Helix Metamaterial,” Proc. of the IEEE Int. Symp. on Antennas and Prop. and USNC/URSI National Radio Science Meeting, Spokane, USA, July 3-8, 2011.
- J. Lumpkin, C. Yuen, N. Burford, E. Gidney, T. McCallister, J. Peng and S. Ghosh, “Evaluation of Magnetic Field Induced Losses of Thermoresponsive, Multifunctional, Magnetic Nano-carriers for Hyperthermia and Controlled Drug Release,” Materials Research Society Fall 2011 Meeting, Boston, USA, Nov. 27 – Dec. 2, 2011.

Planned Publications

- N. Burford and M. El-Shenawee, “A Review of Terahertz Photoconductive Antenna Technology,” submitted to Optical Engineering.
- N. Burford, M. El-Shenawee and Michael Evans “Fabrication and Characterization of Plasmonic Enhanced Thin-Film Terahertz Photoconductive Antenna” Planned for Publication

Appendix H: Copyright Permissions

Copyright permission was obtained for reprint of Figure 1.2.2.1 from the Electronics and Telecommunications Research Institute. Permission was received from an authorized agent on October 18, 2016.

Copyright permissions were obtained for reprint of Figure 1.2.4.1 and Figure 1.4.3.1 from OSA Publishing. Permission was received from an authorized agent on October 17, 2016.

Copyright permissions were obtained for reprint of Figure 1.3.3.1 and Figure 1.5.3.1 from the AIP Publishing. Permission was received through RightsLink[®] on October 12, 2016.

Copyright permission was obtained for reprint of Figure 1.4.4.1 and Figure 1.4.4.2 as part of the Creative Commons Attribution 4.0 International License.